

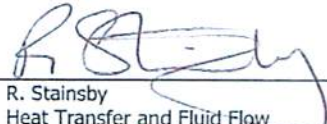


**Investigation of Local Heat Transfer
Phenomena in a Prismatic Modular
Reactor Core**

NR001/RP/001 R02

May 15, 2009

Prepared by:


R. Stainsby

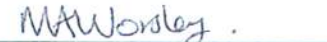
Heat Transfer and Fluid Flow
Consultant
AMEC Nuclear (UK)

Prepared by:


A. Grief

Thermal Hydraulics and CFD
Consultant
AMEC Nuclear (UK)

Prepared by:


M. Worsley


Senior Physicist
AMEC Nuclear (UK)

Verified by:


E. Van Heerden

Senior Analyst
AMEC NSS

Prepared by:


F. Dawson

Analyst
AMEC Nuclear (UK)

Reviewed by:


A. Dennier

TH Applications and Methods
AMEC NSS

Approved by:


W. Bowman

Director – Thermal Hydraulics
AMEC NSS

Revision Summary

Rev	Date	Author	Comments
R00	September 2008	R. Stainsby	For U.S. NRC Review.
R01	March 2009	R. Stainsby	For U.S. NRC Review.
R02	May 2009	R. Stainsby	Incorporate an Executive Summary per U.S. NRC's request.

Executive Summary

This report summarizes the research on Prismatic Modular Core Reactors Heat Transfer from the study "Investigation of the Local Heat Transfer Phenomena in an HTGR Core", solicitation number RES-07-087.

The objective of this work is to identify, and develop where necessary, the computational tools and techniques to resolve local fluid behavior in the core of a high temperature gas reactor (HTGR). This information is needed for U.S. NRC staff to develop the evaluation model that will be used to evaluate licensee calculations under normal operation and accident conditions. Several models have been developed and sensitivity studies have been performed as part of this research based on the thermal fluids and accidents analysis R&D phenomena identification and ranking tables (PIRT) developed by the US NRC for HTGRs. Based on this research, constitutive models will be developed for inclusion into systems codes (such as the code MELCOR) that are being developed to predict the system-wide thermal fluidic behavior of HTGRs.

This report is structured into nine sections. Sections 1 to 3 present an introduction, a discussion of prismatic core HTGRs and a review of the U.S. NRC's Thermofluid and Accident Analysis PIRT exercise. Section 4 presents the scope of the research program covered by this report and how this is linked to the findings of the aforementioned PIRT exercise.

The investigations were divided into three main themes with each theme targeted on groups of the high-priority PIRT items. These themes were chosen to capture the heat transfer mechanisms from the scale of individual fuel compacts out to the scale of the whole core. The accompanying report on the work carried out within this project on Pebble Bed reactors (NR001/RP/002 R01) presents models for the shorter length scale that ranges from within an individual coated particle out to the surface of a pebble. These "micro-scale" models are completely applicable to the cylindrical fuel compacts employed within prismatic cores, so there was no need to consider this shortest length scale within this work. The research themes considered, therefore, are:

1. Fuel element (meso-scale) internal flow and heat transfer models.
2. Fuel element to fuel element heat transfer models.
3. The influence of core bypass flows.

Sections 5 and 6 describe the work and results from investigations of the first theme. Within Section 5 multi-scale models for the heat transfer from within a fuel compact to the coolant have been developed. These models are based on the Fort St Vrain style of fuel blocks as these are used in designs currently under consideration for deployment in the Next Generation Nuclear Plant (NGNP). To aid the development of this model, the length scale ranging from within the fuel compact to the coolant channels, originally considered to be the "meso-scale" has been subdivided into meso

and super-meso scales. The heat source provided by the fuel is decomposed into a spatially averaged value which is applied within the super-meso-scale and a local perturbation in and around a fuel compact, applied within the meso-scale model. This decomposition of the heat source allows two transient partial differential equations to be solved independently and their solutions combined to re-compose the temperature distribution between the fuel compact centre to the coolant channel. A further simplification is made in which the hexagonal domains are approximated as axis-symmetric cylindrical domains, reducing the solutions to be one-dimensional and computationally efficient. Comparisons with finite element simulations have been made and the multi-scale model is seen to perform well both in steady state and severe transient conditions. A refinement was made to introduce contact and gap resistances between the fuel compact and its channel wall in both the multi-scale and finite element models. Initial comparisons showed that the original multi-scale model did not compare well with high contact/gap resistances. A correction was devised which re-scaled the resistance according to the ratio of the actual power in the fuel compact to the size of the power perturbation in the meso-scale model. Introduction of this correction regained the good agreement with the finite element predictions. Most of the work so far has been performed assuming a constant, but low, thermal conductivity for the graphite of the fuel block. An extension of this work would be to validate this model further by comparing the results using realistic temperature and irradiation induced spatial variations in graphite thermal conductivity.

Section 6 presents an analytical model for the determination of the effective thermal conductivity of a complete fuel element, accounting for the presence of the coolant and fuel channels within the graphite matrix. This model is an extension of Maxwell's method to account for the presence of three distinct materials. Finite element simulations of a representative section of fuel block have been made. Two such finite element models were set up to investigate if the thermal conductivity is isotropic. As such, these had heat flow directions aligned, alternatively, with the across-flats and across-corners directions. Eleven different combinations of matrix and fuel compact conductivities were simulated, using graphite conductivities ranging from 15 W/m.K up to 60 W/m.K, and fuel compact conductivities ranging from 10 W/m.K up to 30 W/m.K. The helium conductivity was held constant in all cases at 0.35 W/m.K. This work showed that there is no difference in the thermal conductivity between the across-flats and across-corners directions and that the modified Maxwell's method predicts the effective thermal conductivity reliably with the differences from the finite element predictions ranging from -1.0% up to +1.89% over the range of fuel compact and graphite matrix conductivities considered. No attempt has yet been made to account for the fuel compact-fuel channel contact/gap resistances.

The second research theme, concerned with heat transfer between neighboring fuel elements, is addressed in Section 7. Analytical (network) models of the heat transfers within a single fuel element (intra-block) and between neighboring fuel elements (inter-block), in the presence of power and flow gradients, have been developed. These models were based on a steady state analytical implementation of the multi-scale model presented in Section 5 combined with a two-dimensional numerical conduction solution based on a coarse grid of triangular elements on the macro-scale.

Three test problems were established in which the following heat transfers were modeled:

- (i) between the 6 sectors of single block (the intra-block model),
- (ii) between the adjacent 1/6th sectors of two neighboring blocks (the inter-block models), and
- (iii) across three half-blocks connected in series (the combined intra and inter block model, or more simply, "the combined model").

Finite element and multi-scale models were constructed of the above three test problems and the results compared. In general the finite element results show that, in normal operation with forced cooling, the temperature distribution within a block follows the power distribution. If the power density varies linearly across the block, then the macroscopic temperature also varies linearly. Similarly if the power distribution is flat, then the macroscopic temperature distribution is also flat. Heat loss from (or heat gain through) the edges of the block only perturbs the temperatures in the edge rows of coolant and fuel channels and does not propagate into the centre of the block.

These findings have important consequences for the way in which macroscopic heat transfer is modeled in a coarse-grid whole core model or system code. First, the assumption of simple linear temperature variations within the sectors of the blocks is a poor approximation. Second, the assumption that the real variation in power density can be approximated by piecewise-constant power distribution applied over the triangular sectors within a block is also a poor approximation. Some progress has been made in developing a semi-analytical temperature profile to resolve the edge effects better, but this is applicable only in steady state conditions. Transient simulations will most probably require a much finer grid resolution in the macro-scale solution to resolve the temperature and power distributions correctly.

The third research theme on investigating the influence of core bypass flows is addressed in Section 8. The purpose of this work was to integrate the sub-models of Sections 5 to 7 into a system code model of a part of a prismatic core, and to use this model to study a few coolant bypass scenarios. The RELAP5 code was selected, initially, to be the basis of this model. Subsequently, U.S. NRC's staff implemented the same model using the TRACE code (U.S. NRC's work with TRACE is included in this report as Appendix C).

A literature review was carried out to assemble information to quantify the hydraulic resistances of the block end face leakage paths for different types and magnitudes of column distortions. Useful data sources were found to be Gulf General Atomics' design studies for Fort St Vrain, JAERI's studies for the development of HTTR and the U.S. DOE research into VHTR system modeling needs. All of the quantitative information obtained came from laboratory tests of engineered leak paths – no historical quantitative information from reactor operations could be obtained. Suitable hydraulic resistances for wedge-shaped and parallel sided block end face

displacements were derived using the methods presented in the literature and built into the RELAP5 models.

Two RELAP5 models were constructed, the first "one-channel" model contained one quarter-block column and the surrounding inter-block space which contained all of the fuel blocks up to the full height of the core. The second model, the "six-channel" model represented a radial slice through the annular fuelled region of the GT-MHR core, comprising three half-blocks (or six quarter-blocks), again extending over the full height of the core.

The results of both models show that existence of end-face gap leakage paths encourages flow to bypass the hottest (lowest density and highest hydraulic resistance) regions of the core. This is shown to amplify the effect of a non-uniform power distribution on the non-uniformity of temperature within the core. The work has shown that the behavior of the bypass flows is strongly influenced by the power distribution in the core. Heat loss from the edges of fuel blocks will influence the temperatures, and therefore hydraulic resistances, of the flows in the inter-block gaps. These heat losses have been neglected in the current model, and the work of Section 7 shows that care must be taken in resolving these correctly. Further work is required to couple the block-to-block and coolant leakage flows completely and to achieve this in a manner that will allow transients to be investigated.

Section 9 presents the overall conclusions arising from the work and makes recommendations for further work. These recommendations are summarized as:

1. The work shown in Section 5 should be extended to include in the finite element and multi-scale simulations the spatial and temperature dependence of material properties.
2. Contact resistances between the fuel compacts and fuel channels should be included in the Maxwell model presented in Section 6.
3. The macroscopic model described in Section 7 needs to be revised to correctly model heat transfers within and between fuel blocks in the presence of steep power gradients. The semi-analytical approach is likely only to be suitable for steady state scenarios, so further work is required to develop a model that will work correctly in transient conditions.
4. The core bypass flow model given in Section 8 is only a steady state model at the moment and neglects heat transfer into the inter-block gaps. Refinements of the macroscopic scale model of Section 7, together with a fuller implementation of the meso and super-meso models would allow heat input into the inter-block gaps to be included and transients to be simulated.

Table of Contents

	Page
1.0 INTRODUCTION.....	1-1
1.1 References for Section 1.....	1-2
2.0 PRISMATIC MODULAR REACTOR CORES.....	2-1
2.1 Purpose of Section 2.....	2-1
2.2 Early HTRs.....	2-1
2.2.1 Dragon.....	2-1
2.2.2 Peach Bottom Unit 1.....	2-1
2.2.3 Fort St Vrain.....	2-2
2.2.4 HTTR.....	2-2
2.2.4.1 Pin-in-block-type fuel.....	2-2
2.3 Current HTR Designs.....	2-5
2.3.1 GTHTR300.....	2-5
2.3.2 GT-MHR.....	2-5
2.3.2.1 GT-MHR block-type core.....	2-6
2.3.3 ANTARES.....	2-9
2.4 References for Section 2.....	2-10
3.0 REVIEW OF U.S. NRC THERMOFLUID AND ACCIDENT ANALYSIS PIRT WITH REGARD TO PRISMATIC CORES	3-1
3.1 Purpose of Section 3.....	3-1
3.2 Findings of the PIRT.....	3-1
3.3 Allocation of Research Priorities.....	3-3
3.3.1 Prioritised list of phenomena and scenario pairings.....	3-3
3.3.2 High priority research items.....	3-6
3.4 References for Section 3.....	3-7
4.0 SCOPE OF THE CURRENT PROGRAMME OF RESEARCH.....	4-1
4.1 Purpose of Section 4.....	4-1
4.2 PMR Theme 1.....	4-1
4.3 PMR Theme 2.....	4-2
4.4 PMR Theme 3.....	4-3
4.5 References for Section 4.....	4-4
5.0 MODELS FOR THE PREDICTION OF FUEL AND GRAPHITE TEMPERATURES	5-1

5.1	Purpose of Section 5	5-1
5.2	Finite Element Solutions for the Meso-Scale Domains.....	5-2
5.2.1	Modeled geometry and boundary conditions.....	5-2
5.2.2	Material properties	5-6
5.2.2.1	Model 1.....	5-6
5.2.2.2	Model 2.....	5-7
5.2.3	Boundary values and power density in a fuel compact.....	5-8
5.2.4	Finite element mesh.....	5-8
5.2.5	Model 1 results with a constant graphite thermal conductivity.....	5-10
5.2.5.1	Steady state model results.....	5-10
5.2.5.2	Transient models	5-13
5.2.6	Model 1 results with a varying graphite thermal conductivity	5-15
5.2.6.1	Transient Model 1	5-15
5.2.6.2	Transient Model 2	5-17
5.2.7	Model 2 results with a constant graphite thermal conductivity.....	5-17
5.2.7.1	Steady state	5-18
5.2.7.2	Transient models	5-22
5.2.8	Model 2 results with a varying graphite thermal conductivity	5-23
5.2.8.1	Transient Model 1	5-23
5.2.8.2	Transient Model 2	5-24
5.3	Development of Meso-Scale Sub-Models	5-25
5.3.1	Previous analytical steady state approach	5-26
5.3.2	New multi-scale approach.....	5-34
5.3.3	Inclusion of contact and gap resistances	5-47
5.4	Assumptions and Limitations.....	5-49
5.5	Closure	5-50
5.6	References for Section 5.....	5-50

6.0 DETERMINATION OF THE EFFECTIVE CONDUCTIVITY OF FUEL ELEMENTS
..... **6-1**

6.1	Purpose of Section 6	6-1
6.2	Analytical Model.....	6-1
6.2.1	Maxwell's theory of the conductivity of composite materials.....	6-2
6.2.2	Temperature field around a single cylinder within an infinite domain	6-2
6.2.3	Thermal conductivity of several cylinders	6-4
6.3	Finite Element Models	6-5
6.3.1	Fort St Vrain / GT-MHR fuel block design	6-5
6.3.2	Geometry used for 2-D finite element models.....	6-6
6.3.3	Material properties	6-6
6.3.4	Boundary conditions.....	6-7
6.3.5	Finite element meshes and model variants.....	6-7
6.3.6	Determination of effective conductivities from finite element results.....	6-8
6.3.7	Predicted effective thermal conductivities.....	6-10
6.4	Comparison with Analytical Results.....	6-14
6.5	Closure	6-17
6.6	References for Section 6.....	6-17

7.0	WHOLE-CORE (MACROSCOPIC) HEAT TRANSFER	7-1
7.1	Purpose of Section 7	7-1
7.2	Finite Element Solutions for the Whole Core Conduction Model	7-1
7.2.1	Modeled geometry	7-2
7.2.2	Material properties	7-2
7.2.3	Boundary values and power density in a fuel compact.....	7-3
7.2.4	Model conditions applied	7-5
7.2.4.1	Intra-block model conditions.....	7-5
7.2.4.2	Inter-block model conditions.....	7-6
7.2.4.3	Combined block model conditions.....	7-7
7.2.5	Finite element meshes.....	7-8
7.2.6	Results of the intra-block model	7-8
7.2.6.1	Intra-block Variant 1 results.....	7-8
7.2.6.2	Intra-block Variant 2 results.....	7-9
7.2.7	Results of the inter-block model	7-11
7.2.7.1	Inter-block Variant 1 results.....	7-11
7.2.7.2	Inter-block Variant 2 results.....	7-11
7.2.8	Results of the combined block Model	7-15
7.2.8.1	Combined model Variant 1 results	7-15
7.2.8.2	Combined model Variant 2 results	7-20
7.2.8.3	Combined model Variant 3 results	7-24
7.3	Development of an Analytical Whole Core Conduction Model	7-27
7.3.1	Model cases considered	7-27
7.3.1.1	Intra-block heat transfer.....	7-27
7.3.1.2	Inter-block heat transfer.....	7-28
7.3.1.3	Combined inter- and intra-block heat transfer.....	7-28
7.3.2	Construction of the analytical model	7-31
7.3.2.1	Super-meso-scale solution	7-31
7.3.2.2	Meso-scale solution	7-34
7.3.2.3	Calculating the mean solid temperature	7-37
7.3.2.4	Calculating the Sector Boundary Temperature	7-38
7.3.2.5	Calculating heat transfer across an inter-block gap	7-40
7.3.3	Test case models	7-41
7.3.3.1	Intra-block heat transfer (six triangular sectors forming a fuel block)	7-41
7.3.3.2	Inter-block heat transfer (two triangular sectors with a gap).....	7-44
7.3.3.3	Combined heat transfer (line of nine triangular sectors in three blocks)	7-49
7.4	Closure	7-55
7.5	References for Section 7.....	7-56
8.0	INFLUENCE AND MODELING OF CORE BYPASS FLOWS.....	8-1
8.1	Purpose of Section 8	8-1
8.2	Introduction	8-1
8.3	Review of the Open Literature.....	8-3
8.3.1	Leakage flow due to wedge-shaped gaps between stacked fuel blocks	8-4
8.3.2	Leakage flow due to parallel sided gaps between stacked fuel blocks	8-9

8.3.3	Leakage flow due to the surface roughness of stacked fuel blocks.....	8-10
8.3.3.1	Results for the stacked cylindrical element experiment.....	8-11
8.3.3.2	Results for the stacked HTTR fuel element experiment.....	8-12
8.3.3.3	Application of the Kaburaki et al. leakage flow model to GT-MHR fuel blocks.....	8-16
8.3.4	Leakage flows due to gas permeation through graphite.....	8-16
8.4	Comparison of the Published Correlations for Large End-Face Gaps.....	8-17
8.5	RELAP5 Modeling of Leakage Flows in a PMR Core.....	8-18
8.5.1	Description of the one-channel RELAP test model	8-19
8.5.1.1	Description of the hydrodynamic model used within the one-channel model.....	8-22
8.5.1.2	Description of the cross-flow leakage paths within the one-channel model.....	8-23
8.5.1.3	Description of heat structures used in the one-channel model.....	8-24
8.5.2	Results of the one-channel RELAP model	8-25
8.5.3	Comparison of the RELAP heat structure temperatures with the analytical solution of the super-meso-scale model	8-27
8.5.4	Description of the six-channel RELAP5 test model.....	8-28
8.5.5	Results of the six-channel RELAP model.....	8-31
8.6	Sensitivity Studies Conducted Using The Six-Channel RELAP Model	8-33
8.6.1	Effect of the power distribution on the leakage flow distribution.....	8-33
8.6.1.1	Effect of radial power distribution on the leakage flow distribution	8-35
8.6.1.2	Effect of axial power distribution on the leakage flow distribution.....	8-39
8.6.1.3	Effect of variation of the leakage path gap widths on the leakage flow distribution	8-41
8.7	Closure	8-42
8.8	References for Section 8.....	8-43
9.0	OVERALL CONCLUSIONS AND RECOMMENDATIONS.....	9-1
9.1	Purpose of Section 9	9-1
9.2	Summary of Models Developed and Conclusions.....	9-1
9.3	Recommendations for Further Work	9-2
9.4	References for Section 9.....	9-3
APPENDIX A:	DETAILED DEVELOPMENT OF MECHANISMS INFLUENCING FUEL AND MODERATOR TEMPERATURES.....	A-1
APPENDIX B:	WHOLE-CORE (MACROSCOPIC) HEAT TRANSFER.....	B-1
APPENDIX C:	TRACE MODEL OF A SECTION OF THE CORE INCLUDING BYPASS FLOW BETWEEN THE INTER-BLOCK AND COOLING CHANNEL C-1	

List of Tables and Figures

Figure 2.2.1: Structure of HTTR fuel assembly (image courtesy of Reference 2.2)	2-3
Figure 2.2.2: HTTR coated fuel particle, fuel compact and burnable poison pellet (image courtesy of Reference 2.2).....	2-4
Figure 2.2.3: HTTR fuel block for 33 pin fuel assembly (image courtesy of Reference 2.2)	2-4
Figure 2.3.1: System arrangement of the GTHTR300 (image courtesy of Reference 2.3).....	2-5
Figure 2.3.2: GT-MHR system showing a vertical section through the core (image courtesy of Reference 2.4).....	2-7
Figure 2.3.3: GT-MHR core layout (from Reference 2.4)	2-8
Figure 2.3.4: GT-MHR fuel elements	2-8
Figure 2.3.5: Cross section through a Type-1 GT-MHR fuel element	2-9
Figure 2.3.6: Possible ANTARES plant arrangement (from Reference 2.5)	2-10
Table 3.3.1: Mapping of research priorities onto PIRT rankings	3-3
Table 3.3.2: Prioritised phenomena and scenario pairings from all of the thermofluids and accident PIRTs.....	3-4
Figure 5.2.1: Region of fuel block and sector chosen for the FE model.....	5-3
Figure 5.2.2: Domain boundaries.....	5-4
Figure 5.2.3: Geometry of the finite element model	5-5
Figure 5.2.4: Geometry of the finite element model with contact/gap resistances	5-5
Table 5.2.1: Material properties.....	5-6
Figure 5.2.5: Conductivity ratio of unirradiated graphite as a function of temperature.....	5-7
Figure 5.2.6: Finite element mesh for model 1.....	5-9
Figure 5.2.7: Finite element mesh for model 2.....	5-9
Figure 5.2.8: Steady state temperature distribution.....	5-10
Figure 5.2.9: Steady state temperature profile along the 'upper edge'	5-11
Figure 5.2.10: Steady state temperature profile along the 'lower edge'	5-11
Figure 5.2.11: Steady state temperature profile along the 'right edge'	5-12
Figure 5.2.12: Steady state temperature profile around periphery of the fuel	5-12
Figure 5.2.13: Steady state temperature profile around coolant channel wall	5-13
Figure 5.2.14: Transient 1 - evolution of fuel centre, fuel periphery and channel wall temperatures with time	5-14
Figure 5.2.15: Transient 2 – evolution of fuel centre, fuel periphery and channel wall temperatures with time	5-15
Figure 5.2.16: Steady state temperature distribution.....	5-16
Figure 5.2.17: Transient 1 - evolution of fuel centre, fuel periphery, graphite and channel wall temperatures with time	5-16
Figure 5.2.18: Transient 2 - evolution of fuel centre, fuel periphery, graphite and channel wall temperatures with time	5-17
Figure 5.2.19: Steady state temperature distribution.....	5-18
Figure 5.2.20: Steady state temperature profile along the 'upper edge'	5-19
Figure 5.2.21: Steady state temperature profile along the 'lower edge'	5-19
Figure 5.2.22: Steady state temperature profile along the 'right edge'	5-20
Figure 5.2.23: Steady state temperature profile around periphery of the fuel	5-20
Figure 5.2.24: Steady state temperature profile around surface of the fuel channel	5-21
Figure 5.2.25: Steady state temperature profile around coolant channel wall	5-21

Figure 5.2.26: Transient 1 - evolution of fuel centre, fuel periphery, fuel channel surface, graphite and channel wall temperatures with time	5-22
Figure 5.2.27: Transient 2 - evolution of fuel centre, fuel periphery, fuel channel surface, graphite and channel wall temperatures with time	5-23
Figure 5.2.28: Transient 1 - evolution of fuel centre, fuel periphery, graphite and channel wall temperatures with time	5-24
Figure 5.2.29: Transient 2 - evolution of fuel centre, fuel periphery, graphite and channel wall temperatures with time	5-25
Figure 5.3.1: Unit cell containing one coolant channel and six fuel channels.....	5-27
Figure 5.3.2: A coolant channel unit cell approximated as an annular domain.....	5-27
Figure 5.3.3: Unit cell surrounding a fuel channel	5-30
Figure 5.3.4: Approximate representation of a fuel channel unit cell as an annular domain..	5-30
Table 5.3.1: Parameters and their values used in the steady state model.....	5-32
Figure 5.3.5: Predicted temperatures plotted along a radial line connecting the centres of the coolant and fuel compact channels	5-33
Figure 5.3.6: Predicted temperatures plotted along a radial line connecting the centres of the coolant and fuel compact channels with overlapping parts removed and a linear bridging function inserted.	5-34
Figure 5.3.7: Original hexagonal unit cell with super-meso and meso-scale domains overlaid	5-37
Figure 5.3.8 : Super-meso-scale domain	5-37
Figure 5.3.9 : Meso-scale domain	5-38
Table 5.3.2: Parameters and their values used in the multi-scale model.....	5-42
Figure 5.3.10: Development of the meso-scale temperature distribution with time.....	5-43
Figure 5.3.11: Predicted temperatures along a line between coolant-fuel channel centres t=1.29s.....	5-44
Figure 5.3.12: Predicted temperatures along a line between coolant-fuel channel centres t=5.29s.....	5-44
Figure 5.3.13: Predicted temperatures along a line between coolant-fuel channel centres t=20.29s.....	5-45
Figure 5.3.14: Predicted steady state temperatures along a line between coolant-fuel channel centres	5-45
Figure 5.3.15: Transient development of fuel compact centre, fuel compact edge average and coolant channel wall average temperatures.....	5-46
Figure 5.3.16: Predicted steady state temperatures along a line between coolant-fuel channel centres, with fuel gap resistance included	5-47
Figure 5.3.17: Predicted steady state temperatures along a line between coolant-fuel channel centres, with fuel gap resistance included based on a modified gap conductivity .	5-48
Figure 5.3.18: Transient development of fuel compact centre, fuel compact edge average and coolant channel wall average temperatures, with gap resistance included based on a modified gap conductivity.	5-49
Figure 6.3.1: Finite element model, extent and dimensions.....	6-6
Table 6.3.1: Material conductivities.....	6-7
Figure 6.3.2: Finite element mesh in a unit cell.....	6-7
Figure 6.3.3: Base case – distribution of temperature.....	6-9
Figure 6.3.4: Base case – distribution of heat flux.....	6-9
Table 6.3.2: Fuel block transverse effective thermal conductivities derived from finite element	

analyses.....	6-11
Table 6.3.3 Fuel block effective thermal conductivities for different graphite and fuel compact thermal conductivities	6-12
Figure 6.3.5: Variation of effective transverse thermal conductivity with ratio of graphite to fuel compact thermal conductivity.....	6-13
Figure 6.3.6: Variation of effective transverse thermal conductivity divided by fuel compact conductivity with graphite / fuel compact conductivity ratio.	6-13
Table 6.4.1: Comparison of effective conductivities derived from finite element analysis with the analytical values.....	6-14
Figure 6.4.1: Percentage difference between effective conductivities predicted by FE analysis and those obtained analytically	6-15
Figure 6.4.2: Comparison of effective conductivity using 3-component Maxwell's equation and FE analysis for $k_{fc}=20\text{W/m/K}$	6-15
Figure 6.4.3: Comparison of effective conductivity using 3-component Maxwell's equation and FE analysis for $k_{fc}=10\text{W/m/K}$	6-16
Figure 6.4.4: Comparison of effective conductivity using 3-component Maxwell's equation and FE analysis for $k_m=30\text{W/m/K}$	6-16
Table 7.2.1: Material properties.....	7-3
Figure 7.2.1: Geometry of the intra-block finite element model showing the power densities used for Variant 2	7-4
Figure 7.2.2: Geometry of the inter-block finite element model	7-4
Figure 7.2.3: Geometry of the combined finite element model	7-5
Table 7.2.2: Results for the intra-block model Variant 1	7-9
Table 7.2.3: Results for the intra-block model Variant 2	7-9
Figure 7.2.4: Intra-block Variant 1 temperature distribution.....	7-10
Figure 7.2.5: Intra-block Variant 2 temperature distribution.....	7-10
Figure 7.2.6: Inter-block Variant 1 temperature distribution.....	7-12
Figure 7.2.7: Inter-block Variant 1 temperature profiles along the edges of the gap	7-13
Figure 7.2.8: Inter-block Variant 1 heat flux profiles along the edges of the gap.....	7-13
Figure 7.2.9: Inter-block Variant 2 temperature distribution.....	7-14
Figure 7.2.10: Inter-block Variant 2 temperature profiles along the edges of the gap.....	7-14
Figure 7.2.11: Inter-block Variant 2 heat flux profiles along the edges of the gap.....	7-15
Table 7.2.4: Results for the combined model Variant 1.....	7-16
Figure 7.2.12: Combined model Variant 1 temperature distribution	7-17
Figure 7.2.13: Combined model Variant 1 temperature profiles along the edges of the gaps.....	7-18
Figure 7.2.14: Combined model Variant 1 heat flux profiles along the edges of the gaps.....	7-19
Table 7.2.5: Results for the combined model Variant 2.....	7-20
Figure 7.2.15: Combined model Variant 2 temperature distribution	7-21
Figure 7.2.16: Combined model Variant 2 temperature profiles along the edges of the gaps.....	7-22
Figure 7.2.17: Combined model Variant 2 heat flux profiles along the edges of the gaps.....	7-23
Table 7.2.6: Results for the combined model Variant 3.....	7-24
Figure 7.2.18: Combined model Variant 3 temperature distribution	7-25
Figure 7.2.19: Combined model Variant 3 temperature profiles along the edges of the gaps.....	7-26
Table 7.3.1: Power densities and coolant temperatures used in combined Variant 2	7-29
Table 7.3.2: Power densities used in combined model Variant 3.....	7-29
Figure 7.3.1: Schematics of the inter-block, intra-block and combined cases to which the macroscopic analytical models are applied	7-30

Figure 7.3.2: The super-meso-scale model domain	7-32
Figure 7.3.3: The meso-scale model domain.....	7-35
Figure 7.3.4: Sector centroid and boundary temperatures and distances.....	7-38
Figure 7.3.5: Inter-block gap heat flow and temperatures	7-40
Figure 7.3.6: Inter-block gap heat flow and temperatures	7-42
Table 7.3.3: Results for intra-block Variant 2.....	7-43
Table 7.3.4: Intra-block Variant 2 – comparison of FE and analytical models.....	7-44
Figure 7.3.7: Inter-block gap heat flow and temperatures	7-45
Table 7.3.5: Results for inter-block Variant 1	7-46
Table 7.3.6: Results for inter-block Variant 2.....	7-47
Table 7.3.7: Inter-block Variant 1 – comparison of FE and analytical models.....	7-48
Table 7.3.8: Inter-block Variant 2 – comparison of FE and analytical models.....	7-48
Figure 7.3.8: Inter-block gap heat flow and temperatures	7-49
Table 7.3.9: Results for combined Variant 2	7-50
Table 7.3.10: Results for combined Variant 3	7-52
Table 7.3.11: Combined Variant 2 – comparison of FE and analytical models	7-54
Table 7.3.12: Combined Variant 3 – comparison of FE and analytical models	7-54
Figure 8.2.1: Schematic view of core bypass due to crossflow through end-face gaps.....	8-3
Figure 8.3.1: The configuration simulated by Groehn's experimental rig.....	8-5
Table 8.3.1: Evaluation of Groehn's loss correlation, and conversion to hydraulic resistance ..	8-7
Figure 8.3.2: Hydraulic resistance to crossflow through end-face gaps for a full fuel element, as predicted by Groehn's model.....	8-8
Figure 8.3.3: Energy form loss coefficients, based on the area of the end-face gap, predicted by Groehn's model.....	8-9
Figure 8.3.4: JAERI crossflow leakage experiment	8-11
Figure 8.3.5: Simplified flow model for leakage flow from a block edge to coolant channel in a HTTR fuel element.....	8-12
Figure 8.3.6: Pressure distribution surrounding a single HTTR coolant channel near a block edge subject to a 0.5 bar pressure difference	8-13
Figure 8.3.7: Velocity distribution of helium through a 12 micron end-face gap surrounding a single HTTR coolant channel near a block edge subject to a 0.5 bar pressure difference.....	8-14
Figure 8.3.8: Velocity profile of helium at the edge ($x=0$) of a 12 micron end-face gap subject to a 0.5 bar pressure difference	8-14
Figure 8.4.1: Comparison of hydraulic resistances to crossflow through end-face gaps predicted by Groehn (wedge shaped gaps) and GGA (parallel sided gaps).....	8-17
Figure 8.5.1: Section of the GT-MHR core, illustrating the region covered by the six channel RELAP model.....	8-19
Figure 8.5.2: A cross section of the geometry represented by the six channel RELAP model. The RELAP model represents the area enclosed by the red line.	8-19
Figure 8.5.3: Diagram of the one channel, one plenum RELAP model	8-21
Figure 8.5.4: End-face gap areas and configurations used in Groehn's experiment.....	8-24
Figure 8.5.5: Pressure within the coolant channel of the one-channel RELAP model.....	8-26
Figure 8.5.6: Leak flow rates from the inter-block space to the coolant channel in the one-channel RELAP model as a function of axial position within the core.....	8-26
Figure 8.5.7: Gas temperature distribution within the coolant channel of the one-channel RELAP model	8-27

Figure 8.5.8: Comparison of the temperatures within a RELAP heat structure with the analytical solution of the super-meso-scale model (The gas temperature in the associated hydrodynamic volume was 787.3 K)	8-28
Figure 8.5.9: Diagram of the six channel RELAP model with a single inter-block space (pipe component 500, shown on left side of diagram)	8-30
Figure 8.5.10: Mass flow rates through the end-face gap leakage paths for the six-channel RELAP model with a uniform power distribution.....	8-31
Figure 8.5.11: The mass flow rate within the inter-block space, as a function of axial position within the core for the six-channel RELAP model with a uniform power distribution	8-31
Figure 8.5.12: Coolant temperature distribution measured at the end-face gaps with a uniform power distribution for the six-channel RELAP model with a uniform power distribution.....	8-32
Figure 8.5.13: Pressure distributions in the six-channel RELAP model with a uniform power distribution.....	8-32
Figure 8.6.1: The middle-of-cycle power distribution, based on a coupled thermal hydraulic and neutronics study of a VHTR core, obtained from Reference 8.11	8-35
Figure 8.6.2: Mass flow rates through the end-face gap leakage paths for the six-channel RELAP model with a step-wise radial power distribution.....	8-36
Figure 8.6.3: Maximum temperatures within the fuel blocks for the six-channel RELAP model with a step-wise radial power distribution	8-36
Figure 8.6.4: Coolant channel mass flow variation with axial position in the core for the six-channel RELAP model with a step-wise radial power distribution	8-37
Table 8.6.1: Comparison of channel temperature rise and column power distribution.....	8-38
Figure 8.6.5: Mass flow rates through the end-face gap leakage paths for the six-channel RELAP model with a power distribution based on a combined thermal-hydraulic and neutronic analysis	8-39
Figure 8.6.6: Overall (integrated axial) relative distribution of power between the six columns for the combined thermal-hydraulic and neutronic analysis power profile.....	8-39
Figure 8.6.7: Mass flow rates through the end-face gap leakage paths for the six-channel RELAP model with linear axial variation of the power distribution, varying from 50% average power at the top of the core, to 150% at the bottom of the core	8-40
Figure 8.6.8: Mass flow rates through the end-face gap leakage paths for the six-channel RELAP model with linear axial variation of the power distribution, varying from 150% average power at the top of the core, to 50% at the bottom of the core	8-40
Table 8.6.2: Junction areas and cross-flow loss coefficients for different end-face gap sizes	8-41
Figure 8.6.9: Mass flow rates through the end-face gap leakage paths for the six-channel RELAP model with a power distribution based on a combined thermal-hydraulic and neutronic analysis, based on 0.5 mm inter-block gap height	8-41
Figure 8.6.10: Mass flow rates through the end-face gap leakage paths for the six-channel RELAP model with a power distribution based on a combined thermal-hydraulic and neutronic analysis, based on 2 mm inter-block gap height.....	8-42

1.0 INTRODUCTION

This report summarizes the research on Prismatic Modular Core Reactors Heat Transfer from the study "Investigation of the Local Heat Transfer Phenomena in an HTGR Core", solicitation number RES-07-087 (Reference i.1). A study has also been performed looking at heat transfer in a pebble bed reactor (PBR) core, the results of which are reported in Reference 1.2.

The objective of this work is to identify, and develop where necessary, the computational tools and techniques to resolve local fluid behavior in the core of a high temperature gas reactor (HTGR). This information is needed for U.S. NRC staff to develop the evaluation model that will be used to audit licensee calculations under normal operation and accident conditions. This report presents the research performed on the local heat transfer phenomena in a prismatic core. Several models have been developed and sensitivity studies have been performed as part of this research based on the thermal fluids and accidents analysis R&D phenomena identification and ranking tables (PIRT) developed by the US NRC for HTGRs. Based on this research, constitutive models will be developed for inclusion into systems codes (such as the code MELCOR) that are being developed to predict the system-wide thermal fluidic behavior of HTGRs.

This report has been structured in nine sections as follows:

Section 1 – "Introduction", this section.

Section 2 – "Prismatic Modular Reactor Cores" which gives the background on prismatic modular core reactors, and their typical geometries.

Section 3 – "Review of U.S. NRC Thermofluid and Accident Analysis PIRT" with regard to Prismatic Cores. This section summarizes the review of the PIRT performed by the U.S. NRC, which led to the selection of the research studies documented in this report.

Section 4 – "Scope of the Current Programme of Research" summarizes the scope of the work documented in the report. Three research themes were identified based on the PIRT and these are described in Sections 5 through 8.

Section 5 – "Models for the Prediction of Fuel and Graphite Temperatures" summarizes a portion of the first research theme.

Section 6 – "Determination of the Effective Conductivity of Fuel Elements" summarizes a portion of the first research theme.

Section 7 – "Whole-Core (Macroscopic) Heat Transfer" summarizes the second research theme.

Section 8 – "Influence and Modeling of Core Bypass Flows" summarizes the third research theme.

Section 9 – Overall Conclusions and Recommendations provides a summary and conclusion for the research performed for prismatic modular cores.

Each section is relatively stand-alone with its own introduction, closure (conclusions), reference list, tables and figures.

1.1 References for Section 1

- 1.1 U.S. NRC Letter from S. Pool to NSS W. Thompson, "Contract No: NRC-04-07-087, August 31, 2007.
- 1.2 Stainsby R. et al., "Investigation of Local Heat Transfer Phenomena in a Pebble Bed HTGR Core", AMEC NSS Report NR001/RP/002 R01, May 2009.

2.0 PRISMATIC MODULAR REACTOR CORES

2.1 Purpose of Section 2

Section 2 details the developments of HTRs from the earlier prismatic modular cores to current designs under development. The different fuel block designs used in test reactors are described below. The Fort St Vrain fuel block design has been used for the subsequent models that have been developed and which are considered in Sections 5 to 8. The most recent HTR designs are also outlined in the sections below.

2.2 Early HTRs

2.2.1 Dragon

Dragon was the world's first high temperature reactor and was designed and built as a fuel and material test facility in support of national high temperature reactor projects such as THTR-300 and Fort St Vrain. The Dragon Reactor Experiment (DRE) was the pioneering experimental reactor of the OECD High Temperature Reactor Project and was situated at Winfrith in the UK. Dragon first reached criticality in 1964 and achieved its full design power of 20 MW in 1966 (Reference 2.1).

The reactor was cooled with helium gas and the fuel elements generally contained highly enriched UO_2 in the form of coated "tristructural isotropic" (TRISO) particles bonded into graphite compacts. The coatings of TRISO particles contain a layer of silicon carbide sandwiched between two layers of pyrolytic carbon. An inner layer of porous carbon is included to accommodate swelling of the uranium dioxide fuel kernel. As well as TRISO particles, Dragon tested a wide variety of experimental fuels. It operated successfully for over 10 years and demonstrated the feasibility of many technologies necessary for the commercial exploitation of HTGRs.

2.2.2 Peach Bottom Unit 1

Peach Bottom Unit 1 was the first HTGR to be built in the USA. It was designed as an experimental reactor with a thermal power of 115 MW and operated commercially between 1967 and 1974.

The core was of a prismatic design with cylindrical full-length fuel elements containing central uranium carbide fuel compacts (Reference 2.1) and again used helium as the coolant.

Reference 2.1 states that two differing cores were used in Peach Bottom Unit 1. The first core was replaced after the fuel particles, coated in a single layer of anisotropic carbon, suffered failures due to distortion and cracking of the particle coatings. The second core used buffer isotropic pyrolytic carbon (BISO) coatings on the fuel particles and operated with no fuel failures. BISO particles are an earlier development than TRISO and do not possess the silicon carbide layer and, as such, are less effective at containing fission products.

2.2.3 Fort St Vrain

Fort St Vrain was a block-type prototype and the second HTGR to be built in the USA. The fuel blocks used in the reactor are outlined in Sub-section 2.3.2.1. The fuel blocks designs for the GT-MHR and ANTARES reactors (see Sub-sections 2.3.2 and 2.3.3) are based on those used in Fort St Vrain.

2.2.4 HTTR

The High Temperature Test Reactor (HTTR) is the first HTGR to be built in Japan. It has a thermal output of 30 MW. The description below, of the HTTR and the fuel design, is taken from Reference 2.2.

The fully loaded core consists of 30 fuel columns, made up from prismatic hexagonal blocks, 580 mm in height and 360 mm in width across flats. These blocks which include control rod guide blocks, fuel assembly blocks, reflector blocks and irradiation blocks, are piled up cylindrically to form the core. The active core consists of 30 fuel columns and 7 control rod guide columns and is 290 cm in height and 230 cm in effective diameter. Each fuel column consists of 2 top reflector blocks, 5 fuel assemblies and 2 bottom reflector blocks.

The HTTR uses pin-in-block type fuel which differs from the Fort St Vrain fuel type.

2.2.4.1 Pin-in-block-type fuel

Each fuel assembly consists of fuel rods (either 31 or 33), two burnable poison rods and a fuel graphite block. A fuel rod consists of a graphite sleeve containing 14 fuel compacts. The fuel rods are inserted into the coolant channels (of 41 mm diameter) of the fuel graphite blocks. Coolant gas flows downward through annular channels formed by the graphite block and the fuel rod.

Each fuel compact contains about 13,000 coated fuel particles embedded in a graphite matrix. The coated fuel particles each consist of a spherical fuel kernel of low enriched UO_2 with a TRISO coating. There are 12 uranium enrichments in the core, with the enrichment of all compacts in a fuel assembly being equal.

The structure of the fuel assembly is shown in Figure 2.2.1. The fuel particles and fuel compacts are shown in Figure 2.2.2 and Figure 2.2.3 shows the fuel block for a 33 pin fuel assembly.

Figure 2.2.1: Structure of HTTR fuel assembly (image courtesy of Reference 2.2)

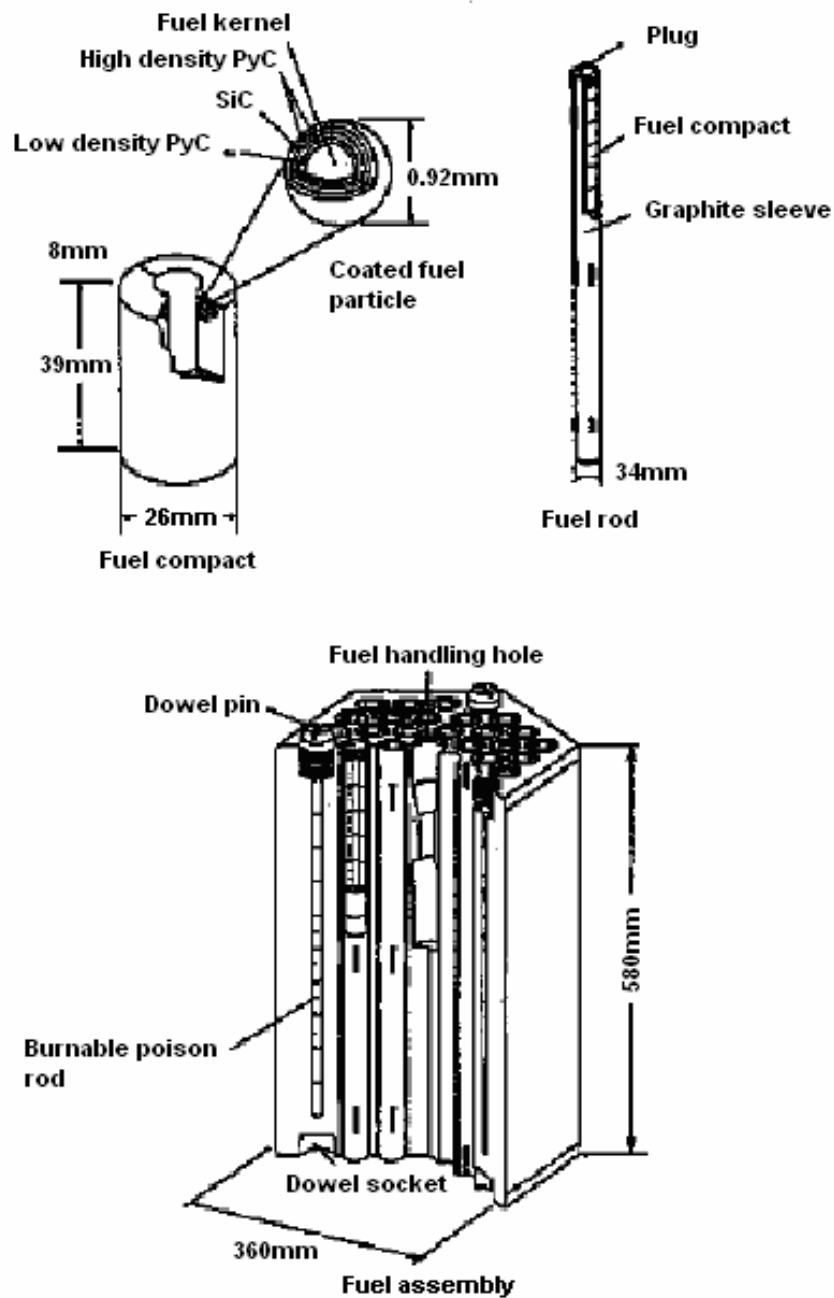


Figure 2.2.2: HTTR coated fuel particle, fuel compact and burnable poison pellet (image courtesy of Reference 2.2)

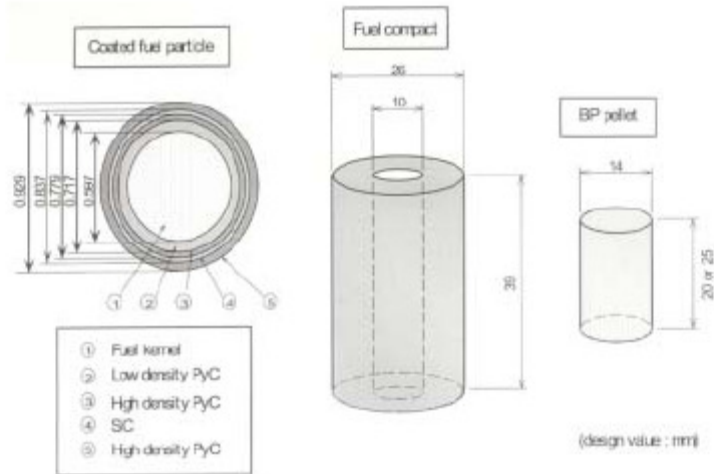
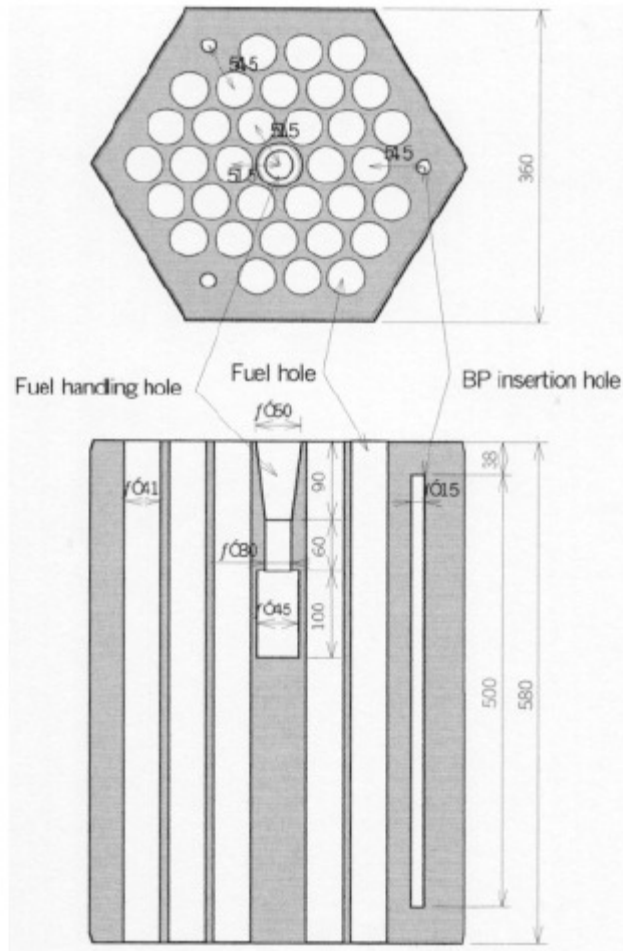


Figure 2.2.3: HTTR fuel block for 33 pin fuel assembly (image courtesy of Reference 2.2)



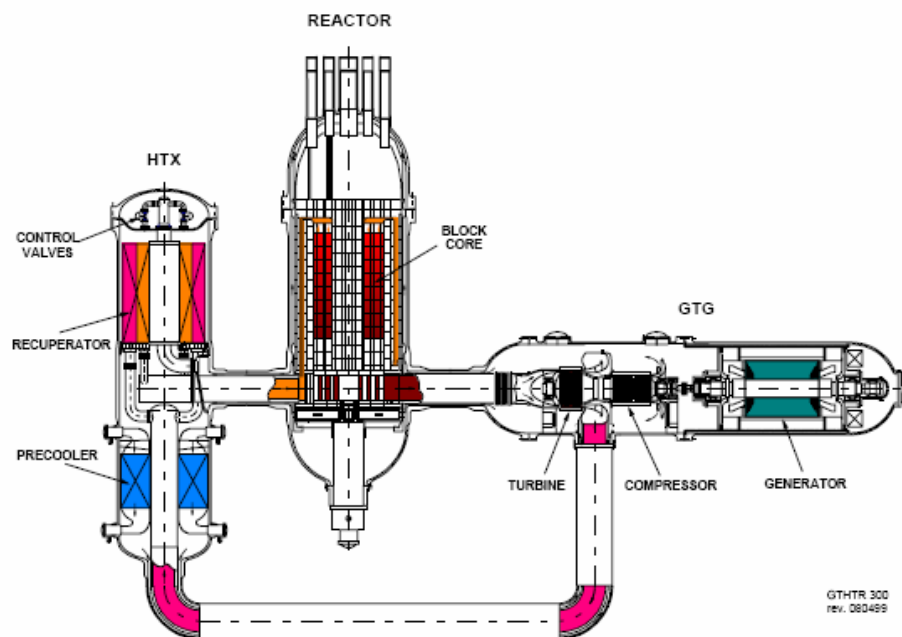
2.3 Current HTR Designs

2.3.1 GTHTR300

The GTHTR300 is a Japanese reactor currently under design, with the aim to build a prototype in the 2010s and a commercial plant in the 2020s. The GTHTR300 uses the pin-block fuel as used in the HTTR. The reactor is designed to be a 600 MW thermal reactor with a direct Brayton cycle. The system arrangement is shown in Figure 2.3.1.

The core consists of 90 annular fuel columns with an effective core of 5.5 m inner to outer diameter, and 8 m in height (Reference 2.3). The fuel column is stacked in 8 axial layers of fuel elements and each fuel element is a hexagonal graphite block with 57 fuel pins, 405 mm across flats and 1000 mm in height. Reference 2.3 states that the fuel pin has been improved to pass heat flux more efficiently. The fuel compacts within each fuel pin are made of enlarged coated fuel particles, with a fuel kernel diameter of 550 μm and 140 μm buffer layer.

Figure 2.3.1: System arrangement of the GTHTR300 (image courtesy of Reference 2.3)



2.3.2 GT-MHR

The Gas Turbine-Modular Helium Reactor (GT-MHR) is a USA reactor design by General Atomic. It couples a gas-cooled modular helium reactor with a high efficiency Brayton cycle gas turbine power conversion system (Reference 2.1). The system is shown in Figure 2.3.2. GT-MHR is a 600 MW thermal reactor with a fuel block design based on the Fort St Vrain block-core design.

2.3.2.1 GT-MHR block-type core

The following description is taken from Reference 2.4.

The core consists of an annular stack of hexahedral prismatic fuel assemblies with a width across flats of 360 mm. There are 102 columns, with 10 fuel assemblies in each column. The active core is surrounded by graphite reflector blocks. Figure 2.3.3: shows the layout of the core.

There are two designs of fuel assemblies, those with a channel for control rods or the reserve shutdown system and those without (type-1 and type-2). Twelve of the 102 columns contain fuel assemblies with a hole for control rods, 18 columns have a similar hole for a traveling reserve shutdown system consisting of absorber elements. The two types of fuel assembly are shown in Figure 2.3.4; with a cross section through a type-1 fuel element shown in Figure 2.3.5:

Figure 2.3.2: GT-MHR system showing a vertical section through the core (image courtesy of Reference 2.4)

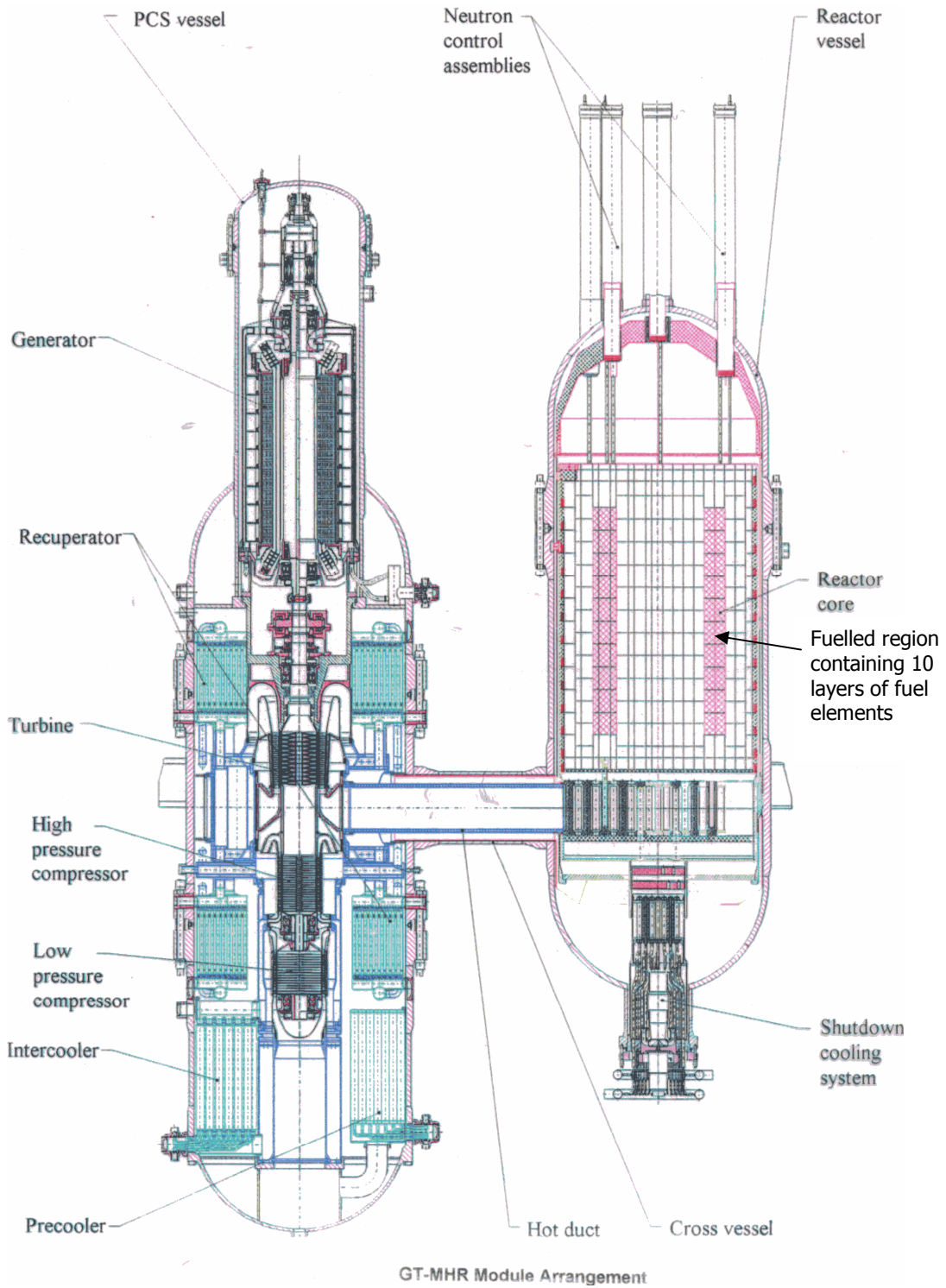


Figure 2.3.3: GT-MHR core layout (from Reference 2.4)

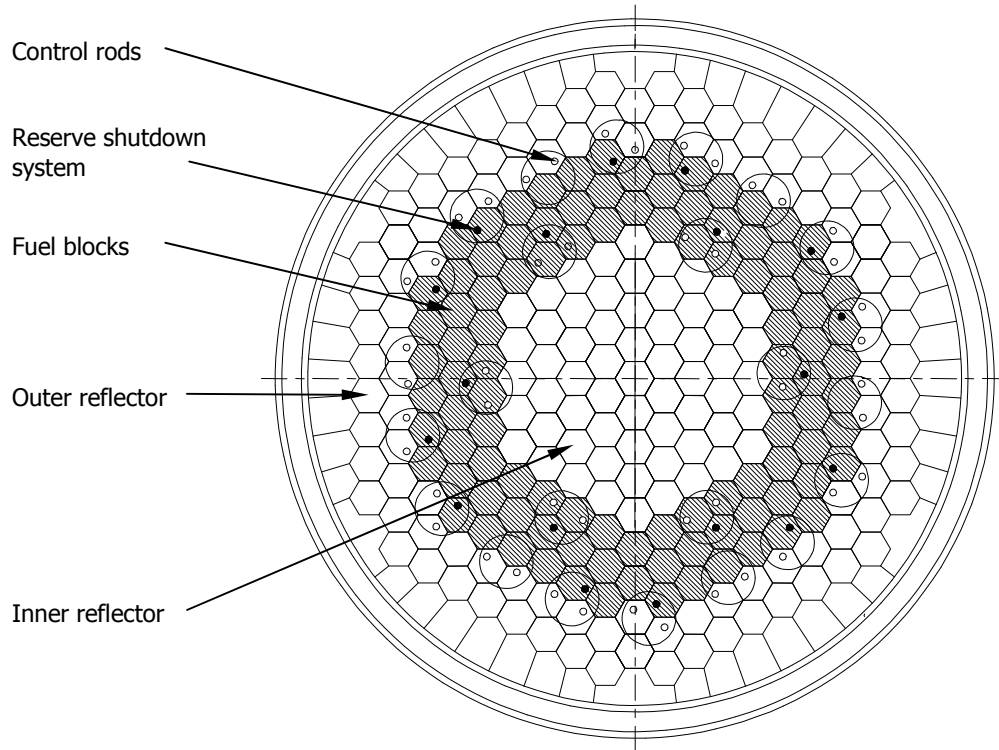


Figure 2.3.4: GT-MHR fuel elements

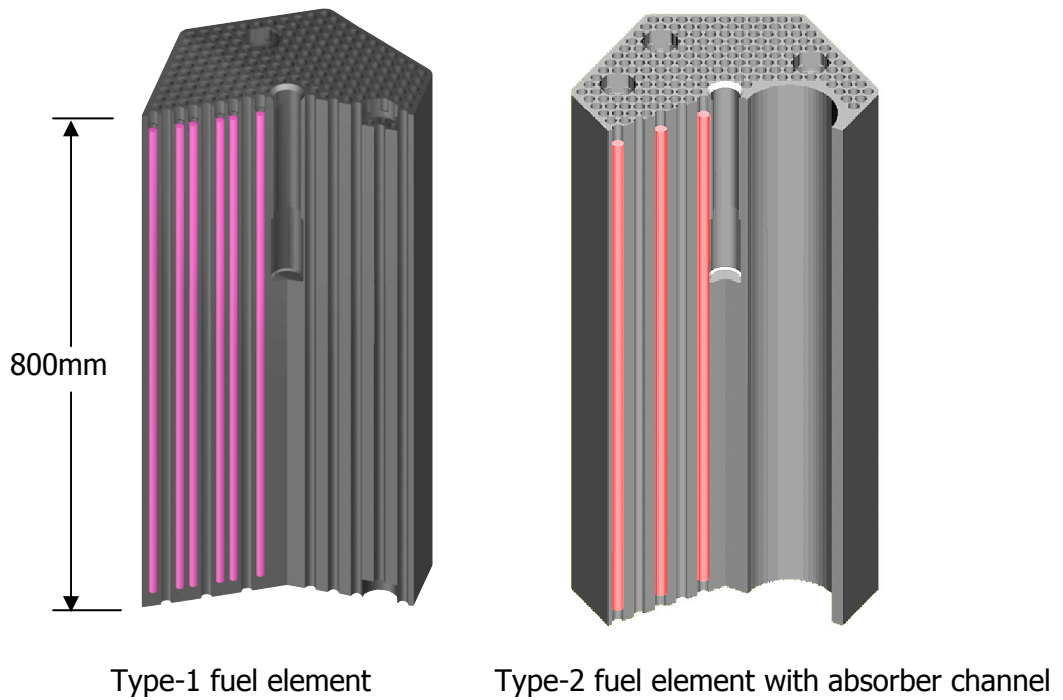
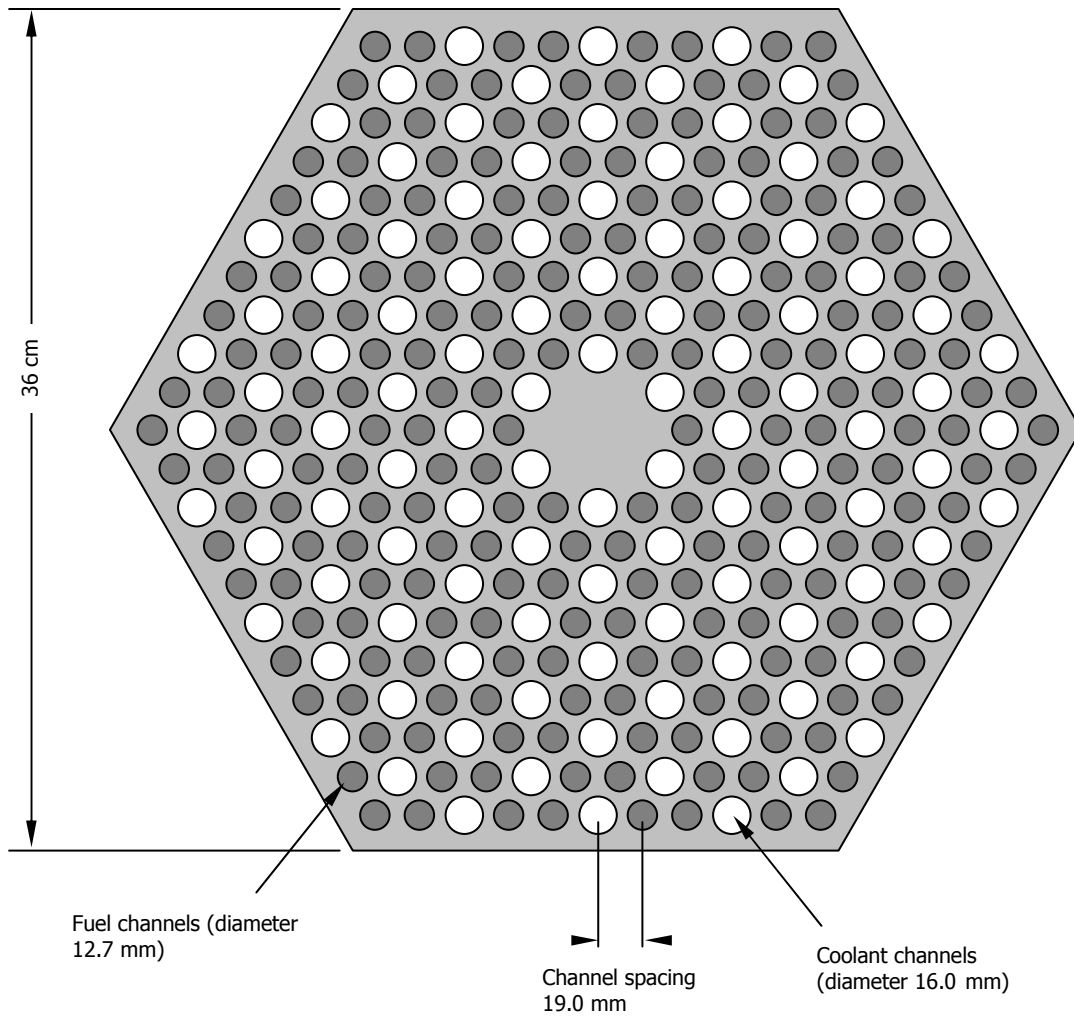


Figure 2.3.5: Cross section through a Type-1 GT-MHR fuel element

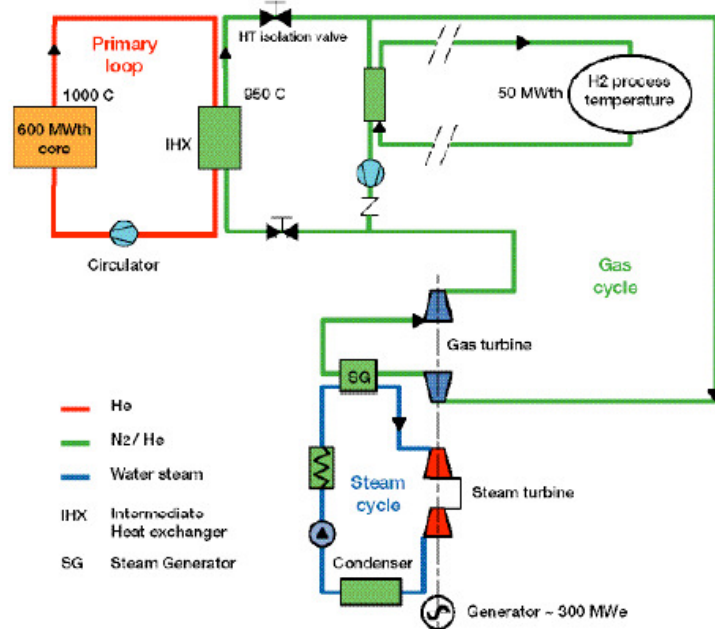


2.3.3 ANTARES

ANTARES is an AREVA designed reactor, similar to GT-MHR, however it utilizes an indirect cycle. The design also has potential to operate at higher temperatures (VHTR, very high temperature reactor), which could potentially be used for hydrogen production coupled with electricity production (Reference 2.5).

As for GT-MHR, the fuel is based on the Fort St Vain type fuel blocks. The system arrangement is shown in Figure 2.3.6.

Figure 2.3.6: Possible ANTARES plant arrangement (from Reference 2.5)



2.4 References for Section 2

- 2.1 GENIV-NNC-VHTR-TR(04)02, Review of UK experience with high temperature reactors for the Generation IV VHTR system, D Buckthorpe et al (AMEC), December 2004.
- 2.2 IAEA-TECDOC-1382, Evaluation of high temperature gas cooled reactor performance: Benchmark analysis related to initial testing of the HTR and HTR-10, February 2001.
- 2.3 Design and development of GTHTG300, X. Yan et al, from HTR2002, 1st international meeting on HTR technology.
- 2.4 IAEA CRP 5, Draft TECDOC II, "Evaluation of High Temperature Gas Cooled Reactor Performance". To be published.
- 2.5 ANTARES, The AREVA HTR-VHTR design, information leaflet from <http://www.aveva-np.com>.

3.0 REVIEW OF U.S. NRC THERMOFLUID AND ACCIDENT ANALYSIS PIRT WITH REGARD TO PRISMATIC CORES

3.1 Purpose of Section 3

This section discusses the findings from a series of Phenomena Identification and Ranking Tables (PIRT) exercises commissioned by the U.S. NRC examining various aspects of HTGR technology. The findings of relevance to the current study are from the Thermofluids and Accident Analysis PIRTs (Reference 3.1). The PIRT exercise also included neutronics, which is outside of the scope of the current study. However, because of the close coupling between thermal hydraulics and neutronics within HTGR systems, the thermal hydraulic influence on primarily neutronics phenomena are considered within this review.

3.2 Findings of the PIRT

The findings of the PIRT exercise are in line with AMEC's experience of HTGR systems. However, two inconsistencies have been identified as well as some possible omissions. The omissions occur both as missing phenomena and missing linkages between listed phenomena and listed scenarios.

The PIRT could have included the following phenomena, or additional linkages with scenarios, which were omitted from the tables presented.

Normal Operation

1. Performance and stability of the core base insulation system. Ceramic insulation materials, such as fused silica, have been researched with a view to forming the insulation layer between the graphite core structures and the metallic core support structure. The main issues with these materials are their thermal and mechanical properties, the dimensional stability at high temperature (avoiding the dimensional changes that occur at the re-crystallization temperaturesⁱ) and accommodation of the differential thermal expansion between the ceramic insulator and the steel core support structure. The suggested ranking is high importance and medium knowledge (H, M).
2. Pre-equilibrium (or burn-in) behavior. Prismatic reactors have to start, at the beginning of their lives, with clean cores, that behave very differently to the equilibrium cores reached after a few refuelling operations with a multi batch core. During this transition phase before quasi-equilibrium is reached shutdown margins may be degraded and particular fuel element powers and temperatures may be higher than those in an equilibrium core. The suggested ranking is high importance and low knowledge (H, L).

ⁱ The material partially re-crystallizes, and the re-crystallized material has a different density to the original material. On cooling the dimensional differences between the original and re-crystallized regions persist and induce stresses which may cause the insulation blocks to crack. Cracks in the insulation would then allow hot gas to reach the metallic support structures.

Pressurized Loss of Forced Circulation (PLOFC)

1. Performance of the vessel/core barrel head insulation system. Whilst not subject to the same magnitude of loads as the core base insulation, the vessel head or core barrel top-plate insulation can be exposed to higher temperatures in a PLOFC transient. Maintenance of mechanical properties and dimensional stability are important issues. The suggested ranking is high importance and medium knowledge (H, M).

Depressurized Loss of Forced Circulation (DLOFC)

1. Degradation of heat transfer surfaces due to graphite dust deposition. The core barrel and inner surface of the reactor pressure vessel (RPV) need to maintain high emissivity. The deposition of a layer of graphite dust may change the emissivities and conductivities of the surfaces. The suggested ranking is medium importance, low knowledge (M, L).
2. Influence of core restraint structures and other congestion in the core-to-core barrel gap on radiation view factor. The suggested ranking is medium importance, medium knowledge (M, M).
3. Linkage of the reactivity temperature coefficients and xenon build-up phenomena with the DLOFC scenario. A DLOFC transient without Scram is often cited as being a design basis transient that an HTGR can withstand. Time to achieve re-criticality is an important parameter and depends upon knowledge of the rate of cooling, xenon decay and the reactivity-temperature feedback effects. The suggested ranking is medium importance, low knowledge (M, L).

Air Ingress

1. Inverted siphon effects through breaks occurring in elevated reactor inlet or outlet pipework. Whilst the RPV inlets and outlets may be below the bottom of the graphite core, elevated external pipework may provide a route by which the helium is siphoned out of the vessel and replaced by air. The suggested ranking is high importance, medium knowledge (H, M).

The first inconsistency concerns the ranking of the power and flux phenomenon (ID 26) in the normal operation PIRT. In the 4th paragraph of Section 4.4, this phenomenon is described as having an (H, L) ranking, whereas Table 2.1 shows it as having a (H, M*) ranking. Logically, if the reactivity-temperature feedback coefficients phenomenon has a (H, L) ranking, the power and flux distribution is strongly dependent on local temperature feedback effects, so should have a (H, L) ranking as well.

The second inconsistency concerns the knowledge level associated with the reactivity-temperature feedback coefficients in association with an ATWS. In the ATWS PIRT, the phenomenon has been ranked as having a high importance with a *medium*

knowledge level (H, M). However, within the normal operation PIRT, the same phenomenon is ranked as having a high importance with a *low* knowledge level (H, L). The phenomenon is identical in both scenarios, and indeed, is important as mitigation in ATWS sequences. The classification of the knowledge level for this phenomenon in both scenarios should be low (H, L).

3.3 Allocation of Research Priorities

The ranking system of the PIRTs is two-dimensional with importance and knowledge assigned values from high to low. In order to sort the list of phenomena in term of decreasing priority for research, this system has been reduced to a one dimensional ranking system. The highest priority has been given to a phenomenon which is highly important in a given scenario in the reactor, for which the knowledge level is correspondingly low. At the opposite end of the spectrum, the lowest priority is given to phenomena which are well understood and of low importance. In this manner, each phenomena/scenario listed in the PIRTs has been assigned a research priority number between 1 and 6, with 1 being of the highest priority. The mapping between PIRT rankings and research priority is shown in Table 3.3.1.

Table 3.3.1: Mapping of research priorities onto PIRT rankings

PIRT Ranking	Research Priority
H, L	1
H, M	2
M, L	2
M, M	3
H, H	4
L, L	4
M, H	5
L, M	5
L, H	6

3.3.1 Prioritized list of phenomena and scenario pairings

The phenomena and scenario pairings from all of the thermofluids and accident PIRTs that are considered relevant to, or dependent upon, the current study on prismatic modular reactors have been ranked according to their assigned research priority and are listed in Table 3.3.2.

The phenomena shown in bold in Table 3.3.2 are those that this research contributes directly towards, and the phenomena shown in *italics* are those for which this research provides a necessary step towards gaining an understanding.

Table 3.3.2: Prioritized phenomena and scenario pairings from all of the thermofluids and accident PIRTs

PIRT ID	Phenomenon	Ranking	Priority
NO-1	Core coolant bypass flow	H,L	1
NO-22	Reactivity-temperature feedback coefficients	H,L	1
NO-2	Core flow distribution, flow in active core	H,M	2
NO-4	Core flow distribution changes due to graphite irradiation	M,L	2
NO-16	Effective fuel element thermal conductivity	H,M	2
<i>NO-20</i>	<i>Shutdown cooling system startup transients during core heatup</i>	<i>H,M</i>	<i>2</i>
NO-26	Power and flux profiles (initial conditions for accidents)	H,M	2
GL-1	Core thermal conductivity (effective)	H,M	2
GL-4	Vessel emissivity	H,M	2
GL-9	Reflectors: conductivity and annealing	H,M	2
GL-10	Core barrel emissivity	H,M	2
<i>GL-21</i>	<i>Decay heat (temporal and spatial)</i>	<i>H,M</i>	<i>2</i>
PL-1	Inlet plenum stratification and plumes	H,M	2
PL-2	Radiation heat transfer from top of the core to upper vessel head	H,M	2
PL-4	Core coolant flow distribution	H,M	2
PL-5	Core coolant bypass flow	H,M	2
PL-6	Coolant flow friction/viscosity effects	H,M	2
DL-1	Core effective thermal conductivity	H,M	2
<i>DL-2</i>	<i>Decay heat and distribution versus time</i>	<i>H,M</i>	<i>2</i>
DL-5	Hydrodynamic conditions for dust suspension (fluid structure interactions)	H,M	2
AI-5	Core support structures	H,M	2

Table 3.3.2: Prioritized phenomena and scenario pairings from all of the thermofluids and accident PIRTs

PIRT ID	Phenomenon	Ranking	Priority
	oxidation		
AI-6	Core oxidation	H,M	2
AI-7	Cavity to reactor vessel air ingress	H,M	2
AI-8	Phenomena that affect cavity gas composition and temperature with inflow	H,M	2
AI-14	Duct exchange flow	H,M	2
AI-15	Molecular Diffusion	H,M	2
AT-3	Reactivity insertion due to steam-water ingress accidents	H,M	2
AT-5	Reactivity temperature feedback coefficients (fuel, moderator, reflectors)	H,M	2
<i>AT-6</i>	<i>Control and scram rods, and reserve shutdown worths</i>	<i>H,M</i>	<i>2</i>
<i>AT-10</i>	<i>Coolant flow restarts during loss of forced circulation ATWS</i>	<i>M,L</i>	<i>2</i>
NO-3	Core flow distribution changes due to temperature gradients	M,M	3
NO-5	Core flow distribution changes due to core barrel geometry changes.	M,M	3
NO-6-PMR	Core flow distribution due to core block stability (prismatic)	M,M	3
NO-11	Core Inlet flow distribution	M,M	3
NO-12	Thermal fluid mixing from separate loops	M,M	3
NO-18	Side reflector - core barrel - vessel heat transfer	M,M	3
GL-2-PMR	Fuel element annealing (prismatic core)	M,M	3
PL-7	Impacts (thermal shock) in SCS due to startup flow transient	M,M	3
AI-2	Heat transfer correlations for mixed gases in core	M,M	3
AI-9	Cavity gas stratification and mixing	M,M	3
AI-16	Chimney effects	M,M	3
AT-1	Reactivity insertion due to pebble core compaction (packing fraction) via earthquake	M,M	3

Table 3.3.2: Prioritized phenomena and scenario pairings from all of the thermofluids and accident PIRTs

PIRT ID	Phenomenon	Ranking	Priority
AT-7	Xenon and samarium build-up	M,M	3
NO-9	Coolant properties - viscosity and friction effects	H,H	4
NO-10-PMR	Coolant heat transfer correlations	H,H	4
GL-3	Core specific heat function	H,H	4
AI-1	Coolant flow and thermal properties for mixed gases in vessel	H,H	4
NO-15	Effective core thermal conductivity	L,M	5
NO-17	Core specific heat	M,H	5
DL-6	Dust effect on coolant properties and flow in vessel	L,M	5
AT-4a	Phenomena for water or steam ingress from SCS, or PCU coolers	L,M	5
AT-13	Reactivity insertion from core support failure due to air ingress corrosion	L,M	5
GL-11	Stored (Wigner) energy releases	L,H	6
AT-12	Reactivity insertion from overcooling transients with ATWS	L,H	6

Key to PIRT ID numbers

General form: Scenario - number of item in relevant PIRT - reactor type (or both if unspecified)

Scenarios:
 NO – Normal Operation
 GL – General Loss of Forced Circulation (GLOFC)
 PL – Pressurized Loss of Forced Circulation (PLOFC)
 DL – Depressurized Loss of Forced Circulation (DLOFC)
 AI – Air Ingress
 AT – Anticipated Transient Without Scram (ATWS)

System specific phenomenon/scenario pairs:

PMR – only applicable to prismatic modular reactors

3.3.2 High priority research items

The topics chosen for investigation were drawn from the items in Table 3.3.2 ranked as research priority 1 or 2. The selection of the research tasks took into account what was technically feasible and realistically achievable, within the time and budget allocation for this project. In addition, many of the items require the use of coupled

thermal hydraulics and neutronics. This has been considered to be beyond the scope of this study, which concentrates on thermal hydraulic aspects only.

Potential modeling approaches identified for all of the thermal hydraulic items ranked as research priority 1 or 2 can be found in Reference 3.2. The topics selected for this work and the modeling approaches taken are discussed in Section 4.

3.4 References for Section 3

3.1 Ball S.J., "Next-Generation Nuclear plant Phenomena Identification and Ranking Tables (PIRTs); Volume 1 – Thermofluids and Accident Analysis PIRTs," Draft NUREG/CR-6944 Vol. 1 (ORNL/TM-2007/xxx Vol. 1), September 2007.

3.2 Stainsby R., "Investigation of Local Heat Transfer Analysis in an HTGR Core," NSS Report No. NR001/PL/001 R01, December 3, 2007.

4.0 SCOPE OF THE CURRENT PROGRAMME OF RESEARCH

4.1 Purpose of Section 4

This section discusses the chosen research themes for the prismatic modular reactor resulting from the PIRT (see Section 3) and describes how these themes have been addressed.

The approach adopted was to select research themes which generally address multiple PIRT items. A similar study has been performed for pebble bed reactors (Reference 4.1) and there are common features between both reactor types. Therefore some of the research topics that are applicable to both reactors, such as the microscopic fuel temperature modeling methods, have only been studied for one reactor type.

For the prismatic modular reactor, the following research themes were investigated:

1. Fuel element (meso-scale) internal flow and heat transfer models
2. Fuel element to fuel element heat transfer models
3. Influence of core bypass flows

Each theme is discussed in more detail in sub-sections 4.2 to 4.4 below.

4.2 PMR Theme 1

The first theme "Fuel element (meso-scale) internal flow and heat transfer models" was chosen as it is necessary for the fuel kernel and moderator graphite temperatures to be predicted correctly. The thermal modeling of a TRISO coated particle and its share of the surrounding graphite, on the microscopic scale is identical to that for the PBR. There are slight differences in modeling at the scale of a cylindrical fuel compact compared with a spherical pebble, but the principles are the same. Within the block fuel of a PMR, the heat transfer path from the fuel compact to the coolant is more complicated requiring the conduction through the fuel block to be modeled. However, unlike PBRs, the convective heat transfer coefficient to the coolant is simple to calculate because the coolant channels are circular.

The two objectives of this theme were:

1. To develop and validate a suitable numerical model that can handle the conduction heat transfer from the surface of a fuel compact to its surrounding coolant channels, both in steady state and transient conditions.
2. To be able to determine the effective thermal conductivity of a fuel block to be able to predict how heat is redistributed within a fuel element block.

This research theme contributes directly to the following PIRT items:

NO-22, AT-5 Reactivity –temperature feedback coefficients

NO-26 Power and flux profiles

NO-16 Effective fuel element thermal conductivity

and is a necessary step towards gaining an understanding of:

NO-20 Shutdown cooling system startup transients during core heat up

GL-1, DL-1 Core thermal conductivity (effective)

GL-21, DL-2 Decay heat (spatial and temporal)

AT-6 Control and scram rods and reserve shutdown worths

AT-10 Coolant flow restarts during loss of forced circulation ATWS

Analytical models have been developed in the past to represent the conduction of heat from the surface of a fuel compact to its surrounding coolant channels (see Section 5). An improvement to this existing model was developed as part of this research theme. These models allow the compact surface, mean graphite and coolant channel wall temperatures to be coupled, with their differences being dependent on the heat flux generated by the fuel. These models are based on the assumption that the geometry of a unit cell, consisting of a coolant channel surrounded by six fuel compacts, can be reduced down to a simple 1-dimensional annular region of graphite, with the fuel contacting the inner surface and the coolant channels smeared over the outer surface. There are two main issues with this approach, first, it is only applicable to steady state conditions and second, the reduction of the geometry from 2-dimensions to an equivalent annular representation is a large approximation.

Within this prismatic fuel element model, the hexagonal block is sub-divided into ten layers, each containing six triangular prismatic cells, with each triangle containing a representative unit cell that contains a coolant channel surrounded by six 1/3 sectors of two channels of fuel compacts. Heat transfer between the neighboring triangles is a function of the effective conductivity of the fuel element, taking into account the presence of the fuel compacts, burnable poison compacts, the irradiated graphite matrix and the coolant channels. Previously, the effective conductivity has been determined using a three-component Maxwell's equation. However, Maxwell's equation is strictly only applicable to a dilute medium and a more elaborate homogenization method should be used and is developed as part of this research theme.

Models produced for the first objective of this research theme are discussed in Section 5. Section 6 describes and gives the results of models derived for the second objective of this research theme.

4.3 PMR Theme 2

The second research theme "Fuel element to fuel element heat transfer models" is necessary to determine how the heat is redistributed between neighboring fuel elements (and reflector blocks) in normal operation and LOFC conditions.

This research theme specifically addresses the following PIRT item:

GL-1, DL-1 Core thermal conductivity (effective)

The methodology used for this research theme is discussed in Section 7.

The effective conductivity of the core, on the scale of a few fuel elements has been determined using a finite element model. Conduction and thermal radiation heat transfer within the block-to-block gaps has been included in the model. The results of the finite element calculation have been compared with an analytical model. This comparison examined whether or not the assumptions made in the model are valid (see Section 7).

The data generated within this research theme can also be applied to the validation of the conduction model within MELCOR (to be considered in Task 4 of this project).

4.4 PMR Theme 3

The third theme "Influence of core bypass flows" is necessary to predict the changes to fuel temperatures that will occur due to bypass flows introduced by manufacturing tolerances, by errors, or by geometry changes that occur during irradiation.

This research theme specifically addresses the following PIRT items:

- NO-1 Core bypass flow
- NO-2 Core flow distribution in the active core
- NO-4 Core flow distribution changes due to graphite irradiation

Core bypass flows can either be a complete bypass, where the coolant effectively short-circuits from the reactor inlet to the reactor outlet, or partial bypass, where only part of the core is starved of flow. Complete bypass is easy to simulate by simply subtracting the bypass flow from the core inlet flow. Partial bypass is more subtle, in that flow can leave the coolant channels through gaps near the top of the core (assuming a downwards core flow) and re-enter through gaps closer to its base, thus only bypassing the mid-height region. The latter scenario requires a hydraulic model in which the inter-block gaps are modeled, with suitable cross-links to the fuel channels at the block end-faces. Determination of the end-face actual gap sizes is feasible, but difficult, requiring the manufacturing tolerances to be accounted for and irradiation-induced distortions to be calculated. In the absence of detailed design information, and detailed neutron flux and temperature distributions, gap sizes were assigned arbitrarily as historical data from Fort St Vrain was not available.

Originally two sub-tasks were proposed for this research theme and these were to modify the hydraulic model in the AMEC PRIMSTER code to include all of the potential bypass flow paths and use this to carry out sensitivity studies looking at different gap sizes and distributions of gaps. However, following the discovery of the complexities involved in modeling the macro-scale heat transfer correctly in the second research theme together with the finding that block-to-block heat transfer is small in normal operation, and to avoid any commercial problems associated with the ownership of the modified PRIMSTER code, the approach was changed to use the system code RELAP5.

Section 8 details the RELAP5 model set up of a section of GT-MHR core and the cases run to demonstrate the influence of different amounts of bypass flow on fuel compact temperatures.

4.5 References for Section 4

- 4.1 Stainsby R. et al., "Investigation of Local Heat Transfer Phenomena in a Pebble Bed HTGR Core", AMEC NSS Report NR001/RP/002 R01, May 2009.

5.0 MODELS FOR THE PREDICTION OF FUEL AND GRAPHITE TEMPERATURES

5.1 Purpose of Section 5

A model that is able to predict the thermal hydraulic behavior of a prismatic High Temperature Gas Reactor (HTGR) core needs to be able to resolve the temperature distribution on three distinct length scales. These are referred to here as the macroscopic scale, the meso-scale and the micro-scale.

The largest length scale, the macroscopic scale resolves the coolant, temperature and power distributions from the scale of the whole core down to a fraction of the size of a fuel element. In such a model a complete hexagonal fuel element could be the smallest scale resolved with all of the coolant channels therein being represented by a single *effective* channel, and similarly all of the channels containing fuel compacts represented by two identical effective fuel channels (because on average there are two fuel channels for every coolant channel in a Fort St Vrain fuel block). A better macroscopic resolution would be obtained if each hexagonal block was subdivided into 6 triangular sectors, with each sector being represented by a single coolant channel and a pair of identical fuel channels. Such a sub-division would allow for a gradient of power across a fuel element to be resolved and for temperature gradients resulting from heat loss through the core boundary to be captured better. A finer resolution would be to sub-divide one of the above triangular sectors into four sub-triangles, with each of these containing a representative coolant channel and a pair of identical fuel channels. In practice, this is the finest resolution that is sensible for a macroscopic scale model when combined with an axial resolution of about eight cells per fuel block. At this level of detail, each sub-triangle contains, on average, 4.5 actual coolant channels and 9 fuel channels.

The meso-scale resolves the temperature distribution on all length scales that is of the order of the pitch of the channels within a block. Therefore, the meso-scale model resolves the local temperature distribution around the single effective coolant channel and the pair of effective fuel channels. Coupling between the macro and meso-scale models allows for the local temperature distributions to be combined with the macroscopic temperature fields so that global heat flows due to the power distribution and external heat losses influence the temperature of individual coolant and fuel channels.

The microscopic scale resolves the temperature on the scale of individual fuel particles. Each fuel compact contains thousand of TRISO coated particles, and ultimately we require the average and maximum temperatures of the fuel kernels and surrounding coatings, both for use in neutronics calculations and to be able to estimate fuel failure fractions and fission product release rates. Combination of the temperature fields on all three length scales leads ultimately to the ability to predict the temperature distribution within a TRISO particle located at any position in which there is a fuel compact in the core.

Resolving the temperature field simultaneously on different length scales is an established mathematical technique known as multi-scale modeling. In essence, the

technique involves successively averaging the behavior of the smaller scale when progressing upwards through each of the larger length scales. The overall behavior of the system is solved for on the largest scale and then each solution on the smaller scales is used as a magnifying glass to progressively zoom-in on the behavior at the finer scales.

With regard to prismatic modular cores, modeling the behavior on the macroscopic scales is presented in later sections of this report, starting with Section 6 that focuses on methods for determining the macroscopic thermal conductivity of either whole or coarsely sub-divided fuel elements. Modeling the microscopic scale behavior of individual TRISO particles within a fuel compact is dealt with in detail, in the context of pebble bed HTGRs in Reference 5.1.

This section concentrates on the development and qualification of models that resolve temperatures on the meso-scale by which the fuel compact and moderator graphite temperatures can be calculated together with the heat transferred to the coolant. The assumption in the development of these models is that the values for coolant flow distribution and local coolant temperature are known, having been supplied by a macroscopic model of the reactor, and that the power distribution is known, either having been prescribed as input to the model or obtained interactively from a coupled neutronics model.

In order to qualify the meso-scale models, reference solutions were generated using the finite element (FE) method to solve the fundamental steady state and transient heat conduction equations in two-dimensions. An FE code is able to solve the basic heat conduction equations without simplification. The development of the reference FE solutions are presented in the next sub-section and these are compared with the meso-scale models in later sub-sections. Some simplifications, such as constant properties and two-dimensionality are introduced into the FE model for ease of comparison with the multi-scale models.

5.2 Finite Element Solutions for the Meso-Scale Domains

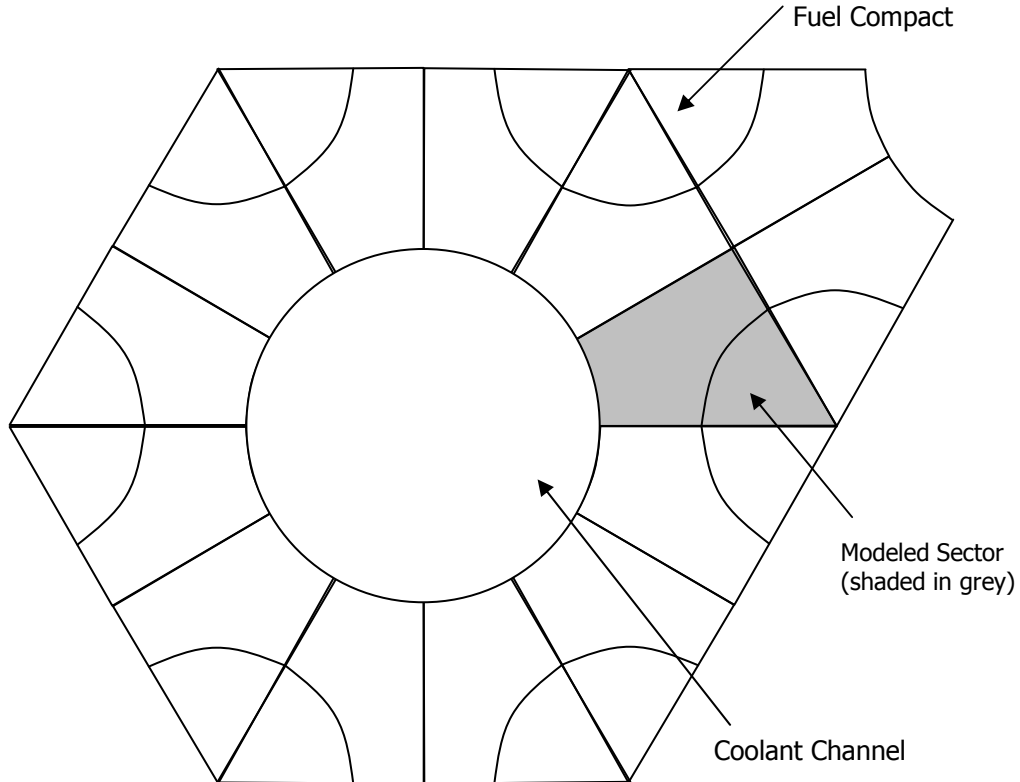
This sub-section describes the steady-state and transient finite element models of a small section fuel block consisting of 1/12 of the periphery of a coolant channel and 1/6 of an adjacent fuel channel with a proportionate region of graphite in between.

The finite element program code for this work was Abaqus/CAE version 6.7-1 and the geometry modeled, material properties and boundary conditions applied, and results obtained are described below.

5.2.1 Modeled geometry and boundary conditions

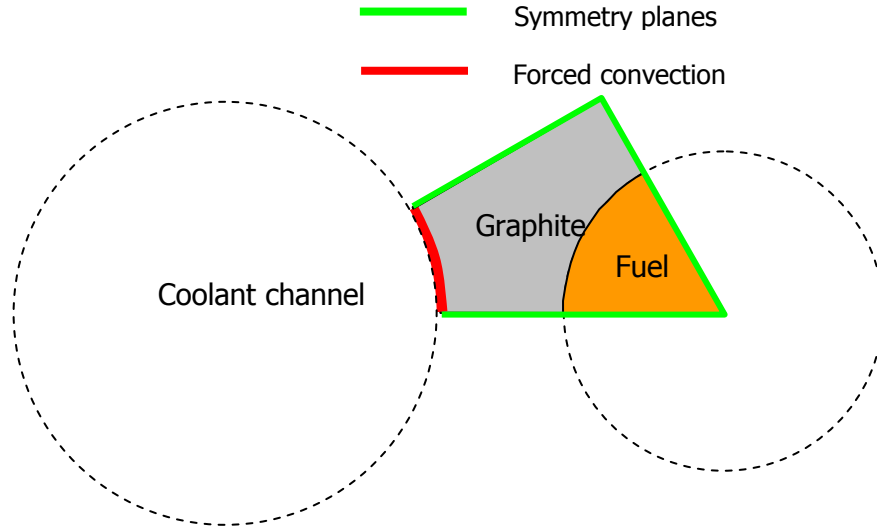
A 2-dimensional finite element model was produced of a small region of a Fort St Vrain / GT-MHR fuel block. The 2-D model represents a horizontal slice through a fuel block passing through six fuel channels surrounding a single coolant channel. The cross section is shown in Figure 5.2.1 and the reduced sub-region chosen to be modeled, by making use of symmetry, has been highlighted.

Figure 5.2.1: Region of fuel block and sector chosen for the FE model



The modeled region consists of 1/6th of a fuel channel (and compact within) surrounded by the graphite of the fuel block bounded by a coolant channel wall on one edge and symmetry planes on all of the others, as shown in Figure 5.2.2. All of the straight edges are symmetry planes and are assumed to be adiabatic, the curved edge that represents the coolant channel wall features a forced convection boundary condition over which a convective heat transfer coefficient and mean coolant temperature are specified.

Figure 5.2.2: Domain boundaries



To recap, the dimensions quoted in Section 2 for this type of fuel block dictate that the coolant channel has a diameter of 16 mm and a fuel channel has a diameter of 12.7 mm, with each fuel channel containing fuel compacts of diameter 12.5 mm. The distance between centers of the fuel and coolant channels is 19 mm, as is the distance between neighboring fuel channels. From these dimensions it is observed that there is a small radial clearance between the fuel compact and the fuel channel wall with an associated thermal resistance.

Two models have been produced with slightly differing geometries. In the first model, (hereafter called 'model 1') for simplicity, the clearance and contact resistance have been neglected so the fuel compacts and fuel channels are assumed to have the same diameter of 12.5 mm. The dimensions of the region used for the finite element model are shown in Figure 5.2.3. The second model (hereafter called 'model 2') includes the contact or gap resistance, so the fuel channel was taken to have a diameter of 12.7 mm. The dimensions of the region used for the 'contact resistance' finite element model are shown in Figure 5.2.4:.

Figure 5.2.3: Geometry of the finite element model

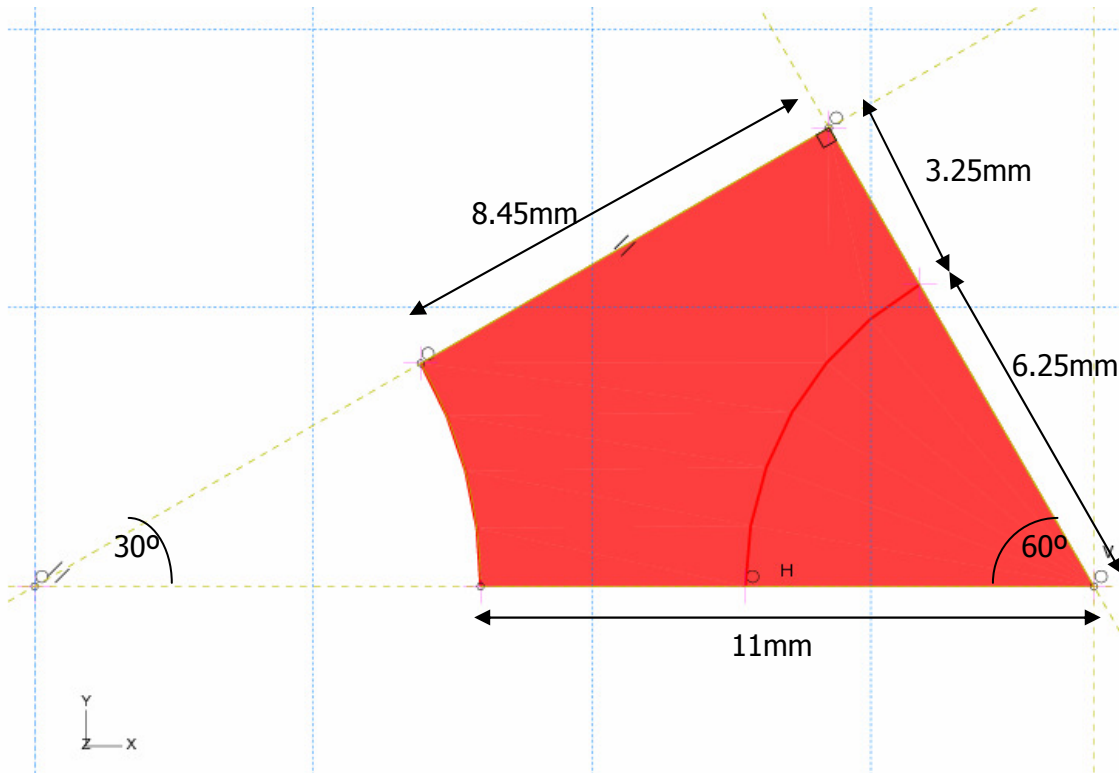
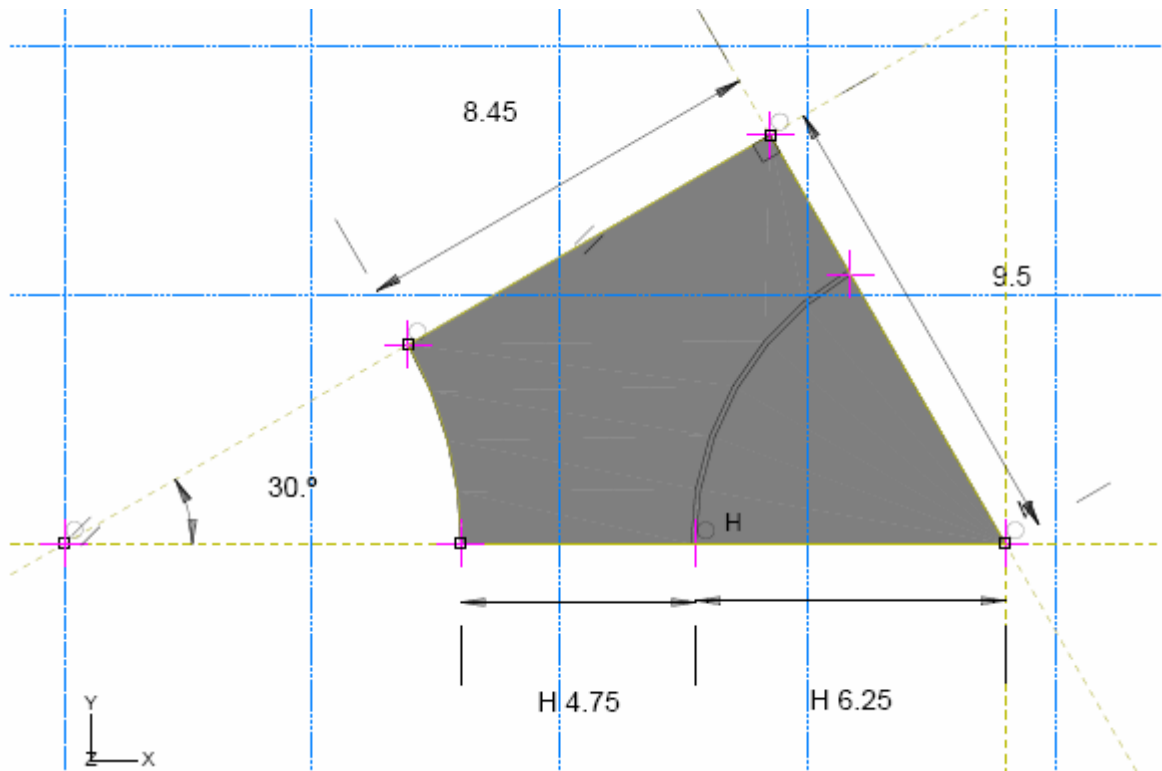


Figure 5.2.4: Geometry of the finite element model with contact/gap resistances



5.2.2 Material properties

5.2.2.1 Model 1

The domain contains two materials, fuel compact and graphite - while the properties of helium are also needed to determine the heat transfer coefficient at the coolant channel wall.

Helium properties were evaluated at conditions representative of those in GT-MHR; a mean coolant temperature of 670°C and pressure of 70 bar. Correlations from the German KTA rules (Reference 5.2) were used, giving a thermal conductivity of 0.35 W/m/K, specific heat capacity of 5.195 kJ/kg/K and dynamic viscosity of 4.421×10^{-5} Pa.s.

Properties assigned to the fuel compact in the model are shown in Table 5.2.1. For the fuel compact a thermal conductivity of 20 W/m/K was chosen to represent the combined influence of the presence of lower conductivity TRISO particles and increased degradation in graphite conductivity (due to greater neutron damage and higher temperatures because the fuel compacts are hotter than the fuel blocks in which they sit).

Two variations of the model were run. The first used a constant conductivity for graphite (shown in Table 5.2.1). The thermal conductivity value of 30 W/m/K is not precise but is considered to be representative of irradiated graphite at typical HTGR core temperatures.

Table 5.2.1: Material properties

Material	Thermal Conductivity (W/m/K)	Density (kg/m³)	Specific Heat Capacity (J/kg/K)
Graphite	30.0	1.72E3	1690
Fuel compact	20.0	1.72E3	1690

The second variation replaced the constant thermal conductivity of graphite with a function of temperature. This variation was requested by the NRC. The aim is that these calculations will provide a benchmark to determine how best to include the effect of temperature dependent thermal conductivity into the simplified meso-scale model as developed by the NRC.

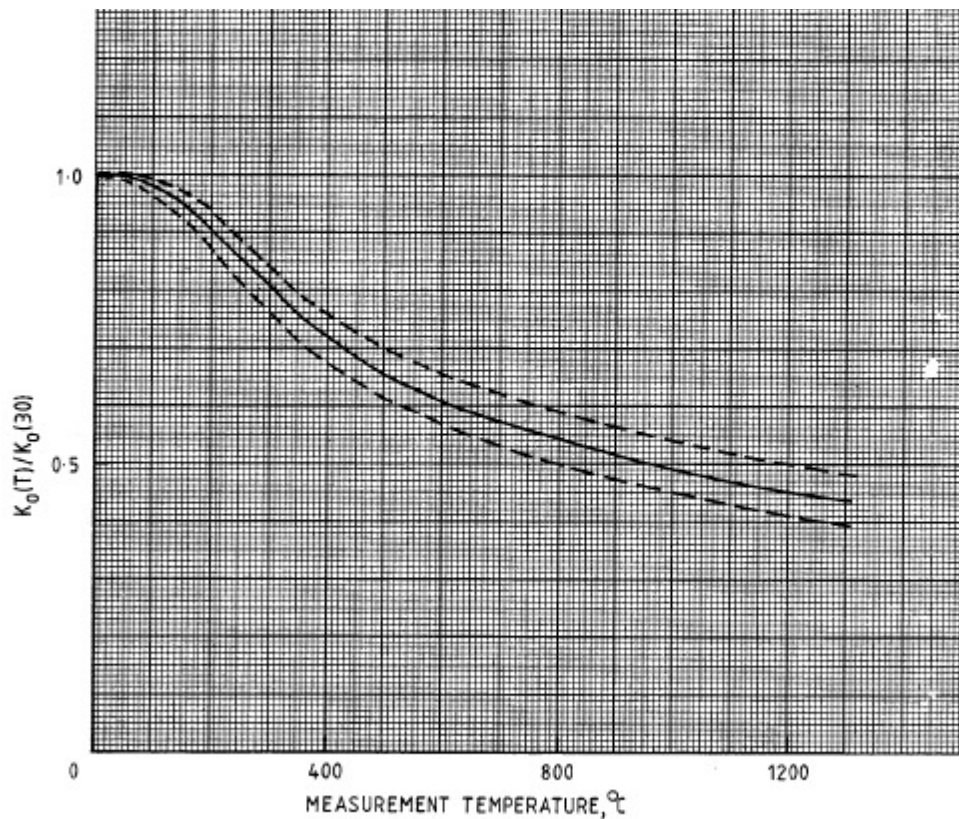
The variation in the conductivity of graphite with temperature and irradiation is discussed in detail in Reference 5.1. Heavily irradiated graphite has a thermal conductivity which is virtually independent of temperature whilst unirradiated graphite shows a much larger variation with temperature.

The request was that the function chosen should overstate its temperature dependence so the variation of unirradiated graphite with temperature has been used

for this work. However, the conductivity of unirradiated graphite is considerably higher than for irradiated graphite (approximate values are 140 W/m/K compared with 30 W/m/K). It was therefore been decided to superimpose the unirradiated temperature variation onto the underlying irradiated graphite thermal conductivity. This gives an artificially increased sensitivity to temperature but also keeps reasonable values for the conductivity as requested.

Reference 5.1 contains a plot of the temperature dependence of unirradiated graphite, compared to a reference value at 30°C (reproduced as Figure 5.2.5). This value has been taken to be 30 W/m/K. Values have been read off the graph and input into the ABAQUS model as a table of temperature against conductivity.

Figure 5.2.5: Conductivity ratio of unirradiated graphite as a function of temperature



5.2.2.2 Model 2

The material properties for model 2 are the same as for the model 1 with the exception of the helium density used for the gap between the fuel compact and fuel channel wall. Again two variations of the model were run, one with a constant thermal conductivity for graphite and the other with a thermal conductivity that varies as a function of temperature.

The density of helium varies as a function of temperature and a table has been inserted of density against temperature. This was calculated using:

$$\rho = \frac{P}{RT}$$

Where: P is the pressure in Pa (taken to be 70 bar = 7×10^6 Pa)

R is 2077.3 J/kg/K for Helium

T is the temperature in K

5.2.3 Boundary values and power density in a fuel compact

For GT-MHR the helium mass flow rate through the whole core is 316 kg/s (Reference 5.3). Ignoring the presence of blocks containing control rod channels, there are typically 108 coolant channels per block and 102 columns of fuel blocks, therefore there are approximately 11000 coolant channels in the core giving an average mass flow rate of 0.029 kg/s per coolant channel. Based on the above properties and this mass flow rate, the average Reynolds number in a coolant channel is 51.6×10^3 , giving a Nusselt number, based on the Dittus-Boelter correlation of 119 and a resulting heat transfer coefficient of 2.615 kW/m²/K (a rounded value of 2.6 kW/m²/K was used in the model).

The power density in a compact was set to the average value for the whole core. The steady state thermal power in GT-MHR is 600 MW and there are 2.92 million fuel compacts in the core (Reference 5.3), therefore the average power per compact is 205 W. The diameter and length of a fuel compact are 12.5 mm and 50 mm respectively, so the average steady state power density is 33.41 MW/m³.

5.2.4 Finite element mesh

A finite element mesh was constructed within the solution domain made-up from 8-node quadratic quadrilateral elements. The mesh used for model 1 is shown in Figure 5.2.6 and contained 725 elements and 2288 nodes in total. The mesh used for model 2 contained 4304 elements and 12931 nodes in total and is shown in Figure 5.2.7.

The boundary between the fuel compact and graphite block is shown as a red curve in Figure 5.2.6, this curve also defines a path to Abaqus along which the fuel surface temperatures were to be integrated to give the average fuel surface temperature as an output parameter.

Figure 5.2.6: Finite element mesh for model 1

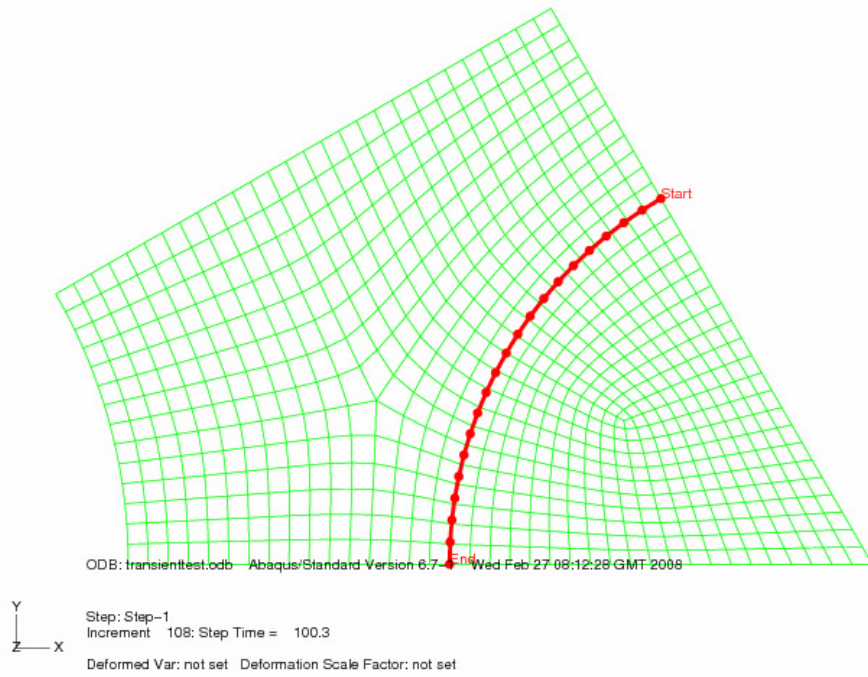
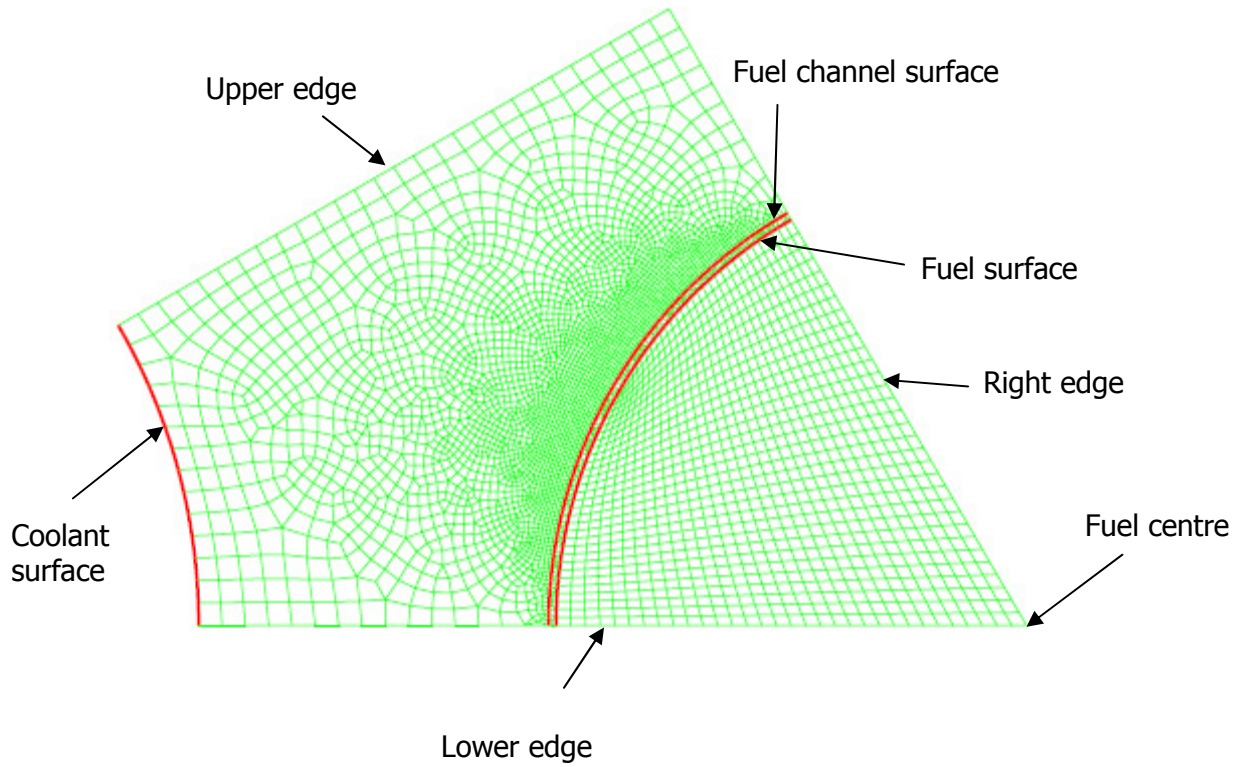


Figure 5.2.7: Finite element mesh for model 2



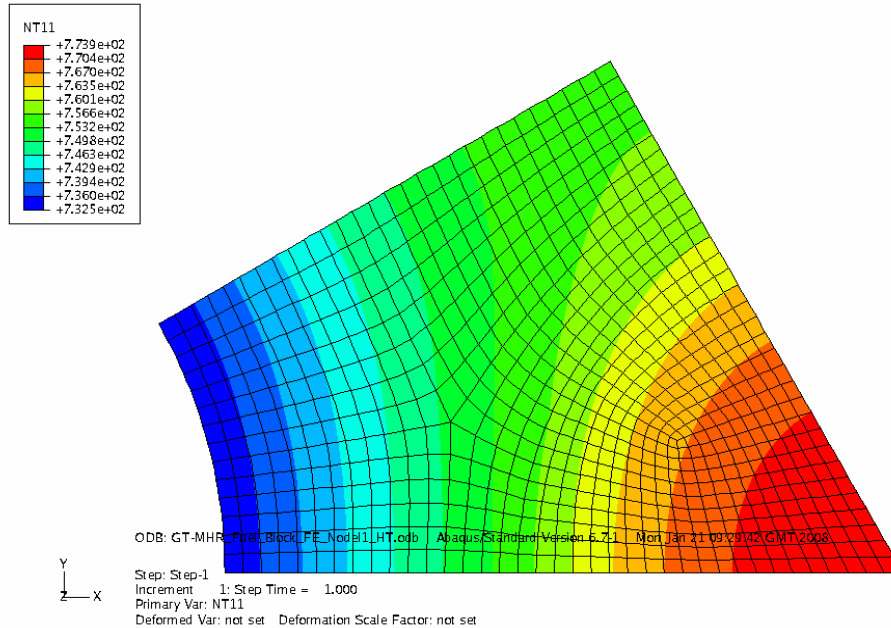
5.2.5 Model 1 results with a constant graphite thermal conductivity

5.2.5.1 Steady state model results

A contour plot of temperature obtained from the steady state model is shown in Figure 5.2.8.

Figure 5.2.8: Steady state temperature distribution

Temperatures given in °C.



Data to generate line graphs of the temperature profiles along the three straight edges and around the peripheries of the fuel compact and coolant channel have been extracted. Identification of the edges is shown in Figure 5.2.7: and the resulting line graphs are shown in Figure 5.2.9 to Figure 5.2.13. The x-axis for the figures showing the temperature along the upper, lower and right edges is from left to right in the model (i.e. from the coolant towards the fuel).

Figure 5.2.9: Steady state temperature profile along the 'upper edge'

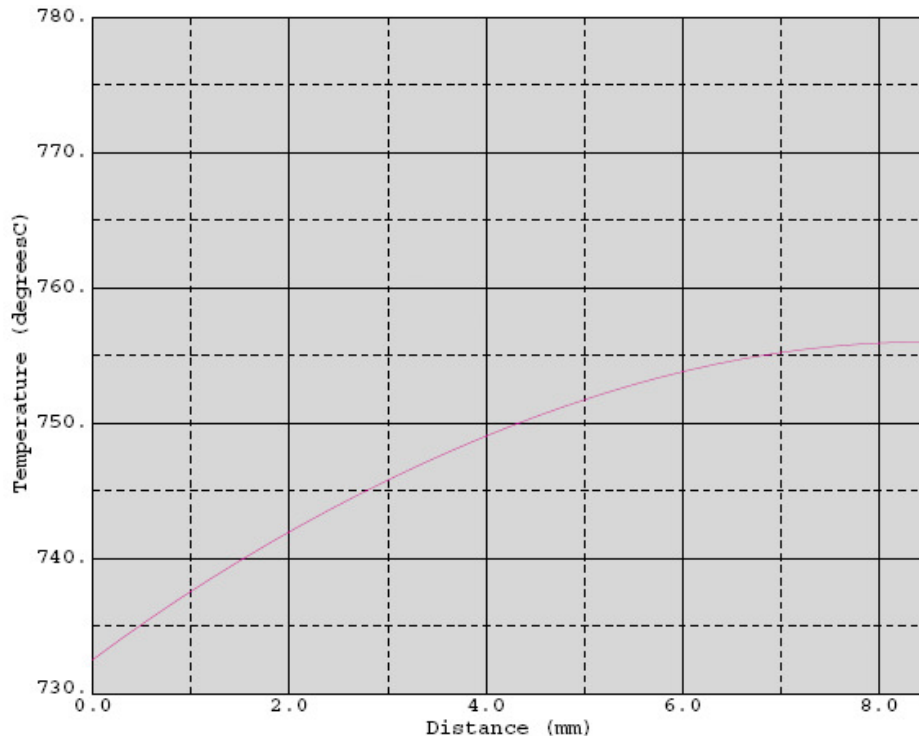


Figure 5.2.10: Steady state temperature profile along the 'lower edge'

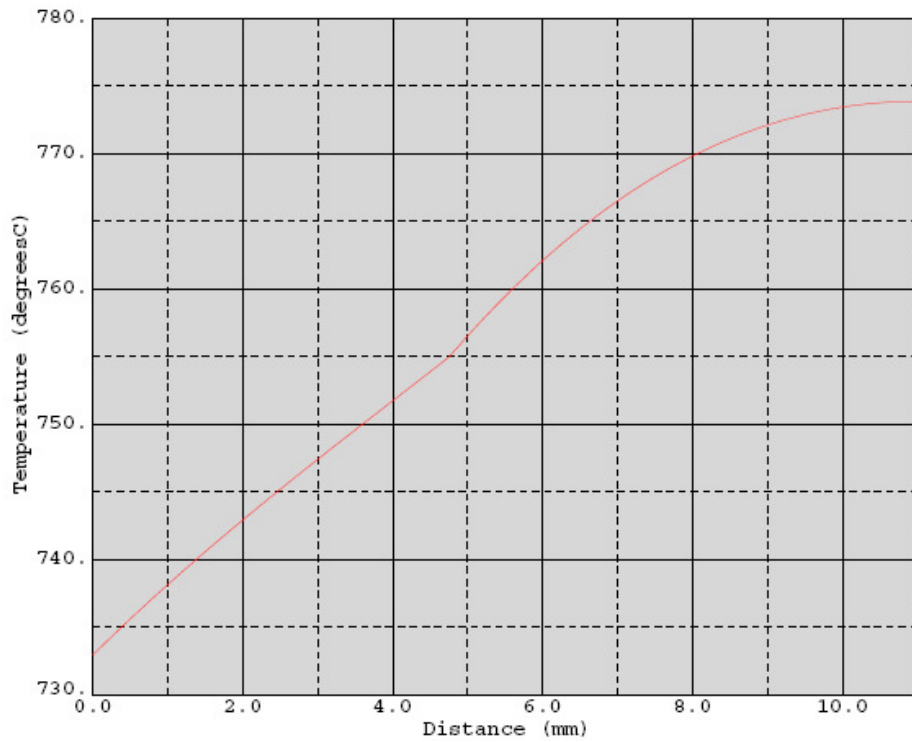


Figure 5.2.11: Steady state temperature profile along the 'right edge'

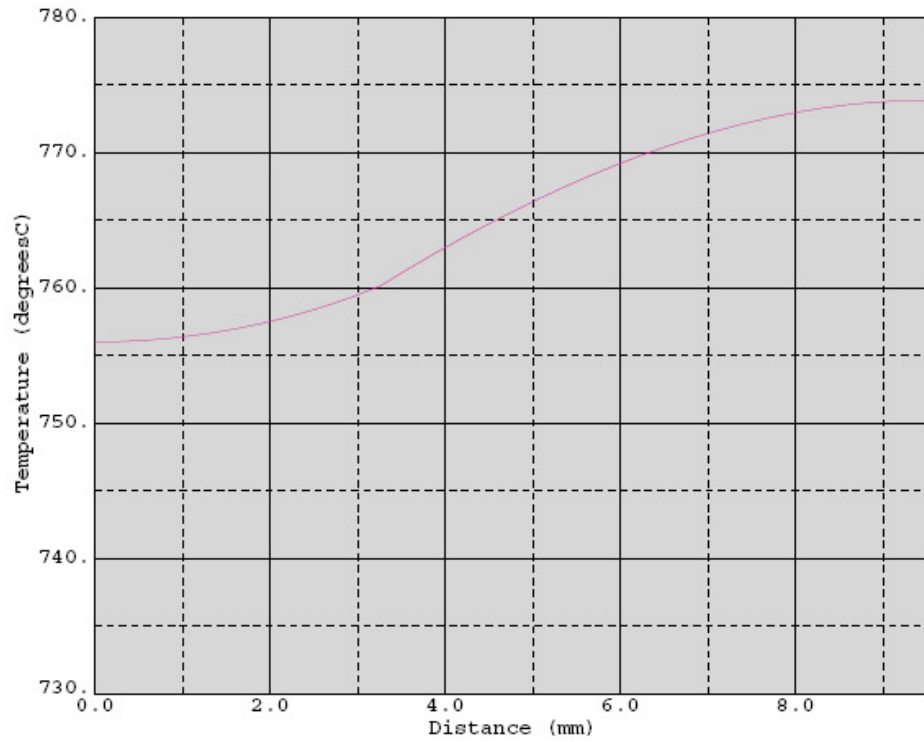


Figure 5.2.12: Steady state temperature profile around periphery of the fuel

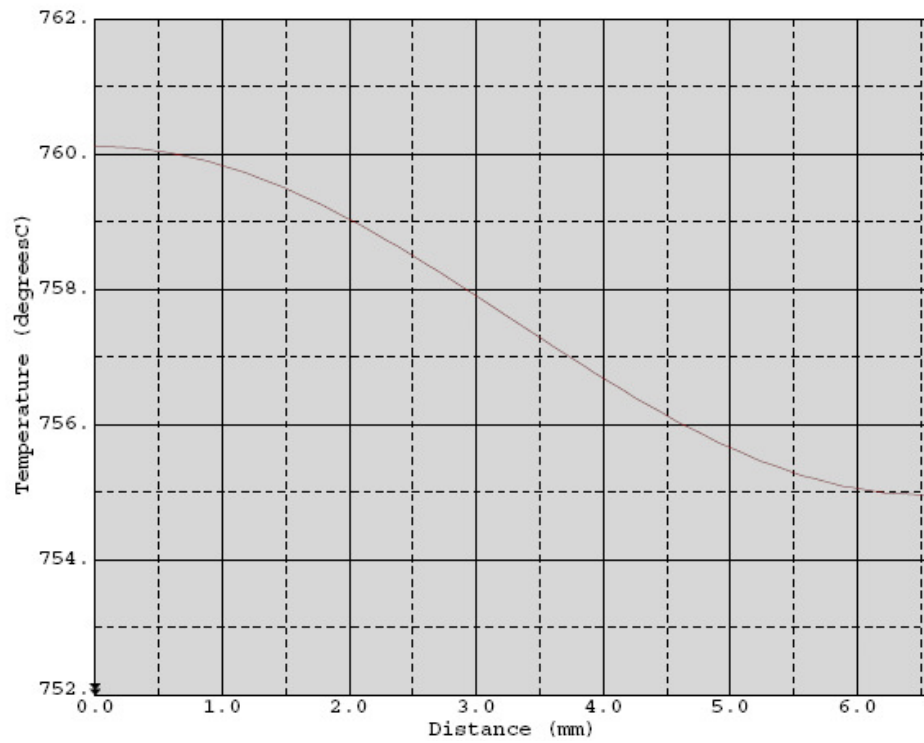


Figure 5.2.13: Steady state temperature profile around coolant channel wall

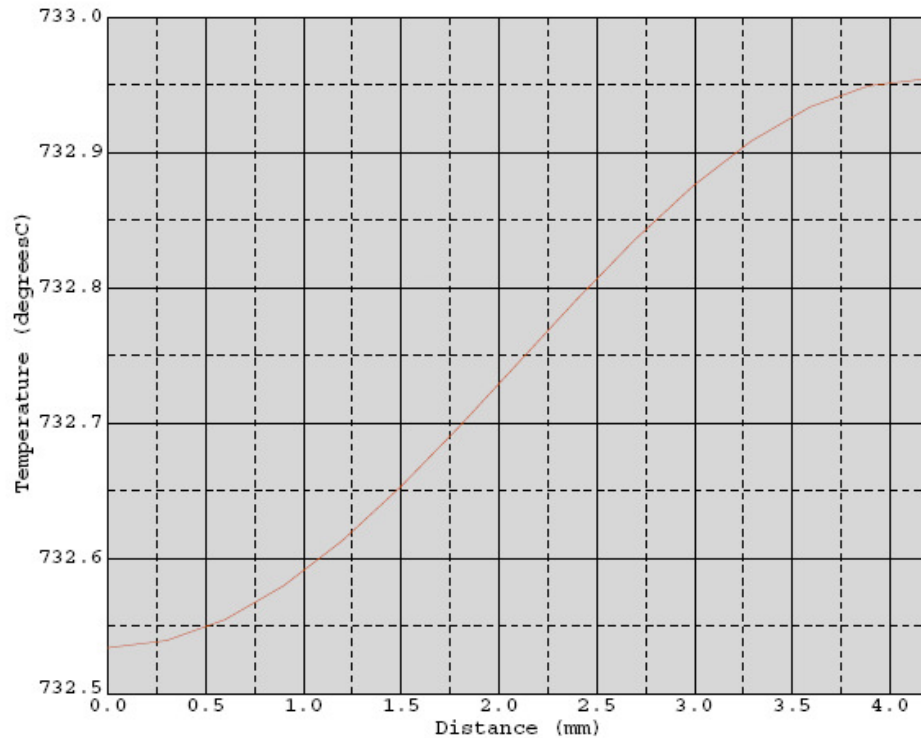


Figure 5.2.12 shows that the temperature varies in an approximately sinusoidal manner around the periphery of the fuel compact, with a peak-to-peak temperature variation of approximately 5.3°C. Figure 5.2.13 shows the temperature around the periphery of the coolant channel; this has a similar shape to that for the fuel compact but with a much smaller peak-to-peak amplitude of approximately 0.4°C. The difference between the average temperatures of the modeled fuel compact surface and coolant channel wall is approximately 25°C while the difference between the coolant of 670°C and the coolant channel wall is approximately 62.5°C.

5.2.5.2 Transient models

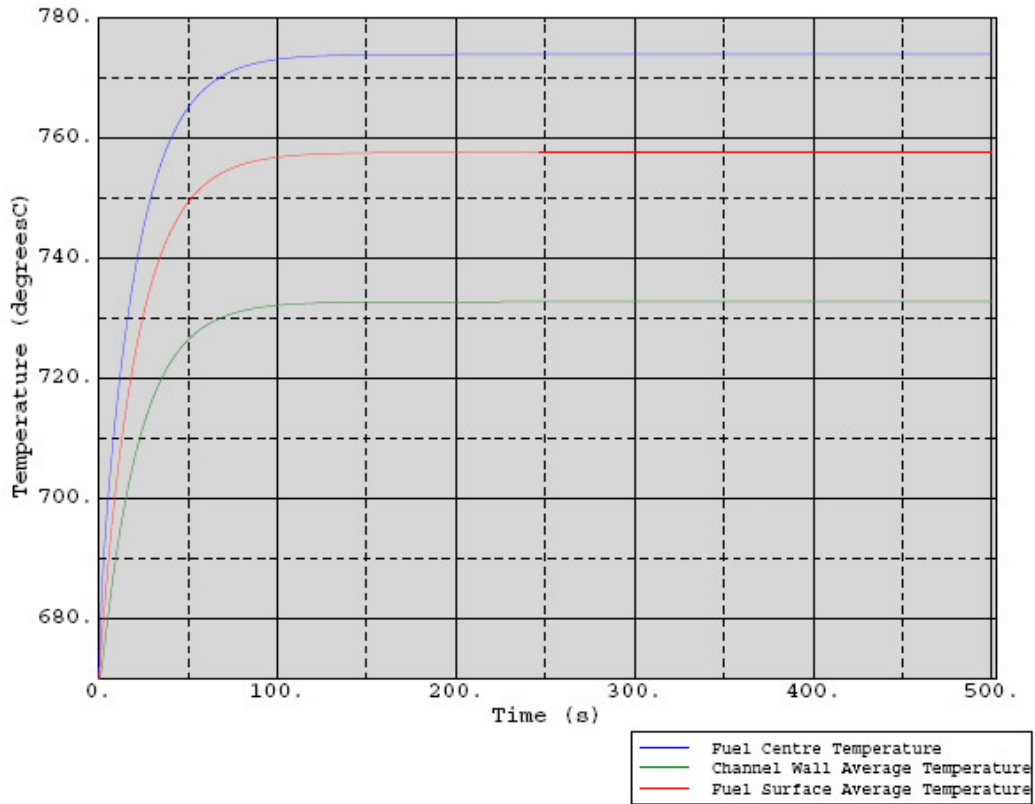
Two transient models were constructed; 'Transient Model 1' and 'Transient Model 2', which started from different sets of initial conditions, however, in all other respects the models were identical.

Transient Model 1

A transient model was run using the same material properties and boundary conditions as for the steady state model. In this case, however, the model was assigned a uniform initial temperature of 670°C everywhere (the coolant temperature) with initially zero heat generation in the fuel compact. The power density in the fuel compact was then ramped-up to its nominal steady state value of 33.41 MW/m³ over 0.001s to approximate a step change in heat input.

Many line graphs of the evolution of the temperatures along the various edges in the model were produced for comparison with the multi-scale model of Sub-section 7.3 and these are displayed in Appendix A.1. The evolution of fuel centre, fuel surface average and channel wall average temperature are shown in Figure 5.2.14.

Figure 5.2.14: Transient 1 - evolution of fuel centre, fuel periphery and channel wall temperatures with time



The time taken for the transient to reach the steady state has been defined, arbitrarily, as the time taken for the temperature of the fuel centre to reach 99% of its steady state value. From the results obtained it was estimated that a steady state was reached, according to the above definition, after approximately 96s.

As a check on the solution, the initial rate of temperature rise in the fuel compact was compared with an expected adiabatic value, calculated by dividing the power density by the volumetric heat capacity. The results from the first few time steps from the finite element model indicated an initial rate of temperature rise of 11.2 °C/s and this compared well with the theoretical adiabatic rate of 11.5°C/s, indicating that the model had been set-up correctly.

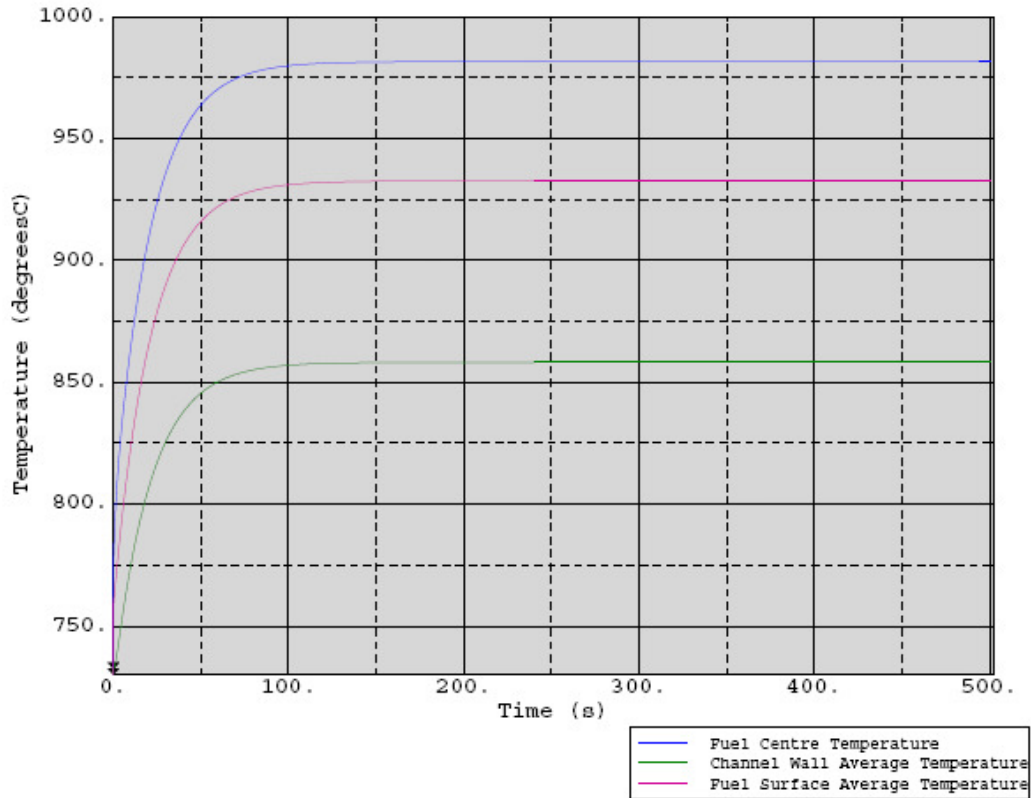
Transient Model 2

A second transient was set up which started from the steady state solution corresponding to a nominal power density as its initial condition. At the start of the

transient the power density in the fuel compact is increased by a factor of three from the nominal value up to 100.23 mW/mm³.

The evolution of fuel centre, fuel surface average and channel wall average temperatures are shown in Figure 5.2.15.

Figure 5.2.15: Transient 2 – evolution of fuel centre, fuel periphery and channel wall temperatures with time



5.2.6 Model 1 results with a varying graphite thermal conductivity

The transient models detailed in Section 5.2.5.2 were run with the only difference being the change in the conductivity of graphite to vary as a function of temperature.

5.2.6.1 Transient Model 1

A contour plot of the temperature after the transient reached a steady state is shown in Figure 5.2.16.

The evolution of fuel centre, fuel surface average, graphite average and channel wall average temperature are shown in Figure 5.2.17.

Figure 5.2.16: Steady state temperature distribution

Temperatures given in °C.

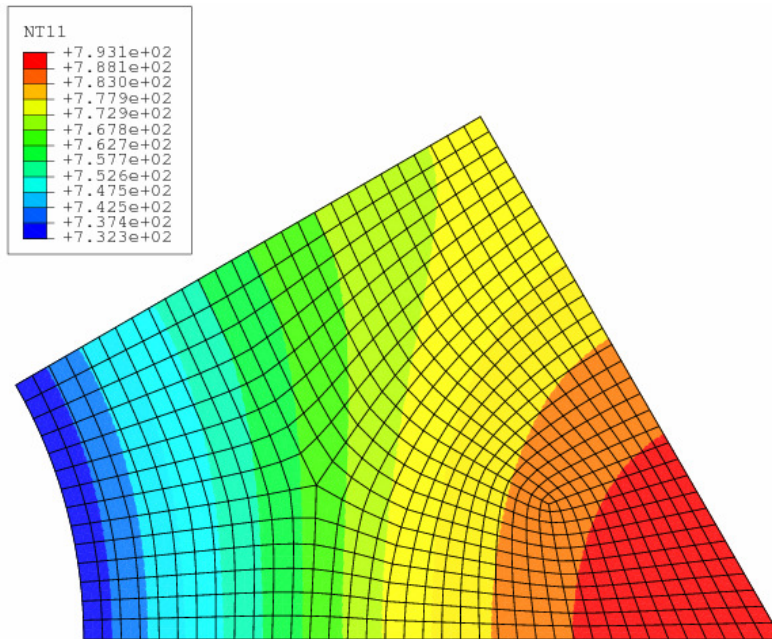
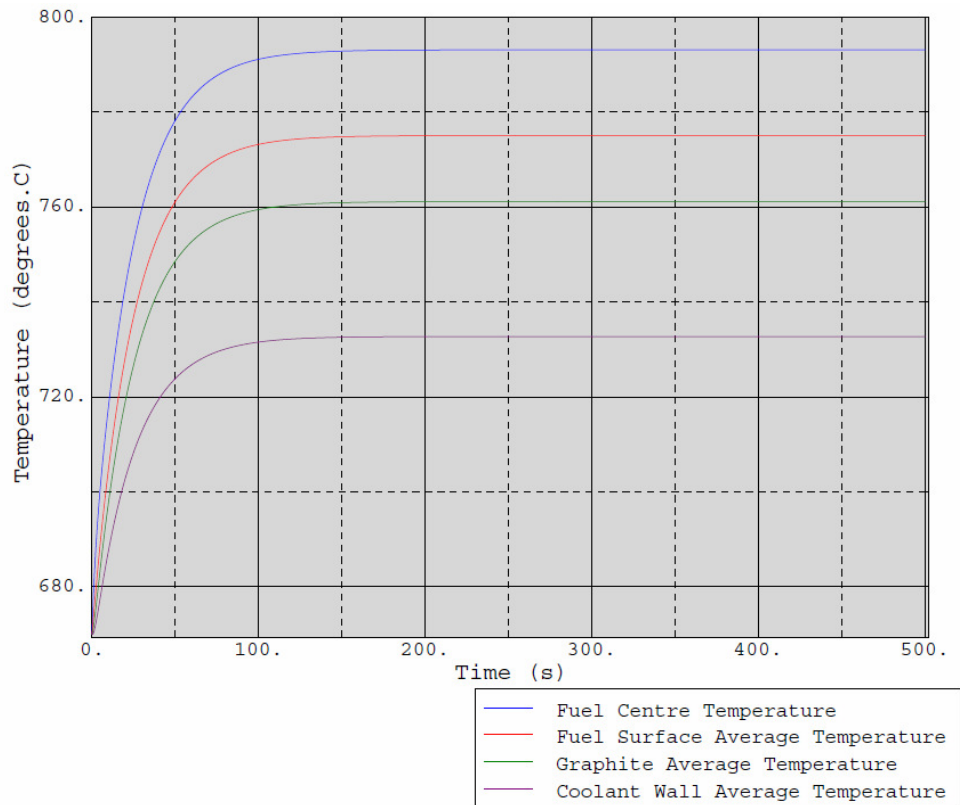


Figure 5.2.17: Transient 1 - evolution of fuel centre, fuel periphery, graphite and channel wall temperatures with time

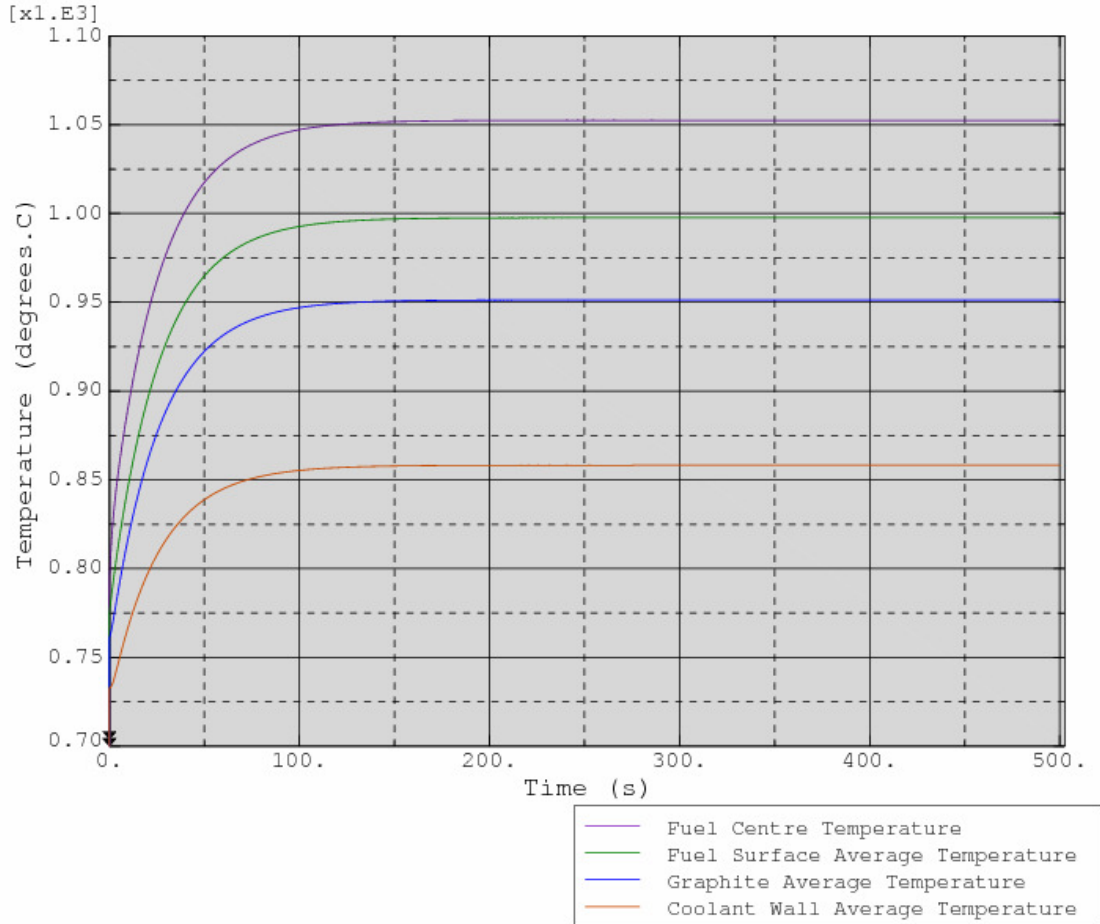


Using the definition given in Section 5.2.5.2, the time taken to reach a steady state was approximately 112s.

5.2.6.2 Transient Model 2

The evolution of fuel centre, fuel surface average, graphite and channel wall average temperatures are shown in Figure 5.2.18.

Figure 5.2.18: Transient 2 - evolution of fuel centre, fuel periphery, graphite and channel wall temperatures with time



5.2.7 Model 2 results with a constant graphite thermal conductivity

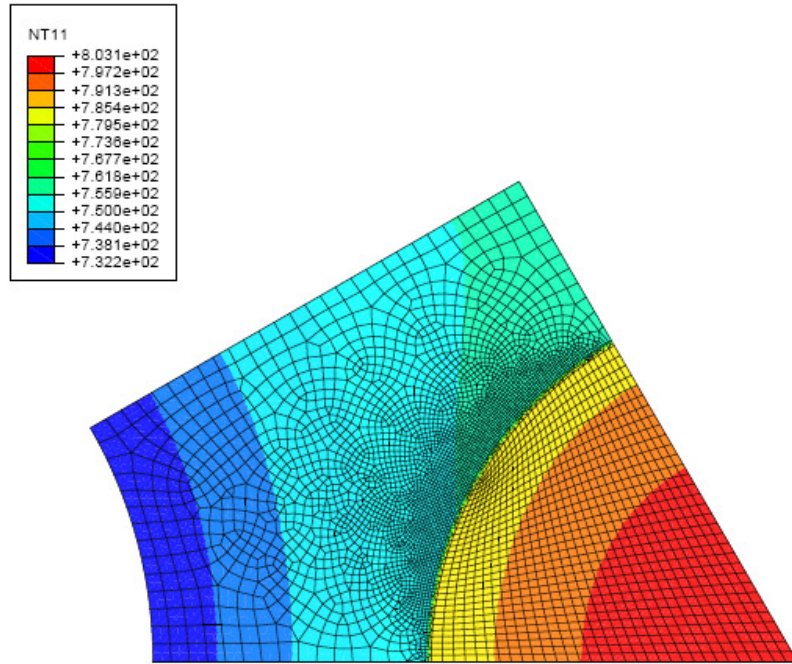
The geometry of model 2 (with the contact resistances) was used to run steady state and transients models with a constant and varying thermal conductivity of graphite. The results are shown in the following sections 5.2.7.1 and 5.2.7.2.

5.2.7.1 Steady state

A contour plot of temperature obtained from the steady state model is shown in Figure 5.2.19.

Figure 5.2.19: Steady state temperature distribution

Temperatures given in °C.



Data to generate line graphs of the temperature profiles along the three straight edges and around the peripheries of the fuel compact, fuel channel and coolant channel have been extracted. Identification of the edges is shown in Figure 5.2.7: and the resulting line graphs are shown in Figure 5.2.20 to Figure 5.2.25.

Figure 5.2.20: Steady state temperature profile along the 'upper edge'

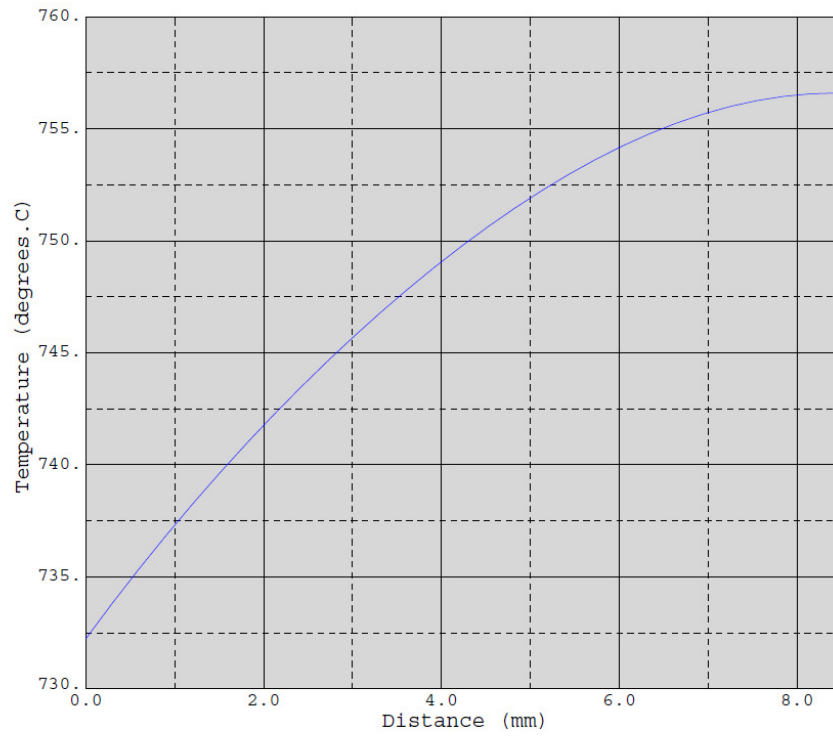


Figure 5.2.21: Steady state temperature profile along the 'lower edge'

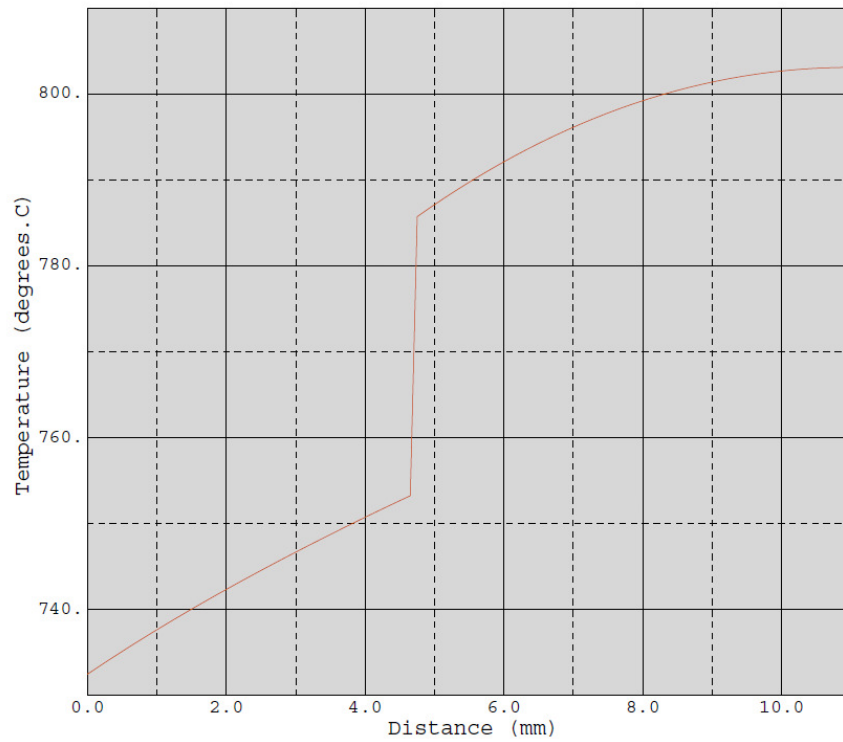


Figure 5.2.22: Steady state temperature profile along the 'right edge'

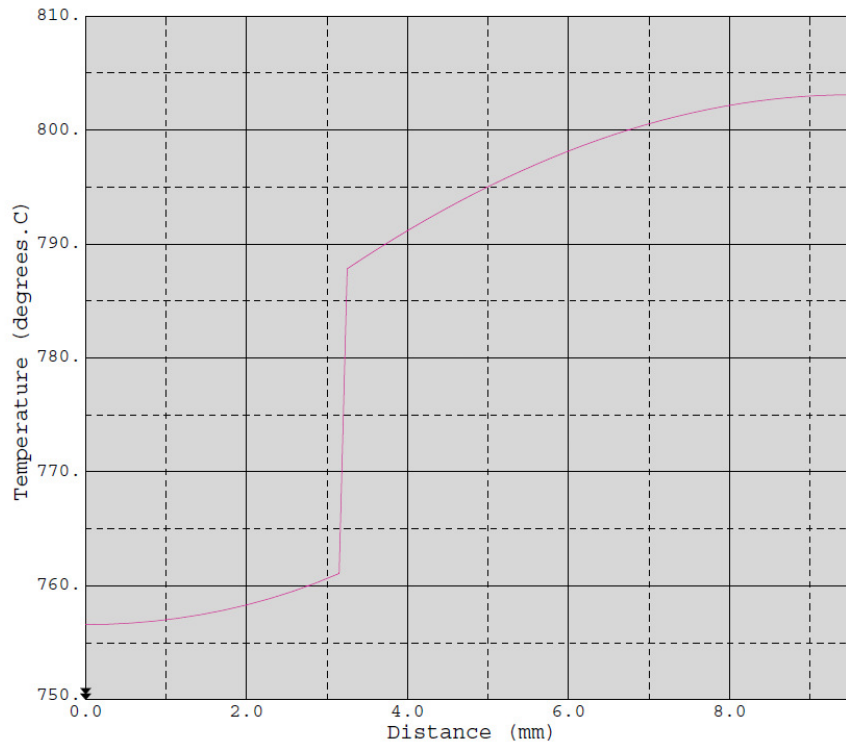


Figure 5.2.23: Steady state temperature profile around periphery of the fuel

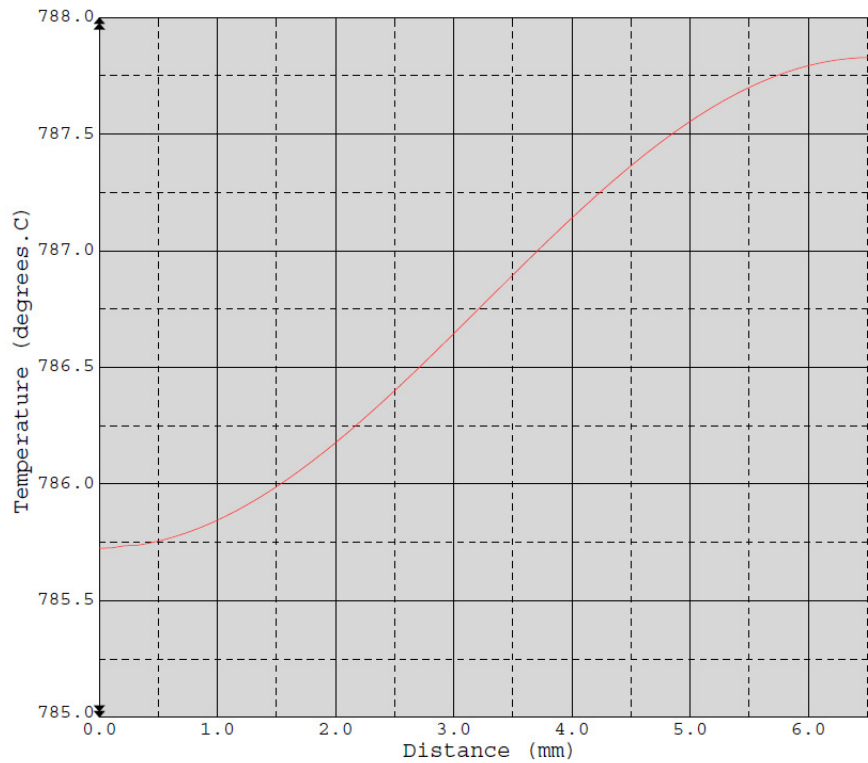


Figure 5.2.24: Steady state temperature profile around surface of the fuel channel

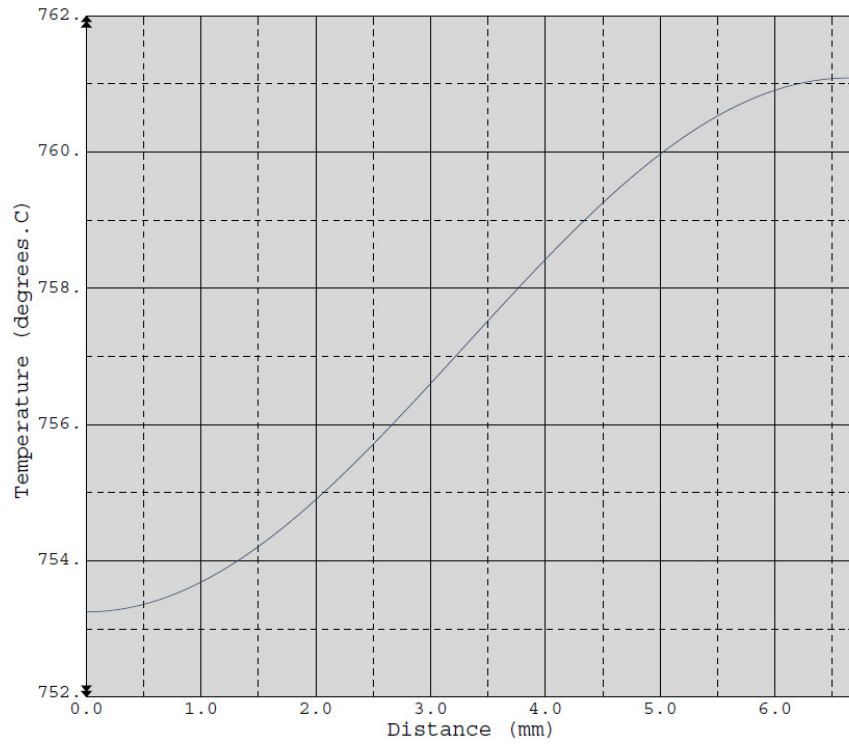
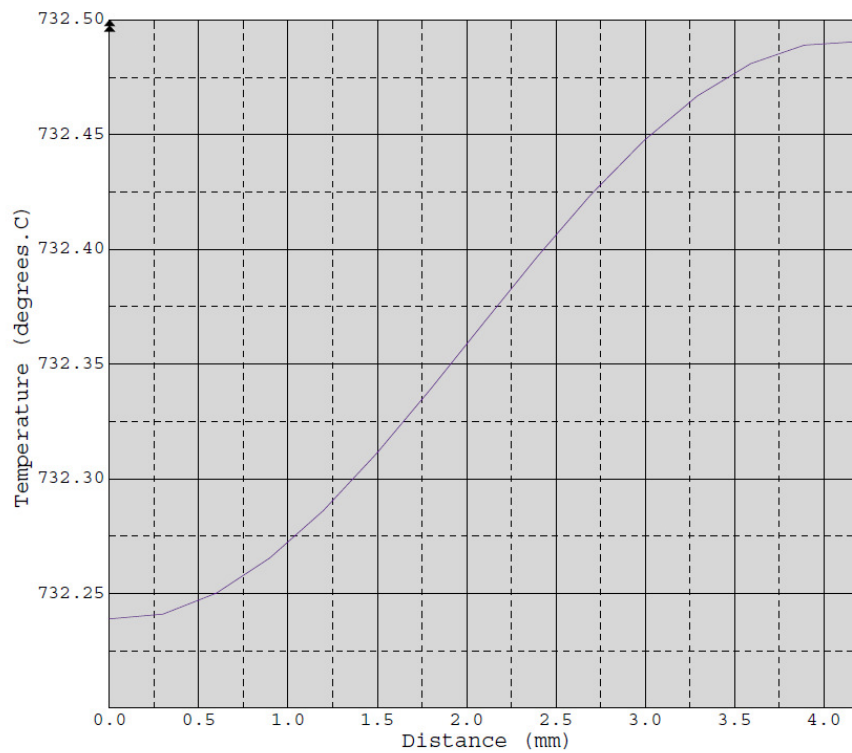


Figure 5.2.25: Steady state temperature profile around coolant channel wall

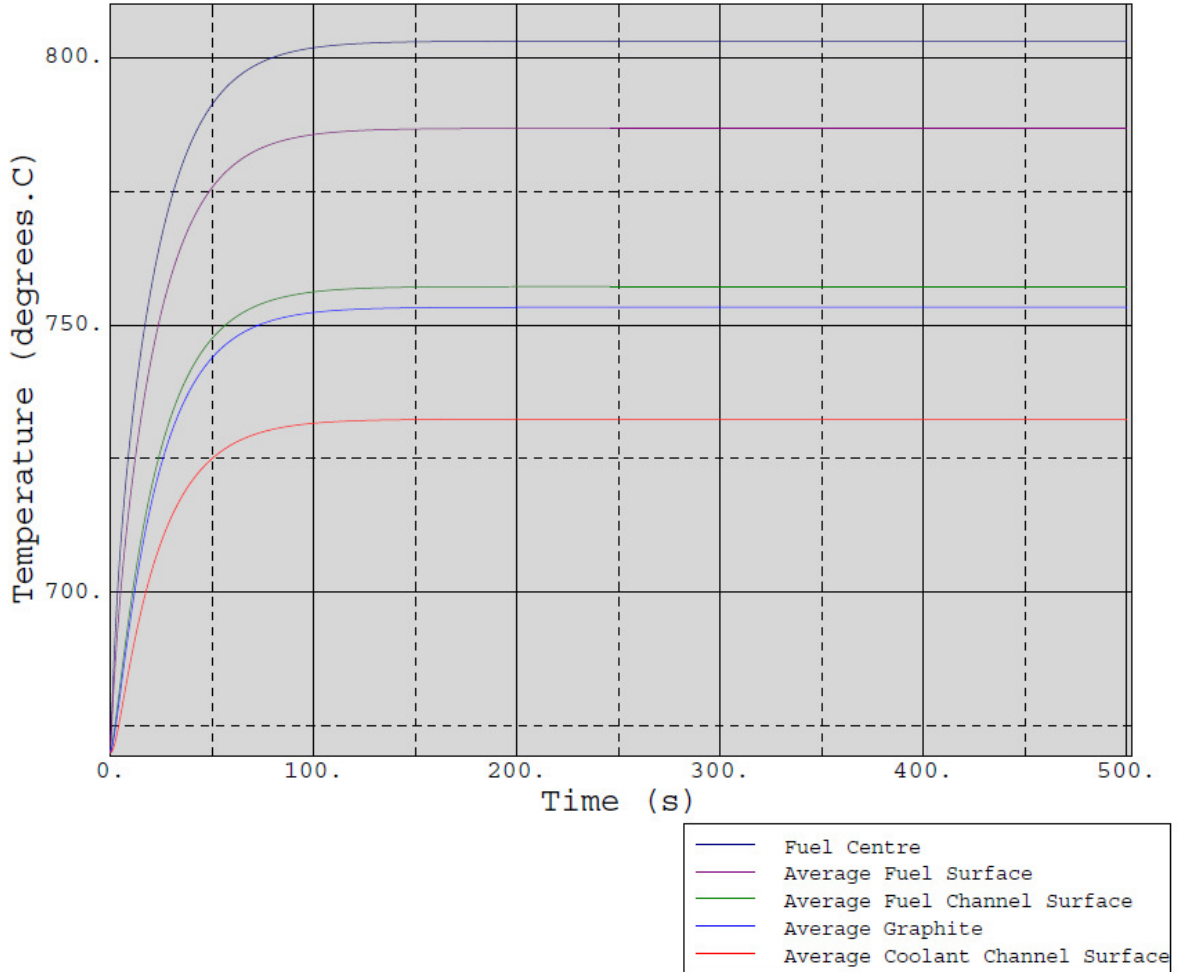


5.2.7.2 Transient models

Transient Model 1

The evolution of fuel centre, fuel surface average, fuel channel surface average, graphite average and channel wall average temperature are shown in Figure 5.2.26.

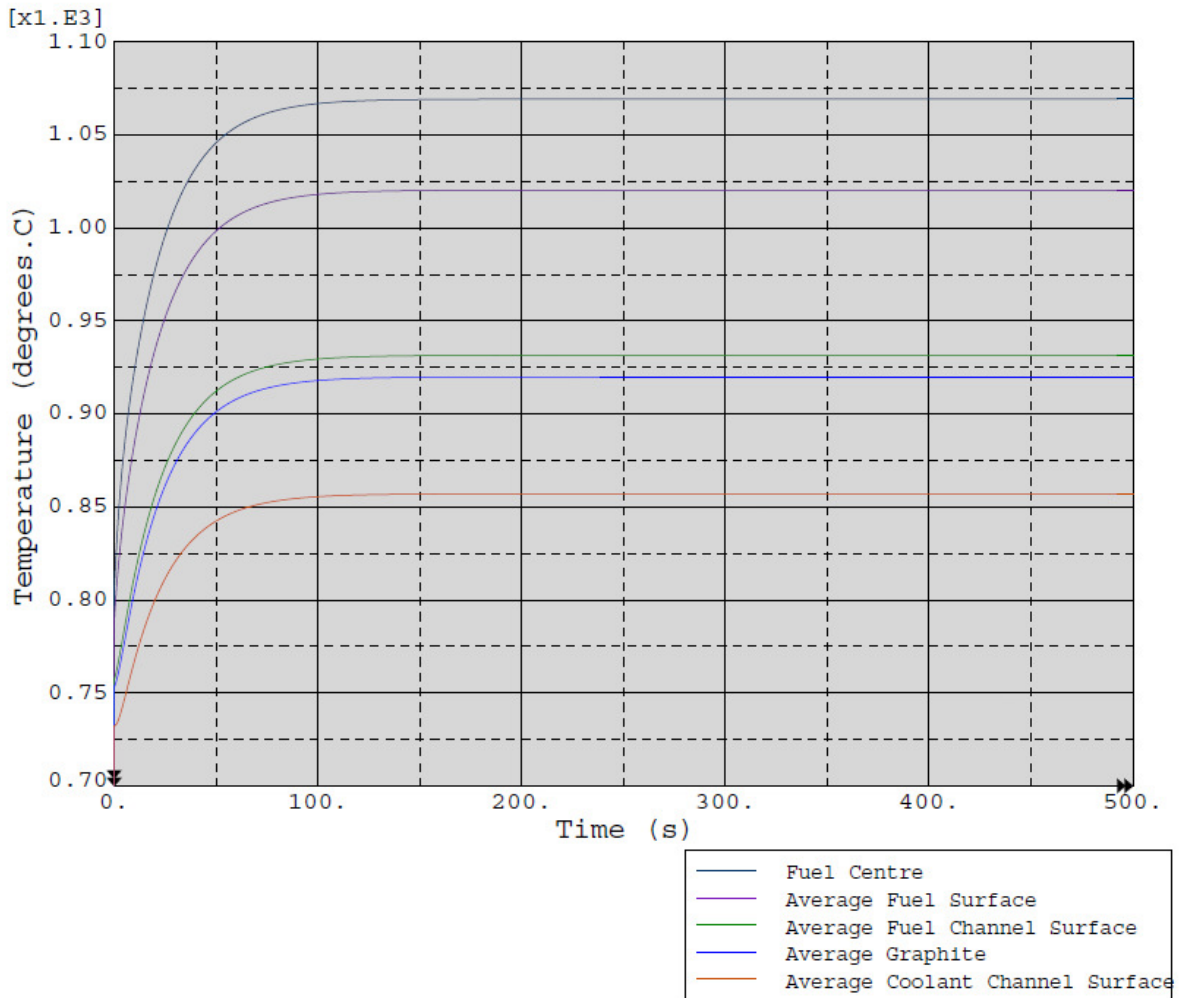
Figure 5.2.26: Transient 1 - evolution of fuel centre, fuel periphery, fuel channel surface, graphite and channel wall temperatures with time



Transient Model 2

The evolution of fuel centre, fuel surface average, fuel channel average, graphite and channel wall average temperatures are shown in Figure 5.2.27:.

Figure 5.2.27: Transient 2 - evolution of fuel centre, fuel periphery, fuel channel surface, graphite and channel wall temperatures with time

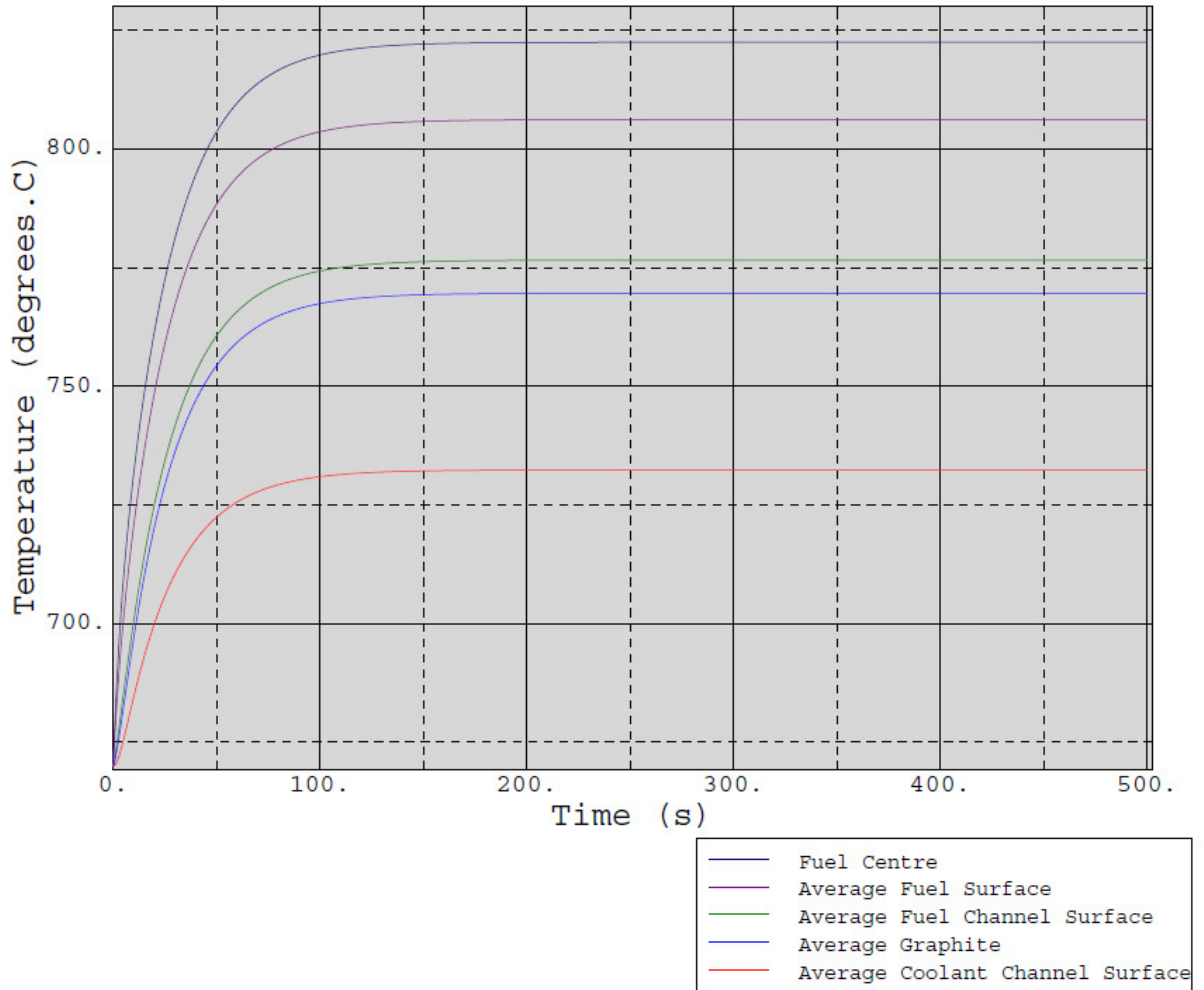


5.2.8 Model 2 results with a varying graphite thermal conductivity

5.2.8.1 Transient Model 1

The evolution of fuel centre, fuel surface average, fuel channel average, graphite average and channel wall average temperature are shown in Figure 5.2.28.

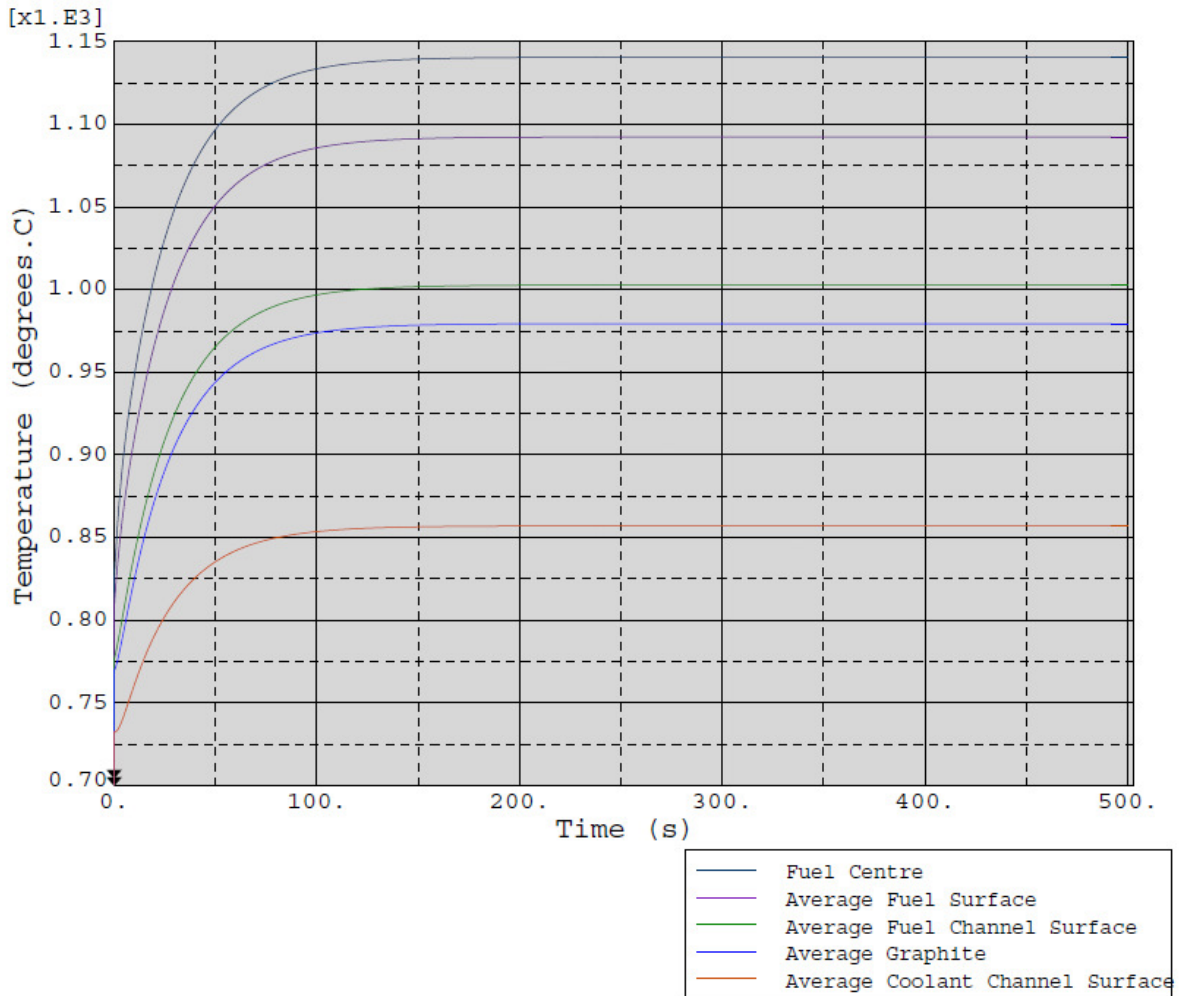
Figure 5.2.28: Transient 1 - evolution of fuel centre, fuel periphery, graphite and channel wall temperatures with time



5.2.8.2 Transient Model 2

The evolution of fuel centre, fuel surface average, graphite and channel wall average temperatures are shown in Figure 5.2.29.

Figure 5.2.29: Transient 2 - evolution of fuel centre, fuel periphery, graphite and channel wall temperatures with time



5.3 Development of Meso-Scale Sub-Models

In previous studies of prismatic core HTGRs, AMEC developed an analytical model to represent the conduction of heat from the surface of a fuel compact to its surrounding coolant channels. This model allowed the compact temperatures to be coupled to those of the mean graphite and coolant channel walls and was derived for steady state conditions and based upon the assumption that the average behavior of a 1/6 sector of a fuel block can be predicted by modeling the heat transfer in a pair of representative unit cells. In the first of these, the circular coolant channel is assumed to be surrounded by a hexagonal cell with 1/3 of a fuel compact located on each of the vertices of the hexagon. The second unit cell consisted of a triangle formed by joining the centers of the three coolant channels that surround a single fuel compact. So each coolant channel receives heat from two fuel channels and each fuel channel shares half a coolant channel with a neighboring fuel channel. Previously, each of these unit cells was approximated by an equivalent circular domain to allow simple

one-dimensional analytical solutions of the conduction equations. The diameters of these annular domains were selected to give cross-sectional areas that were equivalent to those of the original unit cells. The solutions to the one-dimensional heat conduction equations for each cylindrical domain were matched to give the same average temperatures within the graphite of the fuel block. At the time this model was developed, the matched pair of solutions was believed to yield the correct gradients at the compact and fuel channel surfaces, but no qualification of the predicted temperature values was available.

The matching of two separate and approximate solutions is difficult to extend to non-steady situations, attributing the thermal mass correctly between the two domains and the means of simulating the time-dependent progression of a temperature disturbance across the domain boundaries from one domain to the other is not obvious. Further, the assumption that the geometry can be reduced from two dimensions to a pair of 1-dimensional annular domains is a large approximation.

The objective of this sub-section is to present the previous AMEC model and to compare this with a finite element solution of the previous sub-section. The development of a new model, that is applicable to transient conditions, is described and its results are compared with finite element results.

5.3.1 Previous analytical steady state approach

Each coolant channel is surrounded by six channels that contain fuel compacts. Similarly, each fuel compact channel is surrounded by three coolant channels and three neighboring fuel compacts. A unit cell can be constructed around a coolant channel by constructing lines between the centers of the six surrounding fuel compacts as shown in Figure 5.3.1.

Figure 5.3.1: Unit cell containing one coolant channel and six fuel channels

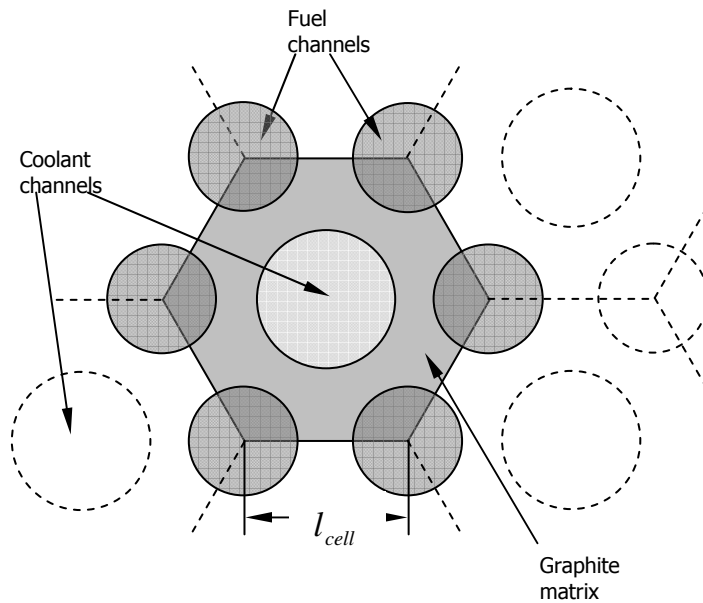
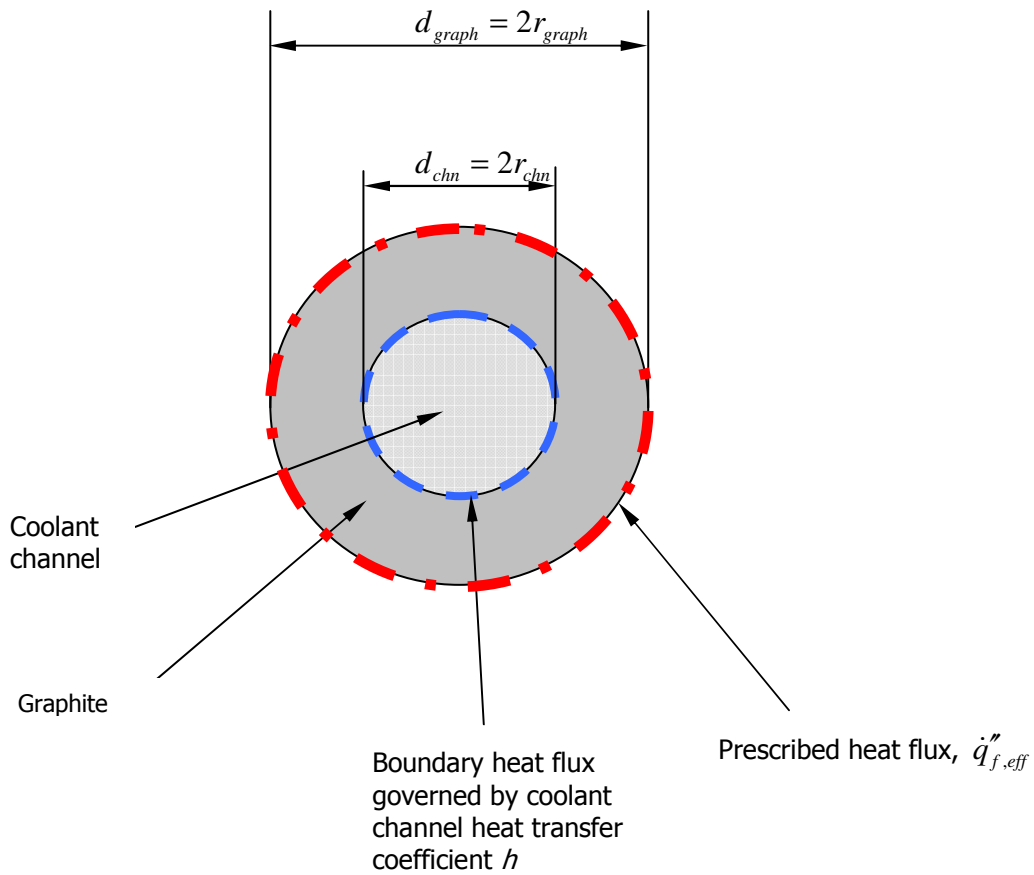


Figure 5.3.2: A coolant channel unit cell approximated as an annular domain



The fuel block graphite in the unit cell, the shaded area in Figure 5.3.1, is approximated by a circle of equivalent area to give a domain as shown in Figure 5.3.2.

Two fuel compacts are smeared around the outer boundary (shown in red in Figure 5.3.2) of the annulus so the steady state heat flux is set to be the linear rating of two compacts divided by the circumference of the outer boundary. Heat transfer from the inner boundary to the coolant occurs by forced convection with the coolant temperature and an appropriate heat transfer coefficient being applied as the boundary condition.

In the following derivation, different forms for the heat generated within the fuel are used, these are:

\dot{q}_f	heat generated within a fuel compact	W
\dot{q}_f''	heat flux through the surface of a compact (\dot{q}_f / [surface area of compact])	W/m ²
$\dot{q}_{f,eff}''$	effective heat flux through surface of compact in the simplified geometry of Figure 5.3.2	W/m ²
\dot{q}_f'''	power density in a compact (\dot{q}_f / [volume of compact])	W/m ³

In the simplified geometry of Figure 5.3.2, neglecting heat generation and axial conduction within the graphite, the one-dimensional heat conduction equation is:

$$\frac{1}{r} \frac{d}{dr} \left(r k_G \frac{dT_c}{dr} \right) = 0,$$

where k_G is the thermal conductivity of the graphite. Integrating twice gives the general solution:

$$T_c = \frac{A_c}{k_G} \ln r_c + B_c,$$

where A_c and B_c are constants of integration. The boundary condition on the outer surface is the imposed *effective* surface heat flux from the fuel. The effective heat flux is used because the circumference of the domain is greater than the combined circumference of two fuel compacts, therefore the heat flux has to be modified so that the correct total heat input is imposed, giving the first constant as:

$$A_c = \frac{\dot{q}_f''' d_{fuel}^2}{4}.$$

Where d_{fuel} is the diameter of the fuel channel.

The heat flux transferred to the coolant by convection is given by:

$$\dot{q}_{chn}'' = h(T_{chn} - T_{He}),$$

where T_{chn} and T_{He} are the coolant channel wall and the Helium coolant temperatures respectively.

This gives the second constant as:

$$B_c = \frac{\dot{q}_{chn}''}{h} - \frac{\dot{q}_f'' d_{fuel}^2}{4k_G} \ln r_{chn} + T_{He}.$$

For steady state heat transfer in the absence of heat conduction out of the unit cell the heat flowing through the channel wall must be the same as the heat generated within the fuel compacts, or:

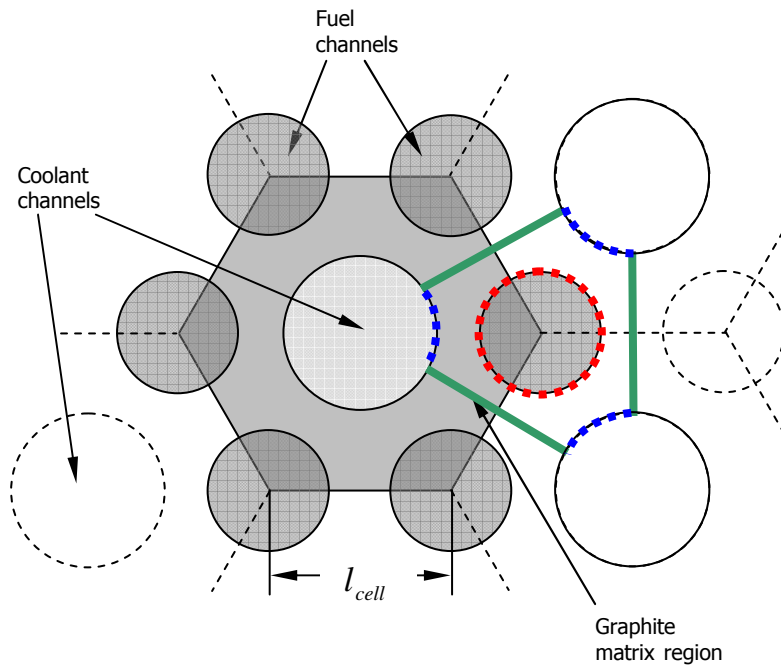
$$r_{chn} \dot{q}_{chn}'' = r_{graph} \dot{q}_{f,eff}'' = \frac{\dot{q}_f'' d_{fuel}^2}{4},$$

giving the temperature profile in the vicinity of the coolant channel wall as:

$$T_c(r_c) = T_{He} + \frac{\dot{q}_f'' d_{fuel}^2}{4} \left(\frac{1}{k_G} \ln \left(\frac{r_c}{r_{chn}} \right) + \frac{1}{h r_{chn}} \right).$$

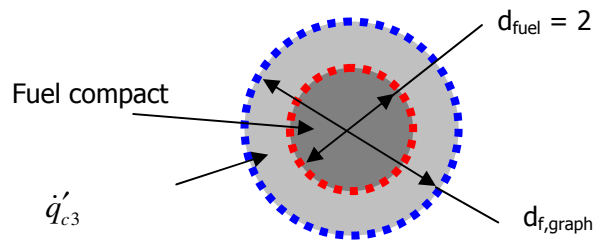
With respect to the fuel compact, the unit cell is triangular as shown as the green triangle in Figure 5.3.3.

Figure 5.3.3: Unit cell surrounding a fuel channel



Once again, the unit cell is approximated as an equivalent annular domain as shown in Figure 5.3.4.

Figure 5.3.4: Approximate representation of a fuel channel unit cell as an annular domain



The differential equation representing heat generation and conduction through the above domain is:

$$\frac{1}{r_f} \frac{d}{dr_f} \left(r_f k_F \frac{dT_f}{dr_f} \right) = \dot{q}_f'''' \quad \text{for } 0 < r_f < r_{fuel}$$

and

$$\frac{1}{r_f} \frac{d}{dr_f} \left(r_f k_G \frac{dT_f}{dr_f} \right) = 0 \quad \text{for } r_{fuel} < r_f < r_{f,graph}$$

The general solution within the graphite annulus that surrounds the fuel compact (i.e., $r_{fuel} < r_f < r_{f,graph}$) is:

$$T_f = \frac{A_f}{k_G} \ln r_f + B_f ,$$

The heat flowing through the boundary between the fuel compact and graphite (shown in red) is the same as that generated within the compact giving the first constant as:

$$A_f = \frac{\dot{q}_f''' d_{fuel}^2}{8} ,$$

so, the graphite temperature in the vicinity of fuel compact is:

$$T_f(r_f) = \frac{\dot{q}_f''' d_{fuel}^2}{8 r_{fuel} k_G} \ln r_f + B_f .$$

The value of the second constant B_f is chosen to enforce equality of the mean graphite temperatures obtained from the coolant channel unit cell and fuel compact unit cell models:

$$\frac{1}{(r_{graph}^2 - r_{chn}^2)} \int_{r_{chn}}^{r_{graph}} T_c r_c dr_c = \frac{1}{(r_{f,graph}^2 - r_{fuel}^2)} \int_{r_{fuel}}^{r_{f,graph}} T_f r_f dr_f .$$

Within the fuel compact, the solution is that for a solid cylinder with uniform heat generation with its surface temperature dictated by the surrounding graphite:

$$T_f(r_f) = T_f(r_{fuel}) + \frac{\dot{q}_f'''}{4k_F} (r_{fuel}^2 - r_f^2) .$$

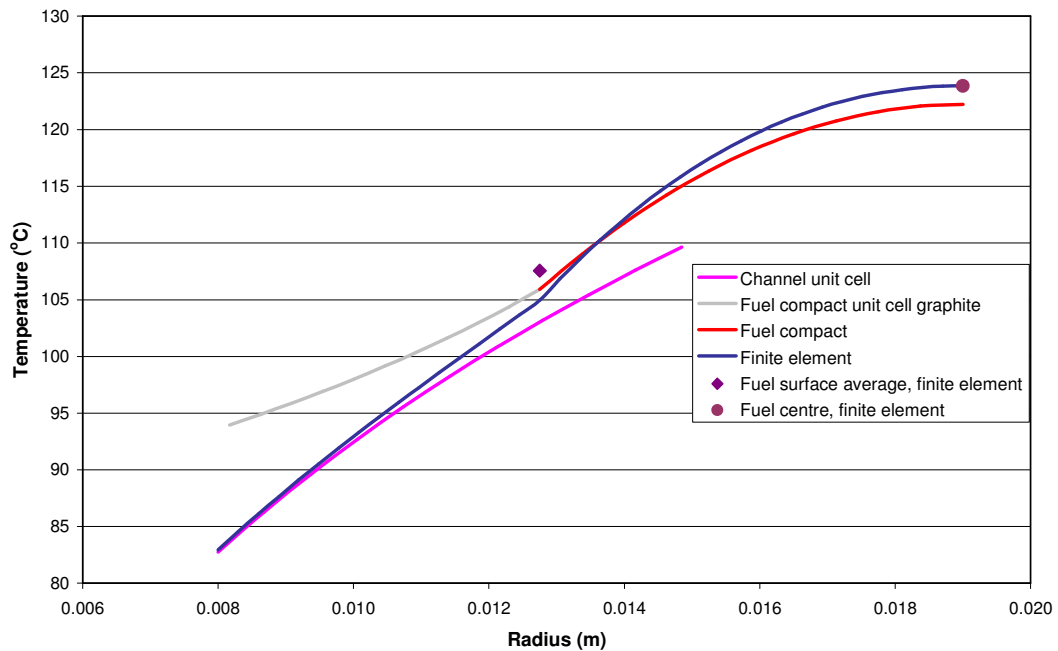
The above equations were coded into an Excel spreadsheet. The parameters were assigned the values given in Table 5.3.1. The geometric values were taken from the GT-MHR benchmark data in Reference 5.4. The diameters of the unit cells were chosen to give circular regions of equivalent areas to the hexagonal geometry shown in Figures 5.3.1 and 5.3.3. The material properties, power density and coolant channel heat transfer coefficient were set to the same values as used in the finite element predictions, but the coolant temperature of 20°C was set for testing purposes only and is not representative of an actual reactor.

Table 5.3.1: Parameters and their values used in the steady state model

Parameter	Symbol	Value
Coolant channel diameter	d_{chn}	16 mm
Coolant channel unit cell outer diameter	d_{graph}	29.693 mm
Fuel compact diameter	d_{fuel}	12.5 mm
Fuel compact unit cell outer diameter	$d_{r,graph}$	21.658 mm
Graphite conductivity	k_G	30 W/m/K
Fuel compact conductivity	k_F	20 W/m/K
Power density in compact	\dot{q}_f'''	33.41 MW/m ³
Convective heat transfer coefficient	h	2600 W/m ² /K
Coolant bulk temperature	T_{He}	20°C

Each of the temperature solutions was evaluated at a number of radial positions with respect to the coolant and fuel channel centers and the results are shown plotted in Figure 5.3.5. The magenta curve is the temperature profile in the vicinity of the coolant channel as predicted by the coolant channel cell model. The grey and red curves represents the temperature profile in the graphite surrounding and within the fuel compact respectively as predicted by the fuel compact cell model. The blue line is the finite element solution plotted along the line that connects the centers of the coolant channel and a fuel compact. The purple diamond and the circle represent the average temperature around the periphery of a fuel compact and the compact centre temperature respectively, as predicted by the finite element model. It can be seen from the latter that the average overall temperature difference from the edge of the compact to its centre is predicted correctly. However this average edge-centre temperature difference is less than the local value predicted by the finite element model because the line along which the FE profile is plotted runs through the azimuthal position on the surface of the compact that is the shortest distance from the coolant channel and is therefore the best cooled (lowest temperature) position.

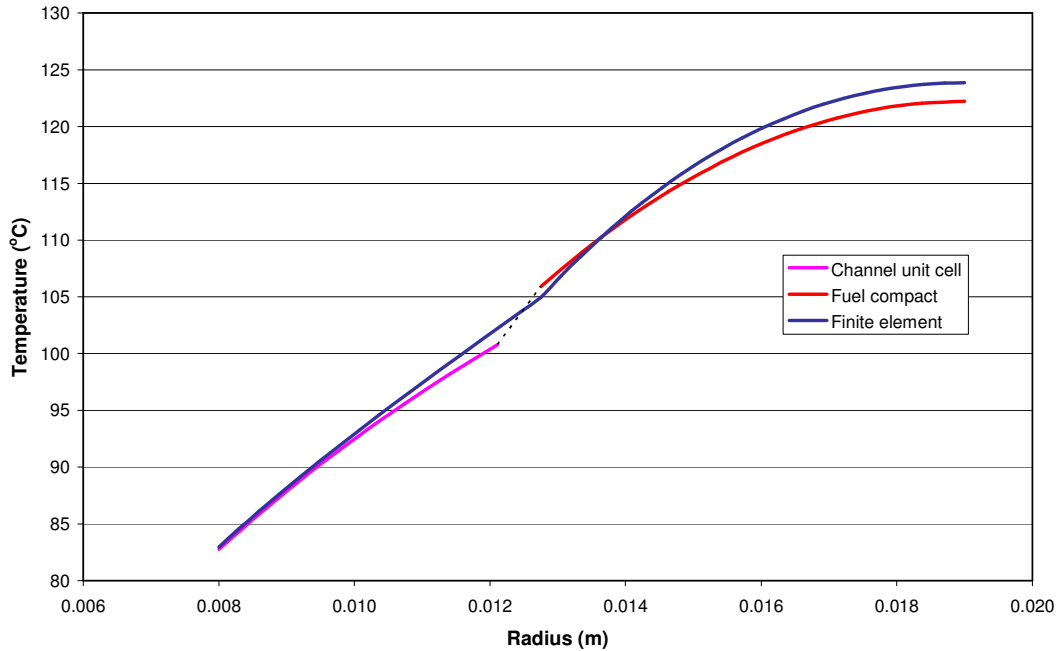
Figure 5.3.5: Predicted temperatures plotted along a radial line connecting the centers of the coolant and fuel compact channels



The graphite temperature profiles from the two unit cell models do not cross, but they do share the same mean value, as the latter was imposed as a constraint applied to essentially two separate domains, i.e., the graphite within them was common to both and, therefore, should have the same mean temperature.

The temperature profile predicted by the coolant channel unit cell model agrees well with the FE results at the channel surface both in terms of value and gradient, but, as expected, deteriorates with increasing distance from the channel surface. Similarly the accuracy of the corresponding profile from the fuel compact unit cell model deteriorates with increasing distance from the surface of the fuel compact. However, these deteriorations are not important because the solution is intended only to relate the coolant channel surface temperature to the graphite mean temperature and to relate the fuel compact centre and edge temperatures to the graphite mean temperature – both of which are achieved with reasonable accuracy. If only the relevant parts of the predicted profiles are retained and connected by a suitable linear “bridge” function, the temperature profile shown in Figure 5.3.6 is obtained.

Figure 5.3.6: Predicted temperatures plotted along a radial line connecting the centers of the coolant and fuel compact channels with overlapping parts removed and a linear bridging function inserted.



The largest discrepancy is at the centre of the fuel compact of 1.7°C, which is about 4% of the temperature rise from the coolant channel wall to the centre of the compact. The model detailed here is simple and computationally efficient being based on two closed-form analytical solutions and believed to be acceptable to carry out steady state calculations, but is not suitable to be extended to transient situations.

5.3.2 New multi-scale approach

To fulfill the requirement that the solution be applicable in steady state and transient situations, a new model was developed such that the steady state solution could be obtained by solving a consistent set of coupled partial differential equations. The difference, therefore, between this and the previous approach, was to arrange the coupling between the channel and compact models at the level of the differential equations rather than at the level of their solutions. The multi-scale models developed for analysis of discrete particles embedded in a graphite pebble, Reference 5.1, were used as the starting point for this. Earlier in this Section, and in the previous approach, the meso-scale was considered to cover length scales up to the size of the shaded unit cell shown in Figure 5.3.1. However, within a multi-scale representation the meso-scale has to be redefined as covering length scales up to the distance between centers and a *super-meso-scale* is introduced to cover length scales up to those covered by the original definition of the meso-scale.

Neglecting heat conduction in the axial direction, for the moment, reduces the problem to a 2-dimensional transient conduction problem with heat generation. Expressing this in polar co-ordinates with the origin of the co-ordinate system at the centre of the coolant channel gives:

$$(\rho c_p)(r, \theta) \frac{\partial T}{\partial t} = \frac{1}{r} \frac{\partial}{\partial r} \left(r k(r, \theta) \frac{\partial T}{\partial r} \right) + \frac{1}{r^2} \frac{\partial}{\partial \theta} \left(k(r, \theta) \frac{\partial T}{\partial \theta} \right) + \dot{q}''(r, \theta, t).$$

If heat generation in the graphite of the block is neglected the heat generation has a simple distribution that has a finite value inside the fuel compacts and zero elsewhere. The above partial differential equation can be solved in two dimensions using, for example, the finite element method. However, the simple form of the heat generation distribution combined with the simple circular shapes of the coolant channel and fuel compact allow a reasonably accurate multi-scale simplification of the domain to be constructed. Such a multi-scale decomposition allows the important features of the temperature field, such as the heat fluxes through the coolant channel and fuel compact surface, mean graphite and compact temperatures, and coolant channel wall and fuel compact centre temperatures to be calculated from the solution of a pair of 1-dimensional equations with acceptable accuracy, without the computational burden of solving many transient 2-dimensional finite element models. The decomposition of the above equation into a multi-scale representation is detailed below.

The shaded hexagonal unit cell of Figure 5.3.1 can be considered, topologically, as being an inside-out two-dimensional pebble, with the coolant flowing past the inside surface, with the particles, in this case fuel compacts, being embedded in graphite radially further out. This hexagonal unit cell has an across-corners dimension of twice the pitch of the channels and, is itself made up of the equivalent of 3 smaller hexagons; one which surrounds the coolant channel, with the other two comprising the sum of the six 1/3 hexagons that surround the neighboring fuel channels. All of these smaller hexagons are the same size and have an across-flats dimension that is the channel pitch. This geometry and its development into the multi-scale representation is shown in Figure 5.3.7. The decomposition into super-meso, meso and micro-scale domains is as described below:

Super-meso-scale domain

Within Figure 5.3.7 it can be seen that an annular domain is overlaid on the original hexagonal unit cell, with the outer diameter chosen to be the same as the across-corners dimension of the original hexagon and the inner diameter being that of the coolant channel. The choice of outer radius, r_B , was made so that the distance from the centers of a fuel compact to the centre of the coolant channel is preserved at the expense of not obtaining an equivalent area. The inner radius, r_{chn} , is simply the radius of the coolant channel. The inner radius of the heated zone, r_A , was chosen to give the same area as the hexagonal cell that contains the coolant channel.

Meso-scale domain

Within Figure 5.3.7, the hexagon of graphite surrounding a fuel compact is represented by an annular domain of the same cross sectional area. The inner and outer radii of this annulus are chosen to be the fuel compact radius, r_{fuel} , and the radius that gives the same area as the hexagonal cell that surrounds a fuel compact, r_D , respectively. Because the distance from the centre of the coolant channel to the centre of a compact is the same as the distance between the centers of two neighboring compacts, the hexagonal cell surrounding a fuel compact is the same size as the hexagon surrounding the coolant channel, thus $r_D = r_A$.

Micro-scale domain

The micro-scale domain, as with the pebble geometry (Reference 5.1), is reserved for modeling the local temperature distribution within and around individual coated particles within the fuel compacts. The mathematics of coupling the micro and meso-scale models are almost identical for pebbles and compacts, with the only difference being spherical geometry in the meso-scale of the former and corresponding cylindrical geometry in the latter. Micro-scale models are not considered in this report, but a full description can be found in Reference 5.1.

The area over which the super-meso and meso-scale domains overlap is identified by the pink shaded annulus in Figure 5.3.7 and this becomes the smeared heat generating zone in the super-meso-scale model. The area of the pink shaded zone is larger than the area of the six 1/3 hexagons of the fuel compacts, therefore this increased area has to be respected when assigning the volumetric heat source and heat capacity to this region to ensure that the total heat generation and thermal inertia within the super-meso-scale model are correct.

Separating the two domains gives the super-meso-scale domain as shown in Figure 5.3.8 and the meso-scale domain as shown in Figure 5.3.9.

Figure 5.3.7: Original hexagonal unit cell with super-meso and meso-scale domains overlaid

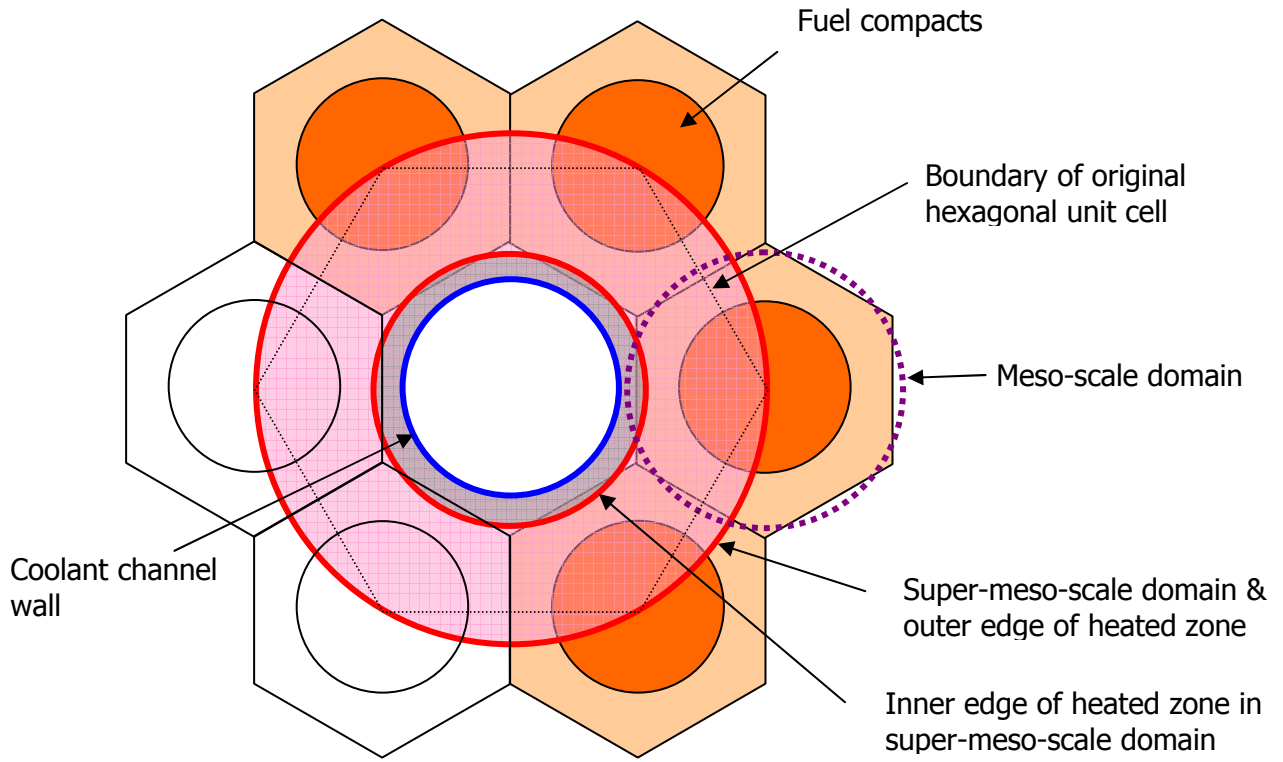


Figure 5.3.8 : Super-meso-scale domain

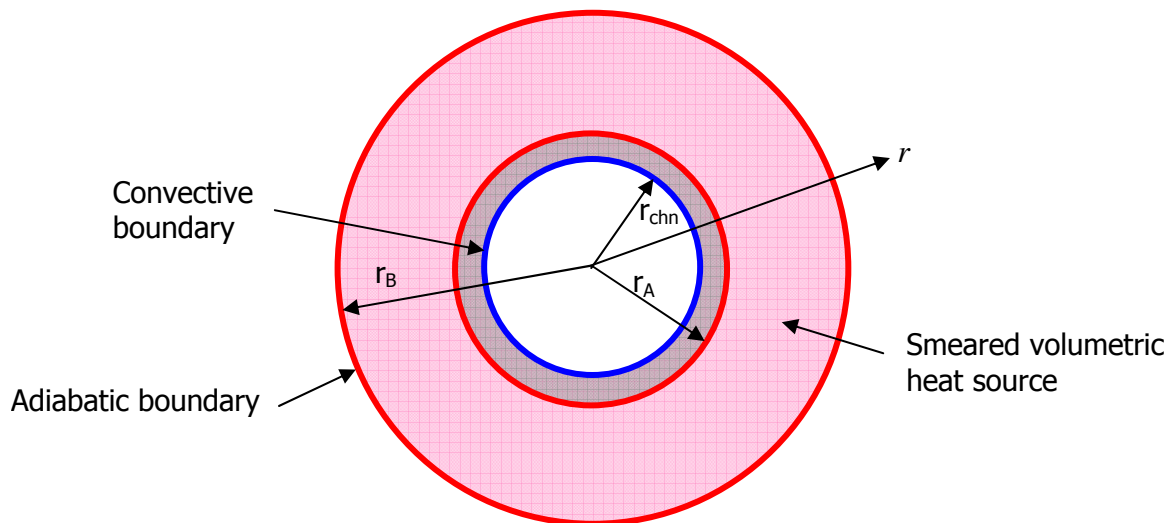
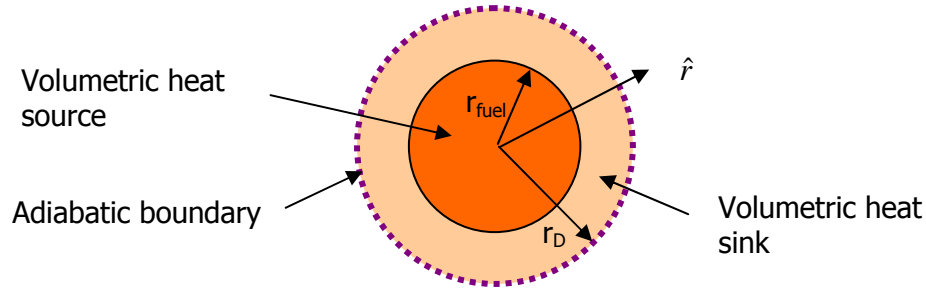


Figure 5.3.9 : Meso-scale domain



With heat generation in the graphite of the block neglected, and assuming that all of the compacts generate the same power and that heat generation within a compact is uniformly distributed, the heat generation has a distribution that is described by a mean value plus a perturbation within the heated zone (the pink region shown in Figure 5.3.8) and zero outside of it:

$$\dot{q}'''(r, \theta, t) = \bar{q}'''(t) + \hat{q}'''(\hat{r}, t) \quad \text{for } r > r_A$$

and

$$\dot{q}'''(r, \theta, t) = 0 \quad \text{for } r < r_A,$$

where the radial co-ordinate with respect to the centre of a compact is not an independent variable in this context, but is a function of r and θ , i.e., $\hat{r} = \hat{r}(r, \theta)$.

The mean power density is the power generated averaged over the area of the heated zone in the original hexagonal geometry, where A_{hex} is the area of the hexagonal unit cell including the sectors of fuel compacts and the coolant channel that lie within, which in this case is 3 times the area of a hexagon that surrounds a fuel compact (or the small hexagon that surrounds the coolant channel, therefore $A_{hex} = 3\pi r_A^2$). The heat generated by two fuel compacts ($6 \times 1/3$) is the heat input into the hexagonal unit cell:

$$\bar{q}'''(t) = \frac{2\dot{q}_f''' r_{fuel}^2}{A_{hex} / \pi - r_A^2} = \frac{\dot{q}_f''' r_{fuel}^2}{r_A^2}.$$

However, in the approximation of the geometry, shown in Figure 5.3.8, the heated zone is circular and has a greater area than the original hexagonal unit cell. Therefore, the average power density is reduced so that the total heat input is preserved:

$$\bar{q}_{eff}'''(t) = \frac{A_{hex} / \pi - r_A^2}{r_B^2 - r_A^2} \bar{q}'''(t) = \frac{2r_A^2}{r_B^2 - r_A^2} \bar{q}'''(t).$$

The perturbation is described, with respect to the distance from the centre of a compact, as:

$$\hat{q}'''(\hat{r}, t) = \dot{q}_f'''(t) - \bar{q}'''(t) \quad \text{for } \hat{r} < r_{fuel} \quad (\text{a heat source within the compact})$$

and

$$\hat{q}'''(\hat{r}, t) = -\bar{q}'''(t) \quad \text{for } r_{fuel} < \hat{r} < r_D \quad (\text{a heat sink in the surrounding graphite})$$

The temperature field is decomposed into super-meso and meso-scale contributions:

$$T(r, \theta, t) = T_{SM}(r, t) + T_M(\hat{r}, t),$$

where again, in this context \hat{r} is not an independent variable, but is a function of r and θ , i.e., $\hat{r} = \hat{r}(r, \theta)$.

The 2-dimensional transient conduction equation with heat generation in cylindrical co-ordinates is decomposed into a pair of 1-dimensional equations representing heat transfer on the super-meso and meso-scales with the effective mean power density and the power density perturbation assigned to these equations respectively. Azimuthal conductivity variations are smeared and the heat capacity is corrected for the non-preservation of domain area (as mentioned above) to give effective values which gives the super-meso-scale differential equation as:

$$\overline{(\rho c_p)}(r) \frac{\partial T_{SM}}{\partial t} = \frac{1}{r} \frac{\partial}{\partial r} \left(r k_{eff}(r) \frac{\partial T_{SM}}{\partial r} \right) + \bar{q}_{eff}'''(t) \quad \text{for } r_A < r < r_B$$

$$\overline{(\rho c_p)}(r) \frac{\partial T_{SM}}{\partial t} = \frac{1}{r} \frac{\partial}{\partial r} \left(r k_{eff}(r) \frac{\partial T_{SM}}{\partial r} \right) \quad \text{for } r_{chn} < r < r_A$$

and

$$(\rho c_p)(\hat{r}) \frac{\partial T_M}{\partial t} = \frac{1}{\hat{r}} \frac{\partial}{\partial \hat{r}} \left(\hat{r} k(\hat{r}) \frac{\partial T_M}{\partial \hat{r}} \right) + \hat{q}'''(\hat{r}, t)$$

for the meso-scale.

Using a forward difference for the time derivative gives an explicit finite difference equation for the super-meso-scale temperature distribution:

$$T_{SMi}^{t+\Delta t} = T_{SMi}^t + \frac{\Delta t}{(\rho c_p)_i} \frac{1}{r_i(r_{ei} - r_{wi})} \left(r_{ei} k_{eff,ei} \frac{T_{SMi+1}^t - T_{SMi}^t}{r_{i+1} - r_i} - r_{wi} k_{eff,wi} \frac{T_{SMi}^t - T_{SMi-1}^t}{r_i - r_{i-1}} \right) + \frac{\Delta t}{(\rho c_p)_i} \bar{q}_{eff,i}''(t)$$

for $r_A < r < r_B$, where,

$$r_{ei} = \frac{(r_{i+1} + r_i)}{2}; r_{wi} = \frac{(r_i + r_{i-1})}{2}; k_{eff,ei} = k_{eff}(r_{ei}); k_{eff,wi} = k_{eff}(r_{wi})$$

and similarly for $r_{chn} < r < r_A$:

$$T_{SMi}^{t+\Delta t} = T_{SMi}^t + \frac{\Delta t}{(\rho c_p)_i} \frac{1}{r_i(r_{ei} - r_{wi})} \left(r_{ei} k_{eff,ei} \frac{T_{SMi+1}^t - T_{SMi}^t}{r_{i+1} - r_i} - r_{wi} k_{eff,wi} \frac{T_{SMi}^t - T_{SMi-1}^t}{r_i - r_{i-1}} \right)$$

Similarly for the meso-scale:

$$T_{Mi}^{t+\Delta t} = T_{Mi}^t + \frac{\Delta t}{(\rho c_p)_i} \frac{1}{\hat{r}_i(\hat{r}_{ei} - \hat{r}_{wi})} \left(\hat{r}_{ei} k_{ei} \frac{T_{Mi+1}^t - T_{Mi}^t}{\hat{r}_{i+1} - \hat{r}_i} - \hat{r}_{wi} k_{wi} \frac{T_{Mi}^t - T_{Mi-1}^t}{\hat{r}_i - \hat{r}_{i-1}} \right) + \frac{\Delta t}{(\rho c_p)_i} \hat{q}_i''(t)$$

The boundary conditions applied to the super-meso-scale equation are a convective boundary condition at the coolant channel surface and adiabatic boundary at the outer edge of the domain. However, at the inner edge of the heated zone, the contribution from the meso-scale solution has to be included because the convective boundary condition applies to un-decomposed temperature field and the contribution from the meso-scale solution is significant because the length scales of both domains are similar. For simplicity, the contribution from the meso-scale solution is added at the surface of the coolant channel, whilst this is an approximation, it is believed to be not significant as the inner edge of the heated zone is only a small radial distance from the coolant channel wall. Therefore, the channel wall boundary temperature is:

$$T_{chn}^{t+\Delta t} = T_{SM0}^{t+\Delta t} + T_{Mn}^{t+\Delta t}$$

and the surface heat flux crossing the coolant channel wall is:

$$\dot{q}_{chn}'' = h(T_{chn}^{t+\Delta t} - T_{He}) = h(T_{SM0}^{t+\Delta t} - T_{He} + T_{Mn}^{t+\Delta t}).$$

In an explicit scheme, this is approximated by using "old" temperatures:

$$\dot{q}_{chn}'' = h(T_{chn}^t - T_{He}) = h(T_{SM0}^t - T_{He} + T_{Mn}^t).$$

This heat flux is used in the above super-meso-scale finite difference equation to replace the conductive heat flux term at the channel wall. The adiabatic boundary at the outer edge of the super-meso domain is applied by setting the temperature gradient at the boundary to zero. The modifications to the super-meso-scale finite difference equation required to incorporate both of these boundary conditions are presented in Appendix A.2.

The boundary conditions on the meso-scale domain are symmetry at the compact centre and adiabatic at the outer edge of the domain. Again, the modified forms of the finite difference equations are presented in Appendix A.2.

The finite difference equations for the super-meso and meso-scales were coded into an Excel spreadsheet and solved by a simple explicit time-marching procedure. The spreadsheet was set up to solve for a transient in which the power is stepped-up from zero to its nominal value in the compacts at $t = 0$ – the conditions used in the 'Transient 1' finite element model. The coolant mass flow rate and temperature remain constant throughout the transient. The geometry and nominal power, thermal conductivities, convective heat transfer coefficient and coolant temperature are identical to those values used with the previous steady-state model. Table 5.3.2 contains all of the parameters that were used in the model. Two of the parameter values in Table 5.3.2 require further explanation and these are listed below:

Super-meso effective conductivity $r > (r_B - r_{fuel})$ – the conductivity of the fuel block is assigned the value of graphite out to a radius at which the fuel compacts are encountered. In the ring which lies beyond this radius, the conductivities of graphite and the fuel compacts are averaged in proportion to the volumes of each material within the ring. Simply weighting according to volume is correct in this sense because it gives a measure of the amount of the circumference of the domain that is occupied by each material.

Super-meso effective heat capacity for $r > r_A$ – as mentioned above, the area of the heated zone in the circular approximation to hexagonal unit cell is greater than in the original hexagonal cell, hence the heat capacity is reduced to compensate for the increased volume of material in the domain.

Table 5.3.2: Parameters and their values used in the multi-scale model

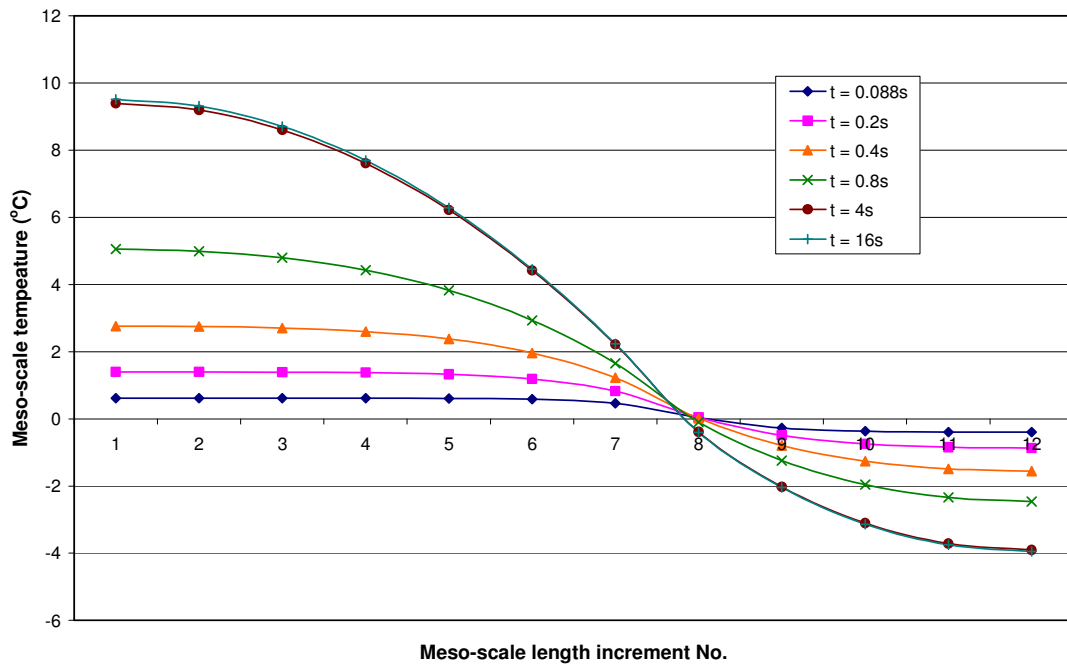
Parameter	Symbol	Value
Coolant channel radius	r_{chn}	8 mm
Super-meso-scale heated zone inner radius	r_A	9.9757 mm
Super-meso-scale domain outer radius	r_B	19.000 mm
Fuel compact radius	r_{fuel}	6.25 mm
Meso-scale domain outer radius	r_D	9.9757 mm
Area of hexagonal unit cell	A_{hex}	937.9055 mm ²
Graphite conductivity	k_G	30 W/m/K
Fuel compact conductivity	k_F	20 W/m/K
Super-meso effective conductivity $r < (r_B - r_{fuel})$	$k_{eff}(r)$	30 W/m/K
Super-meso effective conductivity $r > (r_B - r_{fuel})$	$k_{eff}(r)$	24.0945 W/m/K
Graphite heat capacity	ρc_p	2.9068 MW/m ³ /K
Fuel compact heat capacity	ρc_p	2.9068 MW/m ³ /K
Super-meso effective heat capacity for $r < r_A$	$\overline{(\rho c_p)}$	2.9068 MW/m ³ /K
Super-meso effective heat capacity for $r > r_A$	$\overline{(\rho c_p)}$	2.2125 MW/m ³ /K
Actual power density in compact	\dot{q}_f'''	33.41 MW/m ³
Super-meso mean power density	\bar{q}'''	13.1144 MW/m ³
Super-meso effective mean power density	\bar{q}_{eff}'''	9.9820 MW/m ³
Meso-scale power density inside compact	\hat{q}'''	20.2956 MW/m ³
Meso-scale power density outside compact	\hat{q}'''	-13.1144 MW/m ³
Convective heat transfer coefficient	h	2600 W/m ² /K
Coolant bulk temperature	T_{He}	20°C

The super-meso-scale domain was divided into 18 radial increments, with 4 in the unheated part and 14 within the heated zone, of these, 10 increments lay in the ring in which the fuel compacts were located and thus had a modified thermal conductivity. The meso-scale domain was divided into 11 increments, 7 of which were within the fuel compact and 4 lay in the surrounding annulus of graphite. The finite difference equations presented above constitute an explicit scheme which is subject to a stability criterion which manifests itself as an upper limit on the time step size that can be used. Physically this limit is dictated by the rate at which a temperature disturbance can propagate through the domain, but mathematically the criterion is fulfilled as long as the coefficient of the 'old' time step temperature on the node being evaluated

remains non-negative. The time step size for which a stable solution could be obtained was 0.008 seconds, the exact limiting time step size was not sought, but a small increase led to divergence. The initial condition was for the super-meso-scale temperature field to be set to 20°C everywhere and for the meso-scale temperature field to be set to 0°C everywhere.

Figure 5.3.10 shows the development of the meso-scale temperature field with time. The meso-scale solution reaches steady-state conditions in about 700 time steps (5.6 seconds).

Figure 5.3.10: Development of the meso-scale temperature distribution with time



Figures 5.3.11 to 5.3.14 show temperature profiles plotted along a line that connects the centers of the coolant channel and a fuel compact at times of 1.29 s, 5.29 s, 20.29 s and steady state. Also plotted in these figures are the corresponding finite element solutions for the same times.

Figure 5.3.11: Predicted temperatures along a line between coolant-fuel channel centers t=1.29s

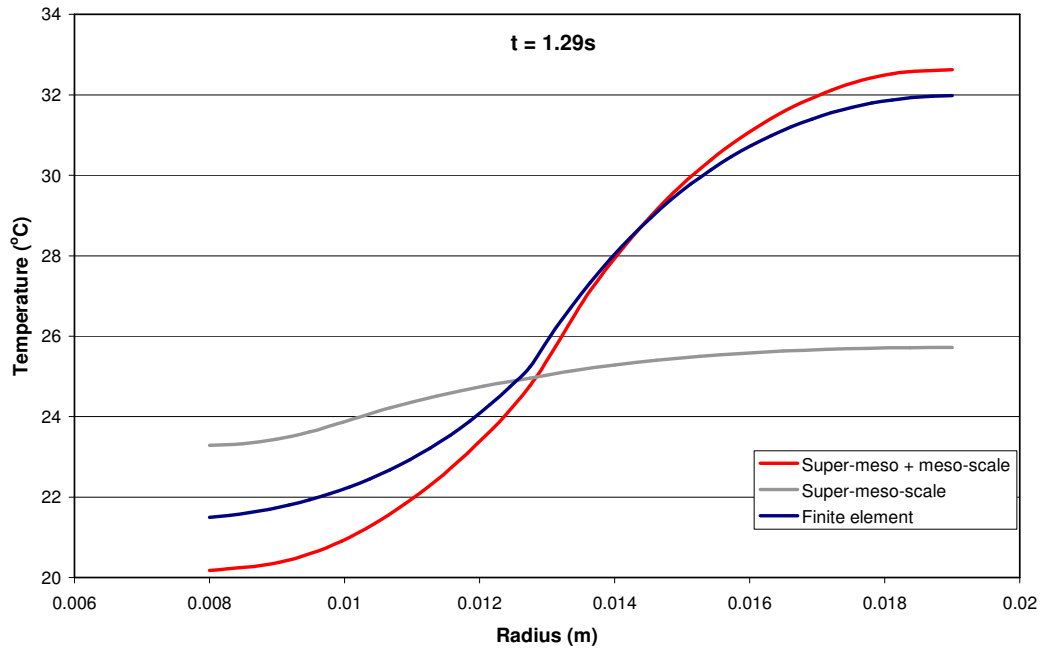


Figure 5.3.12: Predicted temperatures along a line between coolant-fuel channel centers t=5.29s

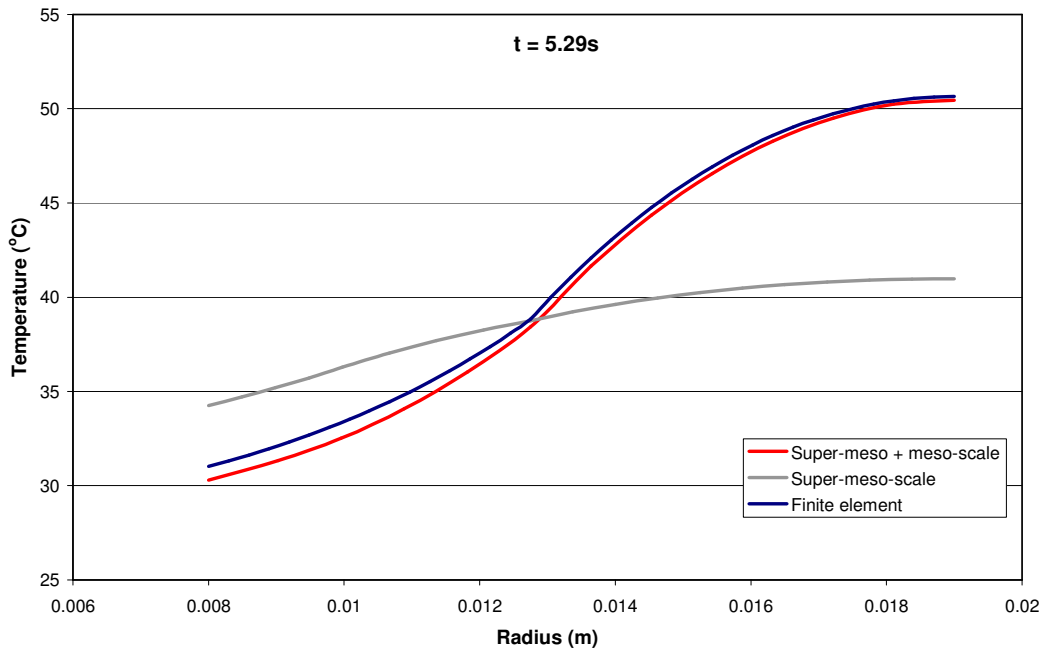


Figure 5.3.13: Predicted temperatures along a line between coolant-fuel channel centers t=20.29s

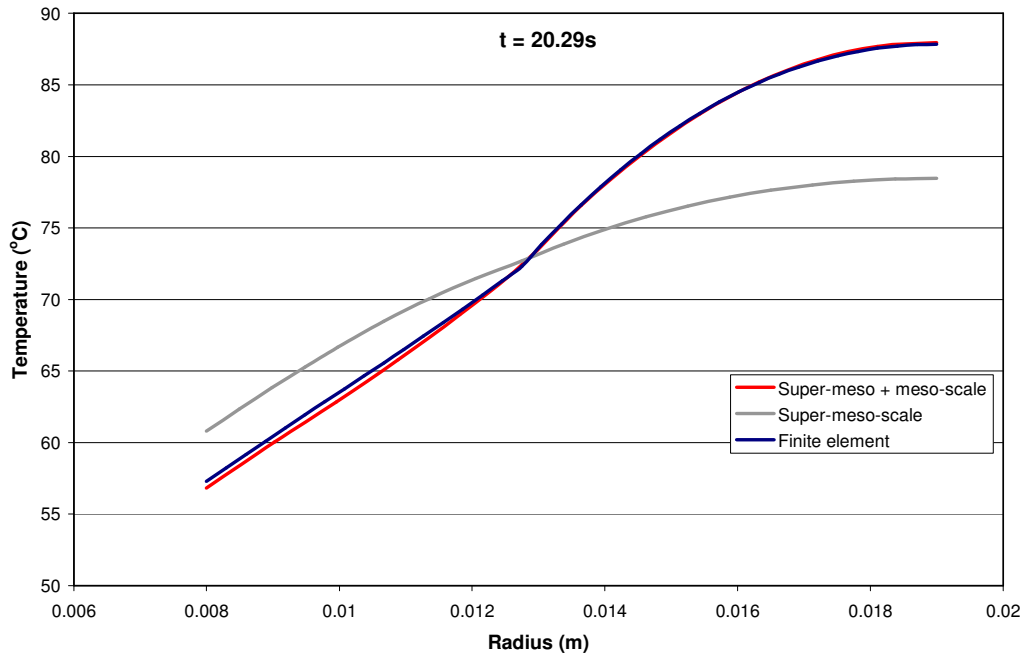
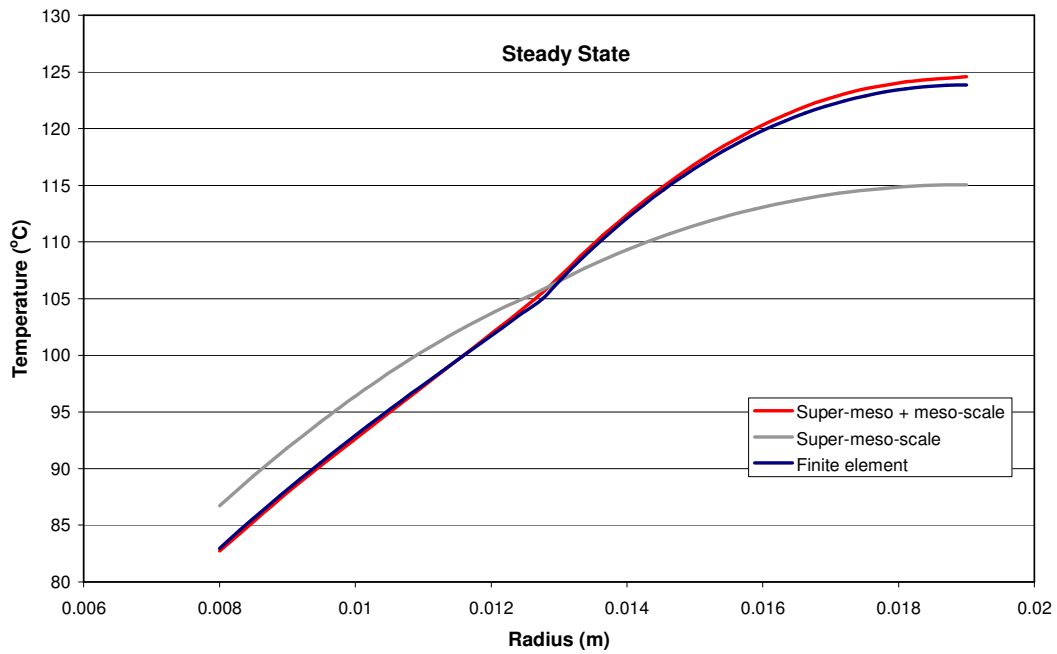


Figure 5.3.14: Predicted steady state temperatures along a line between coolant-fuel channel centers

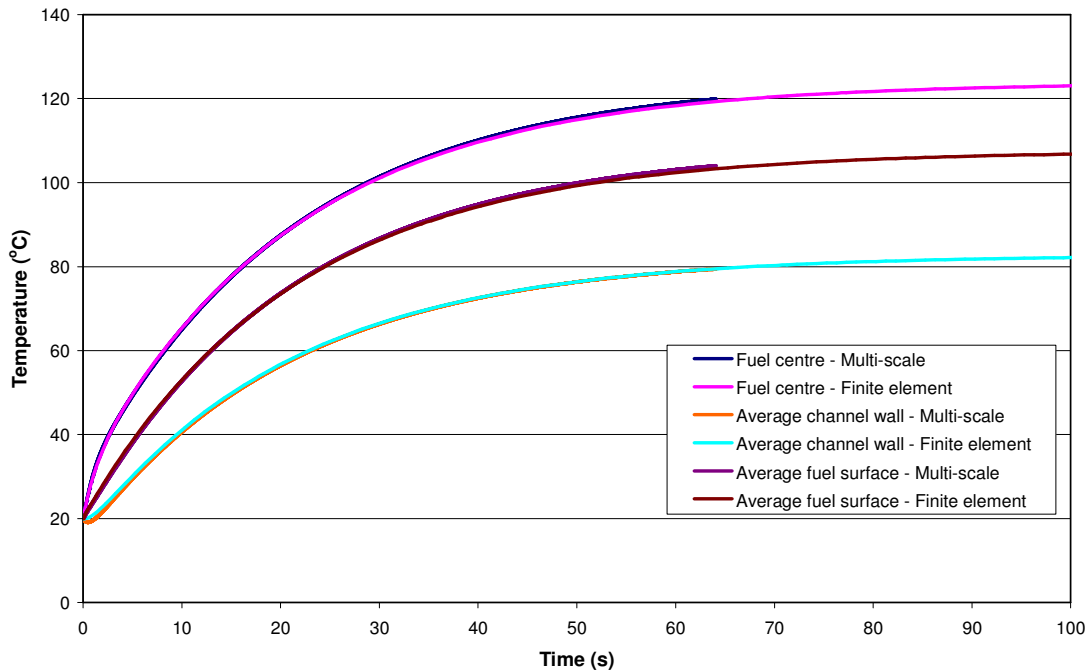


It can be seen in Figures 5.3.11 to 5.3.14 that the temperatures at the channel wall predicted by the super-meso-scale model are higher than the finite element solution. This difference is explained by the fact that the convective boundary condition at the wall is applied to the actual temperature field, i.e., to the sum of the super-meso and meso-scale contributions, through the condition:

$$\dot{q}_{chn}'' = h(T_{chn}^t - T_{He}) = h(T_{SM0}^t + T_{Mn}^t - T_{He}).$$

At all times, the agreement with the finite element solutions are very close, with the difference in the predicted fuel compact centre temperature always remaining less than 1°C. The largest differences are in the predicted channel wall temperatures early in the transient, 1.32°C at 1.29 s. This discrepancy is believed to be due to the small errors introduced by the heated zones in the two circular domains not overlaying each other exactly and the approximation of combing the two solutions at the boundary of the domain rather than at the inner edge of the heated zone. However, the error is not large, but it can drive the coolant channel wall to be slightly colder than the coolant in the first second of the transient. This phenomenon can be seen in Figure 5.3.15 in which the coolant channel wall, fuel compact edge (circumferential mean) and fuel compact centre temperatures are plotted as a function of time. In Figure 5.3.15, it can be seen that the orange curve, corresponding to the channel wall temperature dips below the 20°C line (the coolant temperature) for a short period.

Figure 5.3.15: Transient development of fuel compact centre, fuel compact edge average and coolant channel wall average temperatures



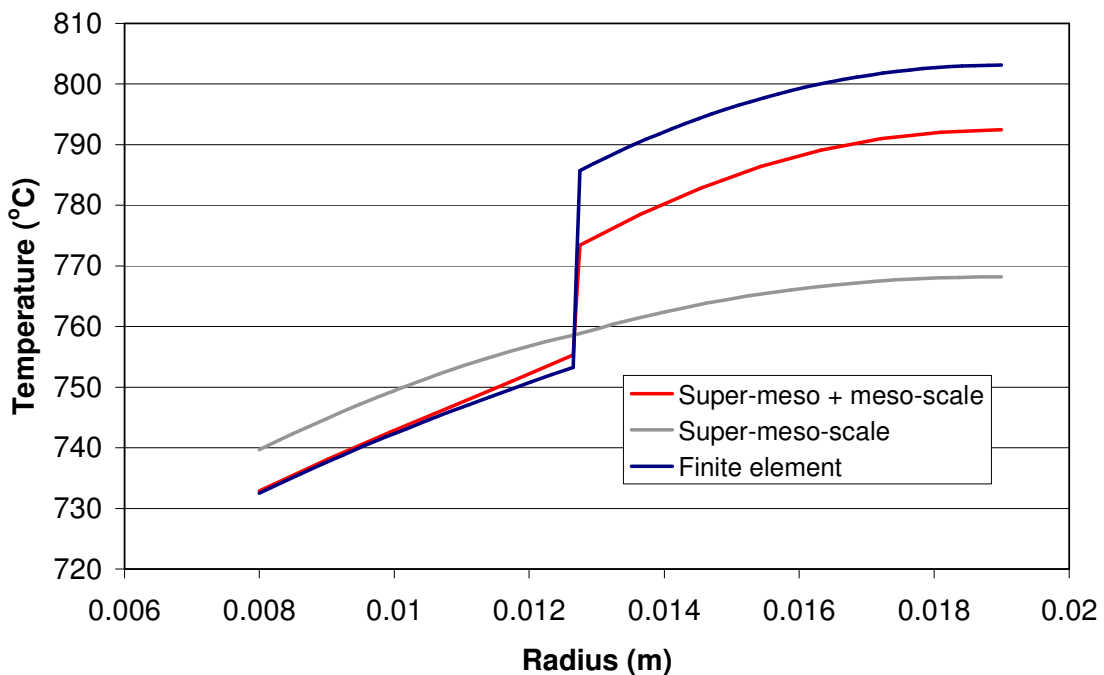
In practice, this slight under-cooling of the channel wall is not believed to be an issue as it can be trapped in the whole reactor code allowing the wall temperature to be fixed to the coolant temperature value until later in the transient. Some care will be needed to ensure that situations in which the coolant will be hotter than the channel wall in reality are handled correctly - hot gas returning to the reactor inlet following a load rejection would be one such situation.

5.3.3 Inclusion of contact and gap resistances

Within the GT-MHR fuel block design, at the start of life, there is a 0.1 mm radial gap between the fuel compact and the wall of the fuel channel. Heat transfer across this gap will be by conduction through stagnant helium and thermal radiation. Later in life the gap may close if the fuel compact swells at a greater rate than the graphite of the fuel block, but there will still remain a contact resistance between the bodies.

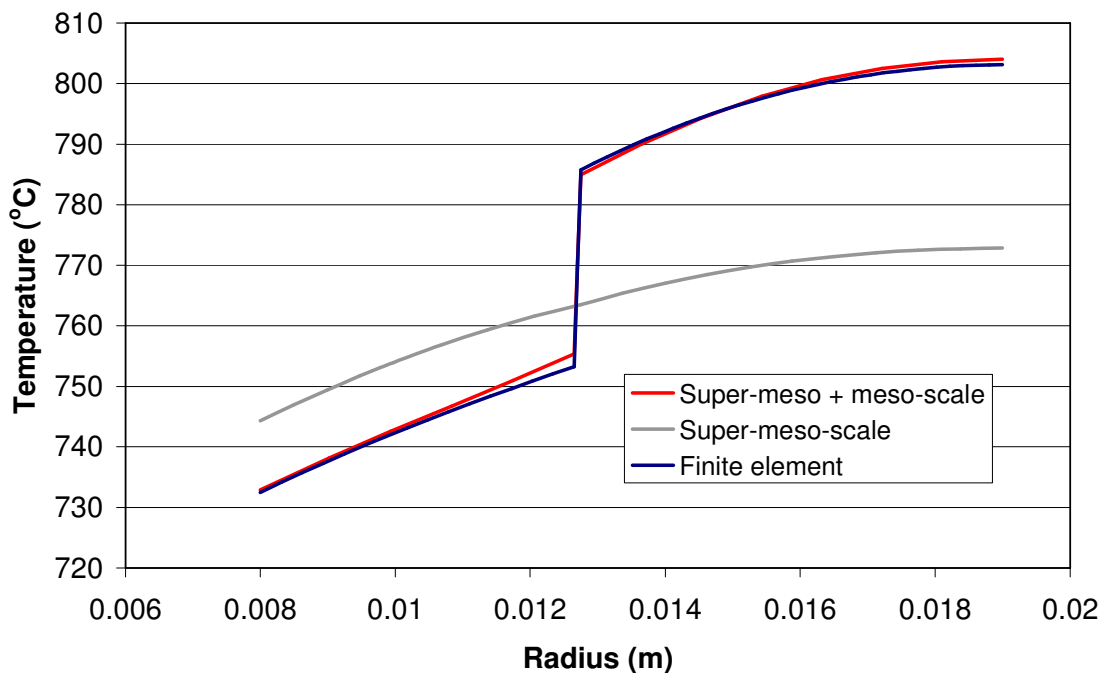
The finite difference solution for the meso-scale conduction equation was modified to introduce two increments in the gap between the fuel compact and the fuel channel wall. For the purpose of testing the thermal conductivity of this gap was set to be that of stagnant helium (0.35 W/m/K) with the enhancement to heat transfer by thermal radiation neglected. This represents an extreme case, and combined with the original "gapless" solutions bounds the full range of possible gap effective conductivities. Figure 5.3.16 shows a comparison of the temperature profile, plotted between the coolant channel and fuel channel centers, with the finite element prediction. Whilst the agreement is good for the coolant and fuel channel walls the compact edge and centre temperatures are under-predicted by about 10°C.

Figure 5.3.16: Predicted steady state temperatures along a line between coolant-fuel channel centers, with fuel gap resistance included



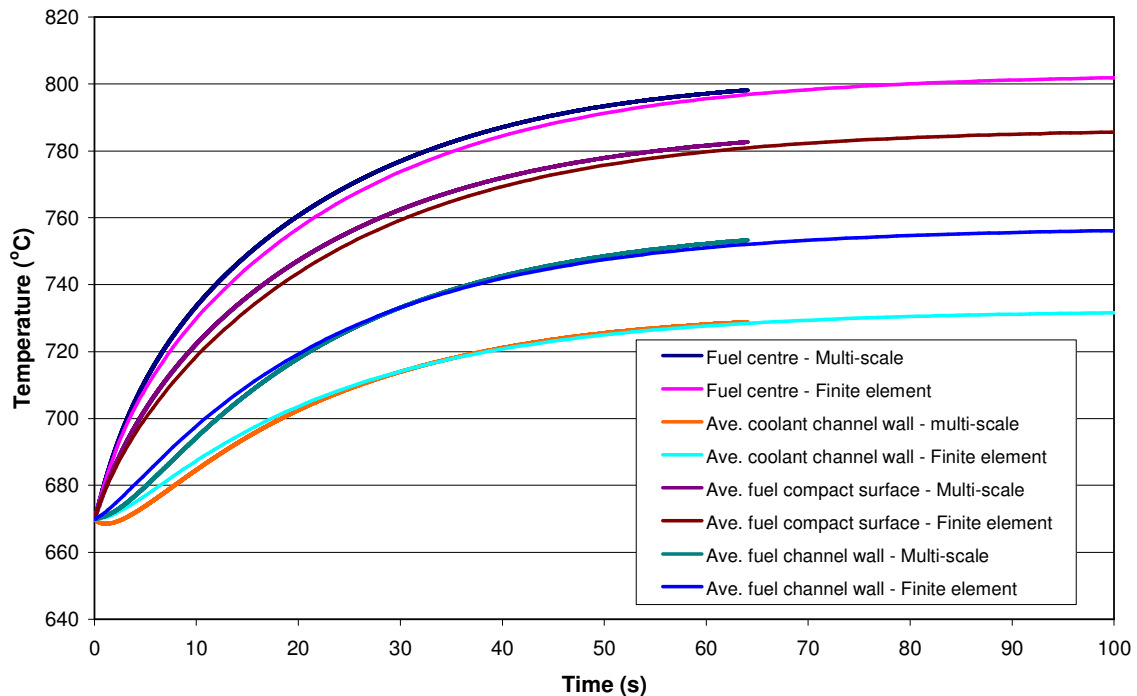
The reason for the under prediction of the fuel compact temperatures lies in the way in which the gap resistance has been introduced, specifically, only into the meso-scale part of the model. The power density in the fuel compact represented within the meso-scale model is only about two-thirds of the combined meso and super-meso power density, so the temperature drop over the compact-to-fuel channel gap is only two thirds of the correct value. To correct this discrepancy, the thermal conductivity of the gap has been modified such that it is multiplied by the ratio of the power density in the fuel compact in the meso-scale model to the actual power density (i.e., the combined meso and super-meso contributions). Using this modified gap conductivity the model predicts the center-to-center temperature profile as shown in Figure 5.3.17, from which it can be seen that the agreement with the finite element solution is very good.

Figure 5.3.17: Predicted steady state temperatures along a line between coolant-fuel channel centers, with fuel gap resistance included based on a modified gap conductivity



The transient response of the modified multi-scale model was compared with the transient finite element solution for 'Transient 1', the results of which are shown in Figure 5.3.18. Agreement of the modified multi-scale model with the finite element solution is considered to be acceptable for such a severe transient (immediate step-up in power from 0% to 100%). Agreement for the fuel compact temperatures could be improved further by re-evaluating the effective conductivity of the zone that contains the fuel channels in the super-meso model. No adjustment was made to this value, which was retained at the area fraction-weighted average conductivity of the compact and the graphite block. Inclusion of the gap conductivity in this average should improve the agreement.

Figure 5.3.18: Transient development of fuel compact centre, fuel compact edge average and coolant channel wall average temperatures, with gap resistance included based on a modified gap conductivity.



5.4 Assumptions and Limitations

The main assumption in the finite element studies is the assumption of two-dimensionality. In general this assumption is considered to be valid as the temperature gradient between the fuel and the coolant channels are much greater than those in the axial direction. The assumption of properties not being dependent upon temperature was made simply for ease of comparison and is not a limitation of the finite element models.

With regard to the multi-scale model, it is assumed that the full solution is obtained from the summation of two separate solutions obtained over domains which *approximately* represent the actual domain. Implicit within this are two further assumptions, that the two solutions are effectively linear, and that the hexagonal sub-domains are adequately represented by circular approximations. The requirement that the solutions are linear, strictly rules-out the use of temperature dependent thermal properties. However, it is assumed here that if the properties are a weak function of temperature, that the solution can be linearized, particularly if sub-domain-average values are taken for the properties. The assumption that the hexagonal sub-domains can be represented by circles appears to be reasonable for the current GT-MHR fuel blocks. The validity of this assumption would need to be re-assessed if the design was changed significantly.

The main limitation with the multi-scale solution, is that it is not practical to capture small scale variations in properties in the super-meso-scale solution. As such, localized and severe changes in properties, such as the conductivity of the gap between the fuel compact and the fuel channel cannot be resolved in the super-meso-scale solution and the meso-scale solution has to be pragmatically “adjusted” to compensate.

5.5 Closure

The temperature field that surrounds a coolant channel and its neighboring fuel channels in a Fort St Vrain / GT-MHR fuel block is two-dimensional. Whilst it is possible, and has been demonstrated within this section, to predict this two-dimensional temperature field by finite element analysis, this is not desirable, or feasible, in a macroscopic thermal model of the whole reactor. Instead, the two-dimensional heat conduction problem has been reduced to a pair of one-dimensional problems by multi-scale analysis. Solution of the resulting one-dimensional finite difference equations is computationally efficient, both in terms of number of arithmetic operations and the amount of memory required – both important factors when applying a whole-core model to a transient situation.

Comparison of the predicted temperatures obtained from the multi-scale model with those from the finite element analyses show good agreement, both in transient and steady state conditions.

5.6 References for Section 5

- 5.1 Stainsby R. et al., “Investigation of Local Heat Transfer Phenomena in a Pebble Bed HTGR Core”, AMEC NSS Report NR001/RP/002 R01, May 2009.
- 5.2 KTA Rule 3102.1, “Reactor Core Design for High-Temperature Gas-Cooled Reactor. Part 1: Calculation of the Material Properties of Helium”, Nuclear Safety Standards Commission (KTA), Germany, June 1978.
- 5.3 IAEA-TECDOC-1198, “Current Status and Future Development of Modular High Temperature Gas Cooled Reactor Technology”, IAEA, February 2001.
- 5.4 IAEA CRP 5, Draft TECDOC II, “Evaluation of High Temperature Gas Cooled Reactor Performance”. To be published.

6.0 DETERMINATION OF THE EFFECTIVE CONDUCTIVITY OF FUEL ELEMENTS

6.1 Purpose of Section 6

In the previous section, models to predict heat transfer on length scales typical of the distance between an individual coolant channel and its surrounding fuel channels, or as defined previously, the meso-scale, were discussed. On the meso-scale the geometry and material properties of the individual structures can be resolved directly. However, modeling of heat transfer on a larger length scale, the macroscopic scale, which governs the flow of heat both within and between fuel elements, requires the fine-scale thermal conductivity variations to be smeared. This smearing of the individual conductivities must be performed on the scale of individual fuel elements, or more precisely, on the scale of the computational cells used in such a macroscopic model, typically 1/6 or 1/24 of the cross-sectional area of an individual fuel element. On these scales, the conductivity will be anisotropic, with the conductivity in the axial direction being different to the values in the transverse directions. Each fuel element contains three materials (on the meso-scale): graphite, helium and the fuel compact composite - consisting of a mixture of graphite and TRISO coated particles. Owing to the prismatic structure of a fuel element, the axial conductivity can be calculated using a simple volume weighted average. However, the transverse conductivities are more difficult to determine because of the complex shape of the heat conduction paths in these directions.

This section presents an analytical method by which the effective thermal conductivities in the transverse directions can be calculated. This method is based on Maxwell's method (Reference 6.1), extended to handle three materials and cylindrical inclusions. Maxwell's method is strictly only applicable to dilute mixtures and does not take account of any structure in the geometrical configuration of the inclusions. Therefore, effective conductivities predicted by Maxwell's method depend only on the conductivities and volume fractions of the component materials and, being independent of the geometrical configuration, are isotropic in all transverse directions.

There was a need to qualify the analytical model, particularly with regard to application of the method when the composite must be assumed to be isotropic and when such a composite cannot be considered to be a dilute mixture. As such, a set of finite element models were produced to provide effective conductivity values for comparison. Within these finite element models, two perpendicular orientations of the hexagonally arranged fuel channels, relative to the principal direction of heat flow, have been studied to see if the effective conductivities are anisotropic in the transverse directions.

6.2 Analytical Model

This sub-section derives an analytical model for the determination of the effective conductivity of Fort St Vrain or GT-MHR type fuel blocks. The starting point for this is Maxwell's method for determining the conductivity of composite materials in which a discrete phase of particles of one material type is embedded in a matrix of a second material type. Maxwell's approach is extended to account for the presence of three

materials and cast in a form that is suitable for cylindrical, as opposed to spherical, inclusions.

6.2.1 Maxwell's theory of the conductivity of composite materials

The effect of a dilute suspension of homogeneous spherical particles on the thermal conductivity of a medium can be modeled using an analysis due to Maxwell (see for example, Reference 6.1). In this sub-section, Maxwell's analysis is re-derived to model the effective thermal conductivity of a composite material consisting of matrix material and a number of cylindrical inclusions of two different materials in a direction normal to the cylinders' axis.

In Maxwell's original theory, the temperature field around a single spherical particle within a background temperature gradient is computed analytically. A relationship is then obtained between the perturbation to the far-field temperature distribution caused by the particle and the thermal conductivity of the particles itself. This relationship is then used as a basis for calculating the effective conductivity of a suspension of a large number of such particles.

6.2.2 Temperature field around a single cylinder within an infinite domain

An infinite cylinder, of thermal conductivity k_c and radius a embedded in an infinite domain of conductivity k_m is modeled. A coordinate system is chosen such that the y -axis is coincident with the axis of the cylinder. A temperature gradient is imposed across the domain, such that the far field temperature satisfies:

$$T \rightarrow Vz \text{ as } z \rightarrow \infty.$$

The temperature fields within the cylinder and surrounding the cylinder are both governed by the heat conduction equation. In steady state conditions the heat conduction equation reduces to Laplace's equation. Using the method of separation of variables in cylindrical coordinates, the following solutions are found:

Outside the cylinder:

$$T = A_m r \cos \theta + B_m \frac{a^2}{r} \cos \theta \text{ for } a \leq r < \infty \quad (6.2.1)$$

Inside the cylinder, the solution proportional to $1/r$ is rejected as it is unphysical at the origin ($r=0$). Therefore:

$$T = A_c r \cos \theta \text{ for } 0 \leq r < a \quad (6.2.2)$$

where A_m , B_m and A_c are unknown constants.

The system is completed by requiring that the temperature and the heat flux are continuous at the surface of the cylinder, $r = a$. The continuity of temperature at $r=a$ imposes the condition that:

$$A_m a + B_m a = A_c a \quad (6.2.3)$$

By requiring the continuity of heat flux at the cylinder surface, $r=a$, we find:

$$k_m \left[A_m \cos \theta - B_m \frac{a^2}{r^2} \cos \theta \right]_{r=a} = k_c A_c \cos \theta \quad (6.2.4)$$

$$A_m - B_m = \left(\frac{k_c}{k_m} \right) A_c \quad (6.2.5)$$

As z tends to infinity, the far-field boundary requires that:

$$A_m = V \quad (6.2.6)$$

Equations (6.2.3), (6.2.5) and (6.2.6) are linear equations for A_m , B_m and A_c . Manipulating these equations leads to:

$$V + B_m = A_c \quad (6.2.7)$$

$$V - B_m = \left(\frac{k_c}{k_m} \right) A_c \quad (6.2.8)$$

Solving these two linear equations using standard methods shows that:

$$B_m = V \left(\frac{k_m - k_c}{k_m + k_c} \right) \quad (6.2.9)$$

Substituting the derived values of A_m and B_m from equation (6.2.6) and (6.2.9) into equation (6.2.1) together with $z = r \cos \theta$, the temperature field outside the cylinder is given by the expression:

$$T = Vz + \left(\frac{k_m - k_c}{k_m + k_c} \right) \frac{Va^2 z}{r^2} \quad \text{at } a \leq r < \infty \quad (6.2.10)$$

6.2.3 Thermal conductivity of several cylinders

Following Maxwell's methodology, we note that if n_1 parallel cylinders of conductivity k_1 , and n_2 parallel cylinders of conductivity k_2 are placed inside a large cylindrical region, $0 \leq r' \leq b$, and a far field temperature gradient is imposed, such that:

$$T \rightarrow Vz \text{ as } z \rightarrow \infty,$$

then, providing that the cylinders are not too closely packed, the overall temperature profile in the far-field region, $z \gg b$, can be computed by the superposition principle, by summing the temperature perturbations caused by each of the individual cylinders. The overall temperature field resulting from the far fields of n_1 and n_2 sub-particles is therefore found to be (by reference to equation (6.2.10)):

$$T = Vz + \left[\left(\frac{k_m - k_1}{k_m + k_1} \right) n_1 a_1^2 + \left(\frac{k_m - k_2}{k_m + k_2} \right) n_2 a_2^2 \right] \frac{Vz}{r'^2} \quad (6.2.11)$$

Alternatively, the region $r' < b$, can be viewed as a single large cylinder formed from a composite material. Representing the effective thermal conductivity of the composite material cylinder as k_{eff} , it may be seen from equation (6.2.10) that the far field temperature perturbation caused by the composite cylinder $r' < b$ is:

$$T = Vz + \left(\frac{k_m - k_{eff}}{k_m + k_{eff}} \right) \frac{Vb^2 z}{r'^2} \text{ for } r' \gg b \quad (6.2.12)$$

Comparing the coefficients of z/r'^2 in the two expressions for the far-field temperature perturbation, equations (6.2.11) and (6.2.12), we note that:

$$\left(\frac{k_m - k_{eff}}{k_m + k_{eff}} \right) b^2 = \left(\frac{k_m - k_1}{k_m + k_1} \right) n_1 a_1^2 + \left(\frac{k_m - k_2}{k_m + k_2} \right) n_2 a_2^2 \quad (6.2.13)$$

To simplify this expression, we note that the volume fractions of the region $r' < b$ occupied by the two types of cylinder are given by the expressions α_1 and α_2 respectively, where:

$$\alpha_1 = \frac{n_1 a_1^2}{b^2} ; \quad \alpha_2 = \frac{n_2 a_2^2}{b^2}$$

Thus, equation (6.2.13) reduces to:

$$\left(\frac{k_m - k_{eff}}{k_m + k_{eff}} \right) = \left(\frac{k_m - k_1}{k_m + k_1} \right) \alpha_1 + \left(\frac{k_m - k_2}{k_m + k_2} \right) \alpha_2$$

By expanding the above equation, the effective thermal conductivity can be obtained in terms of the known thermal conductivities of the matrix material and cylinders, denoted by k_1 , k_2 and k_m and the material volume fractions:

$$k_{eff} = \frac{[k_m(k_m + k_1)(k_m + k_2) - \alpha_1 k_m(k_m - k_1)(k_m + k_2) - \alpha_2 k_m(k_m - k_2)(k_m + k_1)]}{[(k_m + k_1)(k_m + k_2) + \alpha_1(k_m - k_1)(k_m + k_2) + \alpha_2(k_m - k_2)(k_m + k_1)]}$$

which simplifies to;

$$k_{eff} = k_m \left[1 - \frac{2[\alpha_1(k_m - k_1)(k_m + k_2) + \alpha_2(k_m - k_2)(k_m + k_1)]}{[(k_m + k_1)(k_m + k_2) + \alpha_1(k_m - k_1)(k_m + k_2) + \alpha_2(k_m - k_2)(k_m + k_1)]} \right] \quad (6.2.14)$$

The formula presented in equation (6.2.14) allows the conductivity of the composite material to be estimated based on the material composition and the constituent material properties. Note that this calculation applies only to the conductivity normal to the cylinders' axis. The thermal conductivity parallel to the cylinders should be evaluated using a simple area weighted averaging process.

6.3 Finite Element Models

This sub-section describes the development of two-dimensional finite element models of regions of a fuel block to calculate the effective conductivity for comparison with the analytical model for a range of graphite and fuel compact conductivities. Sub-section 6.4 shows the comparison between the effective conductivities thus calculated with those obtained from the three-component Maxwell equation, described in Sub-section 6.2.

Two finite element models were established to investigate the isotropy of the thermal conductivity with respect to the transverse directions of the fuel block. As such, the first model was oriented assuming that the principal temperature gradient, and consequently the heat flow, was aligned with an across-flats direction, whilst the second model assumed that the heat flow was in the across-corners direction.

The finite element code used for this work was ABAQUS/CAE version 6.7-1.

6.3.1 Fort St Vrain / GT-MHR fuel block design

The fuel block design and dimensions are presented in Section 2, but the important features are repeated here. A GT-MHR fuel block is hexagonal in cross section, with a width of 360 mm across-flats and a height of 800 mm. The graphite block contains 108 coolant channels, of 16mm in diameter and 216 fuel channels, of 12.7mm in diameter. The channel centers are arranged on a triangular lattice with a pitch of 19mm. Each fuel channel contains 15 fuel compacts. These are 50mm high graphite cylinders of diameter 12.5mm, containing TRISO fuel particles within a graphite matrix material.

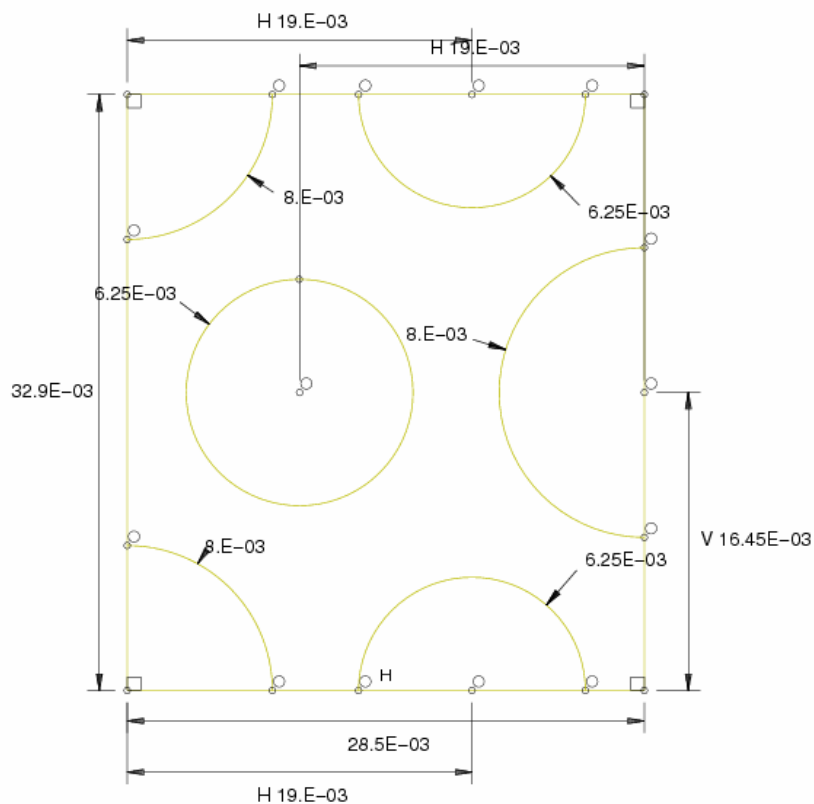
6.3.2 Geometry used for 2-D finite element models

Two-dimensional finite element models were produced of a unit cell taken from the GT-MHR fuel block design. Each two-dimensional model represents a horizontal slice through a fuel block passing through several fuel and coolant channels.

Only limited regions of the fuel block were modeled as a complete block is made of a repetitive structure. A representative unit cell has been chosen by looking at the lines of symmetry in the model and is shown in Figure 6.3.1. This unit cell was translated and/or rotated to reproduce both of the finite element models.

The unit cell contains part of three coolant channels containing Helium, one complete fuel channel and parts of another two fuel channels. The remainder of the unit cell is graphite. Based on the dimensions given in the preceding sub-section, the width of the unit cell is one and a half times the channel spacing and is 28.5mm. The overall length of the representative unit cell is 32.9mm. These dimensions and the unit cell are shown in Figure 6.3.1 (in meters).

Figure 6.3.1: Finite element model, extent and dimensions



6.3.3 Material properties

Thermal conductivities were assigned to each material in the base model and values used are shown in Table 6.3.1. The conductivity of Helium was calculated

corresponding to a pressure of 70 bar and mean coolant temperature of 670°C using the correlation obtained from the German KTA rules (Reference 6.2) as 0.35 W/m/K.

Table 6.3.1: Material conductivities

Material	Conductivity (W/m/K)
Graphite	30.0
Fuel	20.0
Helium	0.35

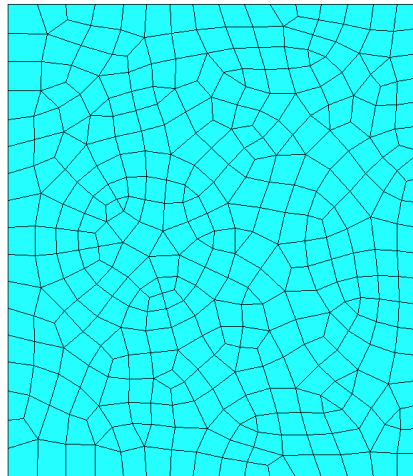
6.3.4 Boundary conditions

In order to assess the conductivity across the region of fuel, a known overall temperature gradient was applied to the model. A temperature difference of 500K was applied to the pair of edges that were normal to the across-flats direction in the first model, and to the pair of edges normal to the across corners direction in the second. In both models, edges parallel to the direction of heat flow were assumed to be adiabatic.

6.3.5 Finite element meshes and model variants

Finite element meshes were generated for three variants of the model. All of the meshes were made up from 4-node, quadrilateral linear elements. The mesh, as constructed within a single unit cell, is shown in Figure 6.3.2.

Figure 6.3.2: Finite element mesh in a unit cell



Such unit cells are arranged to give three model variants:

Base Case

The base case model consisted of one unit cell of fuel element (see Figure 6.3.2) with a temperature difference applied across the top and bottom edges, relative to the orientation shown in the figure. Figures 6.3.3 and 6.3.4 show the resulting temperature and heat flux contour plots.

Long across-flats model

The base case model has been extended to see if there is any difference in the results if the boundary conditions are applied away from the area analyzed for the results. Unit cells have been added to the top and bottom of the base case model, and a temperature difference applied across the very top and bottom edges.

Long across-corners model

To investigate if the conductivity is anisotropic, the effect of applying boundary conditions along the length of the model has also been looked at. The base case model has been extended horizontally by adding on unit cells to either side of the base case model. The same temperature difference has been applied but this time along the vertical edges of the model.

6.3.6 Determination of effective conductivities from finite element results

The finite element simulations compute the temperature and heat fluxes, from the temperature gradients, at every node within the domain. The resulting temperature and heat flux distributions for the base case are shown in Figure 6.3.3 and Figure 6.3.4 respectively.

Figure 6.3.3: Base case – distribution of temperature
 Temperatures given in Kelvin.

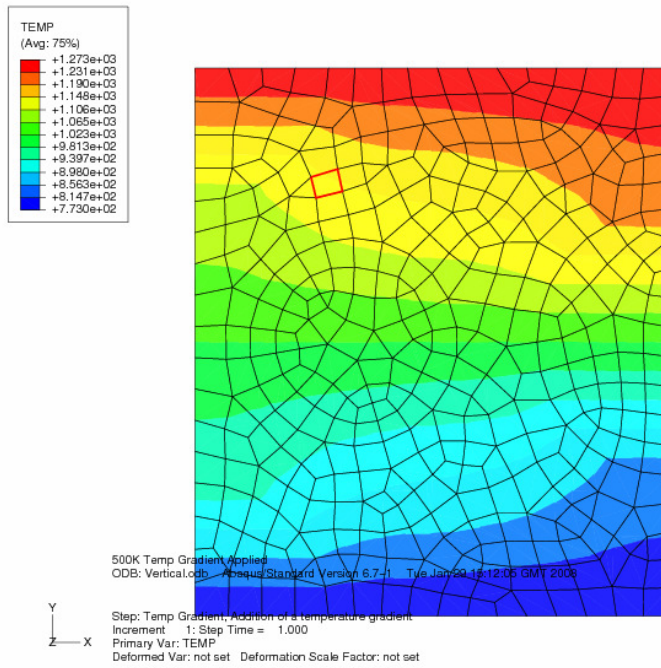
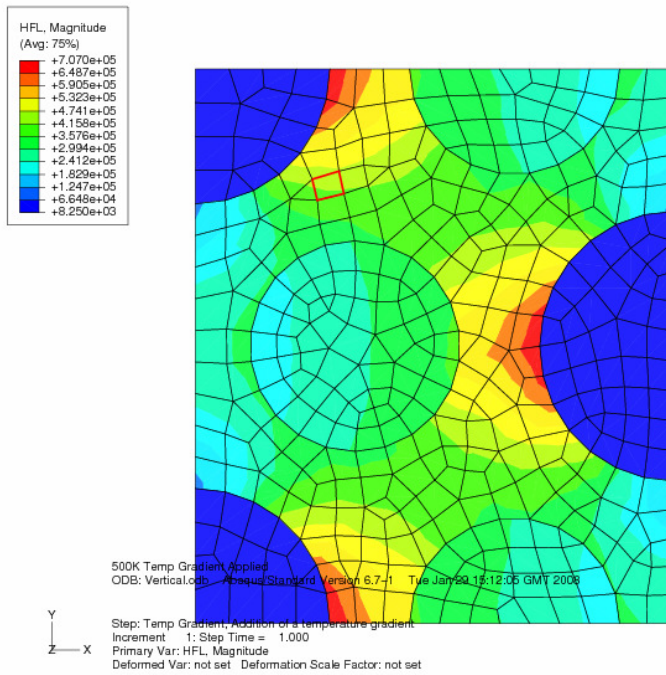


Figure 6.3.4: Base case – distribution of heat flux



Using the temperature and heat flux fields determined by the finite element simulation, the following relationship was applied to calculate the effective thermal conductivities for the various finite element models:

$$k = \frac{\Delta x \dot{q}'}{\Delta T w}$$

Where:

k	effective conductivity (W/m/K)
Δx	length over which the temperature difference is applied or measured (m)
\dot{q}'	heat flow per unit height (W/m)
ΔT	applied or measured temperature difference (K)
w	model width (m)

The values used for each finite element model and the resultant values of conductivity calculated are shown in Table 6.3.2.

For the base case model, the effective conductivity was calculated over the full length of the model. For the other two models, only the central unit cell was used to eliminate any potential end effects. The temperature difference for conductivity calculations with the base case model is the applied temperature difference. For the 'long' models, the temperature difference has been found by integrating the temperature profiles over the width along two lines normal to the direction of heat flow that bound the central unit cell to obtain the averages, followed by taking the difference of these two average temperatures.

Heat flows were determined by integrating the heat fluxes over the width of the model.

6.3.7 Predicted effective thermal conductivities

The results presented in Table 6.3.2 all show very similar values for the effective conductivity. This is as expected for the base case and the extended vertical model. The similar value for the conductivity in the horizontal direction shows that the conductivity is isotropic with regard to the transverse directions fuel block.

Table 6.3.2: Fuel block transverse effective thermal conductivities derived from finite element analyses

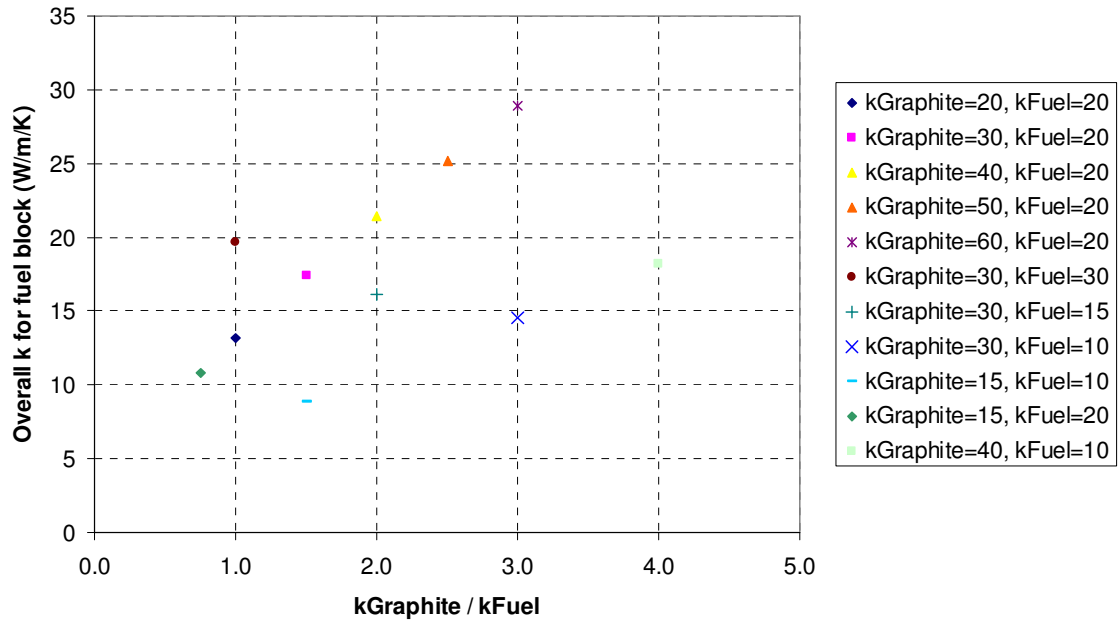
	Model		
	Base Case (across-flats)	Long across-flats	Long across-corners
Length (m)	3.29E-02	3.29E-02	2.85E-02
Width (m)	2.85E-02	2.85E-02	3.29E-02
Temperature Difference (K)	500	166.3	334
Heat Flow per unit height (W/m)	7.56E+03	2.51E+03	6.72e+03
Effective Conductivity (W/m/K)	17.45	17.43	17.43

The effect of changing the ratio of the fuel and graphite conductivities has been investigated. Ten further cases have been run using the geometry of the base case model, with varying ratios of graphite to fuel conductivity. Table 6.3.3 shows the results for the various tests along with the base case model results for comparison. These results are presented graphically as a function of the ratio of graphite conductivity to fuel conductivity in Figure 6.3.5.

Table 6.3.3 Fuel block effective thermal conductivities for different graphite and fuel compact thermal conductivities

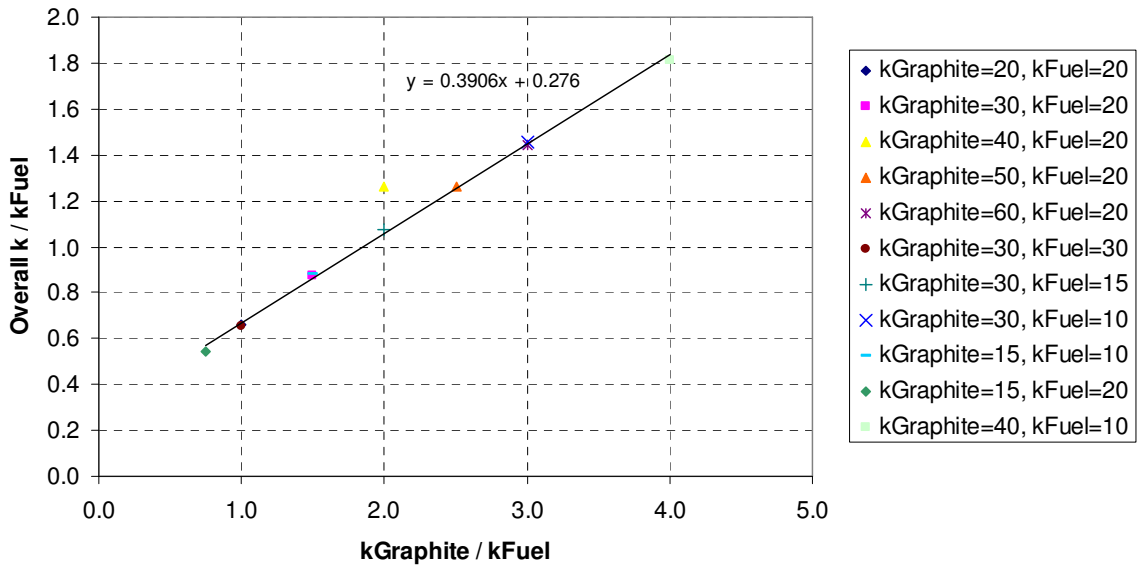
	Base Case	Case 2	Case 3	Case 4	Case 5	Case 6	Case 7	Case 8	Case 9	Case 10	Case 11
Graphite Conductivity k_m (W/m/K)	30.0	40.0	50.0	60.0	20.0	30.0	30.0	30.0	15.0	15.0	40.0
Fuel Conductivity k_{fc} (W/m/K)	20.0	20.0	20.0	20.0	20.0	15.0	10.0	30.0	10.0	20.0	10.0
Ratio of k_m to k_{fc}	1.5	2.0	2.5	3.0	1.0	2.0	3.0	1.0	1.5	0.75	4.0
Helium Conductivity k_h (W/m/K)	0.35	0.35	0.35	0.35	0.35	0.35	0.35	0.35	0.35	0.35	0.35
Effective Conductivity (W/m/K)	17.45	21.41	25.20	28.90	13.17	16.10	14.53	19.66	8.82	10.81	18.15

Figure 6.3.5: Variation of effective transverse thermal conductivity with ratio of graphite to fuel compact thermal conductivity



If the overall conductivity is divided by the fuel compact conductivity, the points lie on an approximately straight line as shown in Figure 6.3.6.

Figure 6.3.6: Variation of effective transverse thermal conductivity divided by fuel compact conductivity with graphite / fuel compact conductivity ratio.



6.4 Comparison with Analytical Results

Analytical effective thermal conductivities were calculated using the three material form of Maxwell's equation as derived in the previous sub-section:

$$k_{eff} = k_m \left[1 - \frac{2[\alpha_1(k_m - k_1)(k_m + k_2) + \alpha_2(k_m - k_2)(k_m + k_1)]}{[(k_m + k_1)(k_m + k_2) + \alpha_1(k_m - k_1)(k_m + k_2) + \alpha_2(k_m - k_2)(k_m + k_1)]} \right]$$

Where, in the above:

k_{eff}	effective thermal conductivity
k_m	matrix (graphite) thermal conductivity
k_1	helium thermal conductivity
$k_2 = k_{fc}$	fuel compact thermal conductivity
α_1, α_2	volume fractions of helium and fuel compacts respectively

The comparison of the effective conductivities determined by finite element analysis with those obtained from the analytical is shown in Table 6.4.1 together with the percentage difference between the two methods. The percentage differences given in the table are shown plotted as a function of graphite to fuel compact thermal conductivity ratio in Figure 6.4.1.

Table 6.4.1: Comparison of effective conductivities derived from finite element analysis with the analytical values

	k_m/k_{fc}	Effective Conductivity from FE Analysis (W/m/K)	Analytical Effective Conductivity (W/m/K)	% Difference
Base Case	1.5	17.45	17.55	0.59
Case 2	2	21.41	21.64	1.07
Case 3	2.5	25.20	25.55	1.41
Case 4	3	28.90	29.37	1.63
Case 5	1	13.17	13.14	-0.23
Case 6	2	16.10	16.27	1.07
Case 7	3	14.53	14.77	1.63
Case 8	1	19.66	19.61	-0.25
Case 9	1.5	8.82	8.87	0.54
Case 10	0.75	10.81	10.70	-1.00
Case 11	4	18.15	18.50	1.89

Figures 6.4.2, 6.4.3 and 6.4.4 present comparisons of the effective conductivities for each of the cases, grouped according to which of the material conductivities was held constant.

Figure 6.4.1: Percentage difference between effective conductivities predicted by FE analysis and those obtained analytically

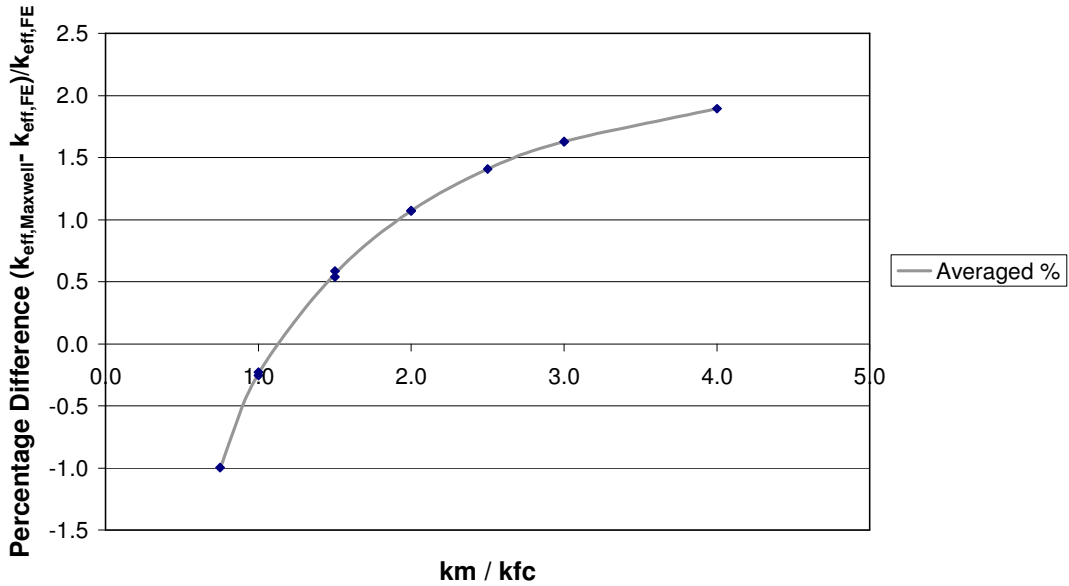


Figure 6.4.2: Comparison of effective conductivity using 3-component Maxwell's equation and FE analysis for k_{fc}=20W/m/K

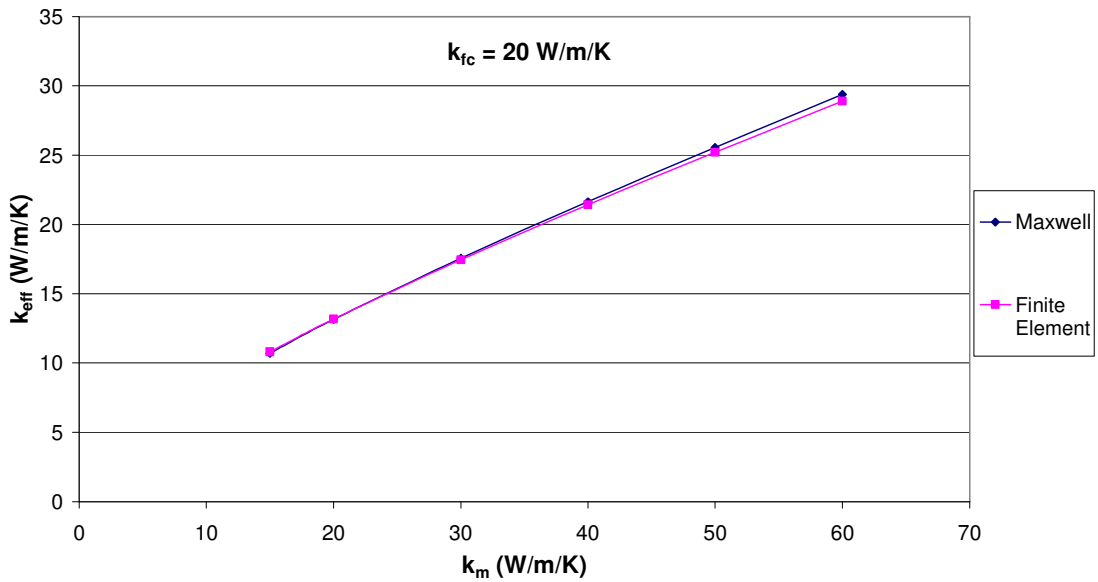


Figure 6.4.3: Comparison of effective conductivity using 3-component Maxwell's equation and FE analysis for $k_{fc}=10\text{W/m/K}$

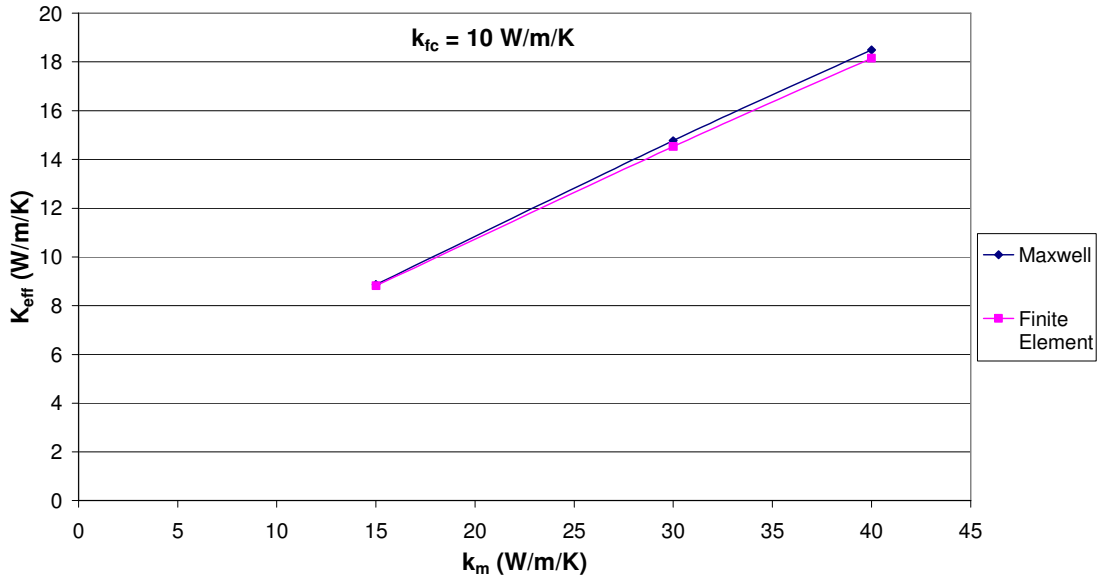
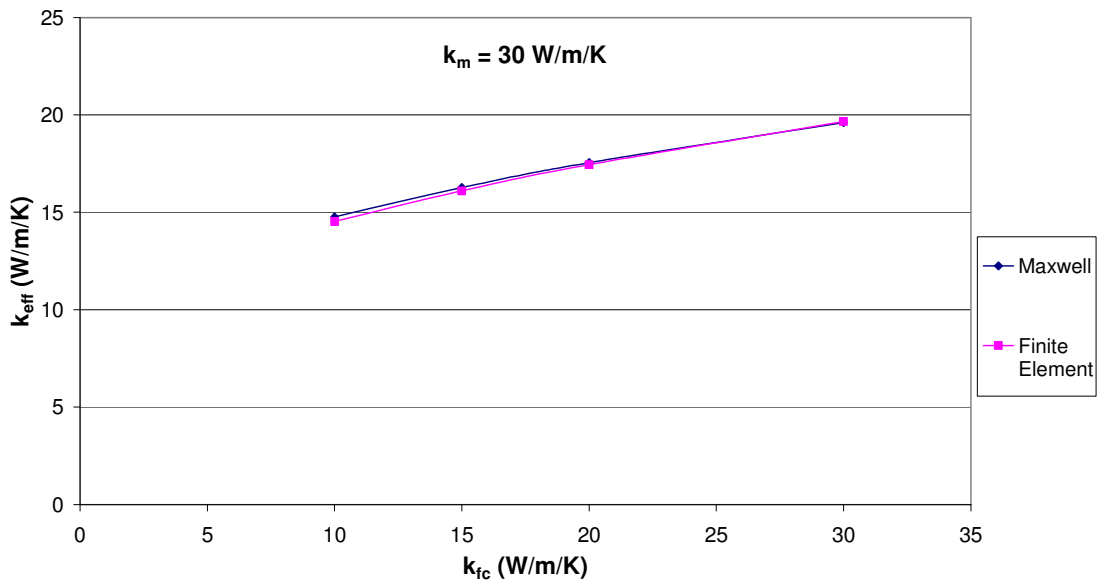


Figure 6.4.4: Comparison of effective conductivity using 3-component Maxwell's equation and FE analysis for $k_m=30\text{W/m/K}$



6.5 Closure

This section has presented the development of an analytical model by which the effective thermal conductivities in the transverse directions of a Fort St Vrain / GT-MHR fuel block can be determined.

Finite element models were created to give a comparison with the analytical model and to examine the isotropy of the predicted thermal conductivities.

Comparison of the analytical and finite element methods shows that the former produces effective conductivities which agree well with those of the latter over a range of matrix to fuel compact conductivity ratios that is wider than will be encountered in practice. For fuel compact conductivities that are as low as 25% of the matrix conductivity, the analytical method produces effective conductivities that are less than 2% greater than those obtained by the finite element analysis.

Comparison of the effective conductivities derived from the finite element models for the two perpendicular heat flow directions shows that the conductivities are isotropic in the transverse direction.

Overall, therefore, the effective conductivities in the transverse directions are isotropic and the analytical method can be used to predict values with an accuracy of better than 98% over the range of matrix to fuel compact conductivity ratios of interest. The volume fractions of the component materials are assumed to be fixed, and at their current values allow a Maxwell-based method to generate accurate values. If the design changes such that the volume fraction of graphite is decreased, i.e., the mixture becomes less dilute, the qualification exercise would need to be repeated.

6.6 References for Section 6

- 6.1 Carslaw, H.S. and Jaeger, J.C., Conduction of Heat in Solids, 2nd edition, Oxford University Press, 1959, p428.
- 6.2 KTA Rule 3102.1, "Reactor Core Design for High-Temperature Gas-Cooled Reactor. Part 1: Calculation of the Material Properties of Helium", Nuclear Safety Standards Commission (KTA), Germany, June 1978.

7.0 WHOLE-CORE (MACROSCOPIC) HEAT TRANSFER

7.1 Purpose of Section 7

Section 5 dealt with the development and qualification of models that resolve temperatures on the meso-scale by which the fuel compact and moderator graphite temperatures can be calculated together with the heat transferred to the coolant. In the development of those models it has been assumed that the coolant flow and local coolant temperature distributions are available from a macroscopic model of the reactor. It is also assumed that the power distribution is known, either having been prescribed as input to the model or obtained interactively from a coupled neutronics model. Modeling of the microscopic scale behavior of individual TRISO particles within a fuel compact is dealt with in detail, in the context of pebble bed HTGRs in Reference 7.1.

This section concentrates on modeling the behavior on the macroscopic scales. The macroscopic scale resolves the coolant, temperature and power distributions from the scale of the whole core down to a fraction of the size of a fuel element. In such a model a complete hexagonal fuel element could be the smallest scale resolved with all of the coolant channels therein being represented by a single *effective* channel. Similarly all of the channels containing fuel compacts could be represented by two identical *effective* fuel channels (because on average there are two fuel channels for every coolant channel in a Fort St Vrain fuel block). A better macroscopic resolution is obtained if each hexagonal block is subdivided into 6 triangular sectors, with each sector being represented by a single coolant channel and a pair of identical fuel channels. Such a sub-division allows for a gradient of power across a fuel element to be resolved and for temperature gradients resulting from heat loss through the core boundary to be captured better.

In order to qualify the macro-scale models, reference solutions were generated using the finite element (FE) method to solve the partial differential steady state heat conduction equations in two-dimensions without simplification. The development of the reference FE solutions are presented in the next sub-section and these are compared with the macro-scale models in Sub-section 7.3.

It is believed that the macroscopic models presented in Section 7.3 are suitable for reactor static calculations, but require some development to handle realistic and continuous spatial variations in power density and coolant temperature. Similarly, a further development is necessary to handle correctly the transition to no flow conditions. Extension and qualification of the model to be applicable to transient conditions will require additional model development and further finite element simulations.

7.2 Finite Element Solutions for the Whole Core Conduction Model

This sub-section describes the steady state finite element models that have been produced of the following cases:

- Heat transfer within a hexagonal fuel block (named the 'intra-block model')
- Heat transfer between two neighboring fuel blocks (named the 'inter-block model')
- Heat transfer through a radial path from the centre of the core outwards, cutting a path through three fuel blocks (named the 'combined model')

The finite element program code for this work was ABAQUS/CAE version 6.7-1 and the following sub-sections describe the geometry modeled, material properties, boundary conditions and fuel compact power densities applied, and the results obtained in each case.

7.2.1 Modeled geometry

Two-dimensional models have been produced of regions of a GT-MHR core:

- Intra-block model geometry – the geometry has been set up of a cross section through a type-1 GT-MHR fuel block. The FE geometry is shown in Figure 7.2.1.
- Inter-block model geometry – an FE model has been set up of two 1/6 sectors of neighboring fuel blocks. The gap between the fuel blocks has been assumed to be 2mm. The FE geometry is shown in Figure 7.2.2.
- Combined model geometry – the geometry has been set up to represent a radial path through the fuel blocks in a GT-MHR core. The path chosen is through three half fuel blocks and the gaps between the fuel blocks have again been assumed to be 2mm. The FE geometry is shown in Figure 7.2.3.

7.2.2 Material properties

The FE models contain two materials, fuel compact and graphite, with the properties of helium used to determine the heat transfer coefficient at the coolant channel wall. Properties assigned to the fuel compact and graphite in the model are shown in Table 7.2.1. The thermal conductivity value used for graphite of 30 W/m/K is considered to be representative of irradiated graphite at typical HTGR core temperatures. For the fuel compact a thermal conductivity of 20 W/m/K was chosen to represent the combined influence of the presence of lower conductivity TRISO particles and increased degradation in graphite conductivity (due to greater neutron damage and higher temperatures because the fuel compacts are hotter than the fuel blocks in which they sit).

Helium properties were evaluated at conditions representative of those in GT-MHR; a mean coolant temperature of 943.15K (670°C) and pressure of 70 bar. Correlations from the German KTA rules (Reference 7.2) were used, giving a thermal conductivity of 0.35 W/m/K.

Table 7.2.1: Material properties

Material	Thermal Conductivity (W/m/K)	Density (kg/m³)	Specific Heat Capacity (J/kg/K)
Graphite	30.0	1720	1690
Fuel compact	20.0	1720	1690

7.2.3 Boundary values and power density in a fuel compact

For GT-MHR the helium mass flow rate through the whole core is 316 kg/s (Reference 7.3). Ignoring the presence of blocks containing control rod channels, there are typically 108 coolant channels per block and 102 columns of fuel blocks, therefore there are approximately 11000 coolant channels in the core giving an average mass flow rate of 0.029 kg/s per coolant channel. Based on the above properties and this mass flow rate, the average Reynolds number in a coolant channel is 51.6×10^3 , giving a Nusselt number, based on the Dittus-Boelter correlation of 119 and a resulting heat transfer coefficient of 2.615 kW/m²/K.

The nominal power density in a compact was set to the average value for the whole core. The steady state thermal power in GT-MHR is 600 MW and there are 2.92 million fuel compacts in the core (Reference 7.3), therefore the average power per compact is 205 W. The diameter and length of a fuel compact are 12.5 mm and 50 mm respectively, however in these models the diameter of the fuel compact has been assumed to be the same as the diameter of a fuel channel (12.7 mm) and so the average steady state power density is 32.366 MW/m³.

Figure 7.2.1: Geometry of the intra-block finite element model showing the power densities used for Variant 2

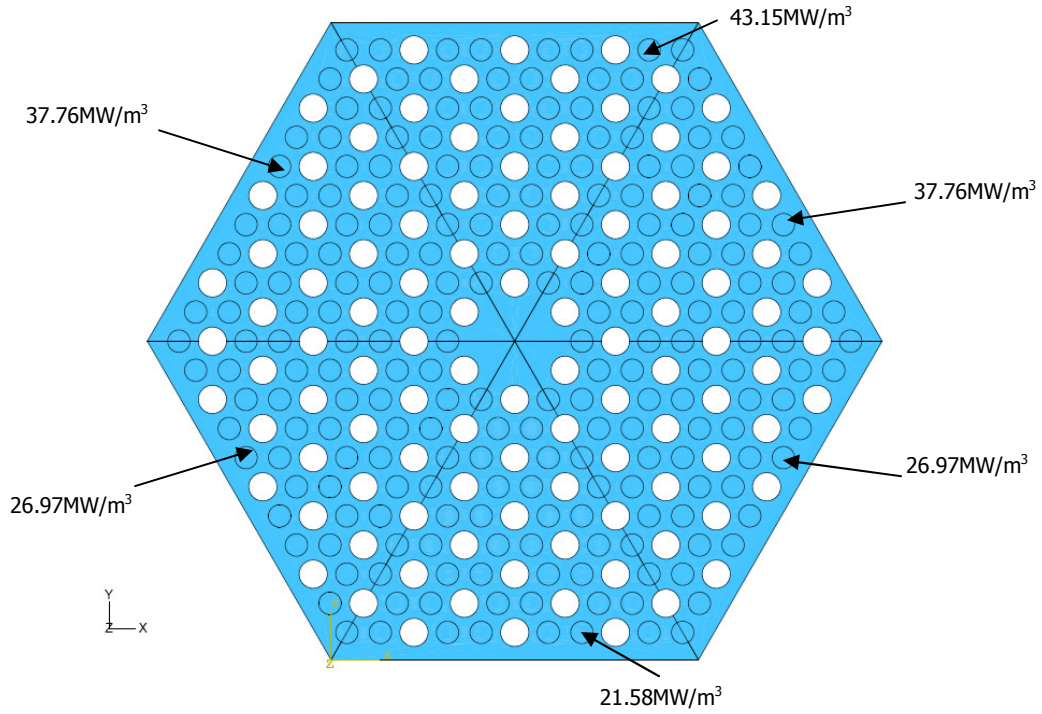


Figure 7.2.2: Geometry of the inter-block finite element model

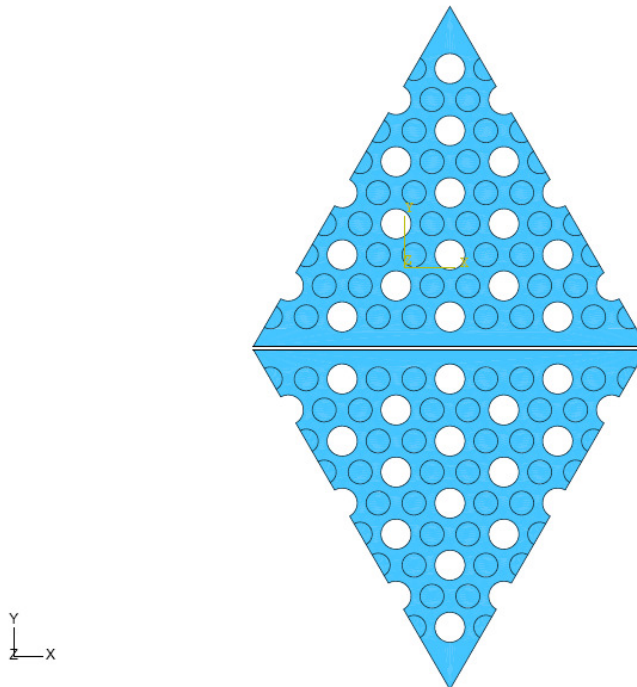
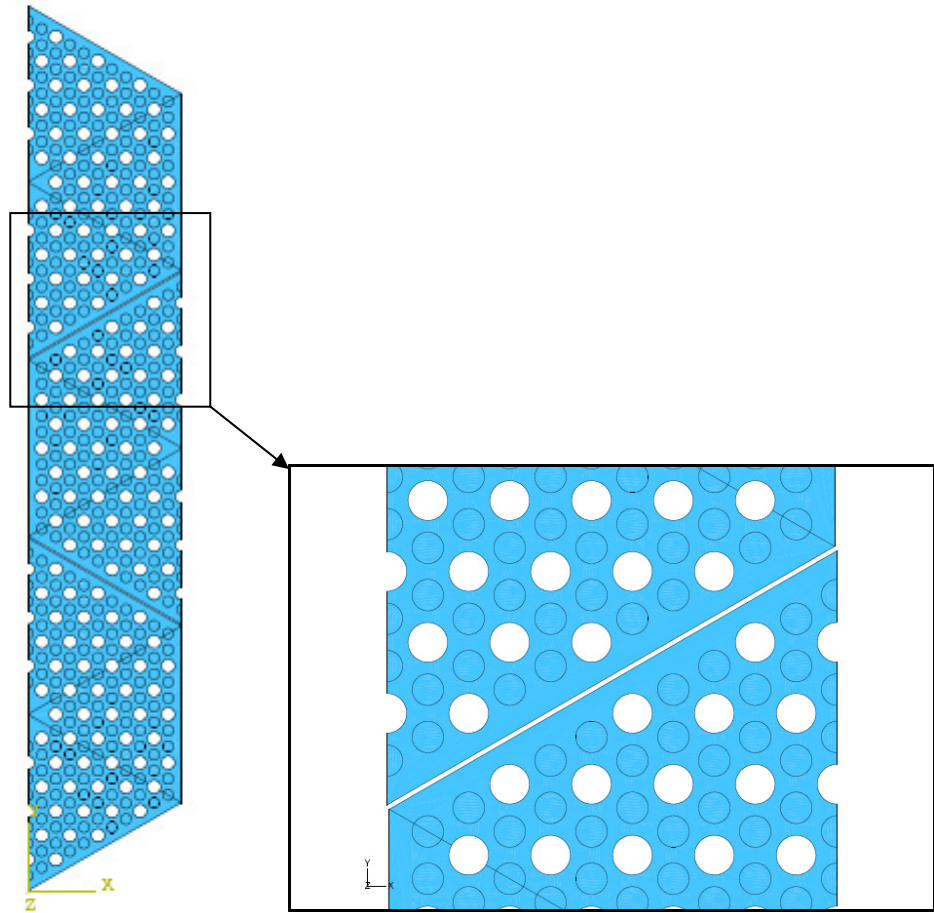


Figure 7.2.3: Geometry of the combined finite element model



7.2.4 Model conditions applied

7.2.4.1 Intra-block model conditions

Two variants of the intra-block model have been considered:

- Variant 1 – Coolant channel wall temperature of 943.15K (670°C) was assigned. The edges of the model are assumed to be adiabatic. The fuel power was applied as a gradient in power across the fuel block. A high power was applied at the top edge, as shown in Figure 7.2.1, of 1.5 times nominal power (48.549 MW/m³), a low power at the bottom edge of 0.5 times nominal power (16.13 MW/m³), and a linear gradient applied in-between.
- Variant 2 – As for Variant 1, a coolant channel wall temperature of 943.15K was assigned and the edges of the model are assumed to be adiabatic. The fuel block was divided into six equal triangles (see Figure 7.2.1) and the fuel compacts in each triangle have been assigned a certain power density (see Figure 7.2.1). Fuel compacts in the uppermost triangle have a power density of four thirds of nominal power (43.15 MW/m³); with the triangles on either

side having power densities of seven sixths of nominal power (37.76 MW/m³). The lowest triangle has a power density of two thirds of nominal power (21.58 MW/m³) and the triangles on either side have power densities of five sixths of nominal power (26.97 MW/m³). The power distribution results in the top half of the fuel block having a higher power density than the lower half of the block, by the same amount as in the linear power variation assumed in Variant 1.

7.2.4.2 Inter-block model conditions

Two variants have been modeled:

- Variant 1 – Each fuel block was assigned the same coolant temperature of 943.15K and the same coolant mass flow rate (which as illustrated in Sub-section 7.2.3, results in a heat transfer coefficient of 2.615 kW/m²/K). The fuel compacts in each block were assigned different power densities. The fuel in the upper block, as shown in Figure 7.2.2, had a power density of 1.5 times nominal power and the fuel in the lower block had a power density of 0.5 times nominal power.
- Variant 2 – Each fuel block had the same coolant flow but the coolant temperature differed. The upper fuel block had a coolant temperature of 943.15K (670°C) and the lower fuel block had a coolant temperature of 843.15K (570°C). The fuel compacts in both blocks were assigned the nominal power density of 32.366 MW/m³.

Between the fuel blocks, heat transfer across the 2mm gap has been modeled by radiation and conduction.

ABAQUS uses the following equation to calculate the radiative heat transfer:

$$q = C \left[(\theta_A - \theta^Z)^4 - (\theta_B - \theta^Z)^4 \right]$$

with,

$$C = \frac{F\sigma}{\frac{1}{\epsilon_A} + \frac{1}{\epsilon_B} - 1}$$

where:

- q is the heat flux per unit area
- θ_A and θ_B are temperatures of the two surfaces, A and B.
- θ^Z is the value for absolute zero of the temperature scale being used
- σ is the Stefan-Boltzmann constant (5.67E-8 W/m²/K⁴)
- ϵ_A and ϵ_B are the surface emissivities
- F is the effective viewfactor

A value of 0.8 has been used for the emissivity of graphite. The viewfactor, F , is defined as a function of the clearance and has a value of between 0 and 1. This has been assumed to be 1.0 across the 2mm gap.

ABAQUS uses the following equation to calculate the conductive heat transfer:

$$q = G[\theta_A - \theta_B]$$

Where q , θ_A and θ_B are defined as above and G is the gap conductance which is equal to the conductivity of Helium divided by the gap size, resulting in a gap conductance of 175 W/m²/K.

7.2.4.3 Combined block model conditions

Three variants of the combined model have been analyzed. In each model heat is transferred across the 2mm gaps by conduction and radiation as detailed in Sub-section 7.2.4.2:

- Variant 1 – This represents the reactor at power. The power density and coolant temperature distributions have been interpreted from previous AMEC studies of GT-MHR (Reference 7.4). The power density variation has been curve-fitted using the following equation:

$$PowerDensity = -64.5y^3 + 192y^2 - 148y + 68$$

Where y is the y -coordinate of the FE model specified in units of m and the power density is in units of MW/m³.

The coolant temperatures have been set up so that the boundary coolant temperature for each of the nine triangles (see Figure 7.2.3) is fixed within each triangle. The temperatures used for each triangle (starting from the centre of the core outwards) are; 1070K, 1045K, 1020K, 1000K, 995K, 1000K, 1015K, 1040K and 1065K. All edges apart from the gaps between the blocks and the coolant channel walls are assumed to be adiabatic.

- Variant 2 – This Variant also models the reactor at power. The coolant temperature distributions are as in Variant 1. The power density is similar to that in Variant 1 but for this model, each triangle is given a power density which is constant within a triangle as follows (starting from the centre of the core outwards); 54.93 MW/m³, 45.23 MW/m³, 38.80 MW/m³, 35.22 MW/m³, 34.05 MW/m³, 34.86 MW/m³, 37.20 MW/m³, 40.66 MW/m³, 44.78 MW/m³ (see Sub-section 7.3.1.3 for more details).
- Variant 3 – This FE model represents a shutdown reactor. No heat transfer to the coolant has been modeled and the fuel compact power density has been set to be 0.5% of the power density distribution of Variant 1 to be representative of decay heat about 48 hours after shutdown. The outer edge

has a fixed temperature boundary condition of 873.15K to simulate heat loss through the core boundary.

7.2.5 Finite element meshes

Finite element meshes were constructed for each geometry. The mesh for the intra-block model consisted of 4-node linear heat transfer quadrilaterals and 3 node linear triangles. The meshes for the other models contained 6-node triangular and 8-node quadrilateral quadratic elements. Sample meshes for each geometry are presented in Appendix B.1.

For each of the models, mesh sensitivity tests have been performed to ensure that the results are independent of the mesh density. This is discussed along the results for each model in Sub-sections 7.2.6, 7.2.7 and 7.2.8.

7.2.6 Results of the intra-block model

The geometry has been set up of a cross section through a type-1 GT-MHR fuel block

7.2.6.1 Intra-block Variant 1 results

For this Variant, the fuel power has been applied with a high power at the top edge and a low power at the bottom edge, with a linear gradient in-between.

The model has been run to a steady state and a contour plot of the temperature distribution is shown in Figure 7.2.4. The corresponding heat flux distribution is shown in Appendix B.1. The hot spots seen in Figure 7.2.4 at the corners of the fuel block are due to these regions seeing less coolant channels than the rest of the block. This can be resolved by putting burnable poisons at the corners of each block or by using no fuel in these regions. The centre of the block is cooler as there is no fuel modeled in this region. GT-MHR fuel blocks have a space in the centre of each block for lifting equipment.

The heat flow from the high power half of the block to the lower power half has been calculated by taking the integral of the heat flux along the dividing line perpendicular to the direction of heat flow, passing through the centre of the block.

The heat flow has been calculated using several mesh densities and the mesh sensitivity calculation results are shown in Table 7.2.2. The heat fluxes used for post processing in ABAQUS have been found to be more sensitive to the mesh density than expected, and the reason for this is not known. The mesh density has a significant impact on the results with the calculated heat flow varying from 1.41 kW/m to 1.47 kW/m, a difference of 6%.

Table 7.2.2: Results for the intra-block model Variant 1

No. of Elements	Heat Flow (W/m)
33134	1411.9
55528	1417.0
68570	1447.4
109819	1474.2
114112	1462.7

7.2.6.2 Intra-block Variant 2 results

The Variant 2 model has been set up with the fuel compacts in each triangle assigned a certain power density (see Figure 7.2.1).

The steady state temperature distribution is shown in Figure 7.2.5. The distribution of heat flux is shown in Appendix B.1. The heat flow from the high power half of the block to the lower power half was calculated in the same way as for Variant 1.

Several mesh densities have been used to calculate the heat flow. The sensitivity calculation results are shown in Table 7.2.3. The calculated heat flow increases as the mesh density increases. However, the results for meshes with 68570 and 114112 elements (an increase of a factor of 1.7), only have a difference of 0.9%. These give a result for the heat flow from the high power to the lower power halves of 6.82 and 6.89 kW/m.

Table 7.2.3: Results for the intra-block model Variant 2

No. of Elements	Heat Flow (W/m)
33134	6719.8
55528	6786.0
68570	6824.3
114112	6887.3

Figure 7.2.4: Intra-block Variant 1 temperature distribution
Temperatures in Kelvin.

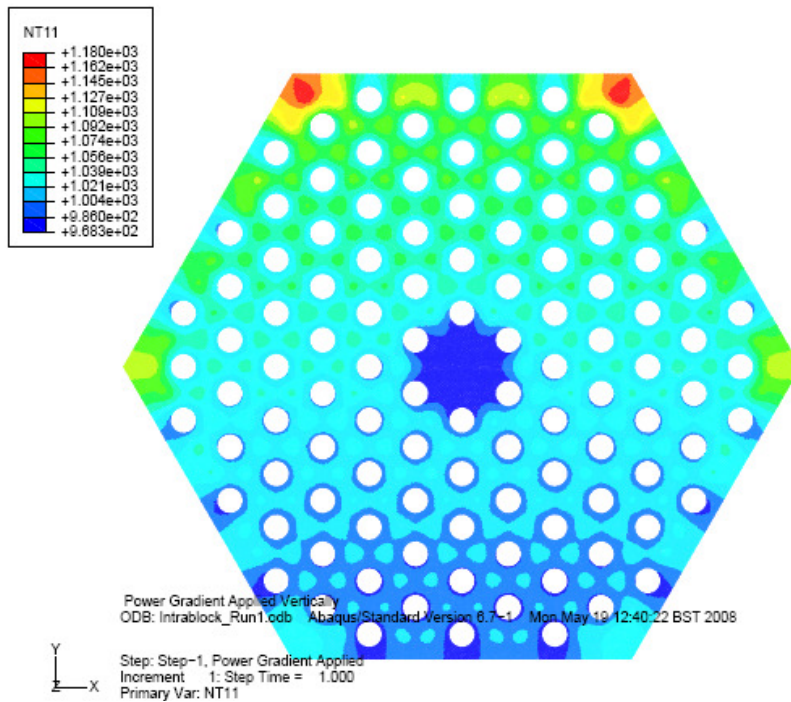
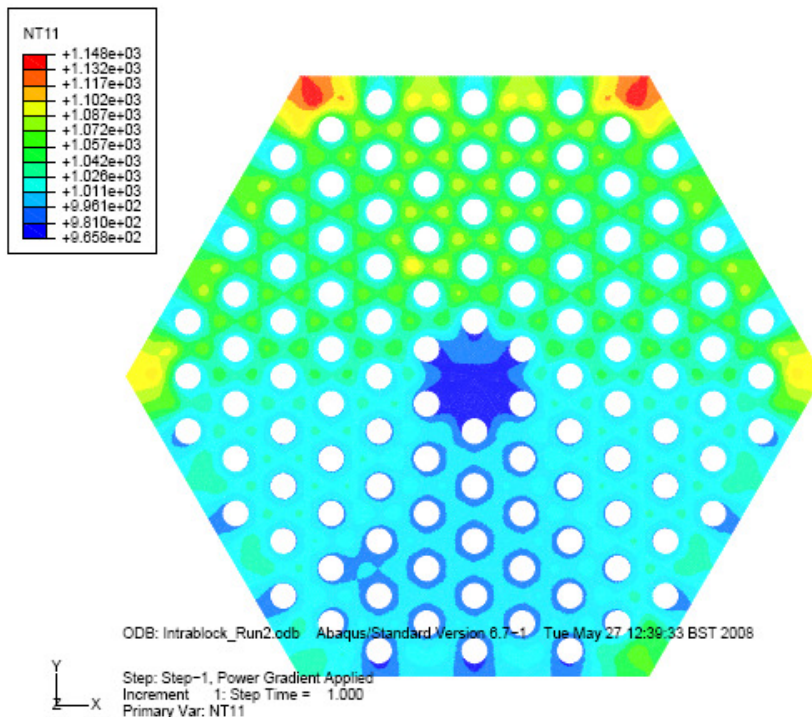


Figure 7.2.5: Intra-block Variant 2 temperature distribution
Temperatures in Kelvin.



7.2.7 Results of the inter-block model

The model represents two 1/6 sectors of neighboring fuel blocks with a gap of 2mm.

7.2.7.1 Inter-block Variant 1 results

For this Variant, the upper block, as shown in Figure 7.2.2, had a power density of 1.5 times nominal power and the lower block had a power density of 0.5 times nominal power.

The steady state temperature distribution is shown in Figure 7.2.6. This figure shows a relatively flat temperature distribution across each block following the flat power distribution applied to each block. The exception to this is at the edges of the gap between the blocks. Heat transfer across the gap is seen in the temperature distribution at the edge of each block but does not propagate through the rest of the fuel block.

Temperature and heat flux profiles along the edges of the gap (with the upper edge corresponding to the fuel block with the higher power) are shown in Figures 7.2.7 and 7.2.8. The heat flux distribution is shown in Appendix B.1.

The heat flow across the gap has been calculated by taking the integral of the vertical component of the heat flux across the upper and lower gap edges.

Using a mesh density of 11842 elements (with 250 elements along the gap edges), the heat flow has been calculated to be -4.06957kW/m along the upper edge and -4.07041kW/m along the lower edge. The negative sign corresponds to heat flowing from the upper block to the lower block. The difference between the calculated values for each edge is 0.02%. The small difference can be seen in the heat flux profiles of Figure 7.2.8 at the very edges of the model where the blue line as well as the red line can be made out.

A sensitivity test of the mesh has been performed using a mesh of 21237 elements (with 350 elements across each gap edge). The heat flow along the upper edge is calculated to be -4.07069kW/m and along the lower edge to be -4.07091kW/m . These results differ by less than 0.03% from those calculated using the lower mesh density and therefore the results are independent of the mesh.

7.2.7.2 Inter-block Variant 2 results

Variant 2 had a nominal power density applied to both fuel blocks and a coolant temperature of 943.15K in the upper block and 843.15K in the lower block.

The temperature distribution is shown in Figure 7.2.9. Temperature and heat flux profiles along the edges of the gap (with the upper edge corresponding to the fuel block with the higher coolant channel temperature) are shown in Figures 7.2.10 and 7.2.11. The heat flux distribution is shown in Appendix B.1.

Using a mesh density of 11842 elements (with 250 elements across the gap edges) the heat flux has been calculated to be -3.9875kW/m along the upper edge and -4.0287kW/m along the lower edge. This is a small difference of 1%.

A sensitivity test of the mesh has been run using a greater mesh density of 21237 elements (with 350 elements across each gap edge). The heat flux along each edge has been calculated to be the same (to 5 significant figures) as for those calculated using a mesh of approximately half the number of elements. This shows that the results are independent of the mesh. However, the discrepancy in heat flux remained at about 1% and the precise reason for this is not understood and appears to be an artifact of the thermal radiation model in ABAQUS.

The gap heat flux profiles shown in Figure 7.2.11 were also difficult to explain. Thermal radiation heat transfer across a narrow gap should be almost one-dimensional so the antiphase behavior of the heat flux profiles cannot be explained unless a significant amount of thermal radiation is being transferred at shallow angles.

Figure 7.2.6: Inter-block Variant 1 temperature distribution

Temperatures in Kelvin.

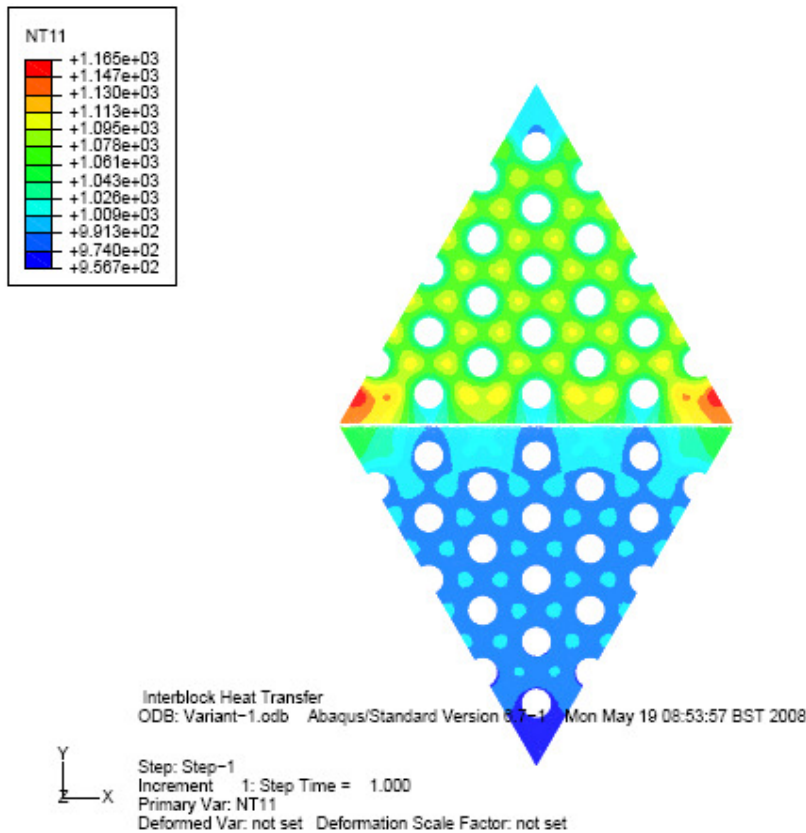


Figure 7.2.7: Inter-block Variant 1 temperature profiles along the edges of the gap

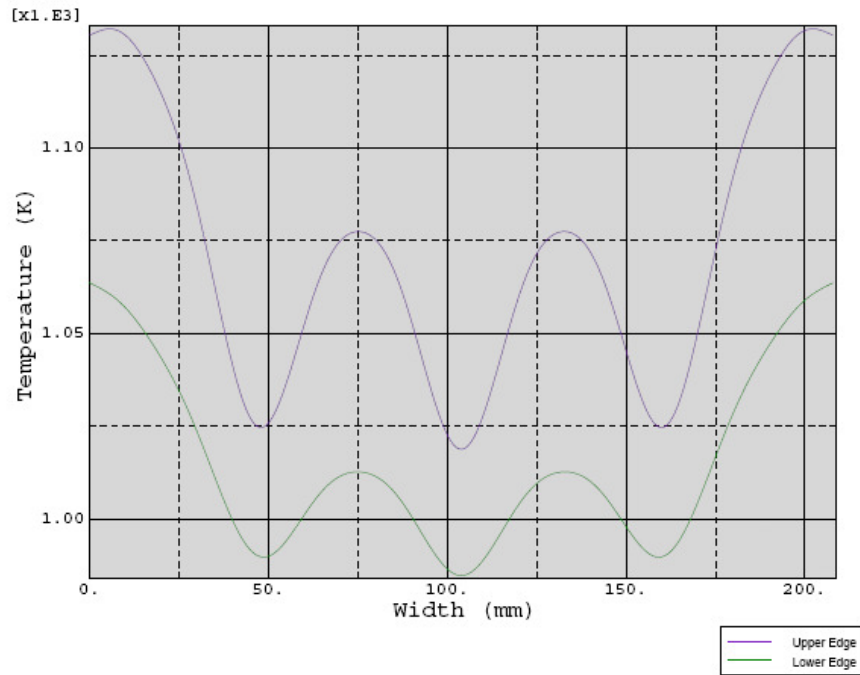


Figure 7.2.8: Inter-block Variant 1 heat flux profiles along the edges of the gap

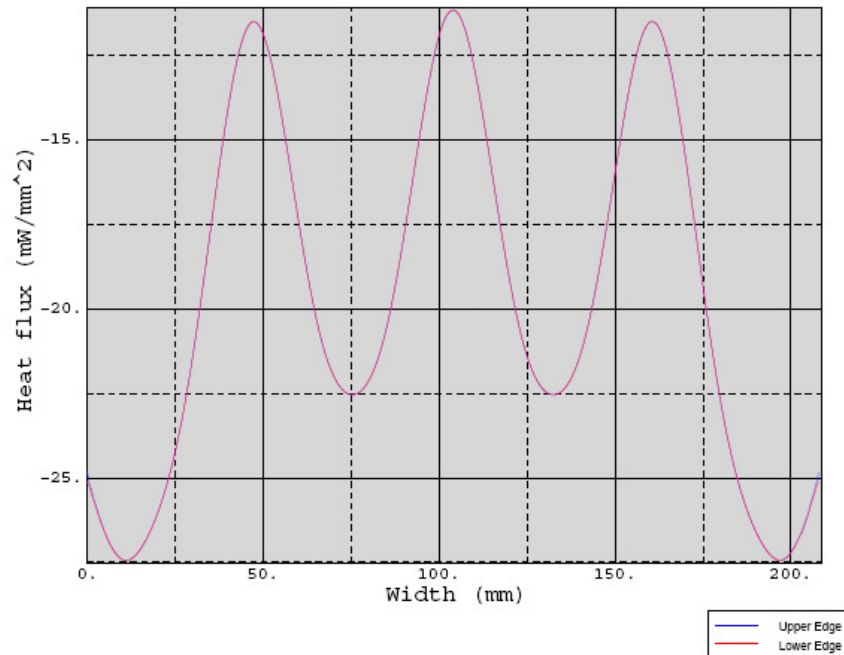


Figure 7.2.9: Inter-block Variant 2 temperature distribution
 Temperatures in Kelvin.

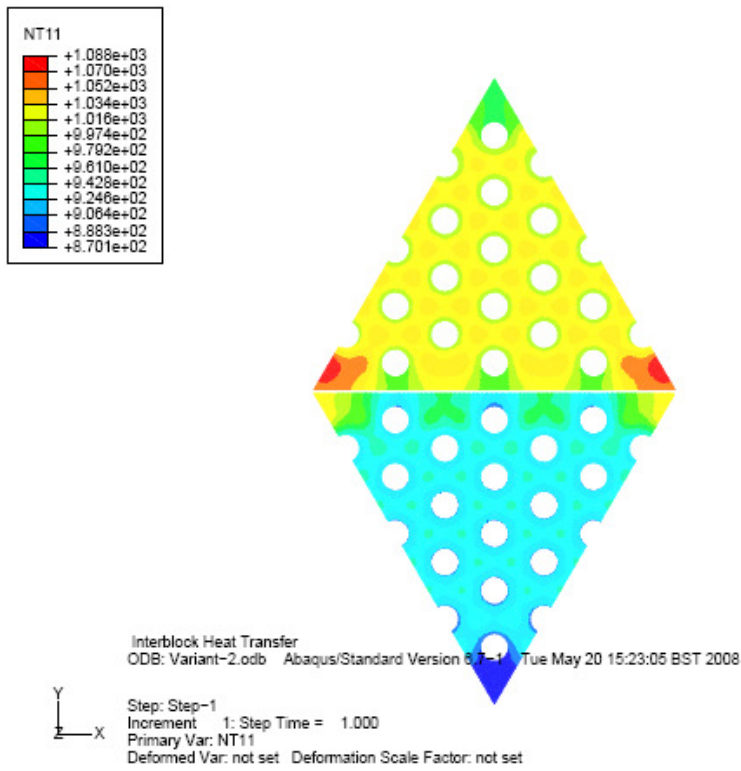


Figure 7.2.10: Inter-block Variant 2 temperature profiles along the edges of the gap

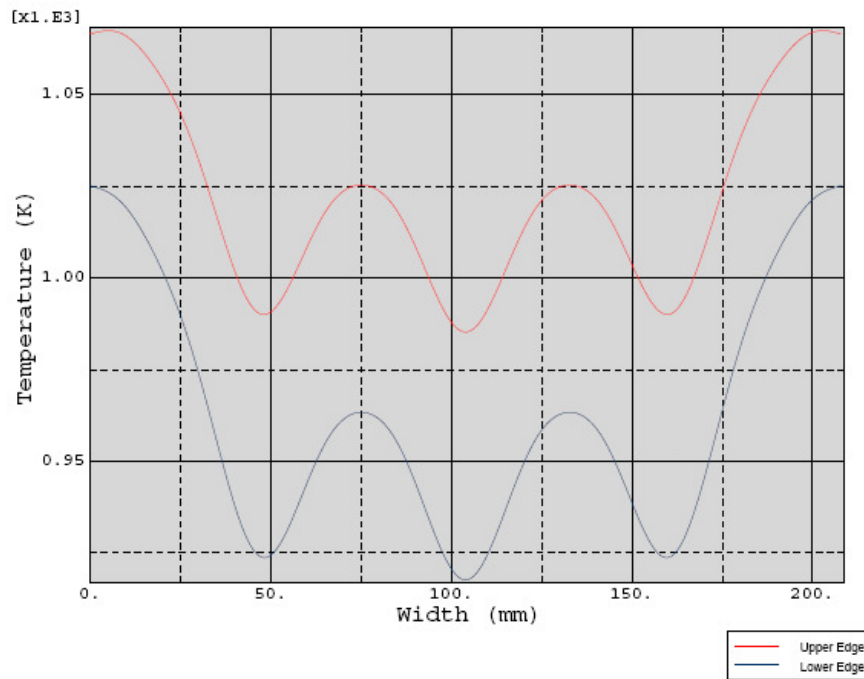
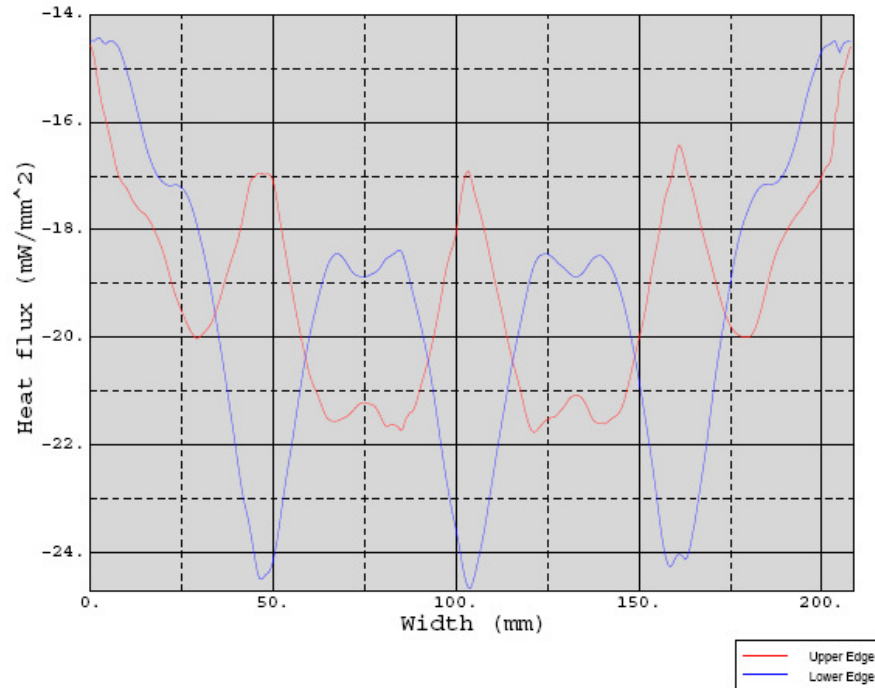


Figure 7.2.11: Inter-block Variant 2 heat flux profiles along the edges of the gap



7.2.8 Results of the combined block Model

The model geometry represents a radial path through the fuelled region in a GT-MHR core. The path chosen is through three half fuel blocks.

7.2.8.1 Combined model Variant 1 results

This Variant represents the reactor at power. The power density variation has been curve-fitted following the equation given in Sub-section 7.2.4.3. The coolant boundary temperature is fixed within each triangle.

The temperature distribution for Variant 1 is shown in Figure 7.2.12. Temperature and heat flux profiles along the edges of each of the 2mm gaps are shown in Figures 7.2.13 and 7.2.14 respectively. The heat flux distribution over the model is shown in Appendix B.1.

The heat flow across the gap edges has been calculated by taking the integral of the heat flux normal to each edge.

The heat flow has been calculated using a mesh of 14648 elements (with 250 elements along each edge) for the four edges. The results are given in Table 7.2.4 (the edge numbering is shown in Figure 7.2.12). The results for Edge 1 and Edge 2 should be equal and the same for edges 3 and 4. Edge 1 and 2 results differ by 1.1% and those for edges 3 and 4 differ by 0.7%. The heat flows are approximately

1.1 kW/m along the edges closest to the core centre and -0.9 kW/m along the edges furthest from the centre.

Results have also been calculated using a mesh of 47094 elements and these results are also shown in Table 7.2.4. The values calculated using the greater mesh density vary by less than 0.5% from those using the lower mesh density showing that the results are independent of the mesh.

Table 7.2.4: Results for the combined model Variant 1

No. of Elements	Edge No.*	Heat Flow (W/m)
14648	1	1106.0
	2	1118.5
	3	-906.6
	4	-900.6
47094	1	1101.8
	2	1118.5
	3	-905.2
	4	-900.2

* Edge 1 is closest to the centre of the core

Figure 7.2.12: Combined model Variant 1 temperature distribution
Temperatures in Kelvin.

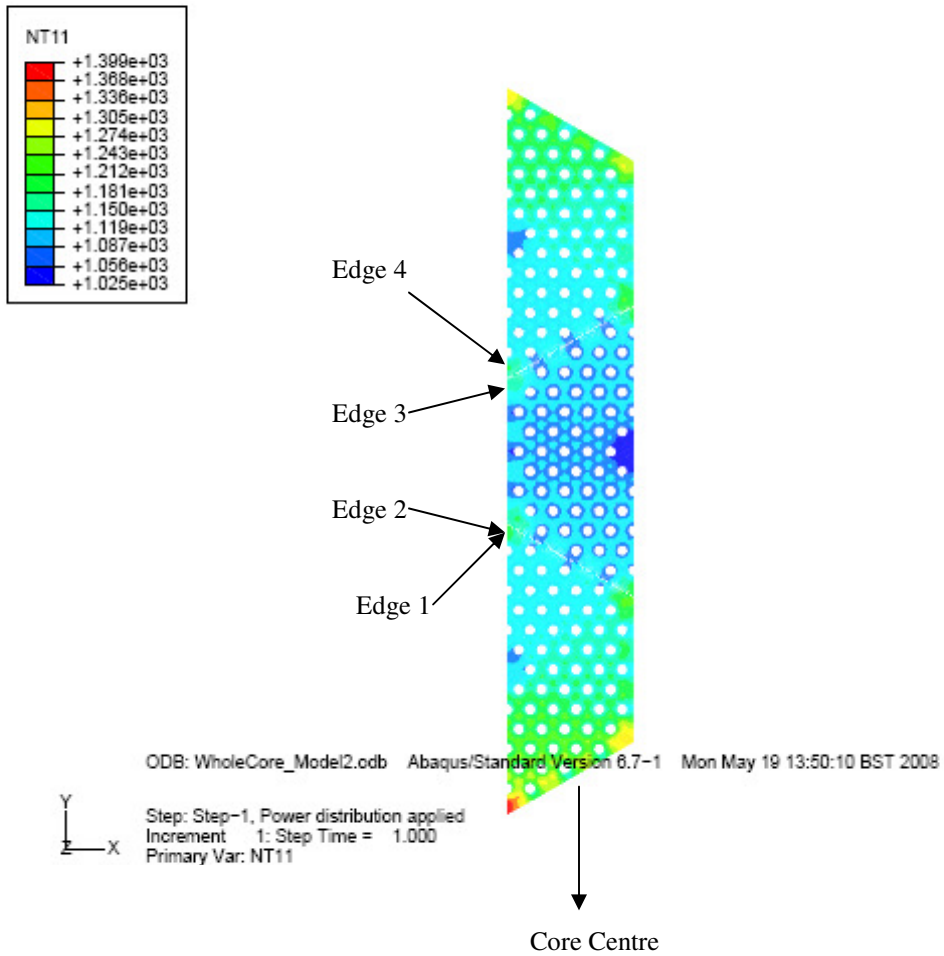
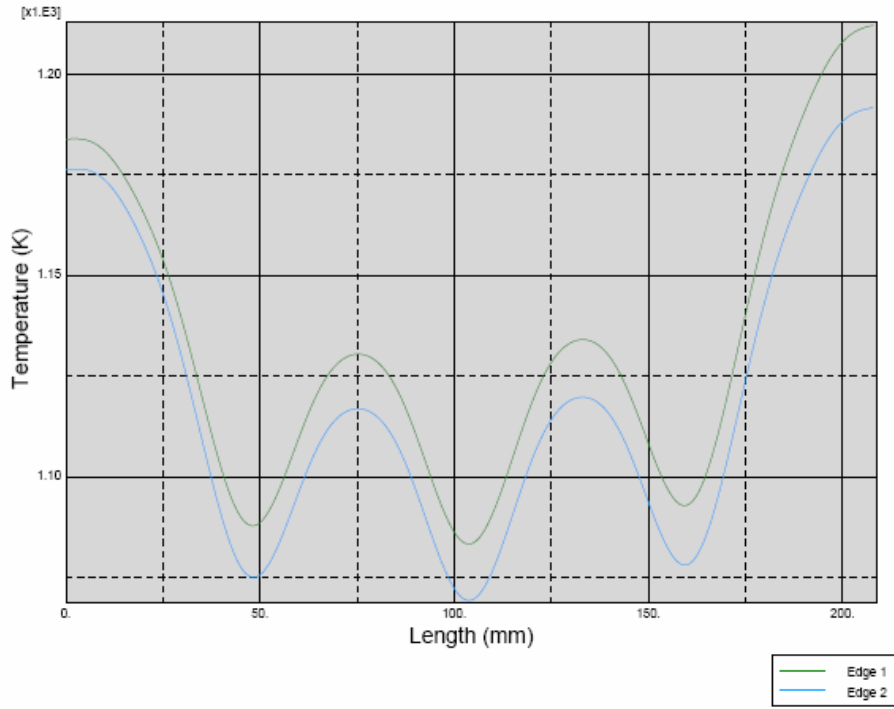


Figure 7.2.13: Combined model Variant 1 temperature profiles along the edges of the gaps

Gap edges closest to centre of core



Gap edges furthest from centre of core

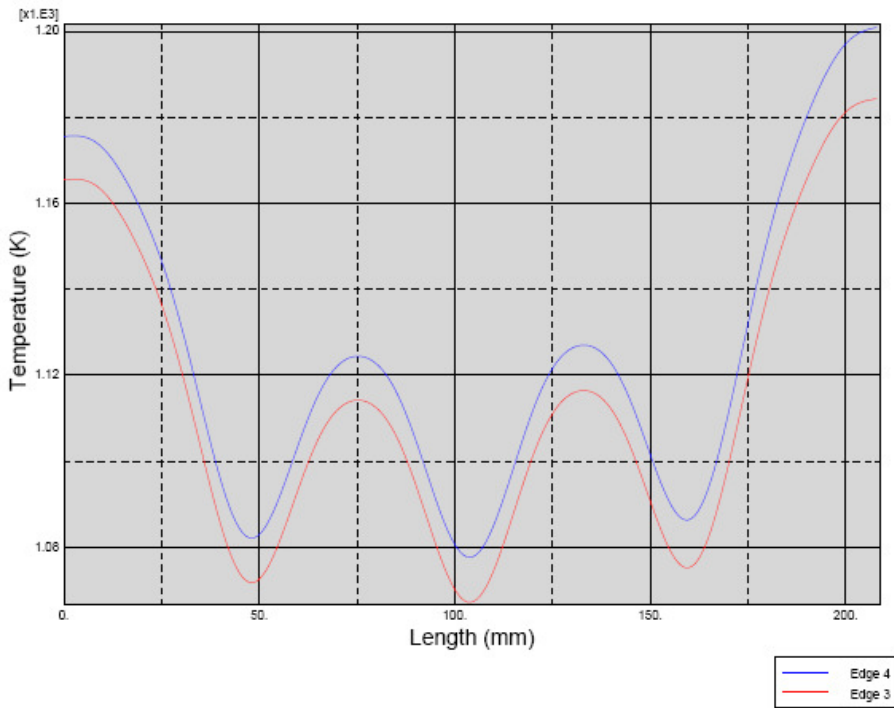
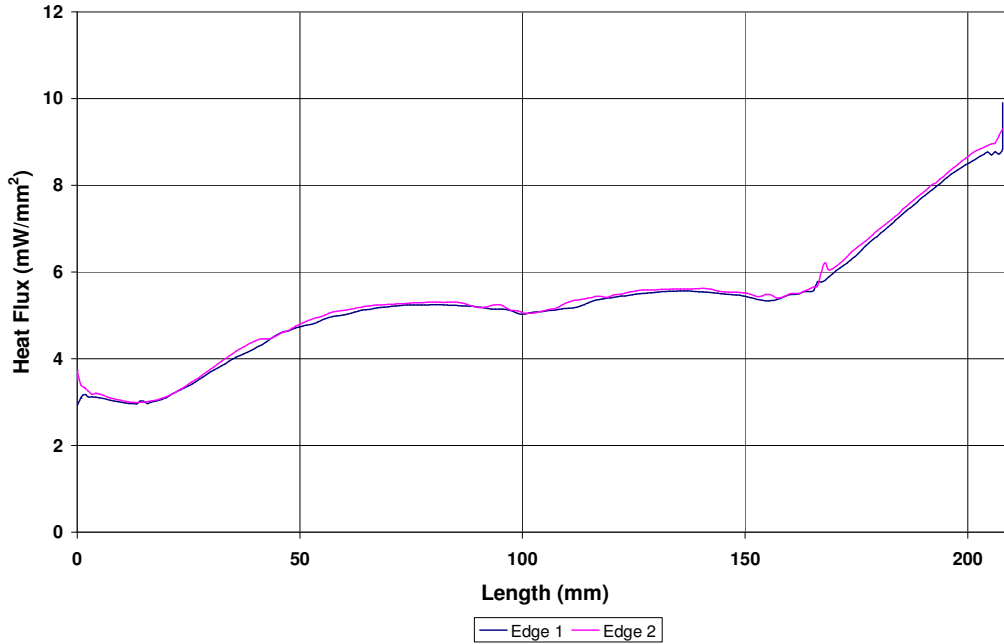
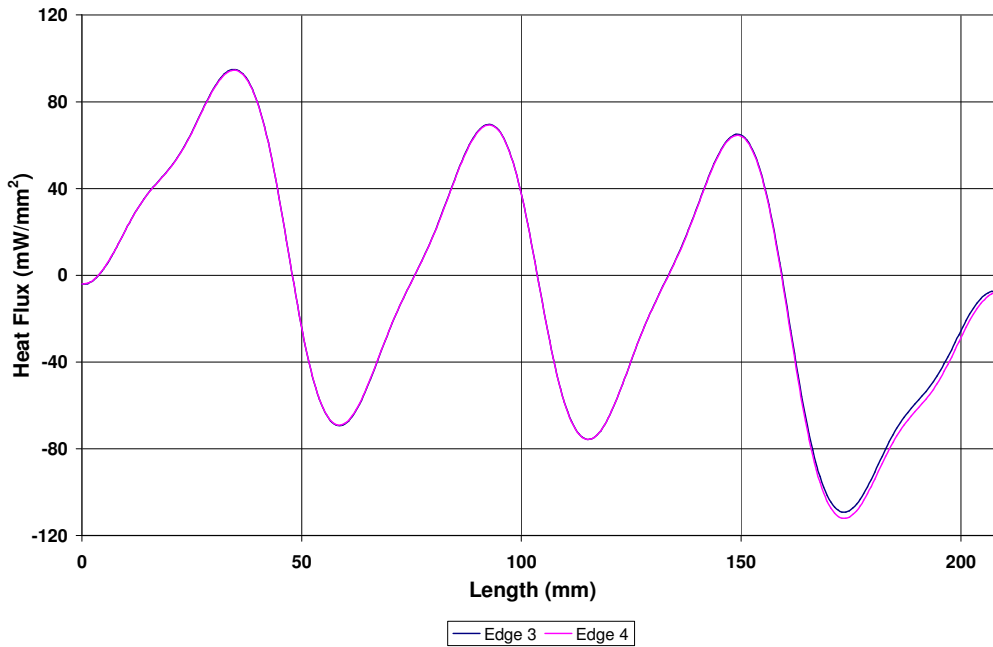


Figure 7.2.14: Combined model Variant 1 heat flux profiles along the edges of the gaps

Gap edges closest to centre of core



Gap edges furthest from centre of core



7.2.8.2 Combined model Variant 2 results

Variant 2 represents the reactor at power and each triangle has been given a constant power density and coolant temperature.

The temperature distribution for Variant 2 is shown in Figure 7.2.15. Temperature and heat flux profiles along the edges of each gap are shown in Figures 7.2.16 and 7.2.17. The heat flux distribution is shown in Appendix B.1.

The heat flow across the gap edges has been calculated by taking the integral of the heat flux normal to each edge and the results for mesh densities of 14635 and 47094 elements are shown in Table 7.2.5.

The heat flow across the gap closest to the centre of the core is approximately 1.5 kW/m and that across the gap further from the centre of the core is approximately 1.2 kW/m. For both meshes the edge 3 and edge 4 results differ by 0.7%. The edge 1 and 2 results differ by 1.6% for each mesh.

The values calculated using the two mesh densities vary by less than 0.3% showing that the results are independent of the mesh.

Table 7.2.5: Results for the combined model Variant 2

No. of Elements	Edge No.*	Heat Flow (W/m)
14648	1	1522.7
	2	1544.9
	3	-1166.8
	4	-1158.9
47094	1	1519.9
	2	1544.9
	3	-1165.8
	4	-1158.3

* Edge 1 is closest to the centre of the core

Figure 7.2.15: Combined model Variant 2 temperature distribution
Temperatures in Kelvin.

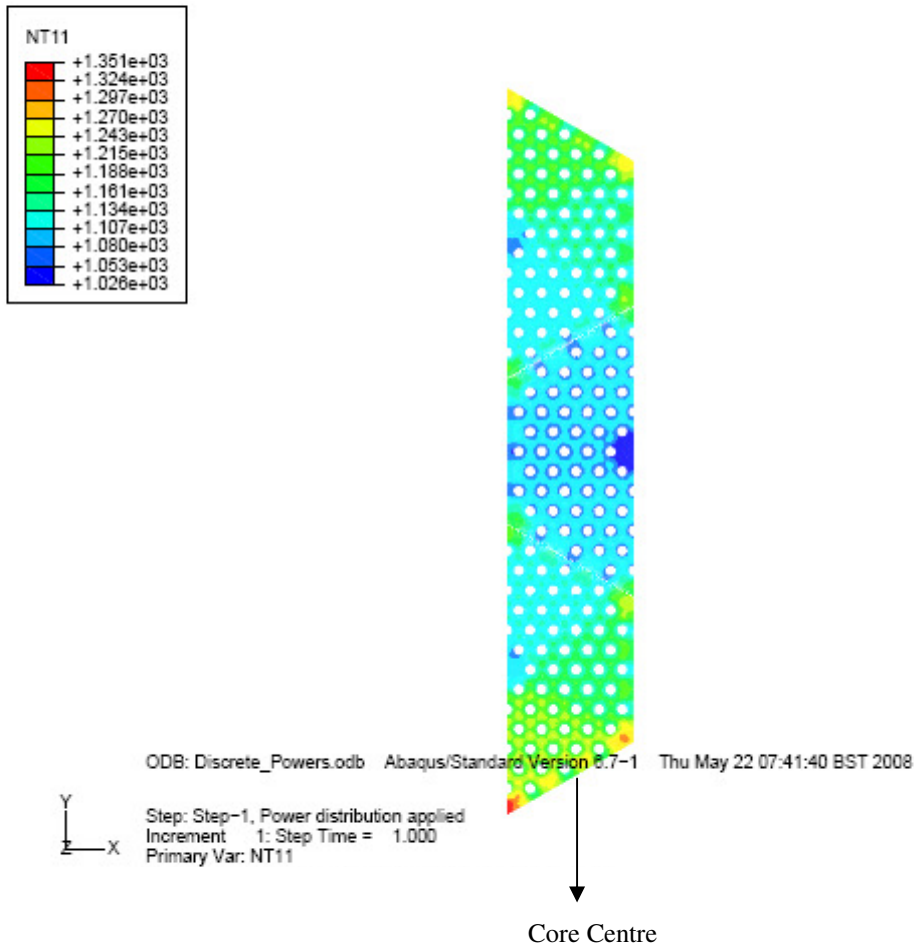
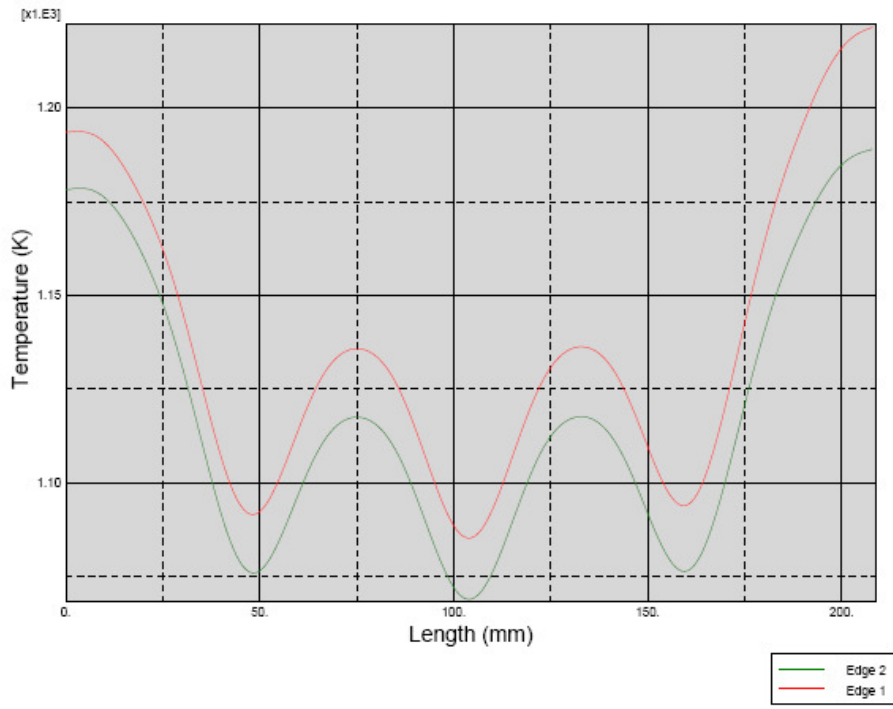


Figure 7.2.16: Combined model Variant 2 temperature profiles along the edges of the gaps

Gap edges closest to centre of core



Gap edges furthest from centre of core

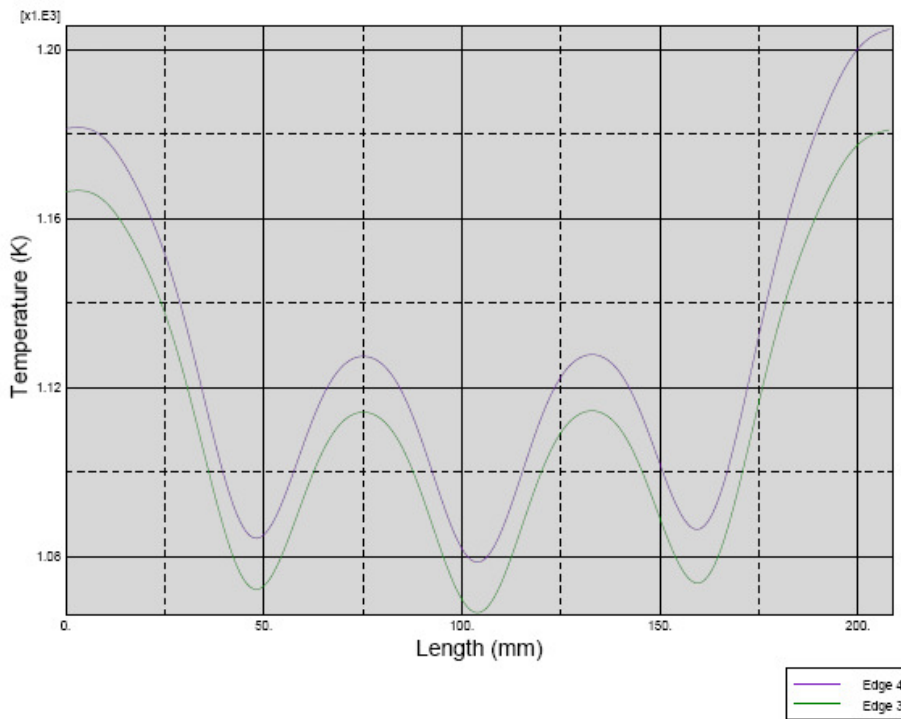
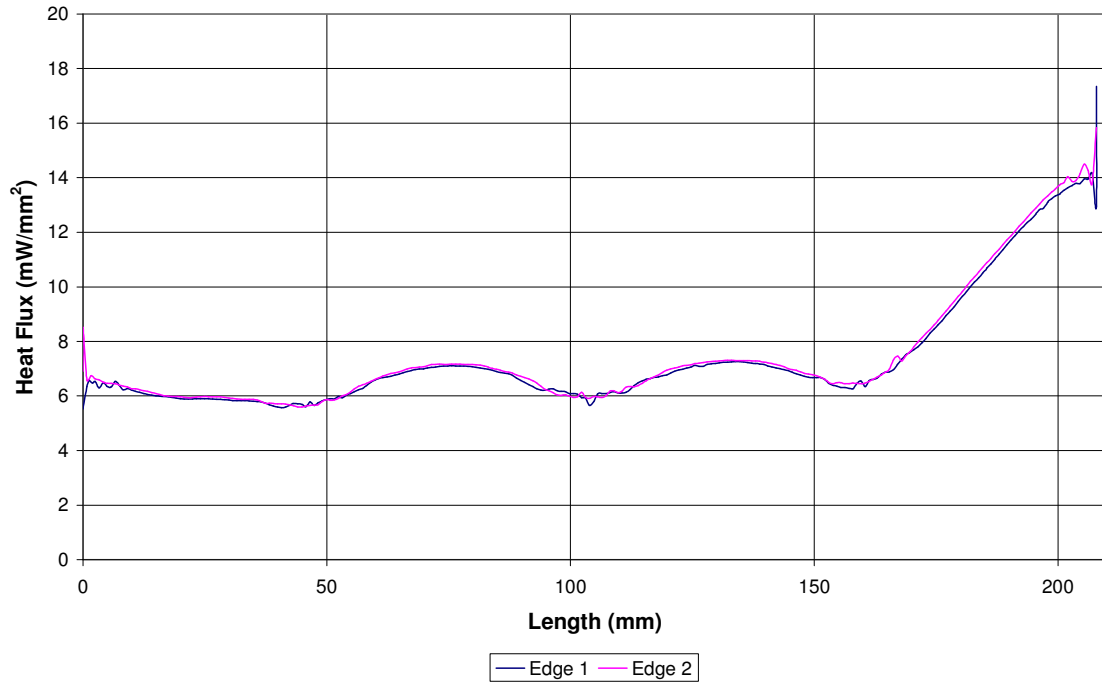
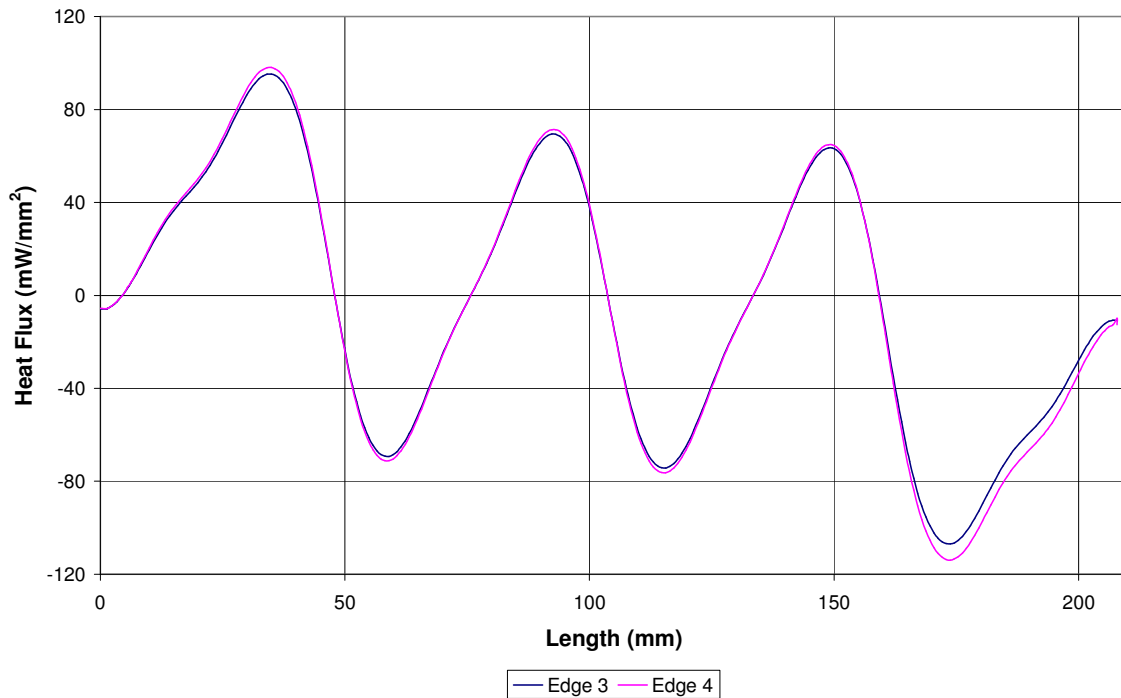


Figure 7.2.17: Combined model Variant 2 heat flux profiles along the edges of the gaps

Gap edges closest to centre of core



Gap edges furthest from centre of core



7.2.8.3 Combined model Variant 3 results

Variant 3 represents a shutdown reactor. The fuel power density is 0.5% of the power density distribution of Variant 1 and there is no heat transfer to the coolant.

The temperature distribution is shown in Figure 7.2.18 and temperature profiles along each edge are shown in Figure 7.2.19. The temperature distribution is much smoother than in normal operation and has a more linear gradient. The heat flux distribution is shown in Appendix B.1.

The heat flow across the gap edges has again been calculated by taking the integral of the heat flux normal to each edge and the results for mesh densities of 14635 and 47094 elements are shown in Table 7.2.6 (the edge numbering is shown in Figures 7.2.12 and 7.2.18). The heat flow across the farthest edge from the centre (that with the boundary condition of 873.15K applied) has also been calculated.

The heat flow across the gap closest to the centre of the core is approximately 3.2 kW/m and that across the gap further from the centre of the core is approximately 5.5 kW/m. The results for edges 1 and 2 and edges 3 and 4 should be equal. For both meshes the edge 1 and 2 results differ by <<0.1%. For a mesh of 14635 elements the edge 3 and 4 results differ by 0.7% and for a mesh of 47094 elements they differ by 0.5%.

The values calculated using the two mesh densities differ by less than 0.2% showing that the results are independent of the mesh.

Table 7.2.6: Results for the combined model Variant 3

No. of Elements	Edge No.*	Heat Flow (W/m)
14648	1	3147.7
	2	3164.0
	3	5534.7
	4	5534.8
	5	8314.4
47094	1	3142.8
	2	3164.9
	3	5536.6
	4	5536.3
	5	8319.5

* Edge 1 is closest to the centre of the core

The results for the gap heat flows can be demonstrated to be in agreement with the heat generated in each fuel block (Appendix B.1).

Figure 7.2.18: Combined model Variant 3 temperature distribution
Temperatures in Kelvin.

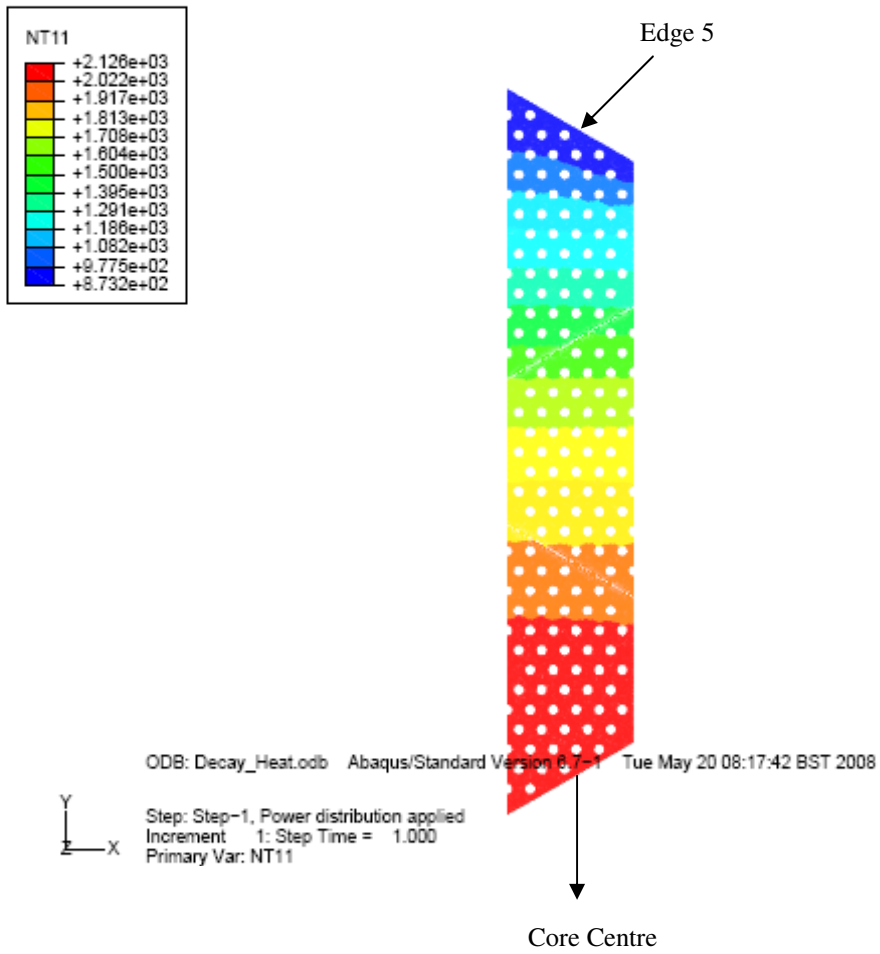
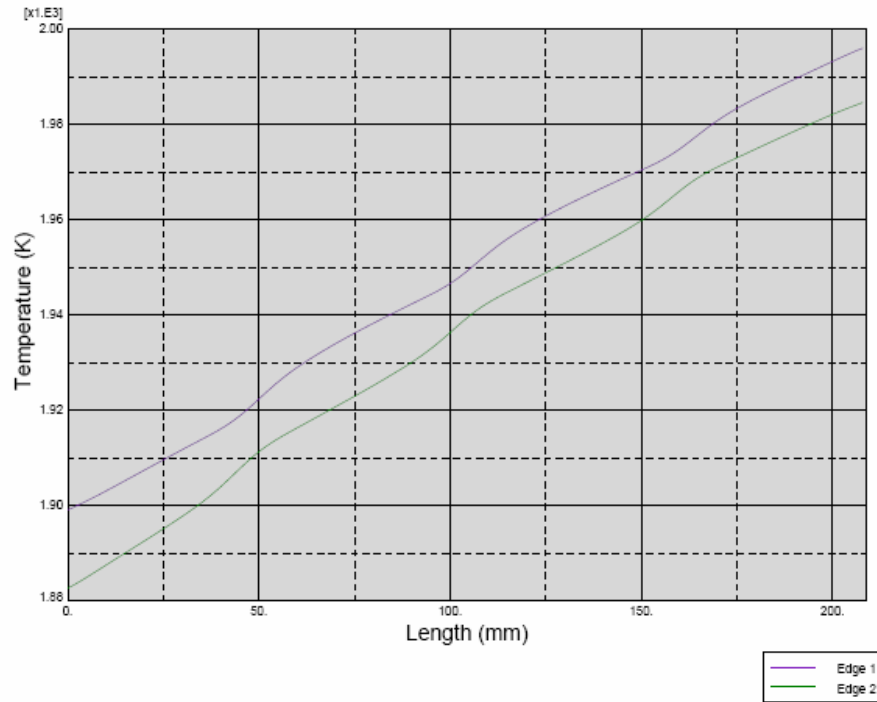
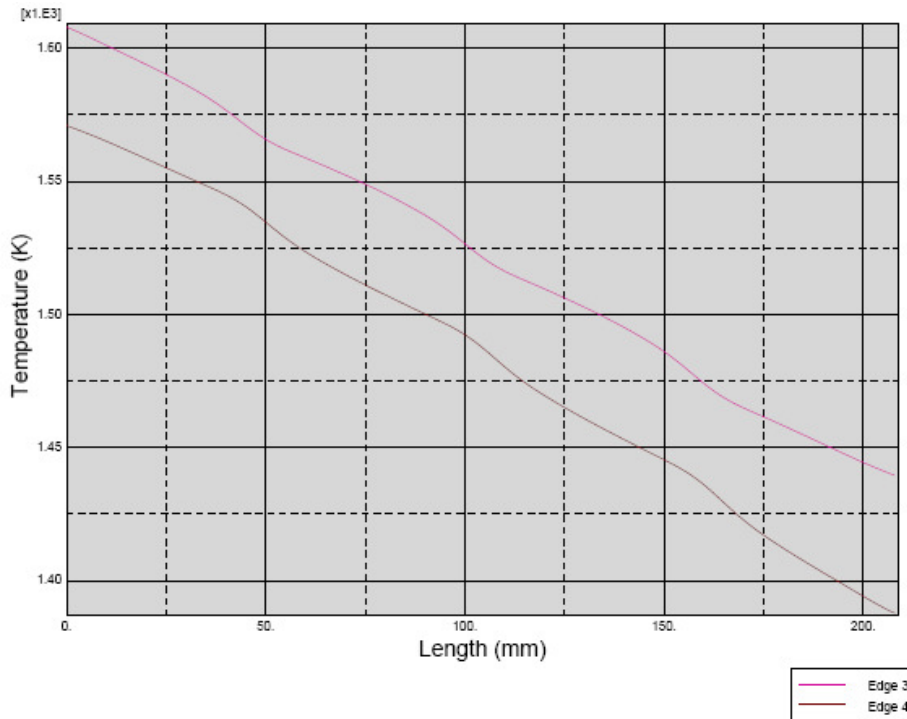


Figure 7.2.19: Combined model Variant 3 temperature profiles along the edges of the gaps

Gap edges closest to centre of core



Gap edges furthest from centre of core



7.3 Development of an Analytical Whole Core Conduction Model

The objective of this sub-section is to present the development of a model for whole core conduction and to compare this with a finite element solution of the previous sub-section.

The analytical approach has been developed in a closed analytical form for steady-state (i.e. non time-dependent) behavior. It uses steady-state analytical solutions for the supermeso- and meso-scale models to calculate heat flows and temperatures between a typical fuel compact and coolant channel, based on fuel compact power, coolant temperature and the heat conducted away on the macroscopic scale.

The macro-scale conduction model accounts for intra-block conduction through a single fuel block and for inter-block conduction across the gap between two separate fuel blocks. The supermeso and meso-scale solution for a typical fuel compact and coolant channel is assumed to apply at the centre of a macro-scale solution cell, which in the cases described here and in Section 7.2, corresponds to a triangular sector. An intra-block model is used to relate the sector centroid to boundary heat flow and the boundary temperature. The inter-block model accounts for both conduction and radiation across an inter-block gap, given the boundary temperatures of the sectors on either side of the gap.

The analytical models use a single fuel power for each sector; because of this, they will only be directly compared against the equivalent FE models from Section 7.2. The FE model Variants which used position-dependent fuel power densities within a single sector will be ignored (i.e. Variant 1 of the intra-block model and Variant 1 of the combined heat transfer model).

7.3.1 Model cases considered

7.3.1.1 Intra-block heat transfer

Variant 2

The first model consists of six triangular sectors arranged into a single complete fuel block (see Figure 7.3.1). There are no inter-block gaps but conduction around the six sectors was considered. A linear power gradient was applied across the assembly, with 1.5x nominal power density along the top face, decreasing to 0.5x nominal power density along the bottom face. This corresponds to a power of 4/3x nominal in the uppermost sector, 7/6x nominal in the two sectors beneath it, 5/6x nominal in the two sectors beneath those, and 2/3x nominal in the lower sector. Nominal power is a linear compact power of 4.100 kW/m, equivalent to a compact power density of 32.366 MW/m³. The coolant temperatures and flow rates are the same in all channels (943.15 K and 70 bar).

7.3.1.2 Inter-block heat transfer

The second model consists of two triangular sectors, separated by a block-to-block gap filled with stagnant helium (see Figure 7.3.1). Each sector is modeled with four temperatures: a mean graphite temperature representing the average temperature of all of the solid material in the sector; a mean coolant gas temperature; a mean coolant channel wall temperature; and a mean sector surface temperature.

This model has been used to find two solutions:

Variant 1

A step change in power between the two blocks: 1.5x the nominal power density in the first (a linear compact power of 6.150 kW/m, equivalent to a compact power density of 48.549 MW/m³) and 0.5x the nominal value in the second (a linear compact power of 2.050 kW/m, equivalent to a compact power density of 16.183 MW/m³). Thermal radiation and stagnant helium conduction were both included in modeling the inter-block gap. The coolant temperature and pressures were 943.15 K and 70 bar, respectively.

Variant 2

Using the nominal power density (a linear compact power of 4.100 kW/m, equivalent to a compact power density of 32.366 MW/m³) in both triangular sectors but with coolant temperatures of 943.15 K (670°C) in the first and 843.15 K (570°C) in the second. Coolant pressure is fixed at 70 bar.

7.3.1.3 Combined inter- and intra-block heat transfer

The third model is a line of nine triangular sectors and corresponds to the three half fuel blocks in a radial line of macro-scale model cells through one of the sides of the reactor core (see Figure 7.3.1).

Variant 2

The power densities and coolant temperatures have been interpreted from the available literature for a line of 3 fuel blocks through the active region of the reactor core. Nominal power densities and coolant temperatures used are shown in Table 7.3.1.

Table 7.3.1: Power densities and coolant temperatures used in combined Variant 2

Sector (numbering from centre of reactor)	Linear power in a compact \dot{q}'_f (W/m)	Power density in a compact \dot{q}'''_f (MW/m ³) ^[1]	Coolant temperature T_c (K)	Coolant pressure p_c (bar)
1	6958.36	54.9300	1070	70
2	5729.25	45.2272	1045	70
3	4915.44	38.8030	1020	70
4	4461.92	35.2228	1000	70
5	4313.66	34.0525	995	70
6	4415.64	34.8575	1000	70
7	4712.84	37.2036	1015	70
8	5150.23	40.6564	1040	70
9	5672.79	44.7816	1065	70

[1] these have been derived from a continuous cubic function describing a best-guess at the typical power profile. The function describes the power density \dot{q}'''_f (MW/m³) as a function of horizontal position (m) measured from the lower left corner of the innermost sector: $\dot{q}'''_f = -64.5x^3 + 192x^2 - 148x + 68$. The values used in the table above are the mean powers found by integrating the power profile over the triangular sector.

Variant 3

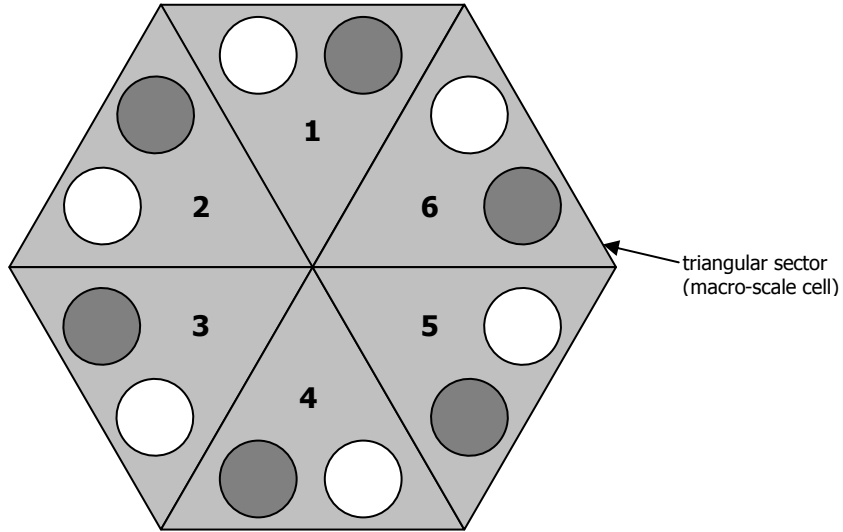
This model is designed to model a shutdown core cooled only by inter-block heat transfer. The powers are 0.5% of those in Variant 2, and heat removal by the coolant will be neglected. The coolant temperature will be set equal to the temperature of the graphite at the coolant channel wall, the pressure will remain at 70 bar.

Table 7.3.2: Power densities used in combined model Variant 3

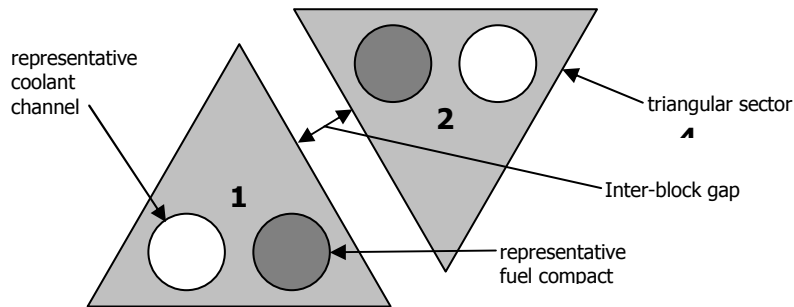
Sector (numbering from centre of reactor)	Linear power in a compact \dot{q}'_f (W/m)	Power density in a compact \dot{q}'''_f (MW/m ³)
1	34.7918	0.274650
2	28.6462	0.226136
3	24.5772	0.194015
4	22.3096	0.176114
5	21.5683	0.170262
6	22.0782	0.174288
7	23.5642	0.186018
8	25.7511	0.203282
9	28.3640	0.223908

Figure 7.3.1: Schematics of the inter-block, intra-block and combined cases to which the macroscopic analytical models are applied

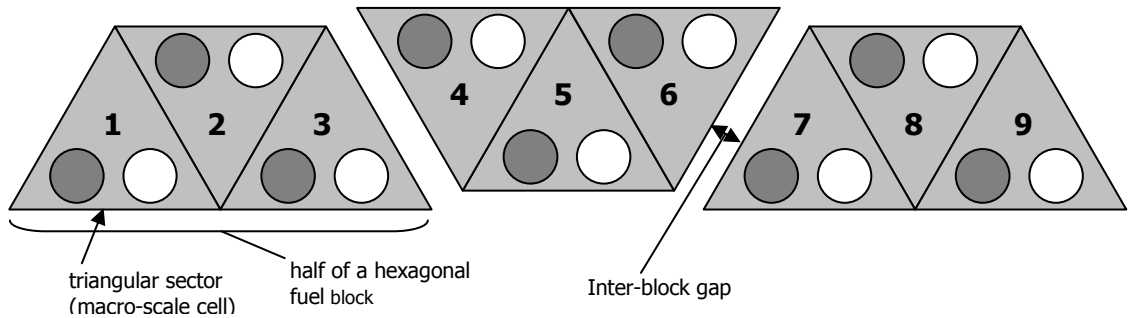
Intra-block



Inter-block



Combined



7.3.2 Construction of the analytical model

The super-meso and meso scale solutions were developed (see Section 5.3) to provide a simplified 1D solution to the temperature distribution within the fuel block in and around the coolant channels and fuel compacts. The solution is based on the supermeso model, which describes the temperature, $T_{SM}(r)$, as a function of the distance, r , from the centre of a coolant channel. The full solution is obtained by perturbing the super-meso temperature by the meso-scale solution, $\hat{T}_M(\hat{r})$ which adjusts the temperature to account for the presence of the fuel compacts. \hat{r} is the distance to the centre of the fuel compact.

For steady-state situations, the multi-scale solution can be presented in a closed analytical form. This is more convenient to implement in a network model than the numerical solution. Thus, this work uses the analytical form for convenience to demonstrate the macro-scale heat transfer models.

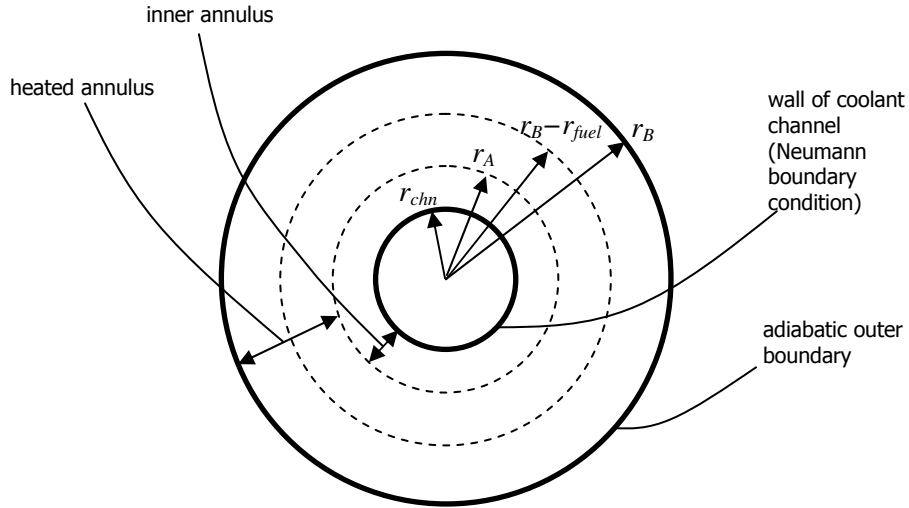
7.3.2.1 Super-meso-scale solution

Domain

The super-meso model is a 1-D model comprised of two annular regions (Figure 7.3.2). The first annulus, with an inner radius r_{chn} , corresponds to the boundary between the bulk graphite and the coolant channel. Heat is transferred to the coolant through the inner wall of this region. The second annulus, extending from radius r_A to r_B , is a region with a volumetric heat input and corresponds to the region in which heat is supplied from the fuel compacts. The outer boundary, at r_B , is adiabatic.

In deriving the steady-state analytical solution, the heated annulus must be further divided into two at a radius $r_B - r_{fuel}$ (where r_{fuel} is the radius of a fuel compact, taken here to be 6.35 mm) where the conductivity changes from that of pure graphite, to an effective conductivity based on the relative volumes of graphite and fuel compact which are smeared into the outer annulus.

Figure 7.3.2: The super-meso-scale model domain



The heated annuli receive a constant effective heat input of \dot{q}_{eff}''' . This is equal to the power input supplied by the equivalent of the two fuel compacts contained within the domain, corrected by a factor to account for the fact that the area of the domain is slightly larger than the hexagonal cell into which the heat from exactly two compacts would be supplied. The effective heat input is related to the linear power a fuel compact, \dot{q}'_f , by:

$$\dot{q}_{eff}''' = \frac{2\dot{q}'_f}{\pi(r_B^2 - r_A^2)}$$

r_B is equal to the distance between the centers of a coolant channel and a fuel compact (exactly 19 mm) and r_A is chosen to preserve the area of the small hexagonal unit cell associated with the coolant channel:

$$r_A = \left(\frac{r_B^2 \sqrt{3}}{2\pi} \right)^{\frac{1}{2}} \sim 9.9757 \text{ mm.}$$

A uniform heat sink, $-\dot{q}_{macro}'''$, is applied to all three annuli, to account for heat conducted away on the macroscopic scale.

Analytic solution

Appendix B.2.1 contains the details of the derivation.

The meso-scale solution, expressed in terms of the distance, r , from the centre of a coolant channel, is:

$$T_{SM}(r) = \begin{cases} \frac{1}{4k_g} r^2 \dot{q}_{macro}''' + \frac{A}{k_g} \ln(r) + B & (r_{chn} \leq r \leq r_A) \\ \frac{1}{4k_g} r^2 (\dot{q}_{macro}''' - \dot{q}_{eff}''') + \frac{C}{k_g} \ln(r) + D & (r_A \leq r \leq r_B - r_{fuel}) \\ \frac{1}{4k_{mix}} r^2 (\dot{q}_{macro}''' - \dot{q}_{eff}''') + \frac{E}{k_{mix}} \ln(r) + F & (r_B - r_{fuel} \leq r \leq r_B) \end{cases}$$

where k_g is the conductivity of pure graphite and k_{mix} is the effective conductivity of the mixture of plain graphite and fuel compacts.

The constants A to F are found from the boundary conditions, namely: continuity of temperature and heat flow at boundaries between the three regions at r_A and $r_B - r_{fuel}$, along with an adiabatic boundary at r_B , and a Neumann boundary condition on the coolant channel wall at r_{chn} . The last condition requires the heat flow into the coolant channel to match the expression relating the channel wall temperature (which is the sum of both super-meso- and meso-scale solutions) and coolant temperature:

$$k_g \left. \frac{\partial T_1}{\partial r} \right|_{r=r_{chn}} = h(T_{SM+M}(r_{chn}) - T_c).$$

The values of the constants are:

$$E = -\frac{1}{2} r_B^2 (\dot{q}_{macro}''' - \dot{q}_{eff}''')$$

$$C = E$$

$$A = E - \frac{1}{2} r_A^2 \dot{q}_{eff}'''$$

$$B = T_c - T_{offset} - \frac{1}{4k_g} r_{chn}^2 \dot{q}_{macro}''' + \frac{1}{2h} r_{chn} \dot{q}_{macro}''' + A \left(\frac{1}{hr_{chn}} - \frac{\ln(r_{chn})}{k_g} \right)$$

$$D = B - \frac{1}{2k_g} r_A^2 \dot{q}_{eff}''' \ln(r_A) + \frac{1}{4k_g} r_A^2 \dot{q}_{eff}'''$$

$$F = D + E \left(\frac{1}{k_g} - \frac{1}{k_{mix}} \right) \ln(r_B - r_{fuel}) + \frac{1}{4} \left(\frac{1}{k_g} - \frac{1}{k_{mix}} \right) (r_B - r_{fuel})^2 (\dot{q}_{macro}''' - \dot{q}_{eff}''')$$

If cooling by convective heat transfer to the coolant gas is removed then the inner boundary becomes adiabatic and the heat removed by long-range conduction must equal the heat input:

$$\dot{q}_{macro}''' = \dot{q}_{eff}''' \frac{(r_B^2 - r_A^2)}{(r_B^2 - r_{chn}^2)}.$$

With this definition of the macro-scale heat removal, the same system of solutions and constants A to F can be used to calculate the solution, requiring only an arbitrary, non-zero value of the convective heat transfer coefficient, h (refer to Appendix B.2.1).

7.3.2.2 Meso-scale solution

Domain

The meso-scale model perturbs the supermeso-scale temperatures due to the presence of the fuel compact. The perturbation is energy-preserving over its own domain, i.e. that the total internal energy (heat capacity x temperature) over the meso-scale model is zero.

The model domain (Figure 7.3.3) is centred on a fuel compact (distances are measured in terms of \hat{r} , the distance from the centre of the fuel compact, rather than r , which is the distance from the centre of the coolant channel as used in the supermeso-scale model). The first region is circular, of radius r_{fuel} and corresponds to the fuel compact. This region has a constant heat input of \dot{q}_{comp}''' from the fuel. The second region is an annulus extending to r_D . This contains a constant heat sink of \dot{q}_{sink}''' . The whole domain is adiabatic, and so:

$$\pi(r_D^2 - r_{fuel}^2)\dot{q}_{sink}''' = \pi r_{fuel}^2 \dot{q}_{comp}'''.$$

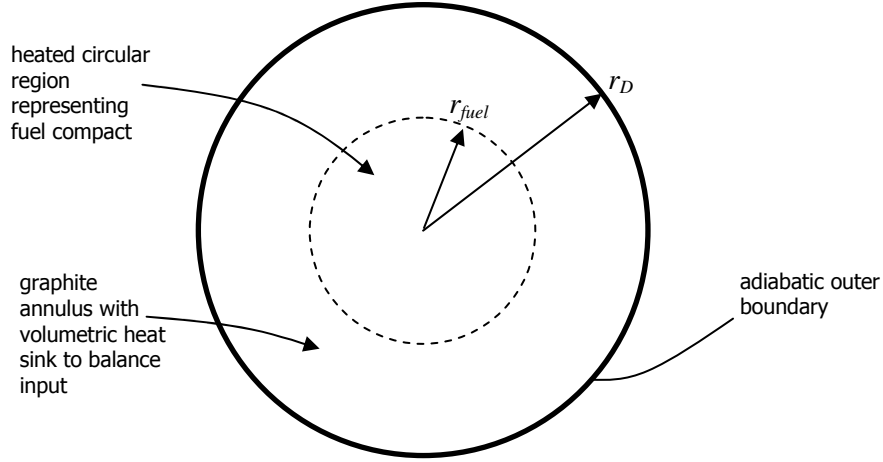
The total heat removal is equal to the heat input from a single compact, averaged over the domain:

$$\dot{q}_{sink}''' = \frac{\dot{q}'_f}{\pi r_D^2},$$

and so the heat input is:

$$\dot{q}_{comp}''' = \frac{(r_D^2 - r_{fuel}^2)}{r_{fuel}^2} \dot{q}_{sink}'''.$$

Figure 7.3.3: The meso-scale model domain



Analytic solution

Appendix B.2.2 contains the details of the derivation.

The meso scale solution, expressed in terms of the distance, \hat{r} , from the centre of a fuel compact, is:

$$T_M(\hat{r}) = \begin{cases} -\frac{1}{4k_f} \hat{r}^2 \dot{q}_{comp}''' + X & (\hat{r} \leq r_{fuel}) \\ \frac{1}{4k_g} \hat{r}^2 \dot{q}_{sink}''' + \frac{Y}{k_g} \ln(\hat{r}) + Z & (r_{fuel} \leq \hat{r} \leq r_D) \end{cases}$$

where k_f is the conductivity of the fuel compact, k_g is the graphite conductivity and X , Y and Z are found from the boundary conditions, namely: continuity of temperature and heat flow at boundary between the two regions at r_{fuel} . The outer boundary is defined to be adiabatic and a final condition comes from the requirement for the total internal energy associated with the meso-scale solution to be zero over its own domain:

$$\begin{aligned} \iint \rho c_p \hat{T}_M dA &= 0, \\ \Rightarrow &\left[\rho_{fuel} c_{p,fuel} \int_{\hat{r}=0}^{\hat{r}=r_{fuel}} \left(-\frac{1}{4k_f} \hat{r}^3 \dot{q}_{comp}''' + X\hat{r} \right) dr \right] \\ &+ \left[\rho_g c_{p,g} \int_{\hat{r}=r_{fuel}}^{\hat{r}=r_D} \left(\frac{1}{4k_g} \hat{r}^3 \dot{q}_{sink}''' + \frac{Y}{k_g} \hat{r} \ln(\hat{r}) + Z\hat{r} \right) dr \right] = 0 \end{aligned}$$

where ρ_{fuel} , ρ_g , $c_{p,fuel}$ and $c_{p,g}$ are the mass density and specific heat capacities of the fuel and graphite.

The values of the three constants are:

$$Y = -\frac{1}{2}r_D^2\dot{q}_{sink}'''$$

$$Z = Z_f + Z_g$$

$$X = Z + \frac{1}{4k_f}r_{fuel}\dot{q}_{comp}''' + \frac{1}{4k_g}r_{fuel}^2\dot{q}_{sink}''' - \frac{1}{2k_g}r_D^2\dot{q}_{sink}''' \ln(r_{fuel})$$

where,

$$Z_f = \frac{\rho_{fuel}c_{p,fuel} \left[\frac{1}{8k_f}r_{fuel}^4\dot{q}_{comp}''' + \frac{1}{4k_g}r_{fuel}^4\dot{q}_{sink}''' + \frac{Y}{k_g}r_{fuel}^2 \ln(r_{fuel}) \right]}{-\rho_{fuel}c_{p,fuel}r_{fuel}^2 - \rho_g c_{p,g}(r_D^2 - r_{fuel}^2)}$$

$$Z_g = \frac{\rho_g c_{p,g} \left[\frac{1}{8k_g}(r_D^4 - r_{fuel}^4)\dot{q}_{sink}''' + \frac{Y}{k_g}(r_D^2[\ln(r_D) - \frac{1}{2}] - r_{fuel}^2[\ln(r_{fuel}) - \frac{1}{2}]) \right]}{-\rho_{fuel}c_{p,fuel}r_{fuel}^2 - \rho_g c_{p,g}(r_D^2 - r_{fuel}^2)}$$

Beyond the outer boundary

The value of r_D used in these calculations is the same as the r_A in the supermeso-scale model, and is chosen to preserve the volume in the hexagonal unit cell around the fuel compact (which is equal to the volume in an equivalent hexagonal unit cell centred on a coolant channel):

$$r_D = r_A = \left(\frac{r_B^2 \sqrt{3}}{2\pi} \right).$$

The meso-scale solution finishes at the edge of its domain at $\hat{r} = r_D$, however, within the real hexagonal geometry there are regions of graphite which are more than r_D away from a fuel compact. The meso-scale perturbation at $\hat{r} > r_D$, is simply defined as the value it takes on $\hat{r} = r_D$:

$$T_{offset} = \hat{T}_M(r_D) = \frac{1}{4k_g}r_D^2\dot{q}_{sink}''' + \frac{Y}{k_g}\ln(r_D) + Z.$$

In practice, only a very small area of graphite in the real geometry exists beyond $\hat{r} = r_D$ and this adjustment has very little impact on any solution.

7.3.2.3 Calculating the mean solid temperature

The mean temperature should clearly be a volume- and heat capacity-weighted average of the temperature, but the region over which the temperature should be averaged is not at all clear since the super-meso and meso solutions are defined over different domains.

The meso-scale correction is small (a few degrees) in comparison to the typical super-meso-scale temperatures. The meso-scale correction is also designed to correspond to a net internal energy of zero, over its own domain at least. It is therefore argued that the simplest definition of a mean graphite temperature should be the volume- and heat-capacity-weighted average of just the super-meso temperature solution, evaluated over its own annular domain.

Numerical integration of the complete (super-meso plus meso) solution, evaluated over the "true" geometry, yields an average temperature within a few degrees of the super-meso temperature averaged over its own domain.

The mean solid temperature, T_g , can be shown to be (see Appendix B.2.3 for details):

$$T_g = \frac{x_1 + x_2 + x_3}{2\rho_u c_{p,u}(r_A^2 - r_{chn}^2) + 2\rho_h c_{p,h}(r_B^2 - r_A^2)},$$

where the terms in the numerator are:

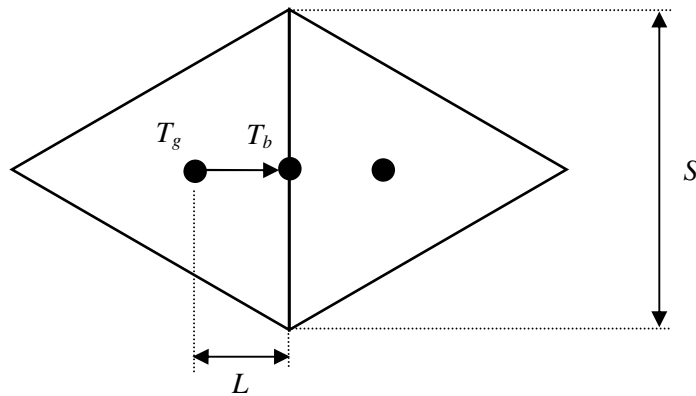
$$\begin{aligned} x_1 &= \frac{1}{4k_g} \rho_u c_{p,u} \dot{q}_{macro}''' (r_A^4 - r_{chn}^4) + \frac{1}{4k_g} \rho_h c_{p,h} (\dot{q}_{macro}''' - \dot{q}_{eff}''') (r_B - r_{fuel})^4 - r_A^4 \\ &\quad + \frac{1}{4k_{mix}} \rho_h c_{p,h} (\dot{q}_{macro}''' - \dot{q}_{eff}''') (r_B^4 - [r_B - r_{fuel}]^4) \\ x_2 &= \frac{2A}{k_g} \rho_u c_{p,u} \left(r_A^2 \left[\ln(r_A) - \frac{1}{2} \right] - r_{chn}^2 \left[\ln(r_{chn}) - \frac{1}{2} \right] \right) \\ &\quad + \frac{2C}{k_g} \rho_h c_{p,h} \left((r_B - r_{fuel})^2 \left[\ln(r_B - r_{fuel}) - \frac{1}{2} \right] - r_A^2 \left[\ln(r_A) - \frac{1}{2} \right] \right) \\ &\quad + \frac{2E}{k_{mix}} \rho_h c_{p,h} \left(r_B^2 \left[\ln(r_B) - \frac{1}{2} \right] - (r_B - r_{fuel})^2 \left[\ln(r_B - r_{fuel}) - \frac{1}{2} \right] \right) \\ x_3 &= 2B\rho_u c_{p,u} (r_A^2 - r_{chn}^2) + 2D\rho_h c_{p,h} ([r_B - r_{fuel}]^2 - r_A^2) + 2F\rho_h c_{p,h} (r_B^2 - [r_B - r_{fuel}]^2). \end{aligned}$$

where ρ_u , ρ_h , $c_{p,u}$ and $c_{p,h}$ are the effective mass density and specific heat capacities of the unheated and heated annuli.

7.3.2.4 Calculating the Sector Boundary Temperature

The mean graphite temperature, T_g corresponds to the macro-scale temperature of the triangular sector. On this macro-scale, heat transfer from one sector to another takes place from the centre of one sector to the centre of its neighbor (Figure 7.3.4). Expressions relating the temperature on the boundary of the sector, T_b , to the mean graphite temperature, T_g , which is taken to be the temperature at the centroid of the sector, will be presented for three distinct cases. For details of the derivations, refer to Appendix B.2.4.

Figure 7.3.4: Sector centroid and boundary temperatures and distances



Assuming a point heat source at the centre of the sector

In this case, the temperature on the boundary of the sector, T_b , is related to the mean graphite temperature at the centroid of the sector, T_g , via:

$$\dot{q}'_b = f \cdot \frac{k_{hex} S}{L} \cdot (T_g - T_b) = f \cdot (2\sqrt{3}) k_{hex} \cdot (T_g - T_b),$$

where \dot{q}'_b is the macro-scale heat flow from the centre of the sector to the boundary, k_{hex} is the effective conductivity of the sector (a smeared region of graphite, coolant channels and fuel compacts), S is the length of the side of the sector (equal to $d_{hex}/\sqrt{3}$, where d_{hex} is the across-flats size of the complete hexagonal fuel block) and L is the distance from the centroid of the sector to the boundary (equal to $d_{hex}/6$). f is a dimensionless "enhancement" factor. $f = 1$ in this case.

Assuming a distributed 1-D heat source

In this case, the temperature on the boundary of the sector, T_b , is related to the mean graphite temperature at the centroid of the sector, T_g , via:

$$\dot{q}'_b = 2 \cdot (2\sqrt{3})k_{hex} \cdot (T_g - T_b).$$

Which is the same form as the expression derived assuming a point heat source, with an enhancement factor of $f = 2$.

Note that this derivation assumes that the $x = 0$ boundary, at the centroid of the sector, is adiabatic. If the heat transfer in the core is dominated by macroscopic inter-block conduction then this condition breaks-down. In this case, the enhancement factor reduces to $f = 1$.

Assuming a distributed 1-D Heat source and the effects of coolant channels

In this case, the temperature on the boundary of the sector, T_b , is related to the mean graphite temperature at the centroid of the sector, T_g , via:

$$\dot{q}'_b = (\alpha k_{hex})^{\frac{1}{2}} \left(\frac{d_{hex}}{\sqrt{3}} \right) \left(\frac{\sinh \left[\left(\frac{\alpha}{k_{hex}} \right)^{\frac{1}{2}} \left(\frac{d_{hex}}{6} \right) \right]}{\cosh \left[\left(\frac{\alpha}{k_{hex}} \right)^{\frac{1}{2}} \left(\frac{d_{hex}}{6} \right) \right] - 1} \right) (T_g - T_b).$$

i.e.:

$$\dot{q}'_b = \left(\frac{\theta \sinh \theta}{\cosh \theta - 1} \right) \cdot (2\sqrt{3})k_{hex} \cdot (T_g - T_b) \quad \text{where } \theta = \left(\frac{\alpha}{k_{hex}} \right)^{\frac{1}{2}} \left(\frac{d_{hex}}{6} \right).$$

Which is the same form as the expression derived assuming a point heat source, with an enhancement factor of

$$f = \frac{\theta \sinh \theta}{\cosh \theta - 1},$$

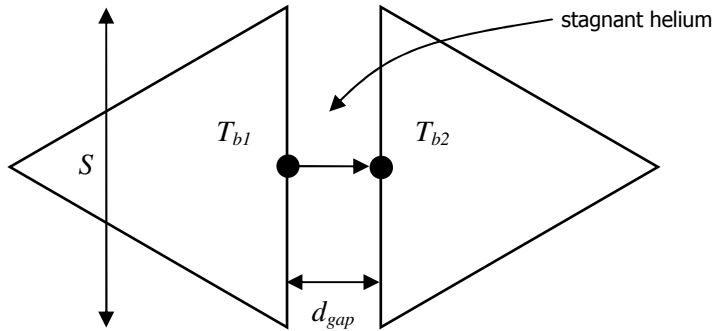
In the limit of poor cooling or high block conductivity the enhancement factor tends to $f \rightarrow 2$, recovering the expected result for distributed heat but with no cooling.

In the limit of very good cooling or low block conductivity, the enhancement factor tends to $f \rightarrow \theta$.

7.3.2.5 Calculating heat transfer across an inter-block gap

Two modes of heat transfer across an inter-block gap are considered. Space has been left in the models to implement convection at a later date if required.

Figure 7.3.5: Inter-block gap heat flow and temperatures



Conduction

The conducted heat flow over the gap is:

$$\dot{q}'_{cond12} = \frac{k_{gap}S}{d_{gap}}(T_{b1} - T_{b2}) = \frac{k_{gap}d_{hex}}{d_{gap}\sqrt{3}}(T_{b1} - T_{b2}),$$

where S is the length of the side of the sector (equal to $d_{hex}/\sqrt{3}$, where d_{hex} is the across-flats size of the complete hexagonal fuel block, $d_{hex} = 0.36$ m for the prismatic HTGR), d_{gap} is the inter-block gap ($d_{gap} = 2$ mm has been assumed in this work) and T_{b1} and T_{b2} are the boundary temperatures of the first and second sectors respectively. The helium conductivity is drawn from the empirical relationship given in the KTA rules (Reference 7.2).

Radiation

Heat can also be radiated directly across the gap. The heat flux between two closely-spaced, flat, parallel surfaces is:

$$\dot{q}''_{rad12} = \left(\frac{\varepsilon}{2 - \varepsilon} \right) \sigma (T_{b1}^4 - T_{b2}^4),$$

where ε is the emissivity of the surfaces ($\varepsilon = 0.8$ for the prismatic Very High Temperature Reactor, VHTR, blocks), σ is the Stefan-Boltzmann constant (5.67051×10^{-8} W/m²/K⁴) and T_{b1} and T_{b2} are the surface temperatures.

Re-writing the expression in terms of the heat flux per unit axial height for between two triangular sectors with a boundary length of $d_{hex}/\sqrt{3}$:

$$\dot{q}'_{rad12} = \frac{d_{hex}}{\sqrt{3}} \left(\frac{\varepsilon}{2 - \varepsilon} \right) \sigma (T_{b1}^4 - T_{b2}^4).$$

7.3.3 Test case models

This section describes how, for each of the test case models (as described in Section 7.3.1), the analytical approach has been applied, the analytical model results and the comparison with equivalent finite element calculation (from Section 7.2). Appendix B.2.5 contains a list of the global parameters relevant to the analytical models.

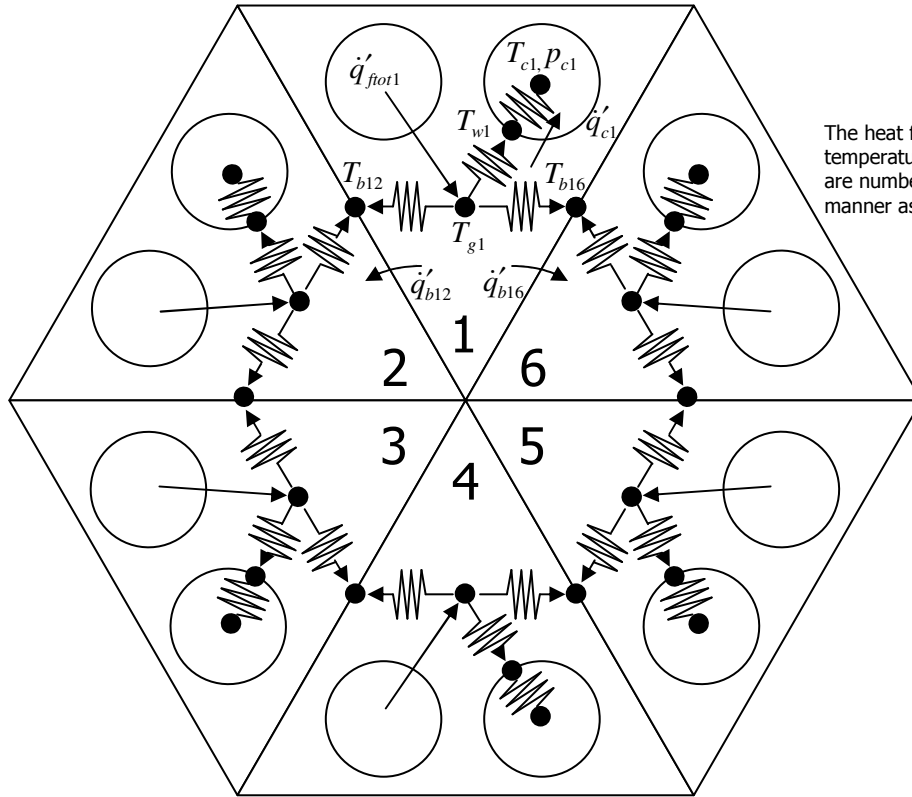
7.3.3.1 Intra-block heat transfer (six triangular sectors forming a fuel block)

Modeling

As for the first model, the situation has been constructed in a spreadsheet with input power, coolant temperature and coolant pressure defined for each of the six sectors.

In sector 1, the macroscopic heat conduction into sector 2, \dot{q}'_{b12} is left as a free parameter (see Figure 7.3.6). In sector 2, the heat transfer to sector 1 is therefore $\dot{q}'_{b21} = -\dot{q}'_{b12}$, but the heat transfer into sector 3, \dot{q}'_{b23} , is a free parameter, etc. A converged solution to the problem is found by solving for the 6 heat transfer values ($\dot{q}'_{b12}, \dot{q}'_{b23}, \dot{q}'_{b34}, \dot{q}'_{b45}, \dot{q}'_{b56}, \dot{q}'_{b61}$) required so that the temperature on the boundary of sector 1 next to sector 2, T_{b12} , is equal to the temperature on the boundary of sector 2 next to sector 1, T_{b21} and so on. A visual basic macro is used to iterate to a solution.

Figure 7.3.6: Inter-block gap heat flow and temperatures



The macro identifies the boundary with the largest temperature difference and then uses a Newton-Raphson method to revise the estimate of the heat flux over the boundary and reduce the temperature discrepancy. For a boundary with a heat flow $\dot{q}'_{b,j}$ and a temperature difference of ΔT_b , then the Newton-Raphson method would predict the updated value of the heat flow, $\dot{q}'_{b,j+1}$, required to find zero ΔT_b to be:

$$\dot{q}'_{b,j+1} = \dot{q}'_{b,j} + f\Delta T_{b,j}(\dot{q}'_{b,j}) \left(\frac{\delta}{\Delta T_{b,j}(\dot{q}'_{b,j}) - \Delta T_{b,j}(\dot{q}'_{b,j} + \delta)} \right).$$

Where a parameter, $0 < f < 1$, is used to slow the speed of the convergence. The accuracy of the solution can be controlled through the tolerance, τ , with the spreadsheet deeming the solution converged when:

$$\left| \frac{\Delta T_{b,j}}{T_{b,j}} \right| \leq \tau$$

for all of the boundaries in contact.

Results

The analytical model results are given in Table 7.3.3. The problem is symmetric about a vertical plane passing through the centre of sector 1 and sector 4. Sector 6 has identical results to sector 2, and sector 5 has identical results to sector 3.

The directions of heat flow and the boundary descriptions used in the Table are with reference to Figure 7.3.6. E.g., for sector 1, the "sector below" is sector 2, for sector 3 the "upper boundary" is the interface with sector 2 and the "lower boundary" is the interface with sector 4.

Table 7.3.3: Results for intra-block Variant 2

Parameter	Sector 1	Sector 2/6	Sector 3/5	Sector 4	Units
heat input per fuel compact	5.467 (4/3 nom)	4.783 (7/6 nom)	3.417 (5/6 nom)	2.733 (2/3 nom)	kW/m
fuel compact power density	43.154	37.760	26.972	21.577	MW/m ³
heat input from all fuel compacts	196.800	172.200	123.000	98.400	kW/m
heat flow into coolant	193.172	170.384	124.814	102.032	kW/m
heat conducted into sector below	1.814	3.630	1.816	0	kW/m
centroid to boundary total conductivity	269.60	269.67	269.87	270.03	W/m/K
maximum fuel compact temperature	1079.5	1063.3	1030.8	1014.6	K
mean graphite temperature	1056.8	1043.3	1016.4	1002.9	K
coolant channel wall temperature	1024.8	1015.2	995.9	986.3	K
coolant gas temperature	943.15	943.15	943.15	943.15	K
sector upper boundary temperature	n/a	1050.0	1029.8	1009.7	K
sector lower boundary temperature	1050.0	1029.8	1009.7	n/a	K

The total heat flow through the horizontal plane of the model is twice the sector 2 to sector 3 conduction and is 7.259 kW/m.

Comparison with FE calculations

The following data (Table 7.3.4) are taken from finite element model calculations (Section 7.2). "Typical" peak fuel and coolant channel wall temperatures were taken by hand from typical locations within the sector away from edge effects.

Table 7.3.4: Intra-block Variant 2 – comparison of FE and analytical models

Parameter		Sector 1	Sector 2/6	Sector 3/5	Sector 4	Units
typical peak fuel compact temperature	Analytical	1079.5	1063.3	1030.8	1014.6	K
	FE	1077	1061	1028	1010	
typical coolant channel wall temperature	Analytical	1024.8	1015.2	995.9	986.3	K
	FE	1040	1024	1005	990	

The maximum fuel compact temperatures agree within ~5 K. The analytical models predicts coolant channel wall temperatures which are cooler than the FE model by ~15 K in sector 1, decreasing to ~4 K in sector 4.

The FE calculation predicts a heat flux across the horizontal plane of ~6.7 to 6.9 kW/m (the value reported by ABAQUS shows some slight dependency on the meshing used). This is within ~0.35 to 0.55 kW/m (~5 to 8%) of the analytical value of 7.259 kW/m. Again, it is noted that the sector-to-sector heat flow is only a few percent of the heat removed by the coolant.

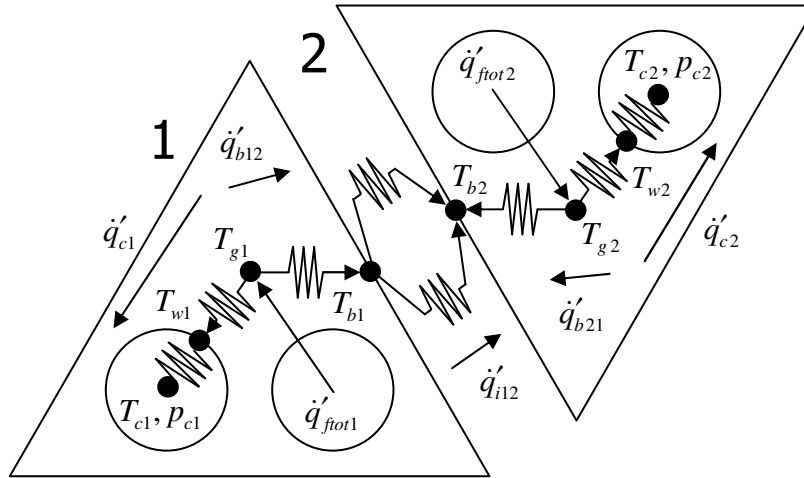
7.3.3.2 Inter-block heat transfer (two triangular sectors with a gap)

Model

The model has been created in an Excel spreadsheet and is shown in Figure 7.3.7. The linear compact power (\dot{q}'_f), coolant temperature (T_c) and pressure (p_c) are defined for each of the two sectors. An initial guess is entered for the block-to-block heat flow (this is entered as the centroid to boundary heat flow for the first sector, \dot{q}'_{b12} , and the negative of this is automatically used for the centroid to boundary flow in the second sector, $\dot{q}'_{b21} = -\dot{q}'_{b12}$). The temperatures and heat flows within each block are calculated by the spreadsheet using the models described in Section 7.3.2. With the calculated sector boundary temperatures, the inter-block heat flow can be calculated, \dot{q}'_{i12} . If the solution is self-consistent then

$$\dot{q}'_{i12} = \dot{q}'_{b12} (= -\dot{q}'_{b21}).$$

Figure 7.3.7: Inter-block gap heat flow and temperatures



A self-consistent solution is found using a very simple iterative scheme, which is coded into a visual basic macro. Given a value of the heat transfer from block 1, $\dot{q}'_{b12,j}$, the spreadsheet then calculates the corresponding inter-block heat flow $\dot{q}'_{i12,j}$. The macro makes a revised guess for the next iteration:

$$\dot{q}'_{b12,j+1} = f \dot{q}'_{i12,j},$$

where $0 < f < 1$ is a parameter which controls the speed of the convergence. The accuracy of the solution can be controlled through the tolerance, τ , with the spreadsheet deeming the solution converged when:

$$\left| \frac{\dot{q}'_{i12,j} - \dot{q}'_{b12,j}}{\dot{q}'_{i12,j}} \right| \leq \tau$$

A value of $f = 0.1$ was found to work given a starting guess of $\dot{q}'_{b12,j=0} = 0$ for the iterations.

Results

The analytical model results for the two Variants are given in Tables 7.3.5 and 7.3.6.

Table 7.3.5: Results for inter-block Variant 1

Parameter	Sector 1	Sector 2	Units
heat input per fuel compact	6.150 (1.5x nominal)	2.050 (0.5x nominal)	kW/m
fuel compact power density	48.549	16.183	MW/m ³
heat input from all fuel compacts	221.400	73.800	kW/m
heat flow into coolant	217.573	77.627	kW/m
heat radiated over 1-2 inter-block gap	1.860		kW/m
heat conducted over 1-2 inter-block gap	1.968		kW/m
total heat transferred to other sector	3.827		kW/m
1-2 inter-block gap conductivity	0.34971		W/m/K
centroid to boundary total conductivity	269.61	270.14	W/m/K
maximum fuel compact temperature	1096.7	997.4	K
mean graphite temperature	1071.1	988.6	K
coolant channel wall temperature	1035.1	976.0	K
coolant gas temperature	943.15	943.15	K
sector boundary temperature	1056.9	1002.8	K

Table 7.3.6: Results for inter-block Variant 2

Parameter	Sector 1	Sector 2	Units
heat input per fuel compact	4.100	4.100	kW/m
fuel compact power density	32.366	32.366	MW/m ³
heat input from all fuel compacts	147.600	147.600	kW/m
heat flow into coolant	143.433	151.767	kW/m
heat radiated over 1-2 inter-block gap	1.910		kW/m
heat conducted over 1-2 inter-block gap	2.257		kW/m
total heat transferred to other sector	4.167		kW/m
1-2 inter-block gap conductivity	0.33663		W/m/K
centroid to boundary total conductivity	269.52	269.97	W/m/K
maximum fuel compact temperature	1044.5	949.5	K
mean graphite temperature	1027.6	932.1	K
coolant channel wall temperature	1003.8	907.3	K
coolant gas temperature	943.15	843.15	K
sector boundary temperature	1012.1	947.6	K

Comparison with FE calculations

The following data (Table 7.3.7) are taken from finite element model calculations (Section 7.2). "Typical" peak fuel and coolant channel wall temperatures were taken by hand from typical locations within the sector away from edge effects.

Table 7.3.7: Inter-block Variant 1 – comparison of FE and analytical models

Parameter		Sector 1	Sector 2	Units
total heat transferred to other sector	Analytical	3.827	-3.827	kW/m
	FE	4.070	-4.070	
typical peak fuel compact temperature	Analytical	1096.7	997.4	K
	FE	1097	994	
typical coolant channel wall temperature	Analytical	1035.1	976.0	K
	FE	1036	974	
average sector boundary temperature	Analytical	1056.9	1002.8	K
	FE	1071.2	1015.4	

The maximum fuel compact and coolant channel wall temperatures compare well with the analytical results, agreeing within ~3 K. The temperature difference across the gap agree within 2 K and the sector 1 to sector 2 heat flows agree to within ~0.2 kW/m (~6%). The absolute boundary temperatures are, however, much warmer in the FE model, which finds average values which are ~12-14 K higher than the analytical values. This discrepancy is likely to be due to the effect of the hot spots in the corners of the sector (see Section 7.2.6.1) pushing the average up.

Table 7.3.8: Inter-block Variant 2 – comparison of FE and analytical models

Parameter		Sector 1	Sector 2	Units
total heat transferred to other sector	Analytical	4.167	-4.167	kW/m
	FE	3.988 ^[*]	-4.029 ^[*]	
typical peak fuel compact temperature	Analytical	1044.5	949.5	K
	FE	1045	945	
typical coolant channel wall temperature	Analytical	1003.8	907.3	K
	FE	1005	905	
average sector boundary temperature	Analytical	1012.1	947.6	K
	FE	1022.5	962.7	

* these would sum to zero in a perfectly converged model

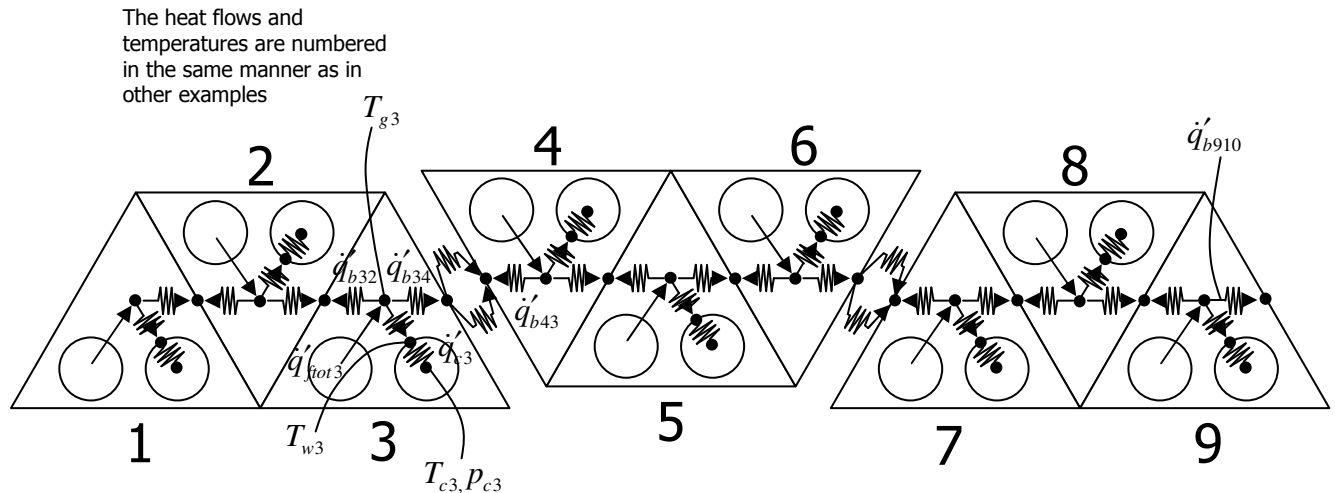
For the 2nd Variant, Table 7.3.8 shows that the agreement between fuel and wall temperatures is again good – within ~ 5 K. The gap temperature differences agree to within ~ 5 K and the inter-block heat fluxes agree within ~ 0.2 kW/m ($\sim 5\%$). The absolute boundary temperatures are again ~ 10 - 15 K higher in the FE model.

In general, the agreement in temperatures and heat fluxes is very encouraging. The error in the inter-block heat fluxes, ~ 0.2 kW/m in both cases, is only a small fraction ($\sim 5\%$) of the total inter-block flux of ~ 4 kW/m, which itself is only a small fraction ($\sim 3\%$) of the power supplied by the fuel (147.6 kW/m in a nominal power block) since most of the heat is transferred straight from a fuel compact into its neighboring coolant channels.

7.3.3.3 Combined heat transfer (line of nine triangular sectors in three blocks)

Modeling

Figure 7.3.8: Inter-block gap heat flow and temperatures



As for the other models, the situation has been constructed in a spreadsheet with input power, coolant temperature and coolant pressure defined for each of the nine sectors. The model is shown in Figure 7.3.8. In each sector the heat transfer to the sector to the right is a free parameter. The heat transfers to the sector to the left are again defined to be equal to the negative of the right-wards heat flow from the adjacent sector. E.g., the heat transferred right-wards from sector 3, q'_{b34} , is free, but the heat transferred from the left into sector 4, q'_{b43} , is known. The outer boundaries are adiabatic in Variant 2 of the model ($q'_{b910} = 0$) but in Variant 3, the heat flow from sector 9 to an external heat sink is positive ($q'_{b910} > 0$).

Finding a consistent solution involves matching a combination of temperatures on contacting boundaries (as in the intra-block model) and finding consistent heat fluxes on boundaries separated by a gap (as in the inter-block model). An iterative scheme

is again implemented using a visual basic macro employing the Newton-Raphson method with an acceleration parameter. The solver attempts to match the boundary temperatures on the sector 1-2, 2-3, 4-5, 5-6, 7-8 and 8-9 boundaries by adjusting the values of the right-wards heat flux in each sector. It also attempts to match the heat fluxes across the inter-block gaps at 3-4 and 6-7, this time by matching the right-wards heat fluxes with the total heat flow calculated to flow across the gap given the sector surface temperatures.

The solution is deemed to have converged when the fractional error in the parameters being matched is less than the tolerance.

The Variant 2 model (operating power levels with full cooling) uses the effective intra-block conductivity (Equation 45), which is ~ 270 W/m/K. The Variant 3 model (0.5% nominal power levels and no helium cooling) uses the simple effective conductivity (Equation 37), which is 60.79 W/m/K.

Results

Table 7.3.9 presents the results for Variant 2 (operating power levels with full cooling) and Table 7.3.10 presents the results for Variant 3 (0.5% nominal power levels and no helium cooling).

Table 7.3.9: Results for combined Variant 2

Parameter	Sector 1	Sector 2	Sector 3	Units
heat input per fuel compact	6.958	5.729	4.915	kW/m
fuel compact power density	54.930	45.227	38.803	MW/m
heat input from all fuel compacts	250.501	206.253	176.956	kW/m
heat flow into coolant	244.159	207.123	180.837	kW/m
heat radiated over 3-4 inter-block gap			0.844	kW/m
heat conducted over 3-4 inter-block gap			0.747	kW/m
total heat transferred right-wards	6.342	5.472	1.591	kW/m
3-4 inter-block gap conductivity			0.36688	W/m/K
centroid to boundary total conductivity	269.55	269.79	269.92	W/m/K
maximum fuel compact temperature	1242.5	1190.7	1146.9	K
mean graphite temperature	1213.7	1166.3	1126.1	K
coolant channel wall temperature	1173.2	1132.5	1096.4	K
coolant gas temperature	1070	1045	1020	K
sector left boundary temperature	not calculated	1190.1	1146.3	K
sector right boundary temperature	1190.1	1146.3	1120.2	K

Parameter	Sector 4	Sector 5	Sector 6	Units
heat input per fuel compact	4.462	4.314	4.416	kW/m
fuel compact power density	35.223	34.052	34.858	MW/m ³
heat input from all fuel compacts	160.629	155.292	158.963	kW/m
heat flow into coolant	161.216	157.146	159.266	kW/m
heat radiated over 6-7 inter-block gap			-0.608	kW/m
heat conducted over 6-7 inter-block gap			-0.546	kW/m
total heat transferred right-wards	1.004	-0.851	-1.154	kW/m
6-7 inter-block gap conductivity			0.36625	W/m/K
centroid to boundary total conductivity	269.78	269.85	269.77	W/m/K
maximum fuel compact temperature	1113.4	1105.4	1112.1	K
mean graphite temperature	1094.7	1087.2	1093.5	K
coolant channel wall temperature	1068.1	1061.4	1067.3	K
coolant gas temperature	1000	995	1000	K
sector left boundary temperature	1100.6	1091.0	1090.4	K
sector right boundary temperature	1091.0	1090.4	1097.8	K

Parameter	Sector 7	Sector 8	Sector 9	Units
heat input per fuel compact	4.713	5.150	5.673	kW/m
fuel compact power density	37.204	40.656	44.782	MW/m ³
heat input from all fuel compacts	169.662	185.408	204.220	kW/m
heat flow into coolant	172.899	185.535	199.703	kW/m
total heat transferred right-wards	-4.391	-4.517	0 ^[*]	kW/m
centroid to boundary total conductivity	269.90	269.76	269.57	W/m/K
maximum fuel compact temperature	1136.3	1170.6	1206.0	K
mean graphite temperature	1116.4	1149.0	1182.5	K
coolant channel wall temperature	1088.1	1118.4	1149.4	K
coolant gas temperature	1015	1040	1065	K
sector left boundary temperature	1112.2	1132.7	1165.7	K
sector right boundary temperature	1132.7	1165.7	not calculated	K

* outer boundary condition

Table 7.3.10: Results for combined Variant 3

Parameter	Sector 1	Sector 2	Sector 3	Units
heat input per fuel compact	0.035	0.029	0.025	kW/m
fuel compact power density	0.275	0.226	0.194	MW/m ³
heat input from all fuel compacts	1.253	1.031	0.885	kW/m
heat flow into coolant	0	0	0	kW/m
heat radiated over 3-4 gap			2.557	kW/m
heat conducted over 3-4 gap			0.612	kW/m
total heat transferred right-wards	1.253	2.284	3.169	kW/m
3-4 inter-block gap conductivity			0.59594	W/m/K
centroid to boundary total conductivity	60.79	60.79	60.79	W/m/K
maximum fuel compact temperature	2193.1	2151.9	2076.7	K
mean graphite temperature	2193.0	2151.8	2076.7	K
coolant channel wall temperature	2192.9	2151.8	2076.6	K
sector left boundary temperature	not calculated	2172.4	2114.2	K
sector right boundary temperature	2172.4	2114.2	2024.5	K

Parameter	Sector 4	Sector 5	Sector 6	Units
heat input per fuel compact	0.022	0.022	0.022	kW/m
fuel compact power density	0.176	0.170	0.174	MW/m ³
heat input from all fuel compacts	0.803	0.776	0.795	kW/m
heat flow into coolant	0	0	0	kW/m
heat radiated over 6-7 gap			3.882	kW/m
heat conducted over 6-7 gap			1.661	kW/m
total heat transferred right-wards	3.972	4.748	5.543	kW/m
6-7 inter-block gap conductivity			0.49929	W/m/K
centroid to boundary total conductivity	60.79	60.79	60.79	W/m/K
maximum fuel compact temperature	1962.6	1831.9	1675.7	K
mean graphite temperature	1962.6	1831.9	1675.7	K
coolant channel wall temperature	1962.5	1831.9	1675.7	K
sector left boundary temperature	2014.7	1897.2	1753.8	K

Parameter	Sector 4	Sector 5	Sector 6	Units
sector right boundary temperature	1897.2	1753.8	1584.5	K

Parameter	Sector 7	Sector 8	Sector 9	Units
heat input per fuel compact	0.024	0.026	0.028	kW/m
fuel compact power density	0.186	0.203	0.224	MW/m ³
heat input from all fuel compacts	0.848	0.927	1.021	kW/m
heat flow into coolant	0	0	0	kW/m
total heat transferred right-wards	6.391	7.318	8.339	kW/m
centroid to boundary total conductivity	60.79	60.79	60.79	W/m/K
maximum fuel compact temperature	1461.4	1251.1	1010.4	K
mean graphite temperature	1461.3	1251.1	1010.3	K
coolant channel wall temperature	1461.3	1251.0	1010.3	K
sector left boundary temperature	1552.5	1356.2	1130.7	K
sector right boundary temperature	1356.2	1130.7	873.15 ^[*]	K

* outer boundary condition

Comparison with FE calculations

The following data (Tables 7.3.11 and 7.3.12) are taken from finite element model calculations (Section 7.2). "Typical" peak fuel and coolant channel wall temperatures were taken by hand from typical locations within the sector away from edge effects.

Table 7.3.11: Combined Variant 2 – comparison of FE and analytical models

Sector	typical peak fuel compact temperature (K)		Edge	average sector boundary temperature (K)		total heat transferred right-wards (kW/m)	
	Analytic	FE		Analytic	FE	Analytic	FE
1	1242.5	1242.3	LHS 1	not calculated	1236.3	0	0
2	1190.7	1179.3					
3	1146.9	1143.8	RHS 3	1120.2	1137.6	1.591	1.5227
4	1113.4	1111.8	LHS 4	1100.6	1118.5	-1.591	-1.5449
5	1105.4	1102.6					
6	1112.1	1108.6	RHS 6	1097.8	1113.7	-1.154	-1.1668
7	1136.3	1129.8	LHS 7	1112.2	1128.2	1.154	1.1589
8	1170.6	1167.9					
9	1206.0	1203.4	RHS 9	Not calculated	1201.5	0 ^[*]	0 ^[*]

* outer boundary condition

The maximum fuel compact temperatures agree within ~5 K, apart from for sector 2, in which the FE model predicts a typical maximum temperature ~10 K cooler than the analytical model, although it is important to remember that the FE model temperatures quoted were taken manually and are only indicative. The boundary temperature differences agree within 0.5 K on the 3-4 and 6-7 boundaries (the left edge of sector 1 and the right edge of sector 9 are not calculated analytically and so cannot be compared). The inter-block heat fluxes agree to within 0.07 kW/m (~4%).

Table 7.3.12: Combined Variant 3 – comparison of FE and analytical models

Sector	typical peak fuel compact temperature (K)		Edge	average sector boundary temperature (K)		total heat transferred right-wards (kW/m)	
	Analytic	FE		Analytic	FE	Analytic	FE
1	2193.1	2110	LHS 1	not calculated	2115.7	0	0
2	2151.9	2062					
3	2076.7	2003	RHS 3	2024.5	1948.6	3.169	3.148
4	1962.6	1878	LHS 4	2014.7	1936.5	-3.169	-3.164
5	1831.9	1747					
6	1675.7	1622	RHS 6	1584.5	1524.2	5.543	5.535

<i>Sector</i>	typical peak fuel compact temperature (K)		<i>Edge</i>	average sector boundary temperature (K)		total heat transferred right-wards (kW/m)	
	Analytic	FE		Analytic	FE	Analytic	FE
7	1461.4	1380	<i>LHS 7</i>	1552.5	1484.5	-5.543	-5.553
8	1251.1	1164					
9	1010.4	1000	<i>RHS 9</i>	873.15 ^[*]	873.15 ^[*]	8.339	8.314

* outer boundary condition

This Variant shows much larger differences in the maximum fuel compact temperature, with the analytical model finding peak temperatures of up to ~90 K larger than the FE model. Inter-block heat fluxes agree very well, matching to within 0.03 kW/m (<1%) on the 3-4 gap, 6-7 gap and at the edge of sector 9.

7.4 Closure

This section is concerned with the modeling of heat transfer on the macroscopic scale. Scenarios ranging from heat redistribution within a single fuel block, through heat transfer between two neighboring blocks, to heat transfer through a radial spoke in the fuelled region of GT-MHR, have been modeled.

The above scenarios have been modeled both by finite element analysis and by a coarse-grid finite volume approach. In general the finite element results show that, in normal operation with forced cooling, the temperature distribution within a block follows the power distribution. If the power density varies linearly across the block, then the macroscopic temperature also varies linearly. Similarly if the power distribution is flat, then the macroscopic temperature distribution is also flat. Heat loss from (or heat gain through) the edges of the block only perturbs the temperatures in the edge rows of coolant and fuel channels and does not propagate into the centre of the block.

These findings have important consequences for the way in which macroscopic heat transfer is modeled in a coarse-grid whole core model or system code. First, the assumption of linear temperature variations within the sectors of the blocks is a poor approximation. Second, the assumption that the real variation in power density can be approximated by determining the power density at the centroid of each sector, which is then applied in a piecewise-constant manner over the sectors, is also a poor approximation.

The first of the above consequences demands either a much finer sub-division of the sectors, or for the linear temperature profile to be substituted by a better approximation. In this work, the latter approach was adopted in which the analytical solution to an equivalent one-dimensional problem, with a distributed heat source and distributed temperature-dependent heat sink, was derived and imposed as the assumed temperature variation. The second consequence demands that the power

gradient within each sector be included in the analytical solution, this has not been addressed in the current work and, consequently, only comparisons with the finite element models in which piecewise constant power distributions were applied have been made. Comparing the finite element results for the intra-block model variants, the heat flow from the hot to the cold halves of the block in Variants 1 and Variant 2, with linear and piecewise-constant power distributions respectively; are 1.46 kW/m and 6.89 kW/m i.e. over a factor of four difference. Whilst the model based on the analytical solution agrees reasonably well with the finite element solution for Variant 2, the error will be in excess of 400% if the comparison with Variant 1 is made. For this reason, comparison with Variant 1 of the combined (3 block) model was not attempted.

Whilst the coarse grid finite volume model presented here works reasonably well in normal operation with a piecewise constant power distribution, further work is required to cope with the following situations. First, the analytical solution needs to be extended to cope with realistic (continuous) power distributions. Second, the zero temperature gradient condition imposed at the sector centroid, introduced to solve the differential equation needs to be relaxed. This condition only occurs when the power and coolant temperature distributions are both flat, so imposition of the condition does not yield the correct solution if these distributions are not flat and neither is in the limiting case of no forced cooling (i.e., the passive decay heat removal scenario). At the moment, there is a logical test in the solution, which reverts to linear interpolation in no-flow conditions. Finally, the use of temperature profiles based on one-dimensional analytical solutions is only applicable in steady state conditions. Extension to transient conditions may require a more traditional fine-grid finite volume approach unless a suitable approximation involving the steady state analytical solutions combined with lumped thermal masses can be devised.

It is believed, therefore, that the macroscopic model presented here is suitable for reactor static calculations, but requires some development to handle realistic and continuous spatial variations in power density and coolant temperature. Similarly, a further development is necessary to handle correctly the transition to no flow conditions. Extension and qualification of the model to be applicable to transient conditions will require additional model development and further finite element simulations.

7.5 References for Section 7

- 7.1 R. Stainsby et al., "Investigation of Local Heat Transfer Phenomena in a Pebble Bed HTGR Core", AMEC NSS Report NR001/RP/002 R01, May 2009.
- 7.2 KTA Rule 3102.1, "Reactor Core Design for High-Temperature Gas-Cooled Reactor. Part 1: Calculation of the Material Properties of Helium", Nuclear Safety Standards Commission (KTA), Germany, June 1978.
- 7.3 IAEA-TECDOC-1198, "Current Status and Future Development of Modular High Temperature Gas Cooled Reactor Technology", IAEA, February 2001.

- 7.4 A. Grief, S. Hunter and J. Murgatroyd, "A Combined Neutronics and Thermal Hydraulics Analysis of a Prismatic VHTR Core," AMEC Report 12842/TR/010, March 2006.

8.0 INFLUENCE AND MODELING OF CORE BYPASS FLOWS

8.1 Purpose of Section 8

The purpose of the work of this section was to develop models that would integrate the sub-models presented in sections 5 to 7 which would be able to predict the changes to fuel temperatures that will occur due to core bypass flows. Such bypass flows are introduced either by manufacturing tolerances, or errors, or by geometry changes that occur during irradiation.

Core bypass flows can either be a complete bypass, where the coolant effectively short-circuits from the reactor inlet to the reactor outlet, or partial bypass, where only part of the core is starved of flow. Complete bypass is easy to simulate by simply subtracting the bypass flow from the core inlet flow. Partial bypass is more subtle, in that flow can leave the coolant channels through gaps near the top of the core (assuming a downwards core flow) and re-enter through gaps closer to its base, thus only bypassing the mid-height region. The latter scenario requires a hydraulic model in which the inter-block gaps are modeled with suitable cross-links to the fuel channels, at the block end-faces. Determination of the end-face actual gap sizes is feasible, but difficult, requiring the manufacturing tolerances to be accounted for and irradiation-induced distortions to be calculated.

There is a lack of detailed design information and detailed neutron flux and temperature distributions and therefore part of the work undertaken has been to review the open literature available on gap sizes and leakage flows in previous HTGRs, particularly Fort St Vrain as it used the same type of fuel.

An existing system code, RELAP5 (Reference 8.10) has been used to produce a one-dimensional model of a section of GT-MHR core. This model includes the heat structures to represent the super-meso and meso-scale models reported in Sections 5.0 and 7.0, and includes suitable hydrodynamic volumes to represent the inter-block gaps and junctions to represent the leak paths at imperfect fuel block end-face contacts.

A representative set of cases have been run to demonstrate the influence of different amounts of bypass flow on fuel compact temperatures.

8.2 Introduction

Prismatic HTGR core designs generally consist of an array of stacked graphite blocks, with hexagonal cross section. The layout of the proposed GT-MHR core described in Reference 8.1 is reproduced in Figure 2.3.2 and Figure 2.3.5. The core includes a central reflector, which consists of unfuelled graphite blocks, surrounded by an annular arrangement of fuel blocks, encompassed by an annular side reflector formed of graphite blocks. Layers of unfuelled graphite blocks are placed above and below the core, to form an upper and lower axial reflector. Reactivity control rods and reserve shut-down system channels penetrate the fuelled region and the edges of the reflectors at regular intervals. A GT-MHR fuel block, which is 80 cm in height and 36

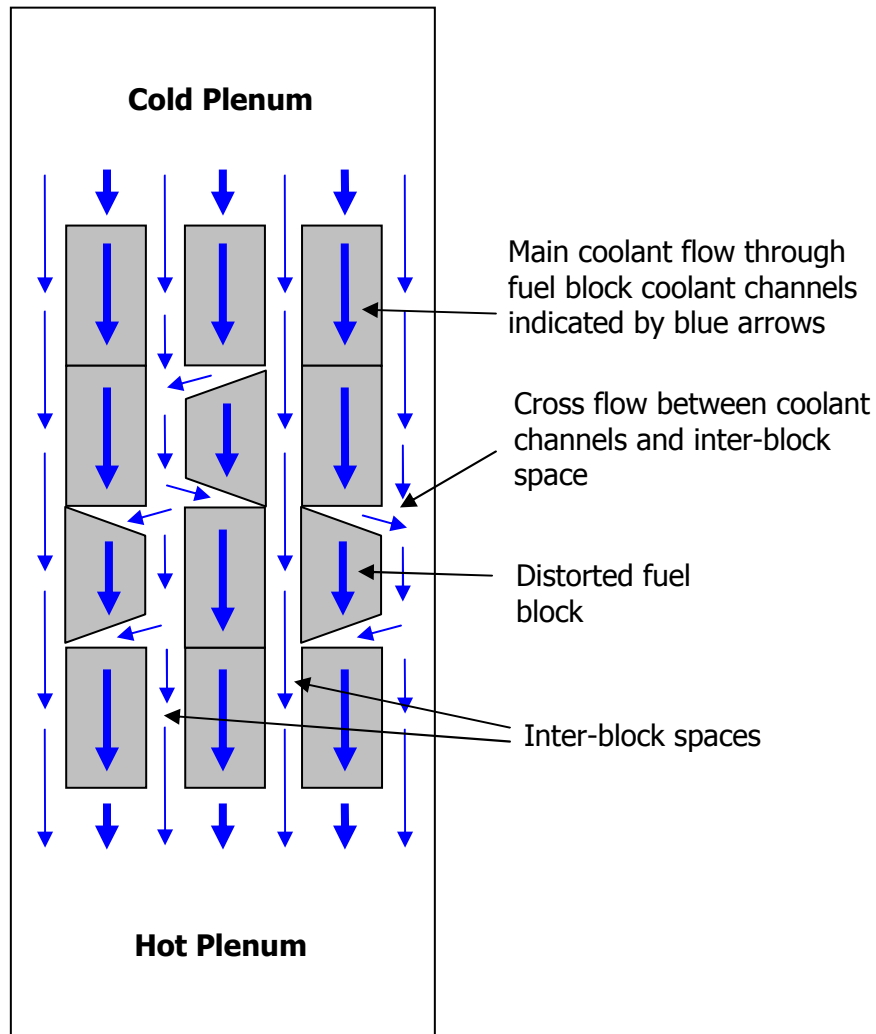
cm across flats, is shown in cut-away view in Figure 2.3.4, and a cross-section view is shown in Figure 2.3.5. Figure 2.3.4 includes a depiction of a fuel element containing a reactivity control channel. Fuel compacts extend along the central 75 cm of each fuel block. The remaining extent of the fuel channels is occupied by 2.5 cm end caps which plug each end of the fuel compact channels.

The arrangement of the lower reflector blocks in a HTGR core is constrained by the metallic core support plate, with the outer blocks of the side reflector restrained by the presence of the core barrel. However, the remaining fuel and reflector blocks are constrained only by the presence of their neighbours. An inter-block spacing of 0.25 cm is allowed (Reference 8.1), to permit the extraction of fuel blocks during refuelling and to allow for thermal expansion of the blocks. Thus limited tilting of the fuel blocks may occur during normal reactor operation.

Temperature and flux gradients within a HTGR core are expected to lead to non-uniform expansion and swelling of the graphite fuel elements during reactor operation. This non-uniform block distortion will cause gaps to form between the end faces of stacked fuel elements, generating a network of core bypass flow paths from the cold gas inlet plenum, through the inter-block spaces, entering the coolant channels through the gaps, as shown schematically in Figure 8.2.1. In addition, end-face gaps may allow flow to pass from the coolant channels into the control rod and reserve shutdown system channels.

In this report, the leakage flows between the inter-block spaces and the coolant channels are examined. Leakage flow into the control rod channels is expected to behave in a qualitatively similar manner, however this type of leakage path is not addressed directly within this report.

Figure 8.2.1: Schematic view of core bypass due to crossflow through end-face gaps



8.3 Review of the Open Literature

A review of open literature was conducted and reports and papers about leakage flow and crossflow within prismatic core reactors were identified. The references fall into three broad categories:

1. Design studies conducted by Gulf General Atomics for the Fort St. Vrain nuclear reactor (Reference 8.2).
2. Design studies conducted by the Japan Atomic Energy Research Institute to support the development of the HTTR reactor (References 8.3 to 8.7).

3. Research conducted for the U.S. Department of Energy by the Nuclear Engineering Division, Argonne National Laboratory in support of the Prioritization of VHTR System Modeling Needs (Reference 8.8).

No quantitative information on leakage flow rates or the fuel block distortion experienced during the operation of prismatic cored reactors was identified within the open literature. However, the published literature contains reports of theoretical and experimental studies of four classes of leakage flows, i.e.,

1. Leakage flows due to wedge shaped gaps between stacked fuel blocks caused by core distortion or core displacement,
2. Leakage flows due to parallel sided gaps between stacked fuel blocks due to core distortion or core displacement,
3. Leakage flows due to imperfect sealing caused by the surface roughness of stacked fuel blocks,
4. Leakage flows due to gas permeation through the graphite body of the fuel block.

The first class of leakage flows, due to wedge shaped gaps, may occur as a result of core displacement (e.g., distortion of the core support structures) or distortion of fuel and reflector elements (due to fast neutron damage and thermal expansion). The second class of leakage flows, due to parallel sided gaps between stacked blocks are considered by some researchers to be unrealistic within operational reactors (Reference 8.4), but have been studied in test rig experiments. The third and fourth classes of leakage flows are inherent within any reactor design, and depend on material properties and machining tolerances.

The four classes of flow identified above are discussed in the following sub-sections, based on the findings of the literature review.

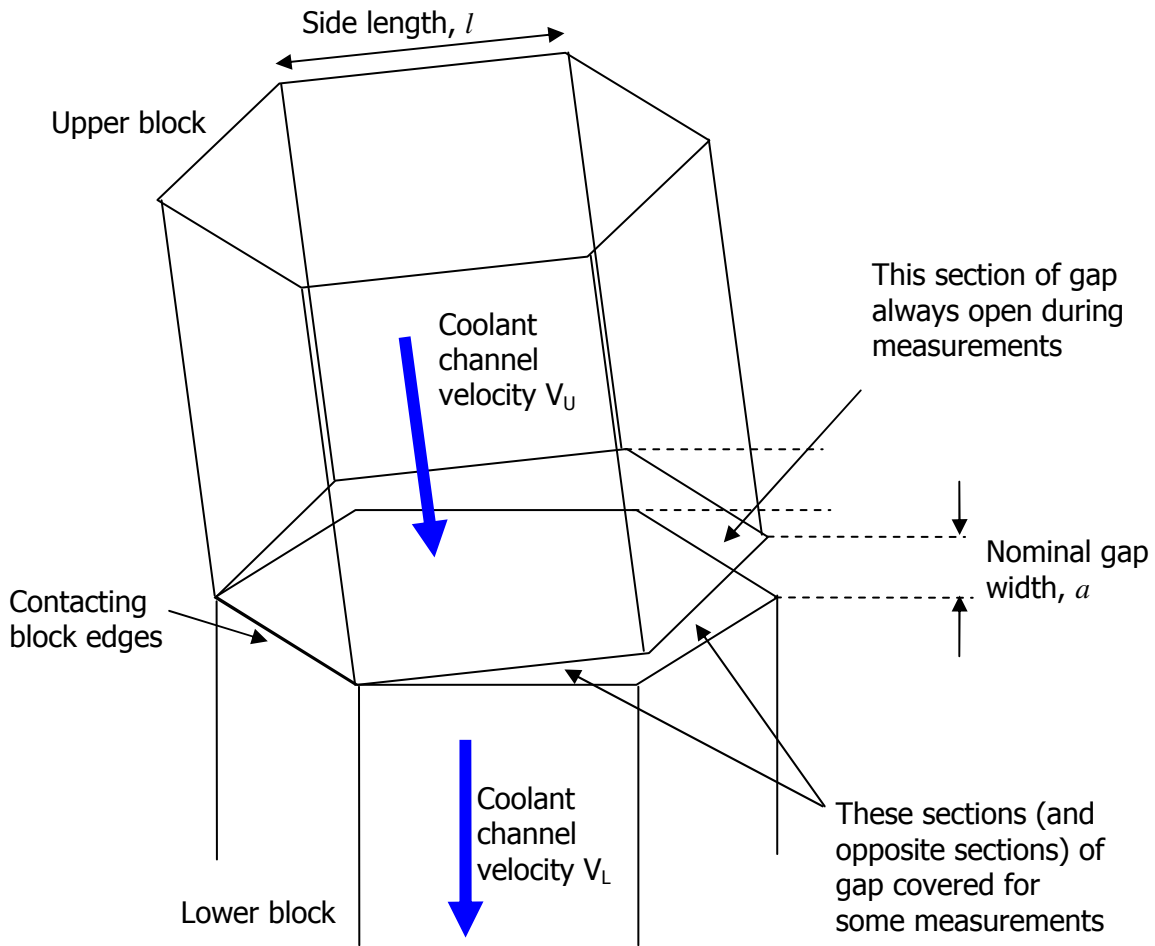
8.3.1 Leakage flow due to wedge-shaped gaps between stacked fuel blocks

Temperature and flux gradients within a VHTR core are expected to lead to non-uniform expansion of the graphite fuel elements. This non-uniform distortion, combined with constraints on the fuel block motion due to surrounding fuel and reflector columns, are expected to lead to wedge shaped gaps forming between stacked fuel elements.

Groehn (Reference 8.9) performed an experimental study of leakage flows between HTGR fuel blocks separated by large wedge shaped gaps. The overall block size, and distribution of coolant channels in the blocks studied were comparable with the current GT-MHR fuel block designs. However, the blocks used by Groehn had a coolant channel diameter of 18 mm, which is larger than the 16 mm diameter channels proposed for the GT-MHR fuel blocks (Reference 8.1).

In Groehn's work, an experimental representation of two stacked hexagonal fuel elements in contact along one pair of edges was used, as shown in Figure 8.3.1. The gap size was defined as the width of the gap on the opposite side of the block from the contacting edges. Between zero and four (i.e. all) of the remaining edges were sealed. Gap sizes of 1.85 mm, 3.75 mm and 6 mm were studied.

Figure 8.3.1: The configuration simulated by Groehn's experimental rig



Groehn developed a correlation relating difference between the mean coolant channel gas velocity above the gap (i.e. in the upper block) to the velocity below the gap (i.e. in the lower block) to the pressure difference, ΔP , between the coolant channels and the gas surrounding the fuel block. Groehn's correlation states:

$$\Delta P = \xi \cdot \frac{\rho \cdot (V_L - V_U)^2}{2},$$

where:

$$\xi = 3.58 \left(\frac{a}{D} \right)^{-2.3} \cdot 6.33 \cdot \left(\frac{A_{Gap}}{a \cdot l} \right)^{-1.68}$$

and

V_U	Coolant channel velocity above gap
V_L	Coolant channel velocity below gap
a	Nominal gap width (see Figure 8.3.1)
D	Coolant channel diameter
l	Side length of hexagonal block
ρ	Gas density
A_{Gap}	Open area of the gap (equal to $3al$ when no sides covered)

Groehn defined a Reynolds number based on the velocity increment across the end-face gap,

$$Re = \frac{\rho \cdot (V_L - V_U) \cdot D}{\mu}$$

Good agreement between the experimental data and the above correlation was found for Reynolds numbers over 3000 for the full range of gap sizes studied, including cases in which the gap was partially sealed. Reasonable agreement with the correlation was obtained for Reynolds numbers between 1000 and 3000, however a degree of scatter was present in this range.

Through simple manipulation, Groehn's correlation can be recast as a relation between the crossflow mass flow rate through the gap, \dot{m}_{Gap} , and the pressure difference between the coolant channels and the plenum surrounding the fuel blocks. Using two expressions for the mass flow through the gap,

$$\dot{m}_{Gap} = \rho \cdot (V_L - V_U) \cdot A \quad \text{and} \quad \dot{m}_{Gap} = \rho \cdot V_{Gap} \cdot A_{Gap}$$

where A is the overall cross section of all the coolant channels within a fuel block, and V_{Gap} is the gas velocity at the edge of the gap, it is found that:

$$\Delta P = K_{Gap} \cdot \frac{\rho \cdot V_{Gap}^2}{2}$$

where the gap loss coefficient, K_{Gap} , is related to Groehn's coefficient ξ by the expression:

$$K_{Gap} = \left(\frac{A_{Gap}}{A} \right)^2 \cdot \xi = \left(\frac{A_{Gap}}{A} \right)^2 \cdot \left[3.58 \left(\frac{a}{D} \right)^{-2.3} \cdot 6.33 \cdot \left(\frac{A_{Gap}}{a \cdot l} \right)^{-1.68} \right].$$

A power-law relationship relates the hydraulic resistance of the gap, $R = K_{Gap} / (A_{Gap})^2$, and the gap width a :

$$R = K_{Gap} / (A_{Gap})^2 \propto a^{-2.3}.$$

The hydraulic resistances and equivalent loss coefficients predicted by Groehn's correlation for 1.85 mm, 3.75 mm and 6 mm gaps are shown in Table 8.3.1. The variation of the hydraulic resistance and loss coefficient for the case where no faces of the wedge shaped gap are covered are shown graphically in Figure 8.3.2 and Figure 8.3.3.

Table 8.3.1: Evaluation of Groehn's loss correlation, and conversion to hydraulic resistance

<i>Data values used by Groehn*</i>	
Fuel block side, l (m)	2.08E-01
Coolant channel diameter, D (m)	1.80E-02
No. of coolant channels per block, N_c	72
Total flow cross section in block, A (m ²)	0.018321768

Gap width, a (m)	No. of blocked faces	Gap area, A_{gap} (m ²)	Groehn's loss coefficient ξ (based on total flow area A)	Hydraulic resistance, R (m ⁻⁴)	Energy form loss coefficient K (based on gap area A_{gap})
1.85E-03	0	1.15E-03	6.70E+02	2.00E+06	2.66
3.75E-03	0	2.34E-03	1.32E+02	3.93E+05	2.15
6.00E-03	0	3.74E-03	4.48E+01	1.33E+05	1.87
1.85E-03	2	9.62E-04	9.11E+02	2.71E+06	2.51
3.75E-03	2	1.95E-03	1.79E+02	5.34E+05	2.03
6.00E-03	2	3.12E-03	6.08E+01	1.81E+05	1.76
1.85E-03	4	3.85E-04	4.25E+03	1.26E+07	1.87
3.75E-03	4	7.80E-04	8.36E+02	2.49E+06	1.51
6.00E-03	4	1.25E-03	2.84E+02	8.45E+05	1.32

*These are similar, but not identical to the current GT-MHR design

Groehn performed measurements of the velocity distribution within the coolant channels of the experimental test rig using a hot wire probe. The results showed that the crossflow entering a fuel element at an end-face gap preferentially flows into the coolant channels nearest the widest part of the wedge shaped gap. This is in agreement with results reported by Kaburaki et al. who performed experiments using simulated wedge shaped gap openings on HTTR fuel elements (Reference 8.4).

Figure 8.3.2: Hydraulic resistance to crossflow through end-face gaps for a full fuel element, as predicted by Groehn's model

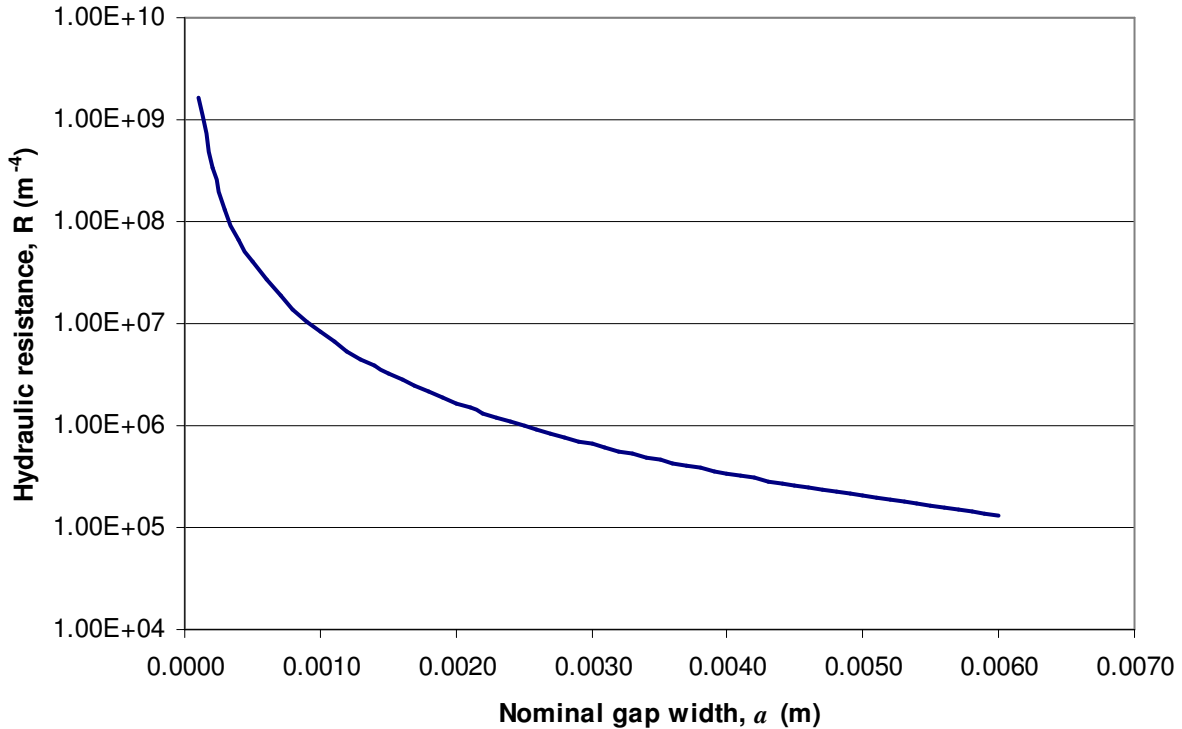
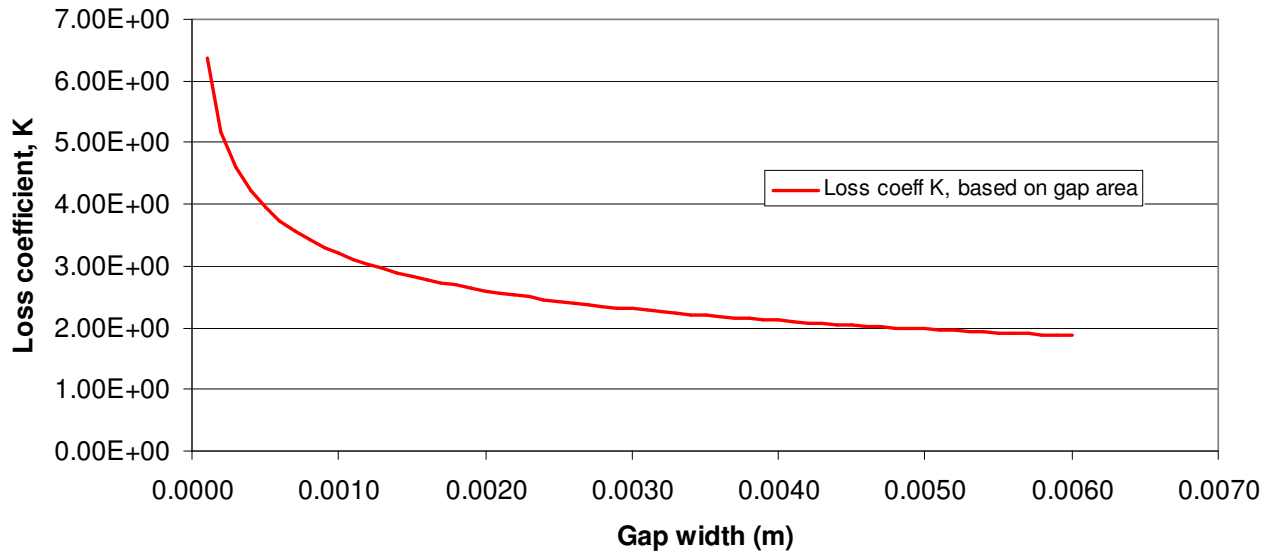


Figure 8.3.3: Energy form loss coefficients, based on the area of the end-face gap, predicted by Groehn's model



8.3.2 Leakage flow due to parallel sided gaps between stacked fuel blocks

G. J. Malek et al. at Gulf General Atomics (GGA) (Reference 8.2) report experimental tests on scale models of HTGR fuel bricks representative of those used in the Fort St. Vrain reactor. Within this work, they present data for the hydraulics resistance (i.e. the loss coefficient divided by the gap area squared, as defined in section 8.3.1) to crossflow between two full size VHTR fuel blocks.

The hydraulic resistance is presented for crossflow through 1/6th of a fuel block (i.e. one block face) against the gap width, a . The graph includes experimental data for gap widths ranging from 0.005 inches to 0.06 inches (i.e., gap widths from 0.127 mm to 1.524 mm). Whilst the experimental data shows significant scatter, Reference 8.2 shows a best fit line on log-log axis, implying a power law relationship between the hydraulic resistance of the gap, R , and the gap width,

$$R = (K / A^2) = p a^q$$

The values of the coefficients p and q corresponding to the best fit line have been computed from the graph presented in Reference 8.2. From this fit, the coefficients p and q are estimated to be (with the area A is measured in square inches, and gap width a is measured in inches):

$$p = 0.160355, \quad q = -1.63634.$$

Converting to SI units of m and m⁻⁴, the value of the coefficient p is multiplied by a factor of $1/(0.0254)^{(q+4)} = 5894.3$, and the correlation takes the form:

$$R = (K / A^2) = p_{SI} a^q, \quad \text{where} \quad p_{SI} = 945.18, \quad q = -1.63634.$$

It may be noted that the exponent $q = -1.63634$ in this correlation between the hydraulic resistance R and the gap width a is significantly different to that predicted by Groehn for wedge shaped gaps (Section 8.3.1).

The area A is the product of the gap width, a , times the length of a block edge l (0.208 m for GT-MHR fuel blocks), such that $A = a \cdot l$. Therefore, the correlation can be simplified for a GT-MHR size block to obtain:

$$K = r \cdot a^s$$

where

$$r = p_{SI} \cdot l^2 = 40.89 \quad \text{and} \quad s = 2 + q = 0.36366.$$

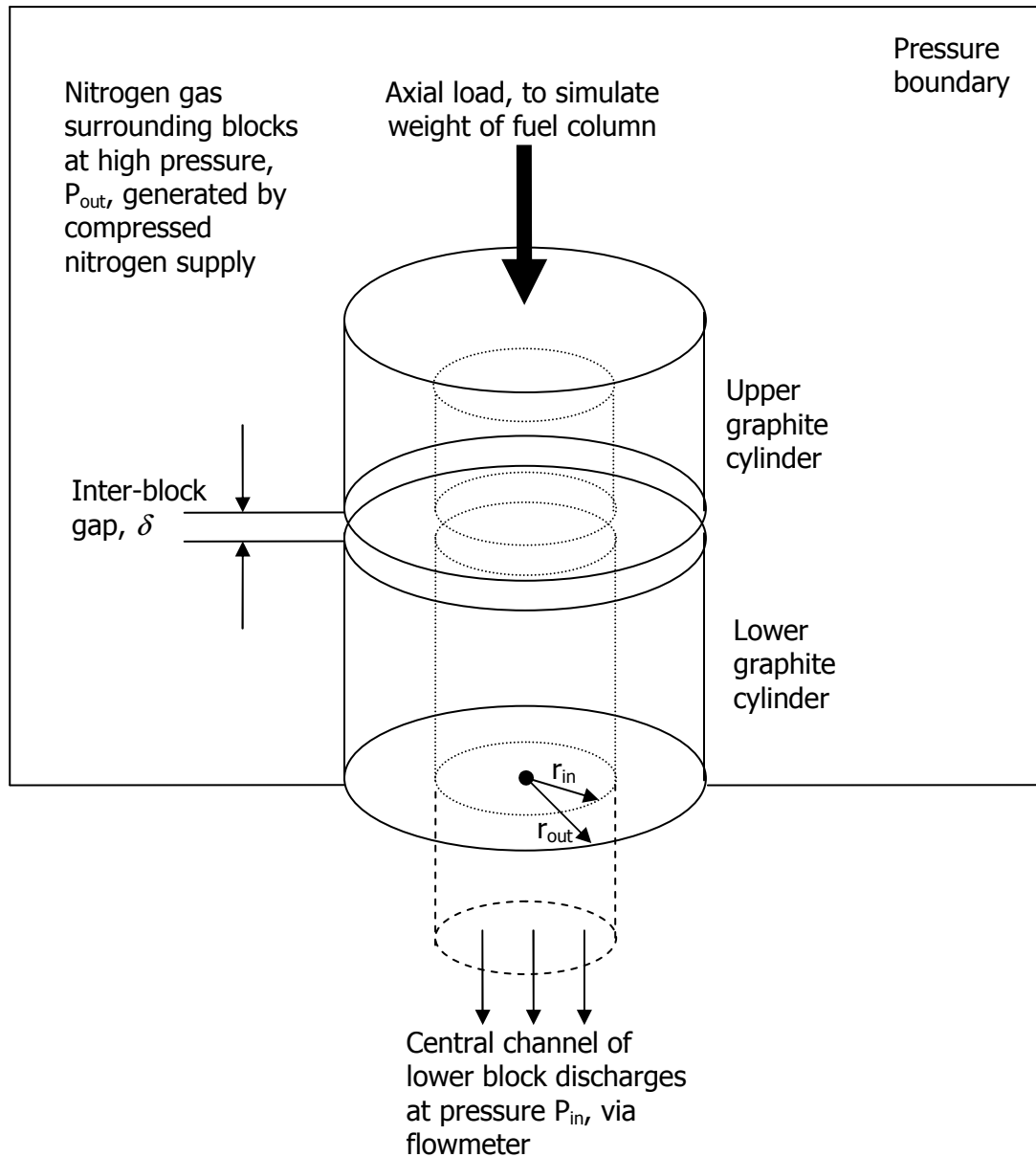
8.3.3 Leakage flow due to the surface roughness of stacked fuel blocks

Hideo Kaburaki et al. (Reference 8.3), of the Japan Atomic Energy Research Institute (JAERI), conducted studies of leakage flow between contacting graphite surfaces. Studies were conducted using simple annular cylindrical geometries and stacked full scale HTTR fuel elements.

The test elements were stacked normally and a pressure difference was induced between the channels within the annular cylinder / fuel element and the gas surrounding the element, as shown in Figure 8.3.4.

The applied pressure difference, $\Delta P = P_{out} - P_{in}$, generated a flow through the small gaps between the contacting elements caused by surface roughness. This 'crossflow' was monitored for a range of applied pressure differences. During the testing the outer surfaces of the graphite elements were coated with sealant, to prevent gas permeation through the bodies of the test elements. In addition, a compressive axial load was applied to the graphite elements to simulate the contact pressures generated by the weight of stacked fuel elements in a reactor core. By varying the applied load, changes in the nature of the contact and gaps between stacked fuel elements could be examined.

Figure 8.3.4: JAERI crossflow leakage experiment



8.3.3.1 Results for the stacked cylindrical element experiment

The narrow nature of the end-face gaps allowed only a small crossflow to occur. When the pressure difference ΔP was small the experimental results showed the leakage mass flow rate varied in proportion to ΔP . For higher applied pressure differences, when the compressibility of the gas became significant, the mass flow rate increased faster than ΔP .

To understand the experiments, the investigators derived a theoretical flow distribution for the laminar flow of a viscous perfect compressible gas between two parallel circular plates. The solution shows:

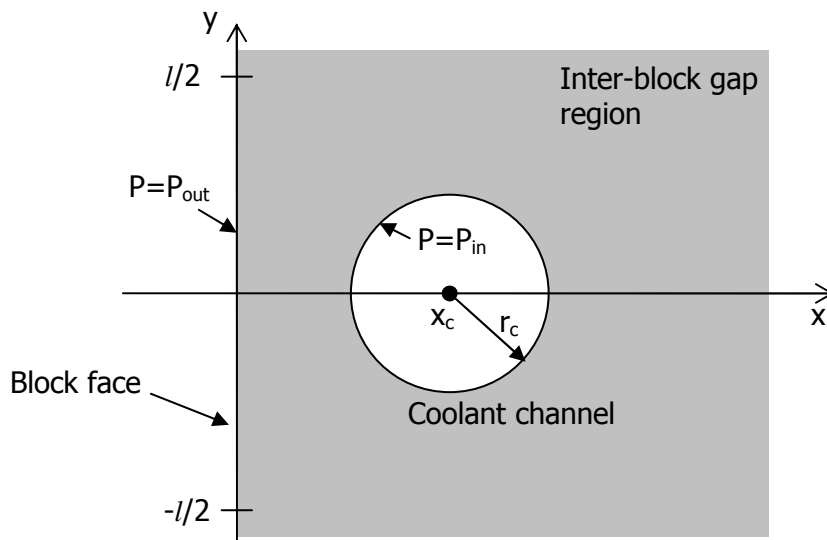
$$\text{Mass flow rate} = -\frac{\pi\delta^3}{6\nu} \cdot \frac{\Delta P}{\ln(r_{out}/r_{in})} \left(1 + \frac{\Delta P}{2P_{in}}\right)$$

where δ is the effective gap width between the plates, and ν is the kinematic viscosity of the gas. Comparison of the measured flow rate between the cylindrical blocks with the theoretical flow distribution allowed an effective gap width to be determined for the experimental data for each axial load. A good correlation between theoretical and experimental results was found with the effective gap width varying slightly from $\delta \sim 13$ microns at low axial loads and $\delta \sim 11$ microns at higher loads.

8.3.3.2 Results for the stacked HTTR fuel element experiment

Crossflow entering the end-face gap between two fuel elements will divide between multiple coolant channels. In order to understand how the leakage flow divides between the coolant channels, a finite element simulation of two-dimensional Hele Shaw flow (Reference 8.12) between the fuel block ends was performed (results not shown in Reference 8.3). The authors report that over 98% of the flow entered the coolant channels near the edge of the fuel block, with very little of the leakage crossflow reaching the inner channels. Based on this knowledge, Kaburaki et al. derived an analytical solution for the flow distribution within the simplified geometry shown in Figure 8.3.5, in which only a single coolant channel near the block edge is considered.

Figure 8.3.5: Simplified flow model for leakage flow from a block edge to coolant channel in a HTTR fuel element



The solution to this two-dimensional compressible gas flow problem is found using complex variable techniques (Reference 8.3):

$$P = \left[P_{out} + \frac{P_{in}^2 - P_{out}^2}{\ln\left(\frac{x_c - \alpha}{x_c + \alpha}\right)} \cdot \ln\frac{(x - \alpha)^2 + y^2}{(x + \alpha)^2 + y^2} \right]^{1/2}$$

where $\alpha = (x_c^2 - r_c^2)^{1/2}$ and x_c and r_c represent the channel centre coordinate and channel entrance radius respectively. The mean gap velocity is given by

$$\bar{\mathbf{u}} = (\bar{u}, \bar{v}) = -\frac{\delta^2}{12\mu} \nabla P$$

where μ is the dynamic viscosity of the gas. The pressure distribution, for $P_{in} = 70$ bar, $P_{out} = 70.5$ bar, based on the HTTR fuel block geometry, $r_c = 23.3$ mm and $x_c = 36.9$ mm is shown in Figure 8.3.6. The corresponding mean gap velocity distribution corresponding to helium flow at 1000 K through a 12 micron end-face gap is shown in Figure 8.3.7. The distribution of the gas flow along the gap edge is shown in Figure 8.3.8.

Figure 8.3.6: Pressure distribution surrounding a single HTTR coolant channel near a block edge subject to a 0.5 bar pressure difference

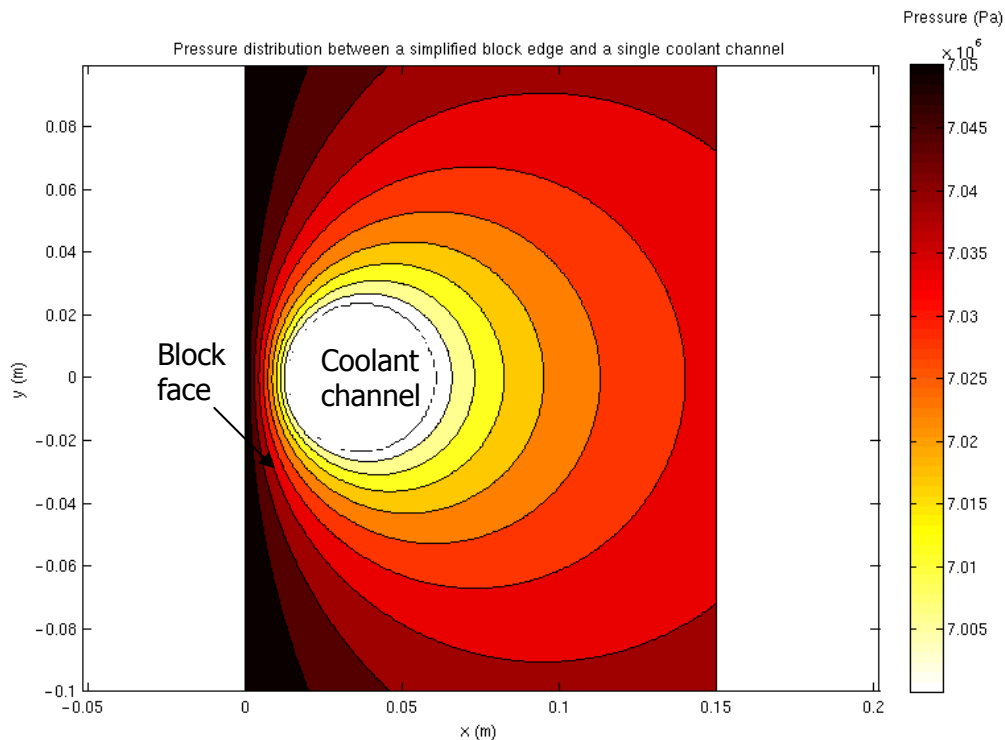


Figure 8.3.7: Velocity distribution of helium through a 12 micron end-face gap surrounding a single HTTR coolant channel near a block edge subject to a 0.5 bar pressure difference

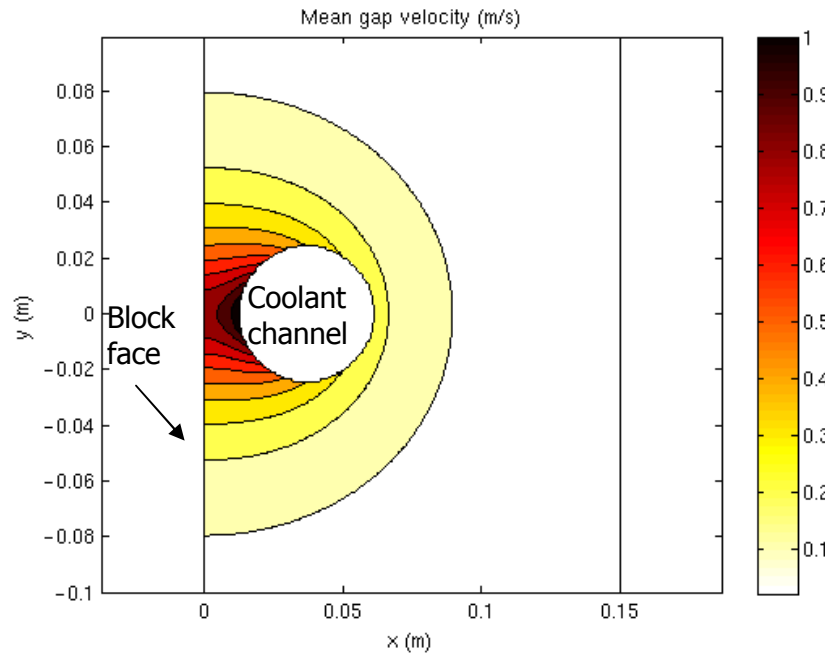
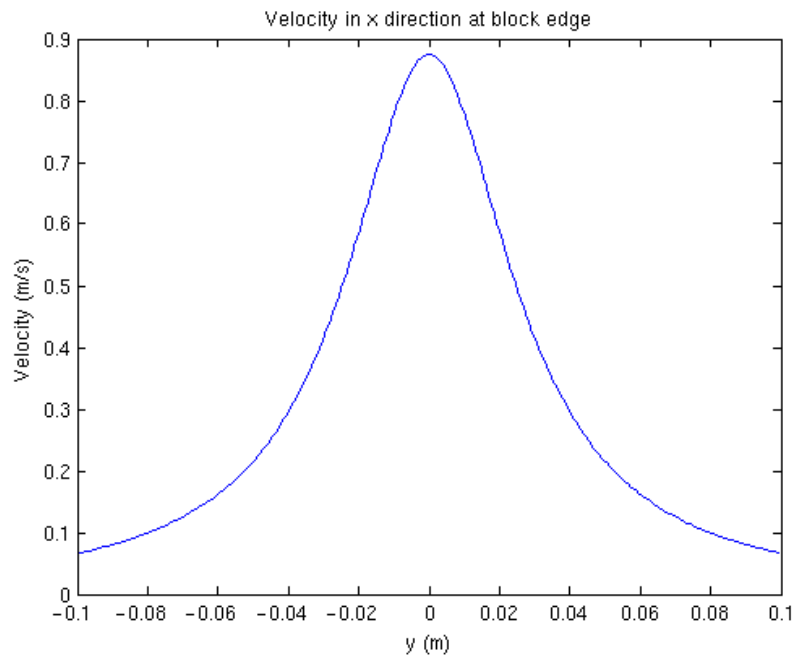


Figure 8.3.8: Velocity profile of helium at the edge (x=0) of a 12 micron end-face gap subject to a 0.5 bar pressure difference



In order to work out an overall mass flow rate across one edge of the hexagonal end-face gap, the mass flow through the gap was integrated between limits $y = -l/2$ and $y=l/2$. The lengthscale l was chosen to represent the length of the flat side of an HTTR block. The net mass flow is found to be:

$$\begin{aligned} \text{Mass flow across one block edge} &= \int_{-l/2}^{l/2} \rho \cdot \delta \cdot u(x, y) \cdot dy \\ &= -\frac{2}{3} \frac{\rho \cdot \delta^3}{\mu} \frac{\Delta P}{\ln\left(\frac{x_c - \alpha}{x_c + \alpha}\right)} \left(1 - \frac{\Delta P}{2P_{out}}\right) \tan^{-1}\left(\frac{l}{2\alpha}\right) \end{aligned}$$

Comparing this relation with the usual kinetic loss factor definition (used in system modeling codes such as RELAP):

$$\Delta P = K \cdot \frac{\rho \cdot V^2}{2}$$

and using standard relations for the mass flow rate, Reynolds number and hydraulic diameter:

$$\dot{m} = \rho \cdot V \cdot A, \quad \text{Re} = \rho \cdot V \cdot d_h / \mu, \quad d_h = 4 \cdot A / (2 \cdot l),$$

where V is the gas velocity, A is the cross-sectional area and $2l$ is the wetted perimeter of the gap, it is found that (for the case $|\Delta P| \ll P$ as found in reactor conditions) the loss coefficient associated with in-flow through the gap at one face of a HTTR fuel block to an edge coolant channel is given by the expression:

$$K = \frac{1}{\text{Re}} \left(\frac{\frac{4}{3} \cdot \frac{l}{\delta} \cdot \ln\left(\frac{x_c - \alpha}{x_c + \alpha}\right)}{\tan^{-1}\left(\frac{l}{2\alpha}\right)} \right).$$

This analytical calculation introduces several approximations when compared to the finite element simulation:

The solution is determined for a semi-infinite domain, neglecting the finite extent of a fuel element edge.

Mass flow outside the region $[-l/2, l/2]$ is ignored during the calculation of the total mass flow rate.

However, the loss coefficients computed using the finite element study and the simplified analytical derivation differed by only 0.65 % for the cases studied in (Reference 8.3).

By comparing the theoretical flow rate with experimentally measured values, an effective gap thickness could be computed. Kaburaki et al.'s analysis of their experimental results yielded an effective gap width of 10.5 microns to 13 microns, in good agreement with the values computed for their simpler cylindrical block experiments.

8.3.3.3 Application of the Kaburaki et al. leakage flow model to GT-MHR fuel blocks

Whilst Kaburaki et al.'s analysis of surface roughness gap flows proved successful when applied to HTTR fuel blocks, some caution may be necessary in applying this work directly to GT-MHR style fuel blocks. This is due to the closer packing of coolant channels and the presence of multiple coolant channels on each face of the fuel block. Reasons for caution include:

- The closer coolant channel spacing in GT-MHR fuel blocks may invalidate the use of the simplified semi-infinite geometry used in Kaburaki's analytical model
- Neglect of the interaction of leakage flows into adjacent coolant channels within the model
- Uncertainty of the appropriate choice for the lengthscale a used to evaluate the mass flow rate into each channel.

However, Kaburaki's analysis of surface roughness leakage flows has been applied to GT-MHR fuel blocks by researchers at Argonne national Laboratory (Reference 8.8). In this work Vilim et al. evaluated Kaburaki's loss coefficients by replacing the length scale l used in the determination of the leakage mass flow rate by dividing the perimeter of the block evenly among the 18 coolant channels located at the periphery of a GT-MHR fuel block which, for the latter, gives $l = 0.069$ m.

8.3.4 Leakage flows due to gas permeation through graphite

Kaburaki et al. (Reference 8.3), devised a test rig in which high pressure nitrogen could be used to maintain a pressure difference between the inner and outer curved surfaces of an annular graphite cylinder. The pressure difference caused nitrogen gas to permeate through the graphite annulus. The gas flow rate was measured and correlated against the applied pressure drop to quantify gas permeation through the graphite.

The results of the analysis were compared to theoretical analysis based on the Darcy model of flow in a porous media (Reference 8.12) in order to infer the effective permeability of the graphite. During the analysis a systematic variation of the computed graphite permeability with the applied gas pressure was observed, indicating poor agreement between the experimental data and the basic porous medium flow model. This observation led to the use of a modified porous flow model which incorporates the slip of gas molecules over the surface of the micron-sized pores within the graphite. Good agreement between the modified model and the experimental data was obtained.

It should be noted that no experimental analysis of the effect of varying the gas properties or system temperature was performed within Reference 8.3. Therefore the dependence of the permeation flow on gas viscosity presented in this study is unvalidated. The effect of temperature changes on the graphite permeability was also not examined within this work.

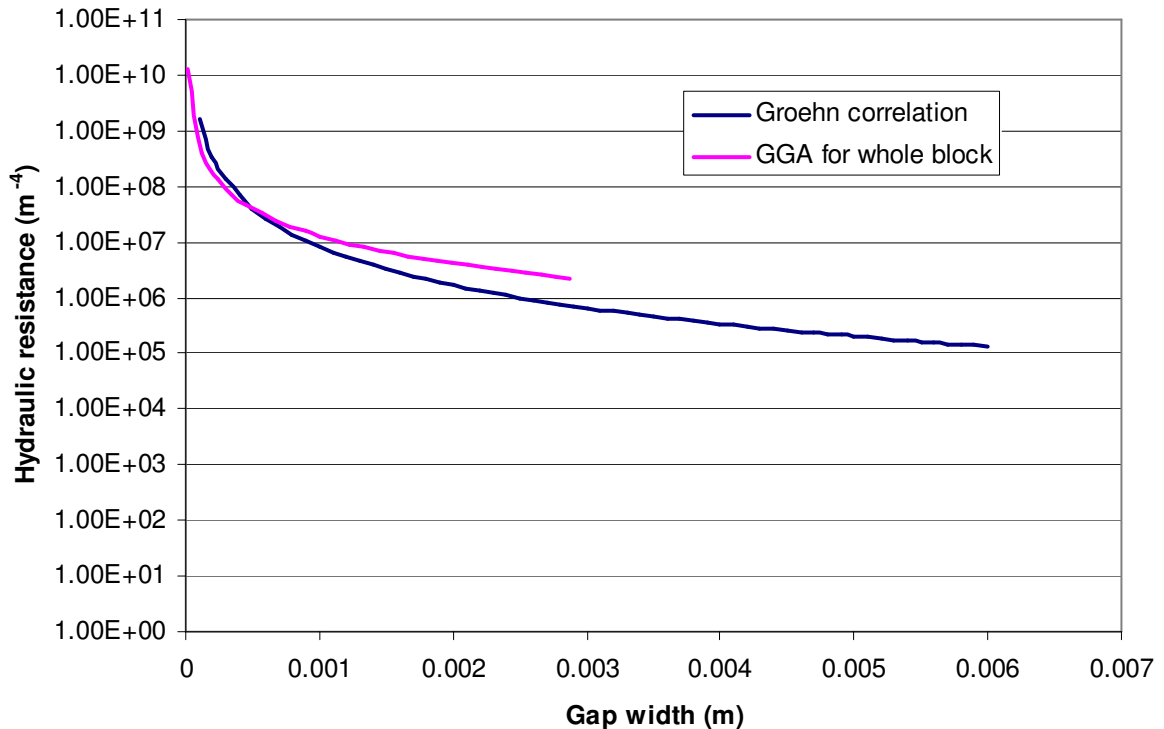
8.4 Comparison of the Published Correlations for Large End-Face Gaps

The hydraulic resistance correlations described in Sections 8.3.1 and 8.3.2 apply to different end-face gap geometries. However, some similarity may be expected between the results. Both correlations take the form of a power-law relationship between the hydraulic resistance and the gap width. However, the exponents of the relationship differ significantly:

Wedge shaped gaps (Section 8.3.1):	$R \propto a^{-2.3}$
Parallel sided gaps (Section 8.3.2):	$R \propto a^{-1.63634}$

In order to facilitate a direct numerical comparison of the data, the parallel gap correlation was normalized to represent the hydraulic resistance for a full fuel element (i.e., 6 block faces). The two correlations are shown in Figure 8.4.1. Significant differences between the predicted hydraulic resistances are apparent.

Figure 8.4.1: Comparison of hydraulic resistances to crossflow through end-face gaps predicted by Groehn (wedge shaped gaps) and GGA (parallel sided gaps)



8.5 RELAP5 Modeling of Leakage Flows in a PMR Core

In order to investigate the leakage flow within a PMR system, RELAP5 models have been created to represent sections of a GT-MHR core.

RELAP5 (Reference 8.10) was originally developed as a water reactor transient analysis tool. However, the code features a rigorously derived and implemented non-equilibrium two-phase thermal hydraulics model. This model is capable of handling water/gas mixtures in which the gas phase can be a mixture of a condensable component (steam) and, simultaneously, up to six non-condensable gases. A library of non-condensable gas species is provided and one of these is helium. RELAP5 is thus capable of modeling helium cooled reactor circuits without modification if the void fractions are set to one in all of the gas circuit volumes and the mass fraction of the helium component of the gas phase is set to one also.

Two RELAP5 models were constructed to study leakage flows within PMR reactors:

- A 'one-channel' test model representing a one quarter-block column within the fuelled region of the core, together with the surrounding inter-block space.
- A 'six-channel' model representing a radial slice through the annular fuelled region of the core, comprising of three half-blocks (or six quarter blocks), as shown in Figure 8.5.1 and Figure 8.5.2, together with the inter-block space surrounding the blocks.

In each case, the model extends axially through the entire height of the core, including the upper cold gas plenum, the upper axial reflector, the 10 layers of fuel blocks within the core, the lower axial reflector and the hot lower plenum. The 'super-meso' scale fuel element model described in Section 7 was incorporated into the RELAP5 models to allow the prediction of fuel and graphite temperatures. The models are described in detail in the following sub-sections.

Figure 8.5.1: Section of the GT-MHR core, illustrating the region covered by the six channel RELAP model

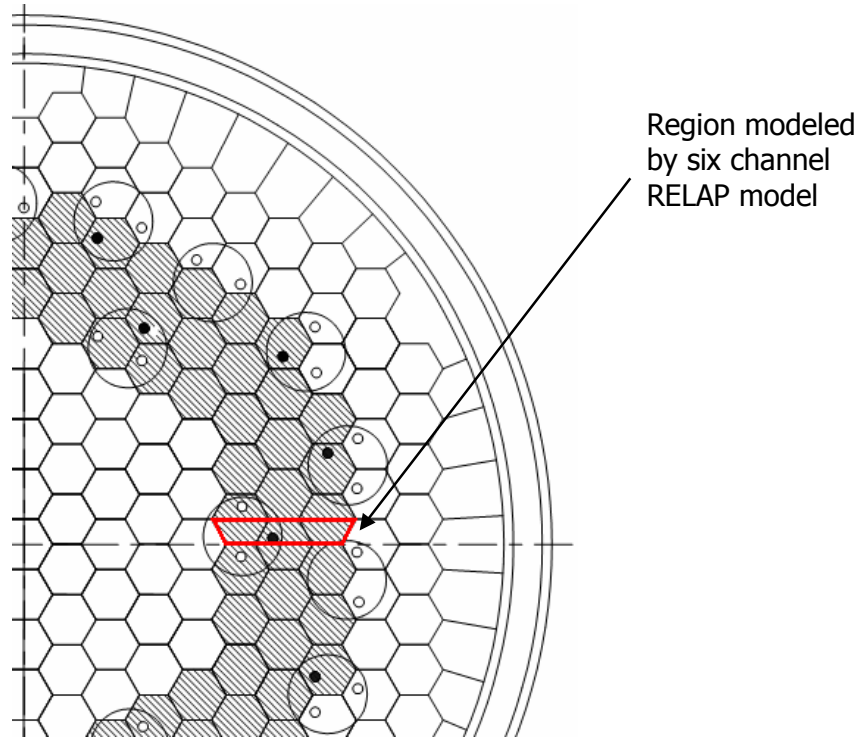
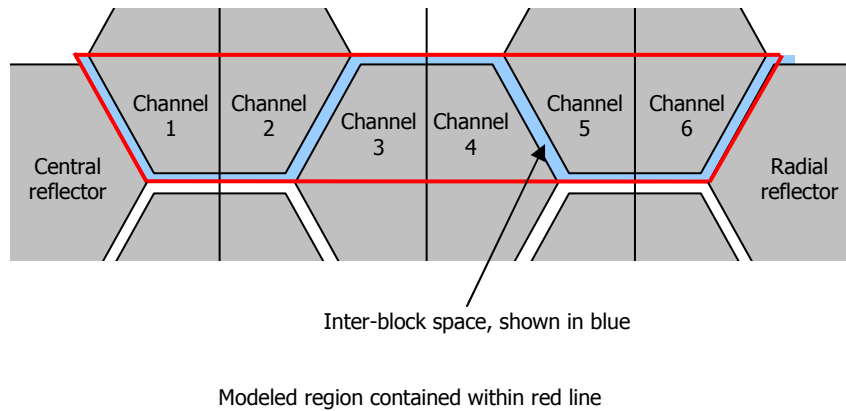


Figure 8.5.2: A cross section of the geometry represented by the six channel RELAP model. The RELAP model represents the area enclosed by the red line.

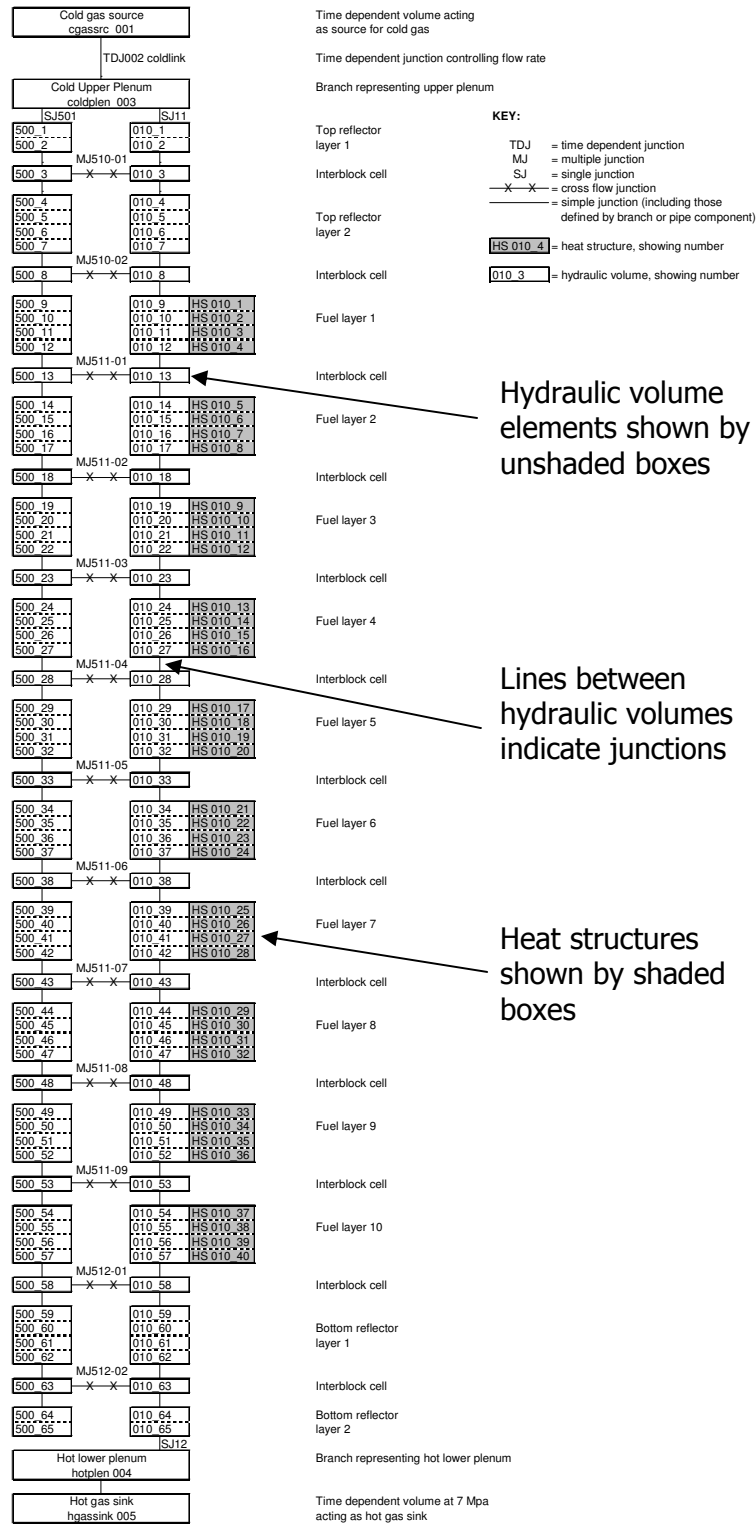


8.5.1 Description of the one-channel RELAP test model

In order to model leakage flows within a PMR core, a simple test model was developed to represent coolant flow and heat transfer within a one quarter-block column within

the fuelled region of the core, together with the surrounding inter-block space. The GT-MHR core contains 102 columns of fuel elements, thus the one-channel RELAP model represents 1/408th of the cross-section of the fuelled-core (Reference 8.1). The RELAP model geometry for the one channel model is shown in Figure 8.5.3, and the model itself is described in detail below.

Figure 8.5.3: Diagram of the one channel, one plenum RELAP model



8.5.1.1 Description of the hydrodynamic model used within the one-channel model

The 27 coolant channels present within one quarter of a GT-MHR fuel block are represented as a single flow channel using a RELAP 'pipe' component. The hydraulic characteristics of the coolant block are imposed by assigning a cross sectional area and hydraulic diameters within the RELAP model. The top and bottom ends of this pipe component are connected to large branch components, representing the cold upper plenum which feeds the core and the hot lower plenum below the core respectively. Entrance and exit loss coefficients of 0.5 and 1.0 respectively are applied at the inlet and outlet junctions of the pipe.

Gas flow into the cold upper plenum at 490°C (763 K) is provided by a time-dependent volume component, with the flow rate regulated by a time-dependent junction component. The nominal GT-MHR core helium mass flow rate is 316 kg s⁻¹, thus a mass flow rate through the model of 0.7745 kg s⁻¹ is prescribed in the one-channel RELAP model. Outflow from the hot lower plenum is facilitated by a time-dependent volume component, which also serves to regulate the system outlet pressure to the GT-MHR operating pressure of 70 bar.

A second RELAP 'pipe' component is used to represent the inter-block space surrounding the fuel blocks. It is assumed that the bottom reflector remains sealed to the core base plate, therefore no connection is made between the inter-block space and the lower plenum. However, flow is free to enter the inter-block space at the top of the core, therefore the pipe component representing the inter-block space is connected to the cold upper plenum using a RELAP 'single junction' component. A loss coefficient of 0.5 is applied at this junction, to represent the entry pressure loss. However, in order to simplify the behavior of this test model, a large area of 4 m², and a large hydraulic diameter of 4 m was assigned to the inter-block space. This ensured the flow rates and pressure drops within the inter-block space were small (realistic inter-block space dimensions are applied in the full six-channel RELAP model described in Section 8.5.4).

In order to resolve the axial variation of the gas temperature within the core and the presence of cross-flow leakage paths between blocks, a detailed axial discretisation of the core is required. This was achieved as follows:

- The 0.75 m central portion of each fuel element (which lies adjacent to the fuel compacts, see Section 8.1) is divided into four 0.1875 m high volumes elements.
- The 0.025 m high region surrounding the fuel channel end plugs at the base of each block was combined with the corresponding 0.025 m region at the top of the block below to form a single 0.05 m hydrodynamic volume centred on the block-to-block interface.
- Each axial reflector was discretised in a manner similar to the fuel blocks. The top-most upper reflector blocks and the bottom-most lower axial reflector

blocks were assigned a height of 0.4 m and were divided axially into two volumes.

This discretisation led to 65 pipe volume elements being used to resolve each of the pipe components, as shown in Figure 8.5.3. An identical axial discretisation was used for the channel representing the inter-block space.

8.5.1.2 Description of the cross-flow leakage paths within the one-channel model

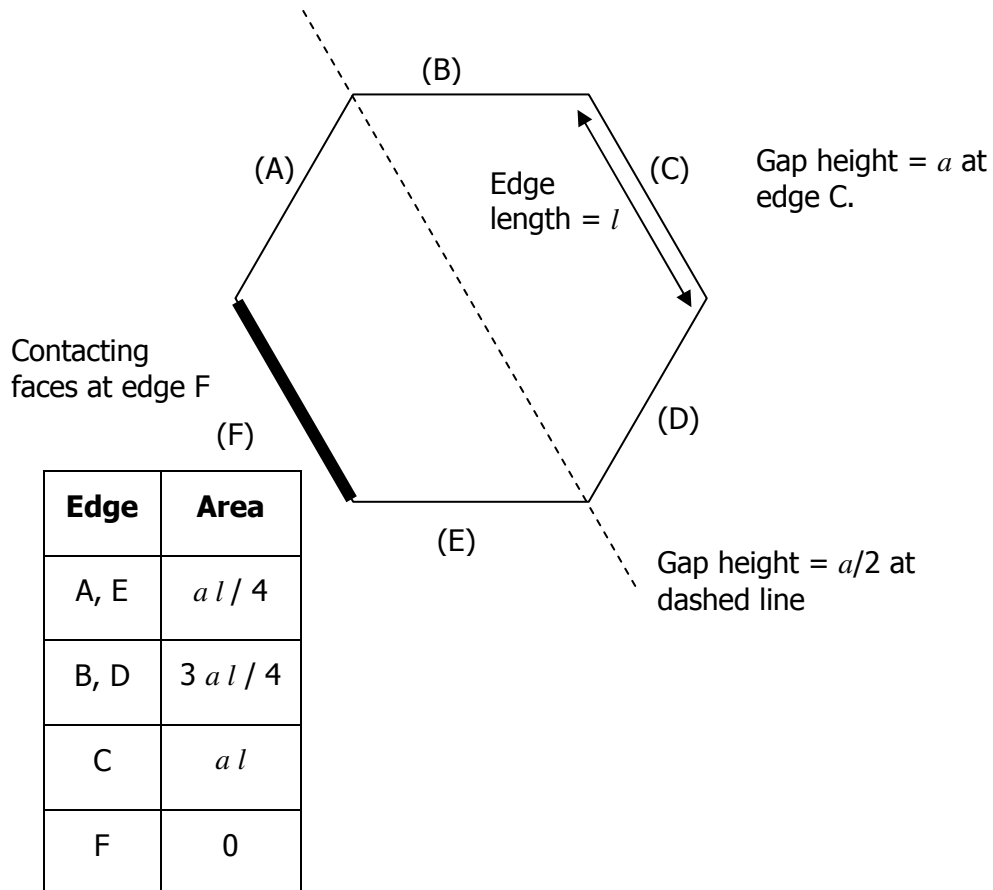
Cross-flow leakage paths between fuel blocks were represented by connections between the 0.05 m high cells located at each block-block interface, using RELAP's cross-flow junction model. Junction flags were set to specify that momentum fluxes were not modeled at these cross flow junctions. The area of the cross-flow junctions is set to be equal to the gap height multiplied by one quarter of the perimeter of the fuel block. In the test model, a gap height of 1 mm was assumed giving a cross-flow leak path area of $3.12 \times 10^{-4} \text{ m}^2$.

The hydraulic resistance of the cross-flow leakage paths is implemented by specifying forward and reverse flow pressure loss coefficients. The forward loss flow coefficient was evaluated using Groehn's correlation (described in Section 8.3.1) with a gap size of 1 mm with no additional blocked gap faces. This leads to a hydraulic resistance for a complete fuel element of $R = 8.22 \times 10^6 \text{ m}^{-4}$. The total area associated with a wedge shaped gap with nominal width 1 mm is (see Figure 8.5.4) $3 \cdot a \cdot l$ or $6.24 \times 10^{-4} \text{ m}^2$. The energy form loss coefficient associated is thus:

$$K_{forward} = R \cdot (A_{wedge})^2 = (8.22 \times 10^6 \text{ m}^{-4}) \cdot (6.24 \times 10^{-4} \text{ m}^2)^2 = 3.2.$$

Within this calculation, no distinction has been drawn between the blocked, partially blocked and open faces of the wedge shaped gap (illustrated in Figure 8.3.1). Thus, this may be considered an average value of the loss coefficient for such a configuration. The published work reviewed in Section 8.3 provides no values for loss coefficients when flow leaves the coolant channels and enters the inter-block space. Therefore the reverse flow loss coefficient was assumed to take a value of 3.2.

Figure 8.5.4: End-face gap areas and configurations used in Groehn's experiment



8.5.1.3 Description of heat structures used in the one-channel model

The graphite and fuel compacts within the fuel elements are modeled using the super-meso-scale model described in Section 5, which is implemented using RELAP5 heat structures.

Heat structures are placed around the coolant channel at each of the 40 axial cells representing heated sections of the fuel elements. Annular heat structures are used, in which the left (i.e., inner) boundary at a radius of $r = 0.008$ m represents the coolant channel surface, and the right (or outer) boundary at a radius of $r = 0.019$ m represents the symmetry boundary at outer edge of the super-meso scale model. RELAP5 cannot readily model axial conduction between adjacent heat structures. Therefore, no heat structures are applied in the unheated regions surrounding the fuel channel end plugs or axial reflectors. The locations of the heat structures are indicated in Figure 8.5.3, by labels of the form HS_010_01.

The three distinct annular material zones within the super-meso scale model (unheated graphite, heated graphite and heated graphite/fuel mix as described in Section 5) are specified within each RELAP heat structure. Constant volumetric heat

capacity and conductivity data were implemented within each region, based on the data presented in Section 5. The radial mesh in the heat-structure is divided into 18 increments (19 mesh points), to replicate the mesh used in Section 5, with 4 mesh increments in the unheated zone, 10 mesh increments within the heated graphite zone and a further 4 mesh increments within the heated graphite/fuel mix zone.

For the one channel test model, a simple uniform axial power profile is applied to the heat structures surrounding the channel. Each heat structure represents a fraction of 1/16320 of the overall fuelled-core volume of GT-MHR. Therefore, this fraction is used as the source multiplier applied to ensure a representative power level is applied to each heat structure within the model.

In this model, no heat structures or heat input are assigned to the RELAP pipe component representing the inter-block space.

8.5.2 Results of the one-channel RELAP model

The one-channel RELAP model was run to obtain a steady-state solution.

The pressure profiles within the coolant channel and inter-block space are shown in Figure 8.5.5. The large cross sectional area and hydraulic diameter assigned to the inter-block space causes the pressure within this pipe to remain almost constant over the height of the core. However, the flow within the coolant channel causes a frictional pressure drop of approximately 2.2×10^4 Pa over the height of the column.

The mass flow rates through the leakage paths between the inter-block space and the coolant channel are shown in Figure 8.5.6. This shows that helium passes from the inter-block space into the coolant channel at each end-face gap within the core. The flow rate is greatest at the base of the core, where the pressure difference between the inter-block space and the coolant channel is greatest.

Figure 8.5.7 shows the helium temperature within the coolant channel and inter-block space across the height of the core. The helium within the inter-block space remains at the reactor inlet temperature, due to the absence of heat structures within the model of the inter-block space. Within the coolant channel, gas temperature is constant within each axial reflector block, where no heat input is applied to the coolant. However, a temperature rise is evident across each fuel block, due to the heat input received from the surrounding heat structures. A temperature decrease is apparent at each end-face gap within the column, caused by cold gas introduced by the cross-flow mixing with the helium within the coolant channel.

Figure 8.5.5: Pressure within the coolant channel of the one-channel RELAP model

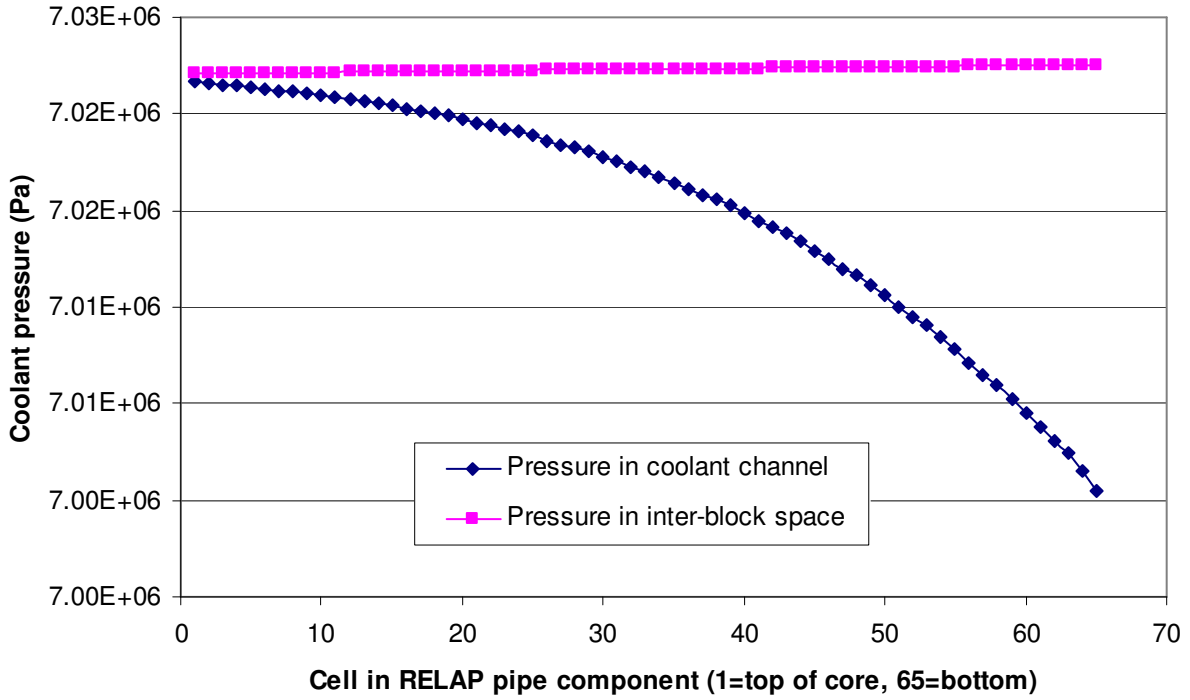


Figure 8.5.6: Leak flow rates from the inter-block space to the coolant channel in the one-channel RELAP model as a function of axial position within the core

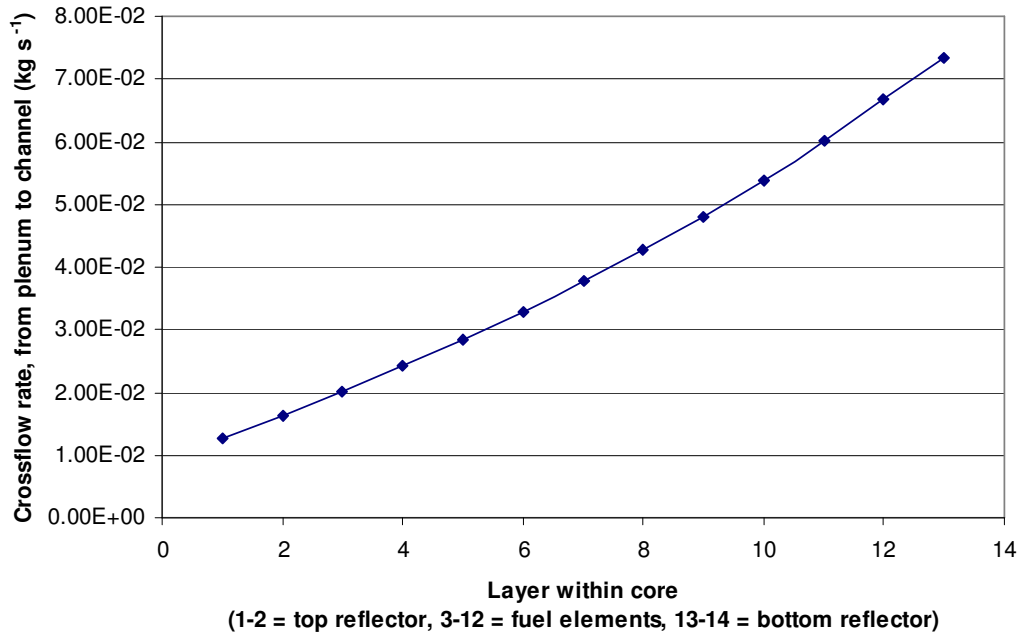
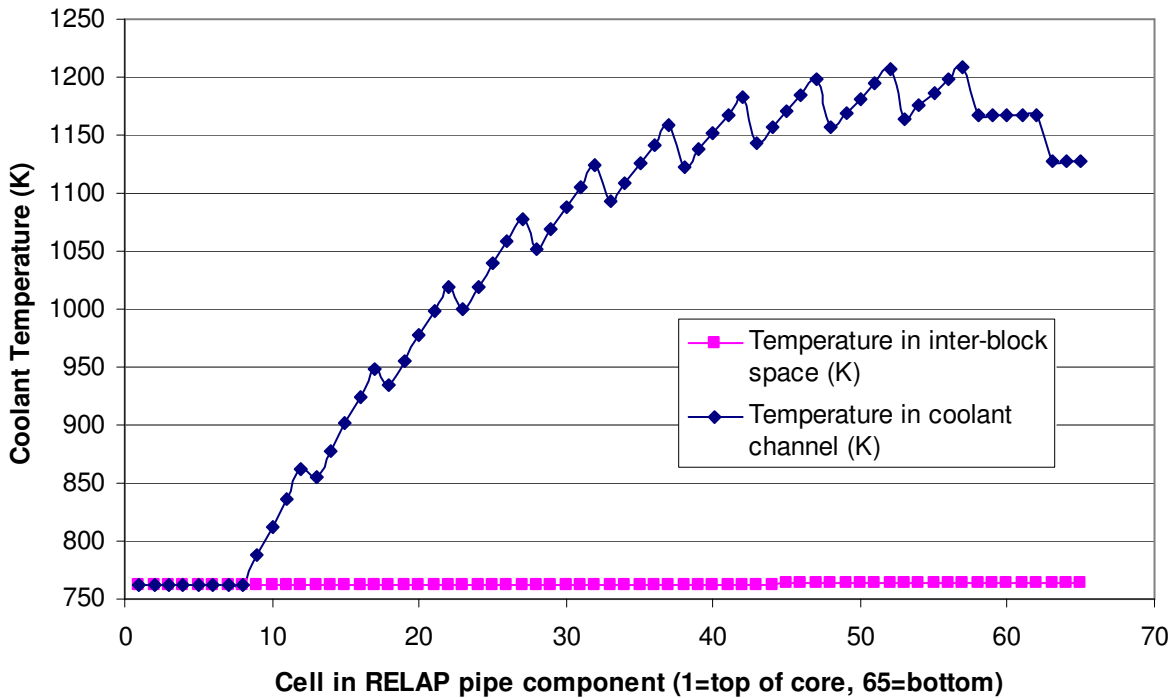


Figure 8.5.7: Gas temperature distribution within the coolant channel of the one-channel RELAP model



The outlet temperature in the hot lower plenum is found to be 1128.3 K, and the temperature within the cold upper plenum is found to be 762.6 K. The predicted temperature increase across the model is thus 365.7 K.

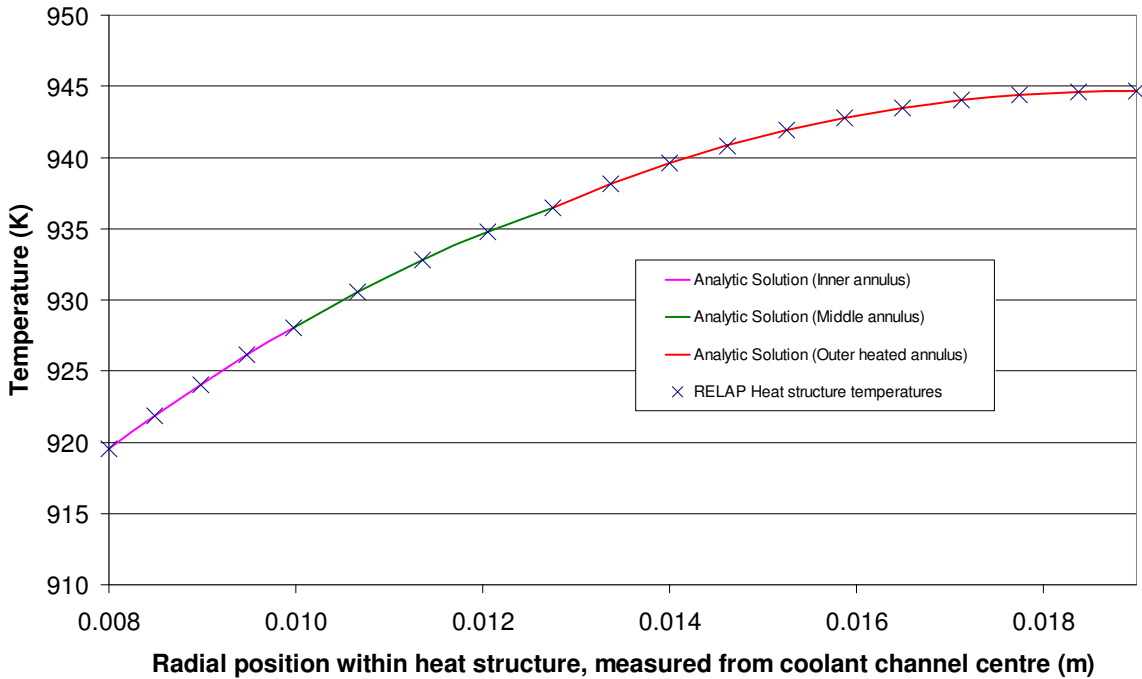
RELAP's output file reports the total power supplied to the coolant channel is 1.47 MW. Thus the expected temperature increase, based on the power input into the column and the helium mass flow rate, is 365.5 K. The small discrepancy between the predicted and expected temperature rise is thought to be due to additional heat generated by work done against the frictional drag forces generated within the flow channels, however convergence and rounding errors introduced by the use of RELAP may also contribute to this small temperature difference.

8.5.3 Comparison of the RELAP heat structure temperatures with the analytical solution of the super-meso-scale model

In order to verify that the super-meso scale model is correctly implemented within the RELAP model, the computed temperature profile within the RELAP5 heat structures has been compared with the analytical solution to the steady state super-meso scale model.

The temperatures at the radial mesh points within the RELAP heat structure located in the top cell of the uppermost fuel block within the channel are plotted in Figure 8.5.8. The heat transfer coefficient applied by RELAP to the left (coolant) boundary of the heat structure was $1092.7 \text{ W m}^{-2} \text{ K}^{-1}$, and the gas temperature in the associated hydrodynamic volume was 787.3 K (both of these values were obtained from the RELAP output file).

Figure 8.5.8: Comparison of the temperatures within a RELAP heat structure with the analytical solution of the super-meso-scale model (The gas temperature in the associated hydrodynamic volume was 787.3 K)



The corresponding analytical solution to the steady state super-meso scale model was evaluated using the method described in Section 5. The analytical solution consists of three distinct expressions, associated with the three annular regions defined by the super-meso scale model. The analytical solutions are plotted as solid lines in Figure 8.5.8. Excellent agreement is apparent between the RELAP results (indicated by 'X' symbols) and the analytical solution.

8.5.4 Description of the six-channel RELAP5 test model

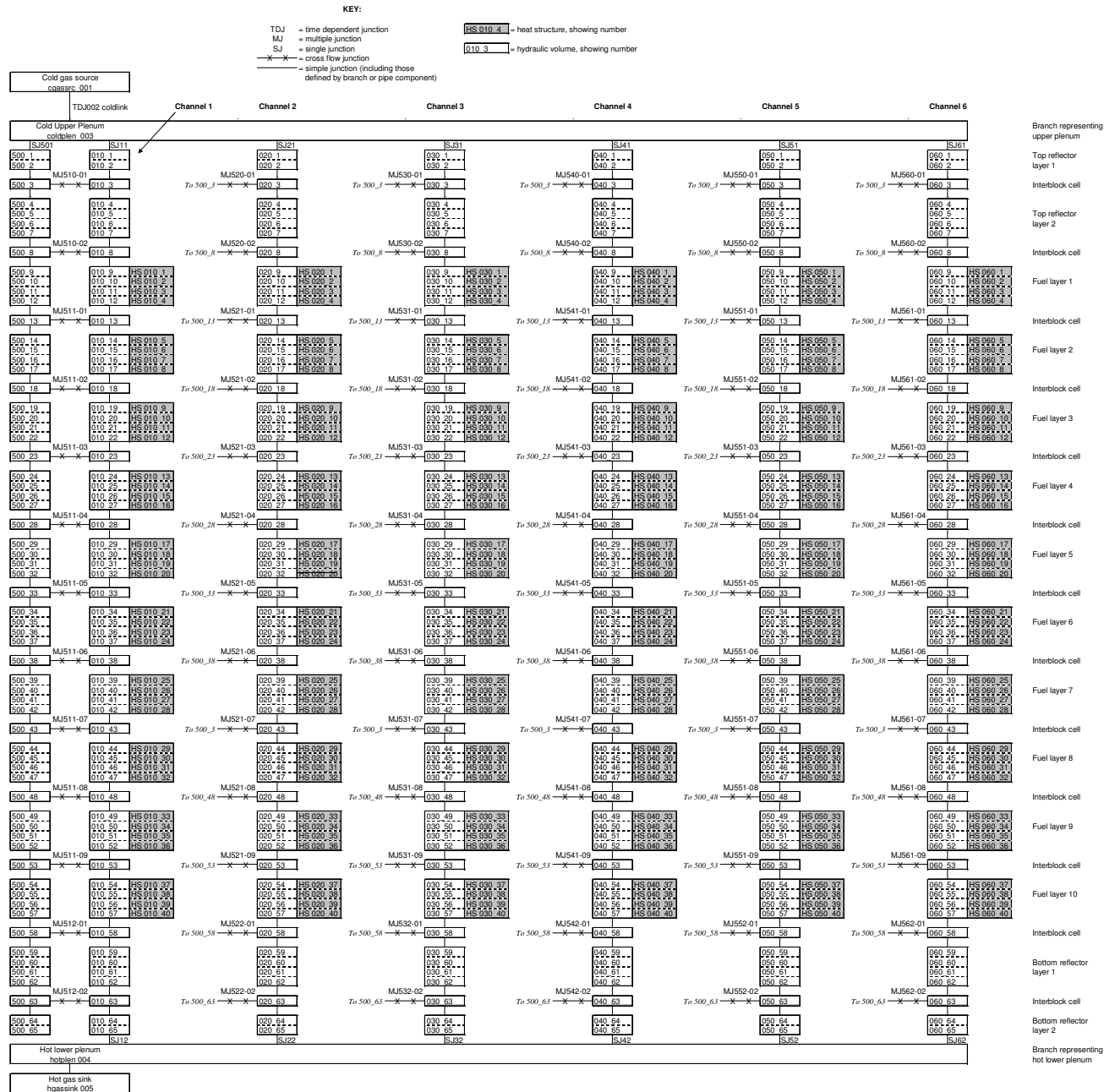
In order to understand the effect of axial and radial power profiles on the leakage flow, a representative slice of the annular GT-MHR core has been modeled using RELAP5. The modeled section of the core is highlighted in Figure 8.5.1. In order to resolve the radial power shape, the section is sub-divided into 6 columns, each representing one quarter of a fuel block column, as shown in Figure 8.5.2. The inter-block space surrounding the six channels is modeled as a single pipe component.

The RELAP5 model is based on the one-channel model described in Section 8.5.1. This was extended by replicating the coolant channel and associated heat structures five times, to form the network shown in Figure 8.5.9. The mass flow rate through the core was set to 6 times the value used in the one-channel test model, resulting in a total mass flow of 4.647 kg s^{-1} through the model.

In the six-channel model, the dimensions of the inter-block space have been set to realistic values, based on an assumed 2 mm gap width between adjacent blocks. The inter-block space surrounding the modeled columns extends over seven block faces, of which three are shared with adjacent fuel element columns and four may be identified with the model core sector only. Thus the cross sectional area of the inter-block space associated with the modeled core section is $2.288 \times 10^{-3} \text{ m}^2$.

The hydraulic diameter of the inter-block space is set equal to twice the gap width, the normal relation for parallel sided channels, giving a value of 4 mm.

Figure 8.5.9: Diagram of the six channel RELAP model with a single inter-block space (pipe component 500, shown on left side of diagram)



8.5.5 Results of the six-channel RELAP model

The six-channel RELAP model was run on to obtain a steady state solution. The results of the model, with a uniform power distribution are shown in Figure 8.5.10 to Figure 8.5.13.

Figure 8.5.10: Mass flow rates through the end-face gap leakage paths for the six-channel RELAP model with a uniform power distribution

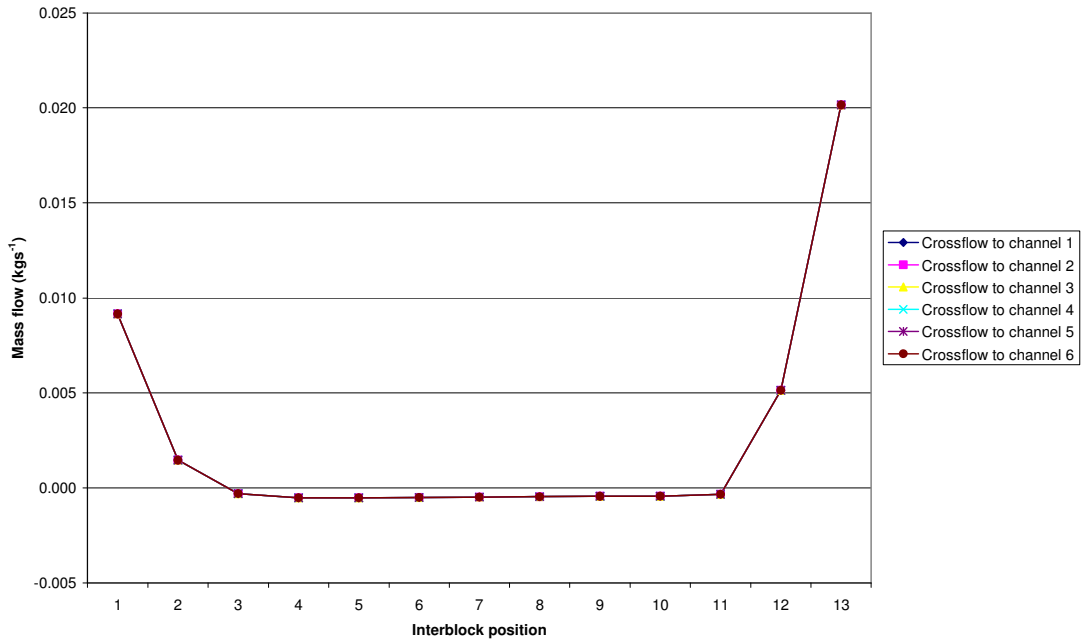


Figure 8.5.11: The mass flow rate within the inter-block space, as a function of axial position within the core for the six-channel RELAP model with a uniform power distribution

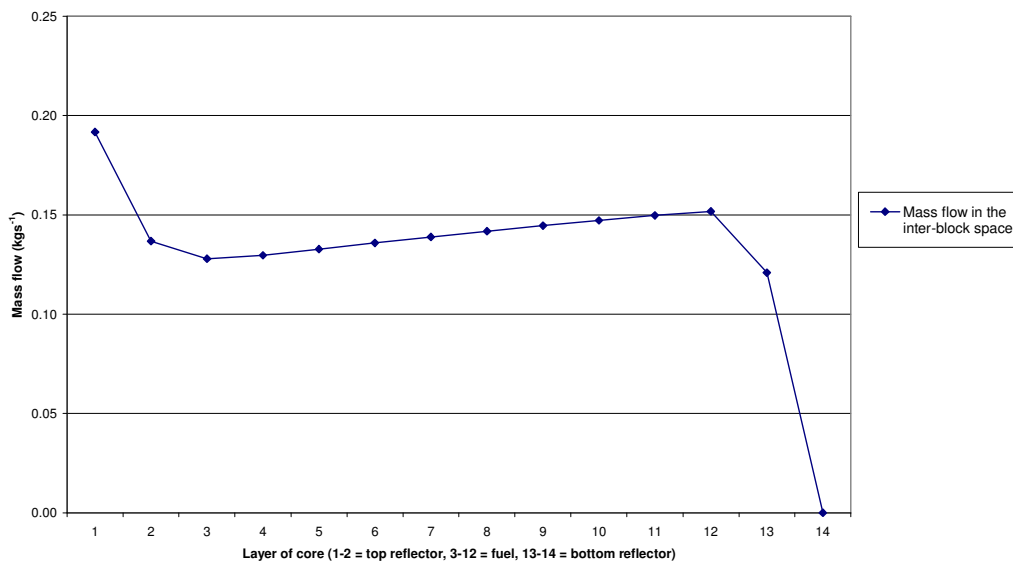


Figure 8.5.12: Coolant temperature distribution measured at the end-face gaps with a uniform power distribution for the six-channel RELAP model with a uniform power distribution

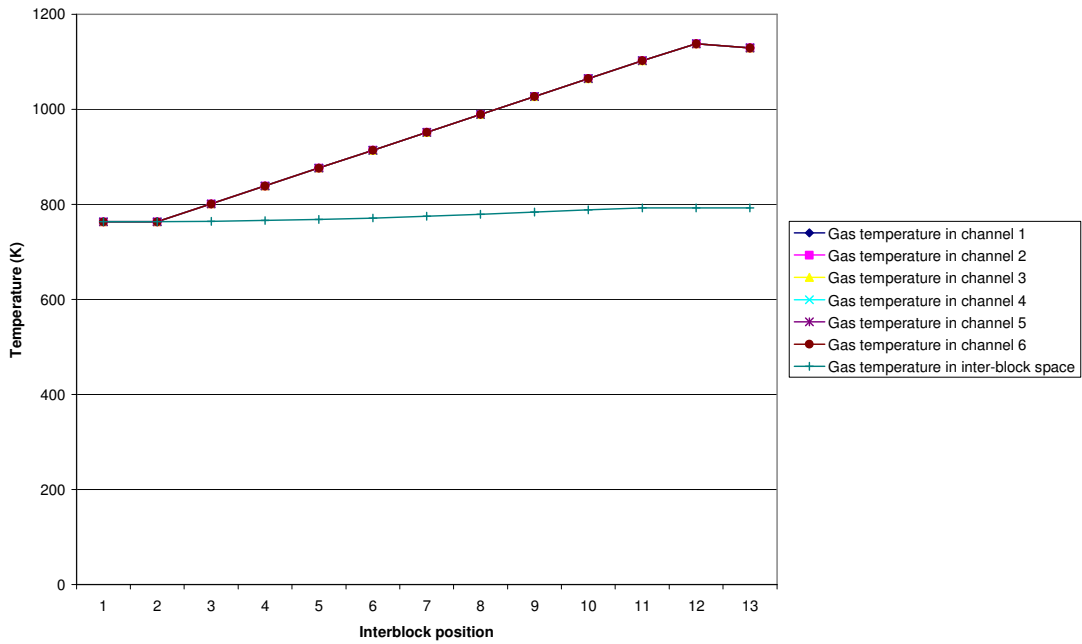


Figure 8.5.13: Pressure distributions in the six-channel RELAP model with a uniform power distribution

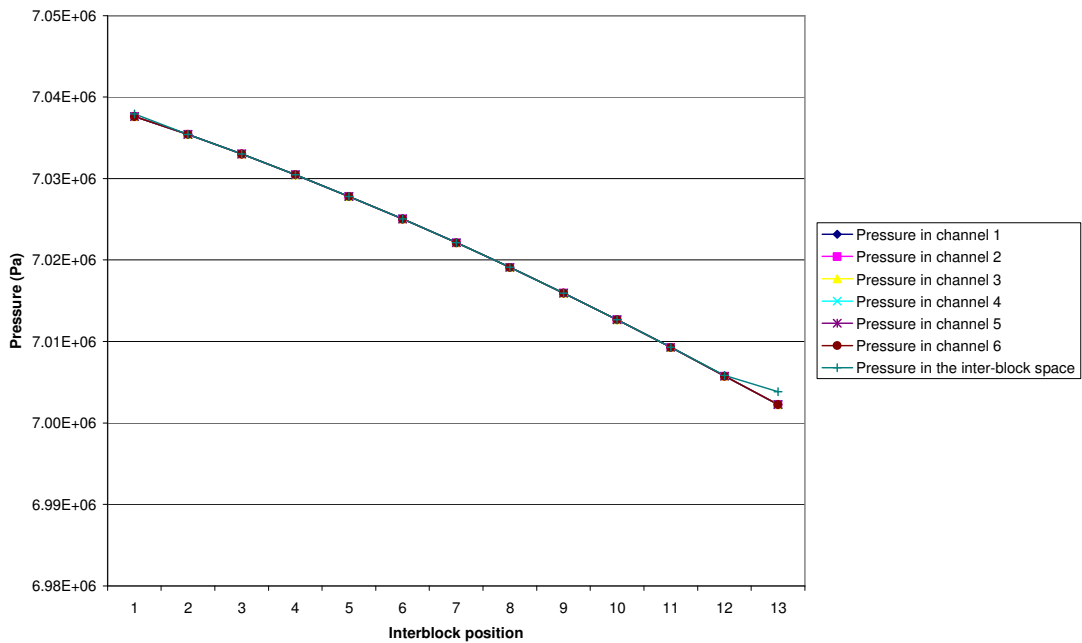


Figure 8.5.10 shows that flow passes from the inter-block space into the coolant channel within the upper and lower axial reflectors. In contrast to the one-channel model results, flow leaks out of the coolant channels, into the inter-block space, within the fuelled region of the core. This input of hot gas from within the fuel block causes a gradual increase in the inter-block space temperatures over the height of the core, visible in Figure 8.5.12. However, the inter-block space remains significantly cooler than the coolant channels in the fuelled region of the core and the lower reflector. The total mass flow rate within the inter-block space, shown in Figure 8.5.11, represents approximately 3.2% of the total flow rate through the six-channel model.

The implementation of a realistic cross sectional area and hydraulic diameter within the model for the inter-block space causes a significant axial pressure drop to occur within this volume, as shown in Figure 8.5.13. However, the flow resistance per unit height of the inter-block space changes little over the core, due to the small variation in gas temperature within this volume. In contrast, the significant increase in gas temperature within the fuel blocks causes the flow resistance within the coolant channels to increase significantly near the base of the core. The resulting variation in the relative resistances of the available flow paths causes flow to redistribute, moving from the coolant channels to the inter-block space, as it passes downwards through the core. The flow redistribution causes the pressures in each flow path to become equal at each axial station within the core, as may be seen in Figure 8.5.13.

8.6 Sensitivity Studies Conducted Using The Six-Channel RELAP Model

In order to understand the variables which affect the coolant channel bypass flows, a range of sensitivity studies have been conducted using the six-channel RELAP model, including:

- Variation of the power distribution
- Variation of the end-face gap widths over the range 0.5mm to 2mm.

These studies are described in the following sub-sections.

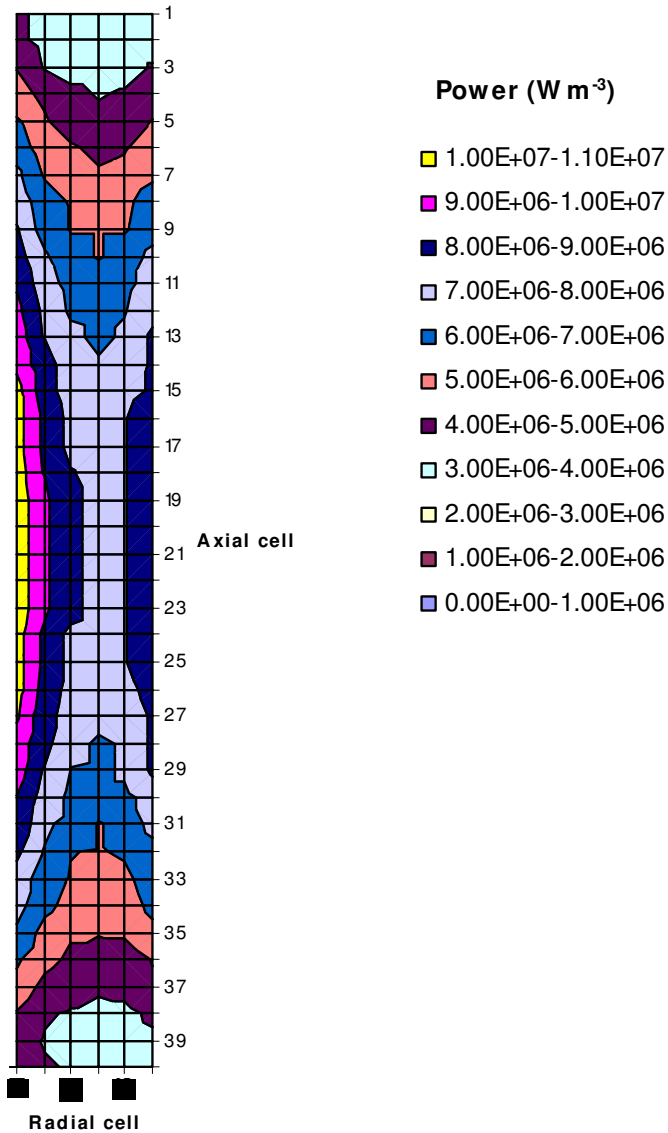
8.6.1 Effect of the power distribution on the leakage flow distribution

The behavior of end-face gap leakage flows have been examined using four distinct power distributions. The four power distributions are described below:

1. A power distribution with a step-wise radial variation, with no axial variation. The power density in columns 1 and 6 are set to 150% of the core average value, to represent the elevated fission power levels expected next to the central and radial reflectors. Columns 2 and 5 are set to the core average power density. Columns 3 and 4 are set to 50% of the mean power level, to ensure the overall power of the six-column model is consistent with the average reactor power.

2. A radially uniform power profile, with a linear axial power distribution, defined such that the top of the core produces 150% of the core average power density, and the base of the core produces 50% of the core average power density. The average power distribution within the model is consistent with the core average value.
3. A radially uniform power profile, with a linear axial power distribution, defined such that the top of the core produces 50% of the core average power density, and the base of the core produces 150% of the core average power density.
4. A middle of cycle power distribution, with control rods withdrawn, computed by a coupled thermal-hydraulic and neutronic analysis of the GT-MHR core design performed by AMEC. The power distribution within a radial slice of the core was obtained from Figure 13 of Reference 8.11. The data from the figure was digitized, and condensed to obtain the six-column, forty layer power distribution shown in Figure 8.6.1, which was applied to the heat structures in the RELAP model.

Figure 8.6.1: The middle-of-cycle power distribution, based on a coupled thermal hydraulic and neutronics study of a VHTR core, obtained from Reference 8.11



8.6.1.1 Effect of radial power distribution on the leakage flow distribution

RELAP results for the step-wise variation of the radial power profile are shown in Figure 8.6.2 to Figure 8.6.4. The results show leakage flow enters the inter-block space from the coolant channels in the high power columns (columns 1 and 6, adjacent to the reflectors). However, the leakage flow passes from the inter-block space into the coolant channels of the low power columns (columns 3 and 4).

Figure 8.6.2: Mass flow rates through the end-face gap leakage paths for the six-channel RELAP model with a step-wise radial power distribution

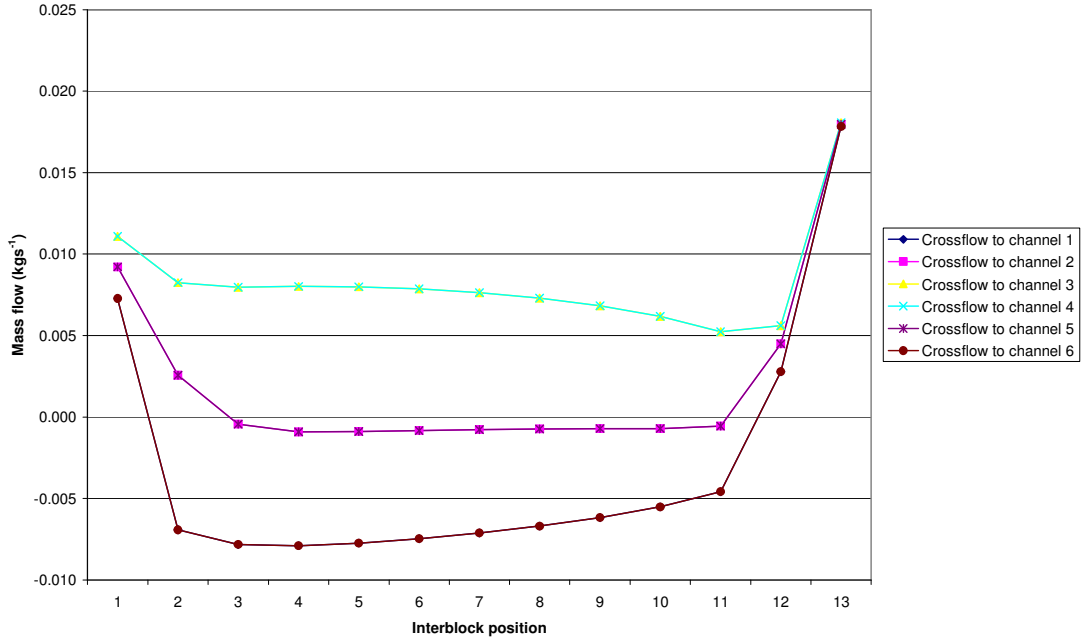


Figure 8.6.3: Maximum temperatures within the fuel blocks for the six-channel RELAP model with a step-wise radial power distribution

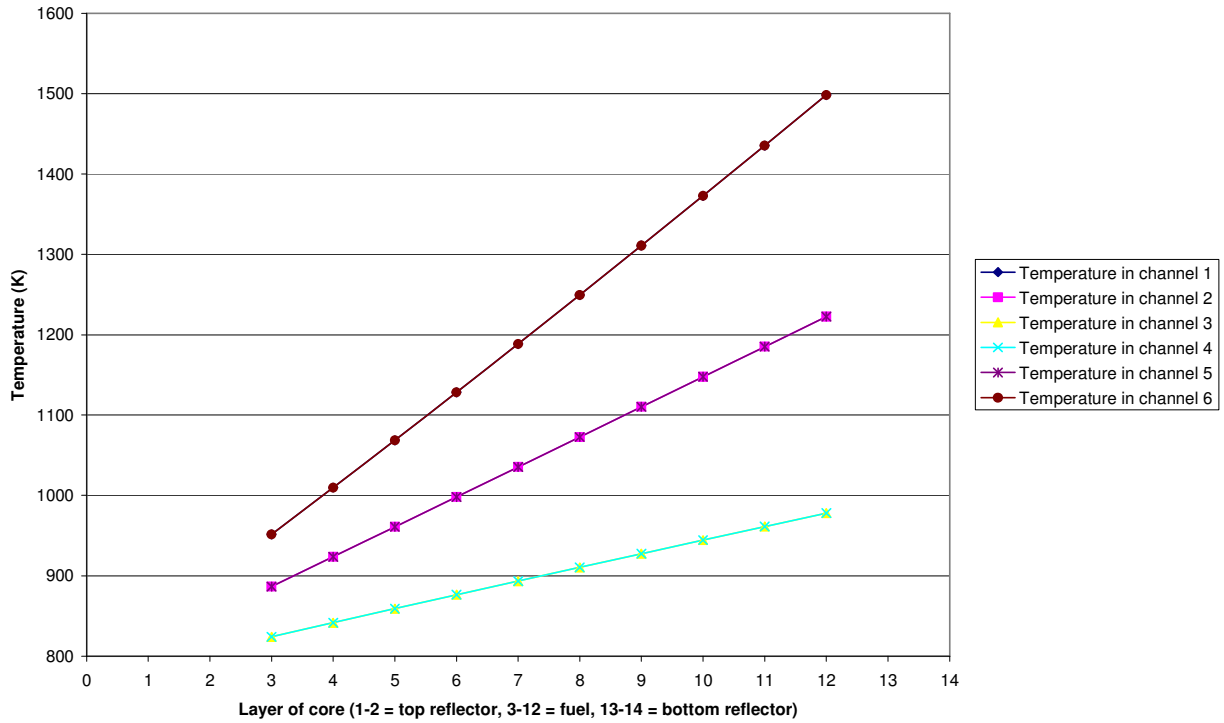
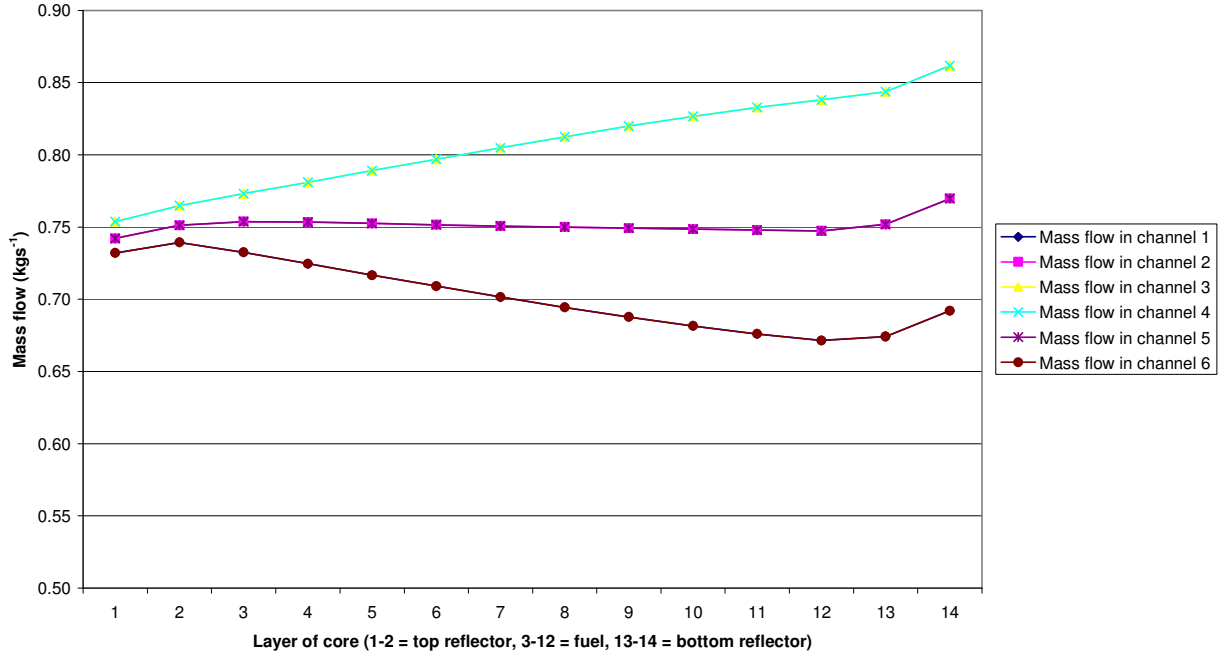


Figure 8.6.4: Coolant channel mass flow variation with axial position in the core for the six-channel RELAP model with a step-wise radial power distribution



This behavior may be understood by noting that thermal expansion of the coolant gas causes the flow resistance in the hotter high power columns to be greater than the flow resistance in the cooler low power columns. Therefore as the coolant heats up during its passage through the core, it will exhibit a tendency to redistribute towards the cooler low power sections of the core.

The flow redistribution mechanism described above results in the coolant bypassing the hottest sections of the core, and flowing preferentially to the cooler columns of fuel elements. The impact of the flow redistribution on reactor temperatures may be assessed by comparing the coolant temperatures at the outlet of the six columns with the power distribution within the corresponding heat structures. The results, shown in Table 8.6.1, indicate that the temperature rise across channels 1 and 6 is 163% of the core average value, although these columns receive only 150% of the core average power density. Similarly, the cooler columns 3 and 4 exhibit just 48% of the core average temperature rise, although they receive 50% of the core average power density.

Table 8.6.1: Comparison of channel temperature rise and column power distribution

Core inlet temperature	762.6 K
Average coolant temperature rise across core	365.2 K

Column Number	1	2	3	4	5	6
Channel Power level (as percentage of core average)	150%	100%	50%	50%	100%	150%
Channel outlet temperature	1358.1 K	1134.9 K	938.9 K	938.9 K	1134.9 K	1358.1 K
Channel temperature rise	595.5 K	372.3 K	176.3 K	176.3 K	372.3 K	595.5 K
Channel temperature rise (as percentage of core average)	163%	102%	48%	48%	102%	163%

The redistribution of coolant due to radial power variations may also be seen in Figure 8.6.5, which shows the results for the non-uniform power profile computed by a combined thermal-hydraulic and neutronic analysis. The overall power distribution exhibits substantial axial and radial variation, with the greatest power being released close to the reflectors. Thus columns 1 and 6 receive the greatest power input, with the minimum power input occurring in column 4, as shown by Figure 8.6.6. This correlates well with the cross-flow leakage rates shown in Figure 8.6.5, which demonstrate that the coolant leaks out of channels 1, 2 and 6, which are hotter than average. However, leakage flows carry helium into the cooler central columns of the core, numbers 3, 4 and 5. Thus the coolant bypasses the hottest sections of the core, due to the increased flow resistance within these regions, as observed above for the step-wise radial power profile.

Figure 8.6.5: Mass flow rates through the end-face gap leakage paths for the six-channel RELAP model with a power distribution based on a combined thermal-hydraulic and neutronic analysis

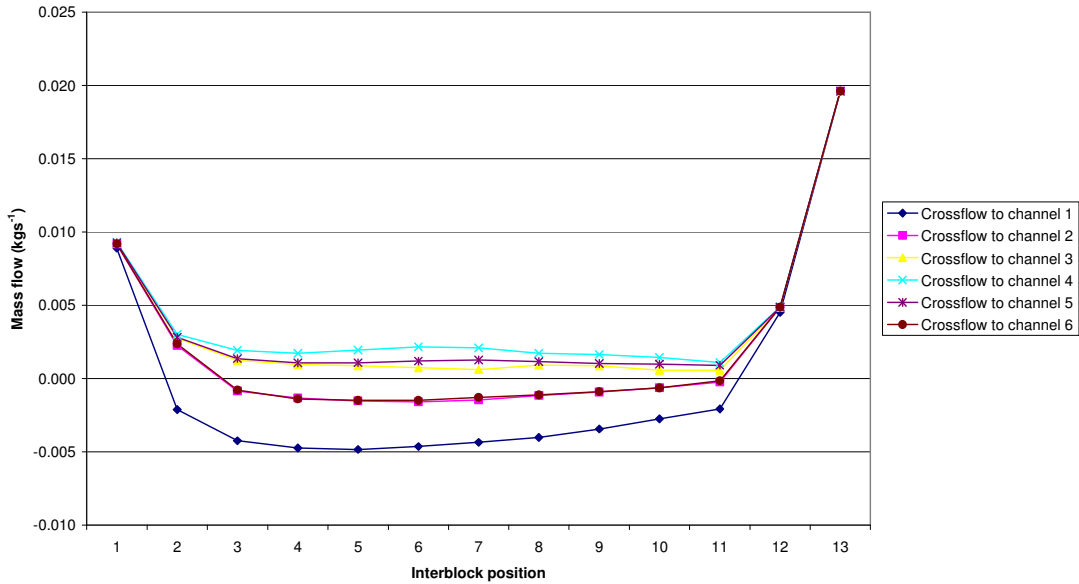
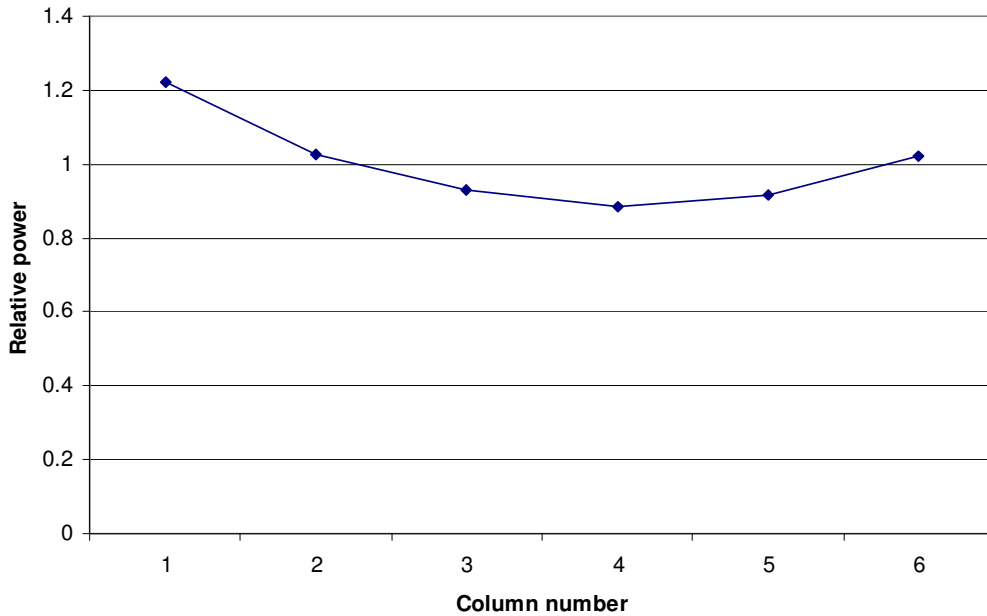


Figure 8.6.6: Overall (integrated axial) relative distribution of power between the six columns for the combined thermal-hydraulic and neutronic analysis power profile



8.6.1.2 Effect of axial power distribution on the leakage flow distribution

Figure 8.6.7 and Figure 8.6.8 report the cross-flow leakage rates for power profiles 3 and 4, in which the power density varies linearly with axial position in the core. The

results show very little difference from the leakage flow rates computed for a uniform power distribution, reported in Section 8.5.5

Figure 8.6.7: Mass flow rates through the end-face gap leakage paths for the six-channel RELAP model with linear axial variation of the power distribution, varying from 50% average power at the top of the core, to 150% at the bottom of the core

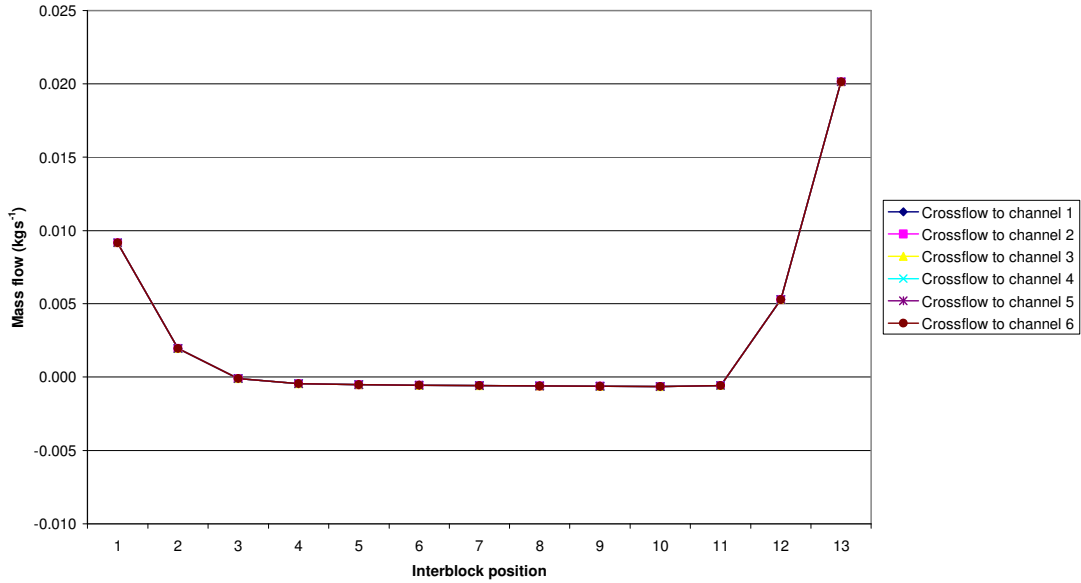
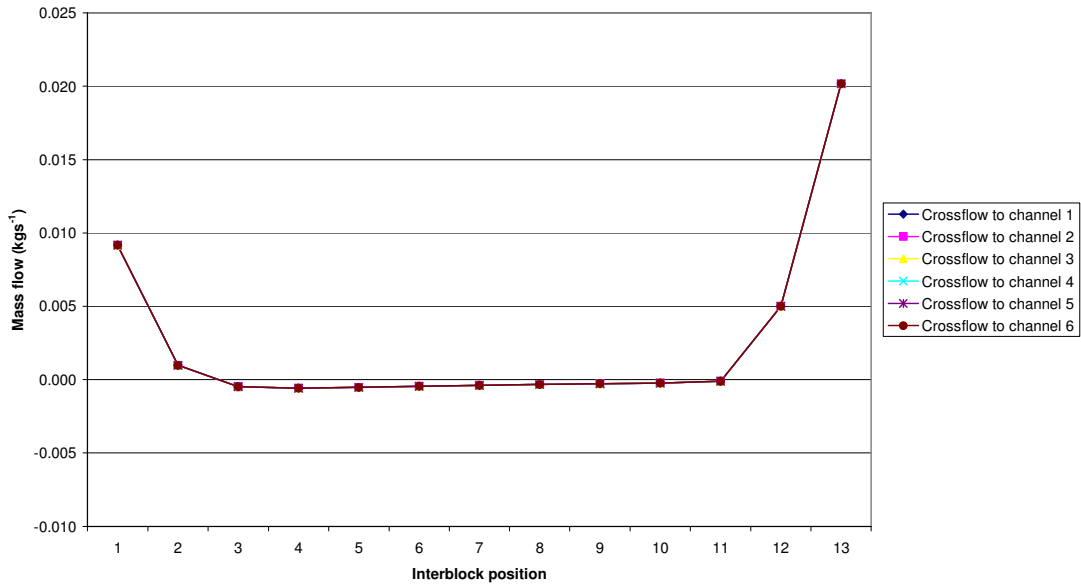


Figure 8.6.8: Mass flow rates through the end-face gap leakage paths for the six-channel RELAP model with linear axial variation of the power distribution, varying from 150% average power at the top of the core, to 50% at the bottom of the core



8.6.1.3 Effect of variation of the leakage path gap widths on the leakage flow distribution

The six-channel RELAP model was run to simulate end-face gap heights of 0.5 mm and 2mm, using the non-uniform power profile based on AMEC's previous coupled thermal-hydraulics and neutronics simulation (Reference 8.11). The junction areas and cross-flow junction loss coefficients were evaluated for each end-face gap size, as shown in Table 8.6.2.

Table 8.6.2: Junction areas and cross-flow loss coefficients for different end-face gap sizes

End-face gap size	0.5 mm (small gap height)	1 mm (reference)	2 mm (large gap height)
Cross-flow junction area in RELAP model:	$1.56 \times 10^{-4} \text{ m}^2$	$3.12 \times 10^{-4} \text{ m}^2$	$6.24 \times 10^{-4} \text{ m}^2$
Cross flow junction loss coefficient, based on Groehn's correlation (Section 8.3.1):	3.94	3.2	2.6

The resulting leakage flows between the inter-block space and the 6 coolant channels are shown in Figure 8.6.9 for the 0.5 mm gap model and Figure 8.6.10 for the 2 mm high end-face gap model. The leakage flows for the 1 mm reference case are shown in Figure 8.6.5. The three sets of results show only a modest difference in the end-face gap flow rates for the three different gap sizes.

Figure 8.6.9: Mass flow rates through the end-face gap leakage paths for the six-channel RELAP model with a power distribution based on a combined thermal-hydraulic and neutronic analysis, based on 0.5 mm inter-block gap height

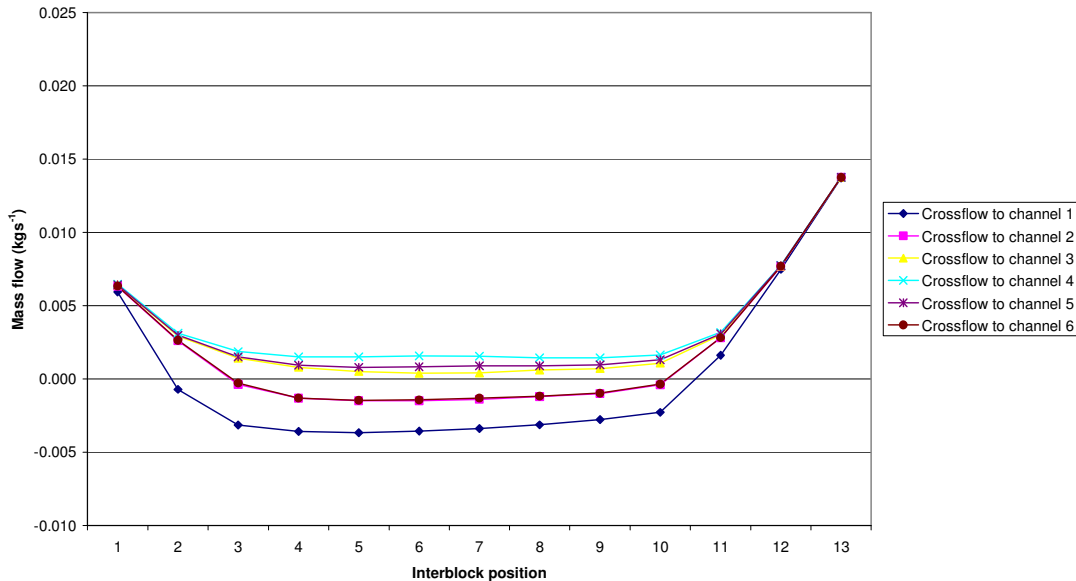
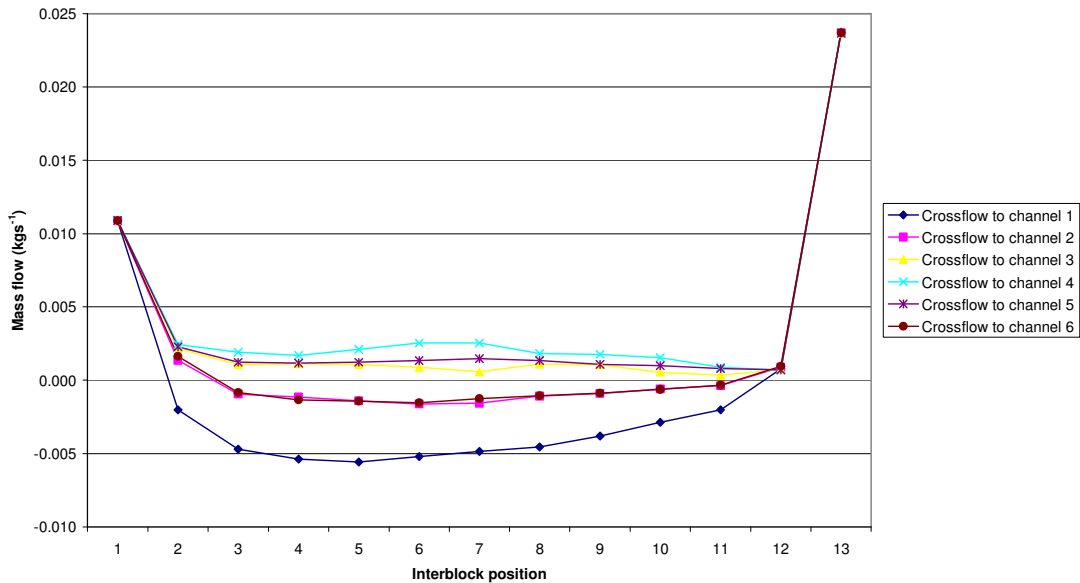


Figure 8.6.10: Mass flow rates through the end-face gap leakage paths for the six-channel RELAP model with a power distribution based on a combined thermal-hydraulic and neutronic analysis, based on 2 mm inter-block gap height



8.7 Closure

A review of the published literature has been performed, and studies of leakage flows within prismatic reactor cores have been identified. Correlations relating cross-flow leakage rates through the gaps between stacked fuel elements (referred to as end-face gap leakage) have been identified, evaluated and compared.

The RELAP thermal-hydraulics modeling code has been used to generate two models representing columns of fuel elements within a prismatic core. Representative power and coolant flow rates were imposed on the models, and cross-flow leakage paths were introduced into the model to allow end-face gap leakage flows to be investigated. The hydraulic resistances of the end-face gaps were evaluated based on correlations identified during the literature review. Heat structures were implemented to simulate the temperature profile within the structure of the fuel elements. The super-meso scale model described in Section 5 was successfully implemented and the results showed good agreement with the analytical solution of this model.

Results of the RELAP model show that the existence of end-face gap leakage paths may allow coolant to bypass the hottest regions of the core. This is shown to amplify the effect of cross-core power variations on the coolant temperature distribution, leading to under-cooling of the hottest fuel elements, and over-cooling of cooler regions of the reactor core.

A range of sensitivity studies were conducted. The results showed that the radial power profile within the core had the most significant effect on cross-flow rates through end-face gaps.

This work has shown that the behavior of the cross-flows within the core is strongly influenced by the power distribution within the core. Specifically the hydraulic resistance of the various flow paths is influenced strongly by the heat transfer occurring within them. Therefore, the flows through the inter-block gaps will be influenced by heat transfer from the outer surfaces of the adjacent fuel blocks and will redistribute according to the distribution of temperatures within the gaps. In the current model, all the inter-block gaps are represented as a single effective pipe component to which heat transfers, through its walls, are neglected. Further work is required to model both heat transfer and transverse flow redistribution within the inter-block gaps accurately. The latter requires refinement of the model presented in Section 7 to represent heat losses from the edges of the fuel blocks correctly.

Following on from the work detailed in this section, the NRC has developed a TRACE model in order to independently verify the RELAP5 core bypass model. The results of this model are provided in Appendix C.

8.8 References for Section 8

- 8.1 'Evaluation of High Temperature Gas Cooled Reactor Performance. Draft of the second CRP-5 TECDOC', IAEA, September 2005.
- 8.2 G.J. Malek, R. Hausermann, 'Analysis of the Multicolumn Flow Distribution Test Data', Gulf General Atomic Technical Report GAMD-8423, 5 June 1968.
- 8.3 H. Kaburaki and T. Takizuka, 'Leakage Flows in High-Temperature Gas-Cooled reactor Graphite Fuel Elements', Journal of Nuclear Science and Technology, Volume 22, Issue 5, May 1985, pp387-397.
- 8.4 H. Kaburaki and T. Takizuka, 'Effect of Crossflow on Flow Distribution in HTGR Core Column', Journal of Nuclear Science and Technology, Volume 24, Issue 7, May 1987, pp516-525.
- 8.5 H. Kaburaki and T. Takizuka, 'Leakage Flow Characteristics of Seal Mechanism for HTGR Core Support Blocks', Journal of Nuclear Science and Technology, Volume 24, Issue 9, September 1987, pp516-525.
- 8.6 Kunihiro Suzuki, Katsuo. Suzuki, H. Mogi, et al. 'Analysis of Core Flow Deviation Caused by the Large Gaps between Horizontal Block Interfaces', Conference article presented at Specialists' meeting on safety and accident analysis for gas-cooled reactors, Oak Ridge, TN (USA). 13-15 May 1985, published in IAEA TECDOC 358, pp313-323.
- 8.7 K. Kunitomi, Y. Inagaki, I. Ioka et al. , 'Experience Obtained from Construction and Preliminary Test of In-core Structure Test Section (T-2)', Conference article presented at Specialists' Meeting on Graphite Component Structural Design, JAERI Tokai (Japan), September 8-11, 1986, published in International Working Group on Gas-Cooled Reactors IWGGCR 11, pp233-238.

- 8.8 R.B. Vilim, W.D. Pointer, T.Y.C. Wei, 'Prioritization of VHTR System Modeling Needs Based on Phenomena Identification, Ranking and Sensitivity Studies', Argonne National Laboratory report prepared for U.S. Department of Energy.
- 8.9 H. Groehn, 'Estimate of Cross Flow in High Temperature Gas-Cooled reactor Fuel Blocks', Nuclear Technology, Volume 56, February 1982., pp392-400.
- 8.10 'RELAP5/MOD3 CODE MANUAL VOLUME II: USER'S GUIDE AND INPUT REQUIREMENTS', NUREG/CR-5535 INEL-95/0174, Idaho National Engineering Laboratory, June 1995.
- 8.11 A. Grief, S. Hunter, J. Murgatroyd, 'A Combined Neutronics and Thermal Hydraulics Analysis of a Prismatic VHTR Core', AMEC Nuclear report GENIV-NNC-VHTR-TR(06)08.
- 8.12 G.K. Batchelor, 'An Introduction to Fluid Dynamics', Cambridge University Press, 1967.

9.0 OVERALL CONCLUSIONS AND RECOMMENDATIONS

9.1 Purpose of Section 9

This section summarizes the work carried out on prismatic modular reactors (PMRs) presented in Sections 5 to 8. Conclusions drawn from this work are presented and topics that would benefit from further investigation are identified.

9.2 Summary of Models Developed and Conclusions

Section 5 was dedicated to the development of multi-scale models of the heat transfer path from the centre of a fuel compact to its neighboring coolant channels. In general this length scale is considered to be the meso-scale. However, for the development of the model the meso-scale was taken to represent a fuel channel and its share of surrounding graphite and a new length-scale, the super-meso-scale was introduced to represent a domain which extended from the centre of a coolant channel out to the centers of the neighboring fuel channels.

The multi-scale model of Section 5 was implemented as a pair of one-dimensional transient finite difference equations solved within cylindrical polar domains. This implementation is fast-running, simple to program in new codes, and readily implemented in existing system codes in which cylindrical heat structures can be adapted to represent the meso and super-meso-scale domains. Comparison of the results of the multi-scale model with finite element simulations showed good agreement both in steady state and transient conditions. The current model allows spatial (temperature and irradiation) dependence of material properties and contact resistance between the fuel compact and their channel walls to be included. However, to ease the comparison with the finite element simulations, spatially constant material properties were assumed (although these differed according to material type).

A model for determining the effective thermal conductivity of complete fuel blocks was presented in Section 6. This model is based on a development of Maxwell's method, extended to include three materials; graphite, fuel compact and helium. The fuel compact itself is a composite solid but, because this has the same structure as a fuel pebble in a pebble bed reactor, the method presented in Reference 9.1 to determine the effective thermal conductivity of fuel pebbles applies to the fuel compact.

Predicted effective thermal conductivities have been compared with values obtained from finite element simulations of sections of fuel block and this comparison shows good agreement over a wide range of fuel compact to fuel block graphite conductivity ratio. Further, the finite element simulations show that the effective conductivities in the transverse directions are isotropic, i.e., the effective conductivity in the across-corners direction is the same as in the across-flats direction. This finding is fortunate as Maxwell's method is based only on the volume fractions and conductivities of the component materials and has no dependence on how the materials are arranged within the composite. As in the work of Section 5, the spatial dependence of thermal conductivities and contact resistances within the fuel channels were ignored.

A first study of macroscopic heat transfer is presented in Section 7. In this, the multi-scale models of Section 5 were extended to couple in the macroscopic scale to allow heat transfer between neighboring sectors in the same block and heat transfers between neighboring blocks to be modeled. Again, finite element simulations of the same scenarios were run for comparison. Unfortunately, macroscopic heat transfer turned out to be more subtle than anticipated and the relatively coarse discretisation of the macro-scale model was unable to capture this subtlety. In particular, heat transfers from the edges of the fuel blocks only affect the edge coolant and fuel channels within the block, with the other channels behaving as if the block dimensions were infinite. An attempt was made to use a semi-analytical temperature profile instead of simple linear functions in the macroscopic model. Whilst this was reasonably successful, it did not satisfy all of the limiting cases and was only applicable to steady state scenarios. Possible further work to improve the macroscopic model is suggested in Section 9.3.

Section 8 presented a study of the influence of core bypass flows in prismatic core reactors. The super-meso-scale model of Section 7 was implemented using the heat structures of a system code, RELAP5/ Mod 3.2. This was used to simulate a 60° sector of a single, full-core-height, column of fuel blocks. This single column was cross-connected at each block end-face to a parallel channel representing the network of inter-block gaps. A further model in which six such columns were represented was also set up to represent a radial spoke of fuel elements through the core. These models showed the pattern of leakage flows is strongly dependent on the power distribution in the core. In general, the leak paths divert flow away from the hotter regions of the core towards the colder, higher coolant density regions. On its own, this is a positive feedback effect, however in reality, the neutronics compensates by reducing the power density in the hot regions and vice versa in the colder regions.

Heating of the coolant in the inter-block gaps will influence the distribution of the leakage flows. However, because of the difficulties found in Section 7, regarding modeling heat loss from the block edges correctly, these heat transfers were neglected in the current model.

9.3 Recommendations for Further Work

The work of Section 5 should be extended to include in the finite element simulations the spatial and temperature dependence of material properties. Further runs of the multi-scale models should be made including these effects for comparison.

Contact resistances between the fuel compacts and fuel channels should be included in the Maxwell model, of Section 6, used for determination of effective thermal conductivities of whole fuel blocks. The finite element model should be modified accordingly to provide a comparison with the Maxwell model.

The macroscopic model of Section 7 needs to be revised to model heat transfers within and between fuel blocks correctly in the presence of steep power gradients. The initially assumed resolution of determining one temperature per 60° sector in a fuel block is inadequate to resolve the complexity in the shape of the temperature

profile within the block. The semi-analytical approach attempted in this work needs to be extended to be consistent with all of the potential limiting cases without the need for ad-hoc switches to different temperature profiles. The semi-analytical approach is likely only to be suitable for steady state scenarios, so further work is required to develop a model that will work correctly in transient conditions.

The core bypass flow model of Section 8 is only a steady state model at the moment and neglects heat transfer into the inter-block gaps. Refinements of the macroscopic scale model of Section 7, together with a fuller implementation of the meso and super-meso models would allow heat input into the inter-block gaps to be included and transients to be simulated.

9.4 References for Section 9

- 9.1 R. Stainsby et al., "Investigation of Local Heat Transfer Phenomena in a Pebble Bed HTGR Core", AMEC NSS Report NR001/RP/002 R01, May 2009.

Appendix A: Models for the Prediction of Fuel and Graphite Temperatures – Additional Results and Derivation of Mathematical Models

This appendix contains additional results and details of derivations presented in Section 5, “Models for the Prediction of Fuel and Graphite Temperatures”.

A.1 Finite Element Solutions for the Meso-Scale Domain

This part of Appendix A presents the results of the transient finite element solutions over the meso-scale domain for the ‘Transient 1’ and ‘Transient 2’ cases referred to in Section 5.2.6. These results are presented as families of curves in Figures A.1.1 to A.1.6, corresponding to different time steps, along each of the straight edges boundaries of the domain for each of the two transients. In these figures, the edges are identified according to the definition given in Figure 5.2.6. The variation with time of the fuel compact average edge and center temperatures and the average temperature of the channel wall are presented in Section 5.2.6 as Figure 5.2.12 and Figure 5.2.13 for the two transients respectively.

Figure A.1.1: Transient model 1 – temperature profiles at various times along the upper edge of the model

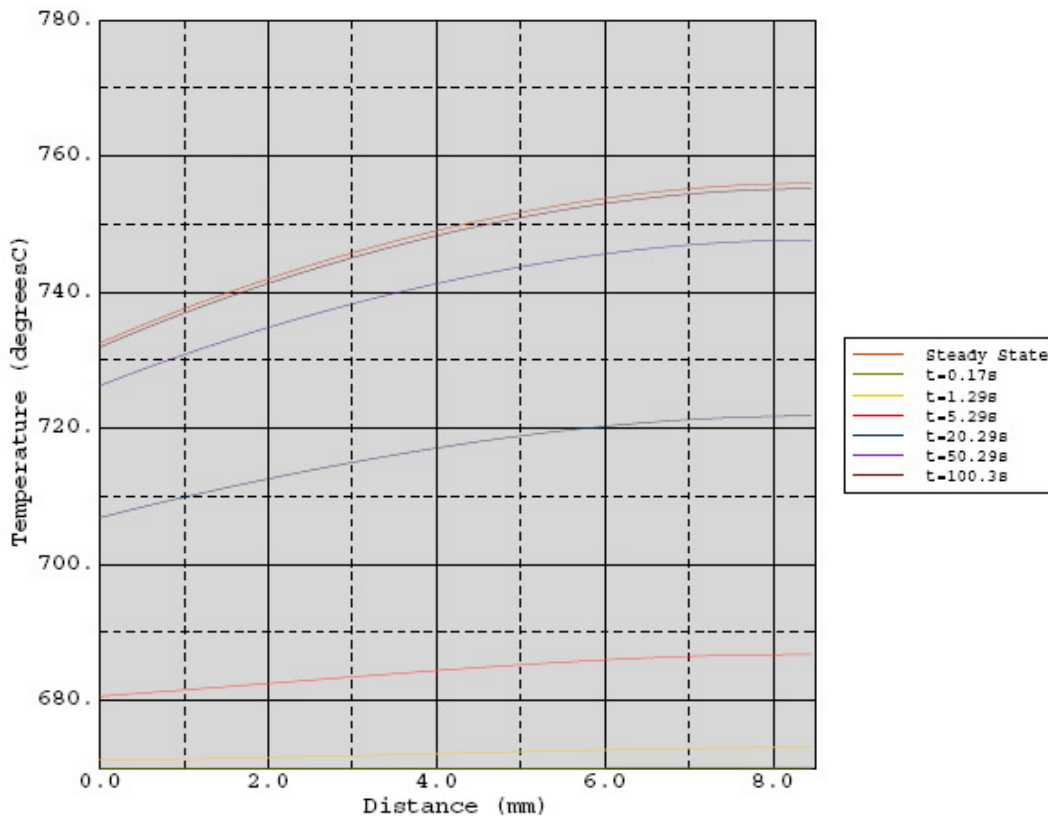


Figure A.1.2: Transient model 1 – temperature profiles at various times along the lower edge of the model

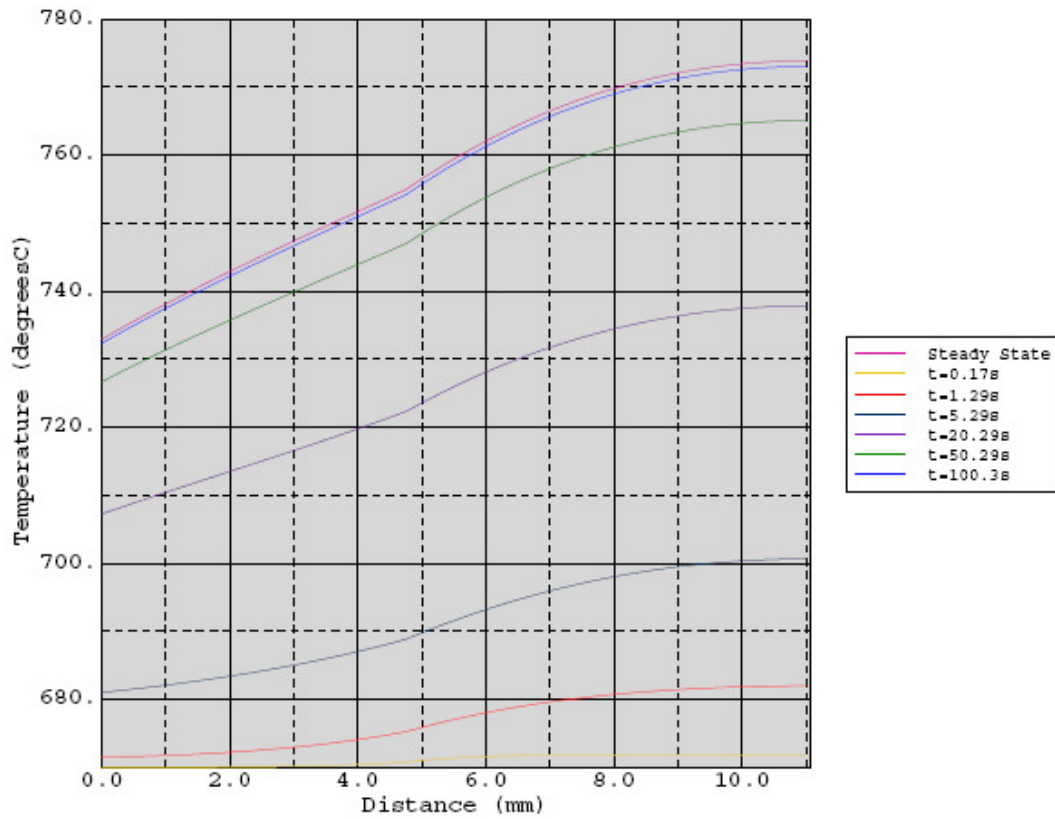


Figure A.1.3: Transient model 1 - temperature profiles at various times along the right edge of the model

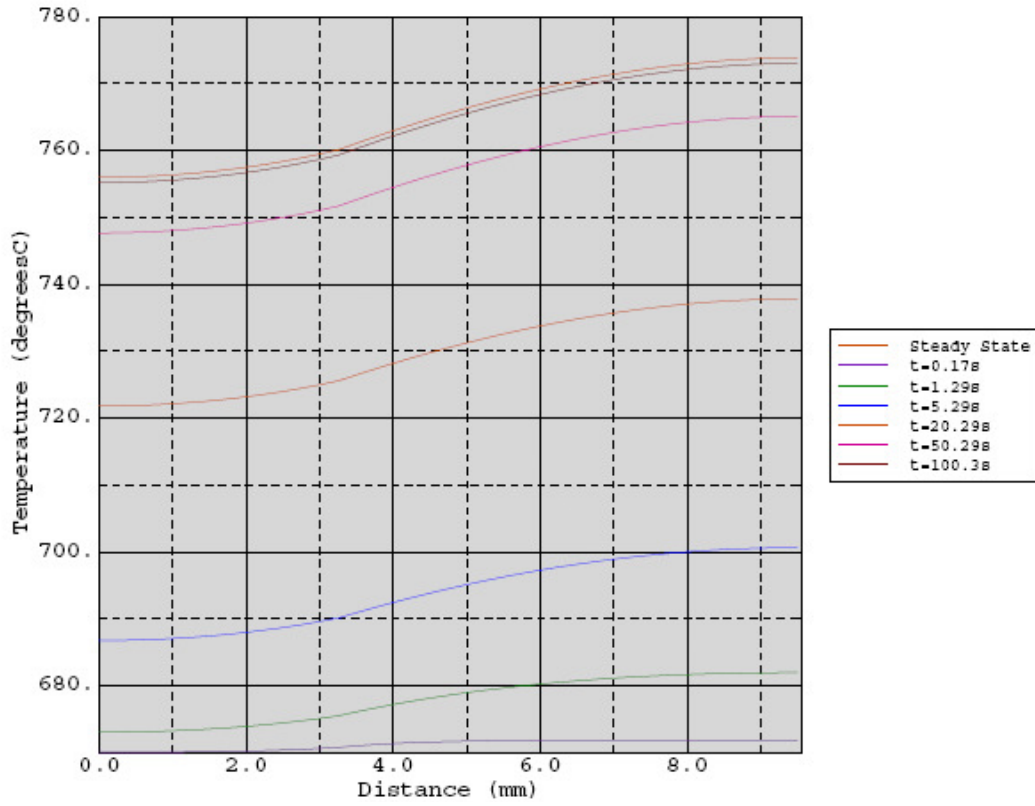


Figure A.1.4: Transient model 2 - temperature profiles at various times along the upper edge of the model

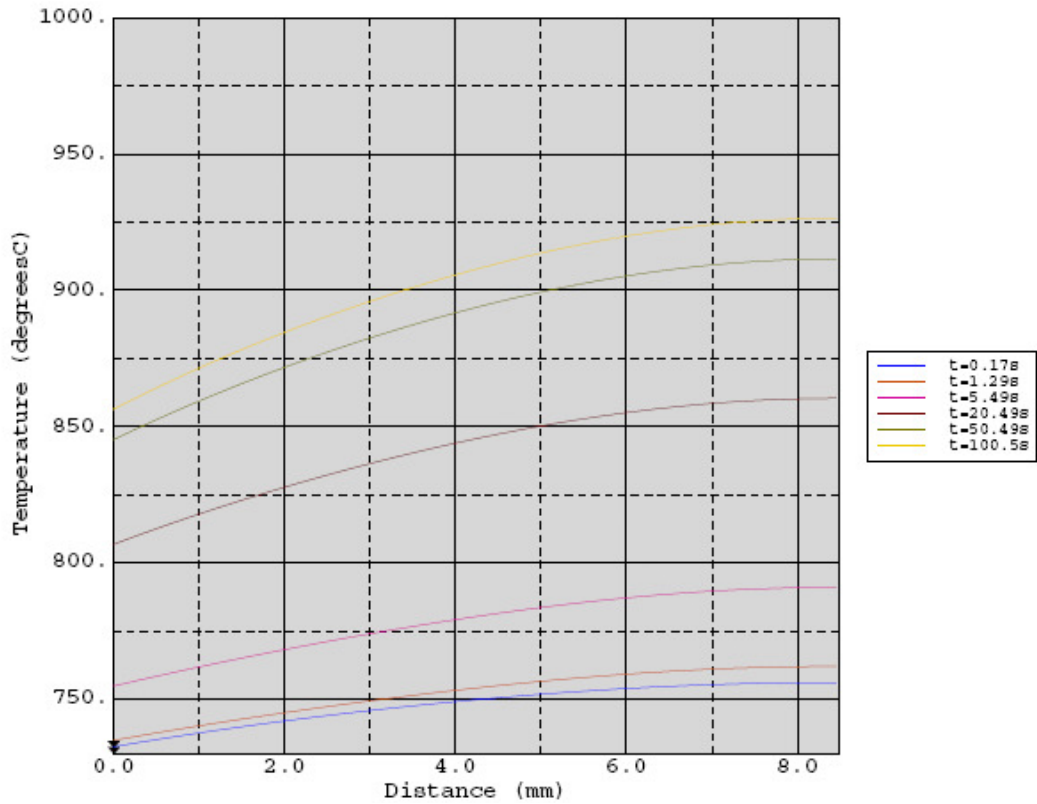


Figure A.1.5: Transient model 2 - temperature profiles at various times along the lower edge of the model

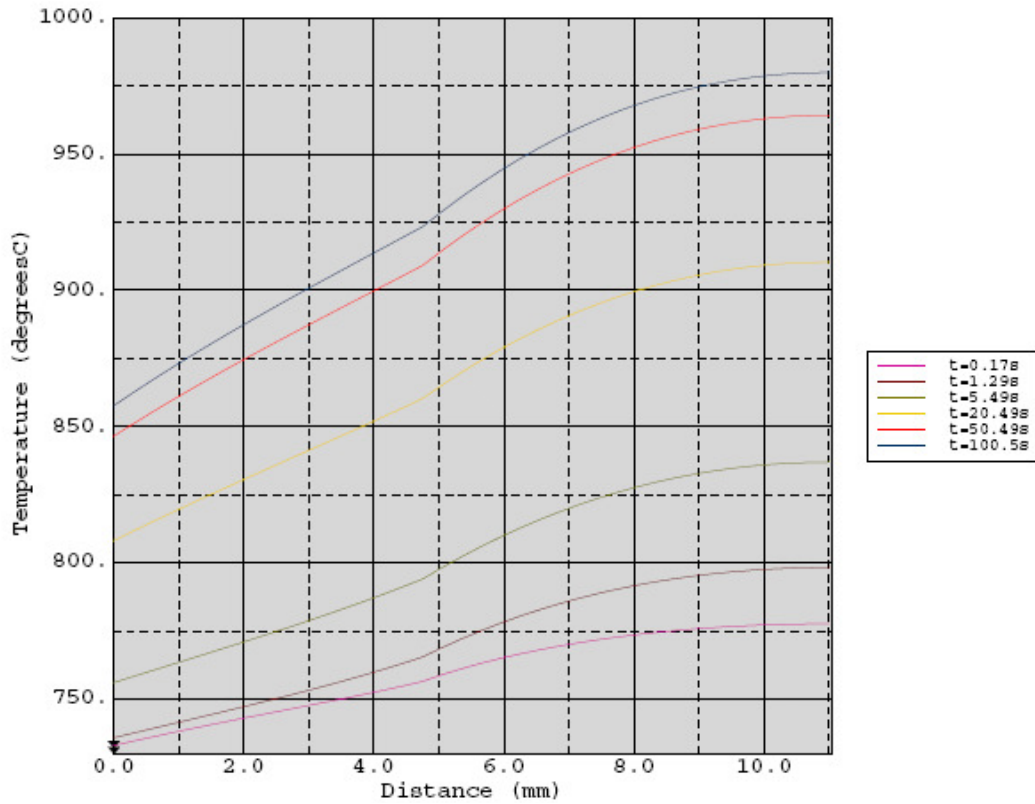
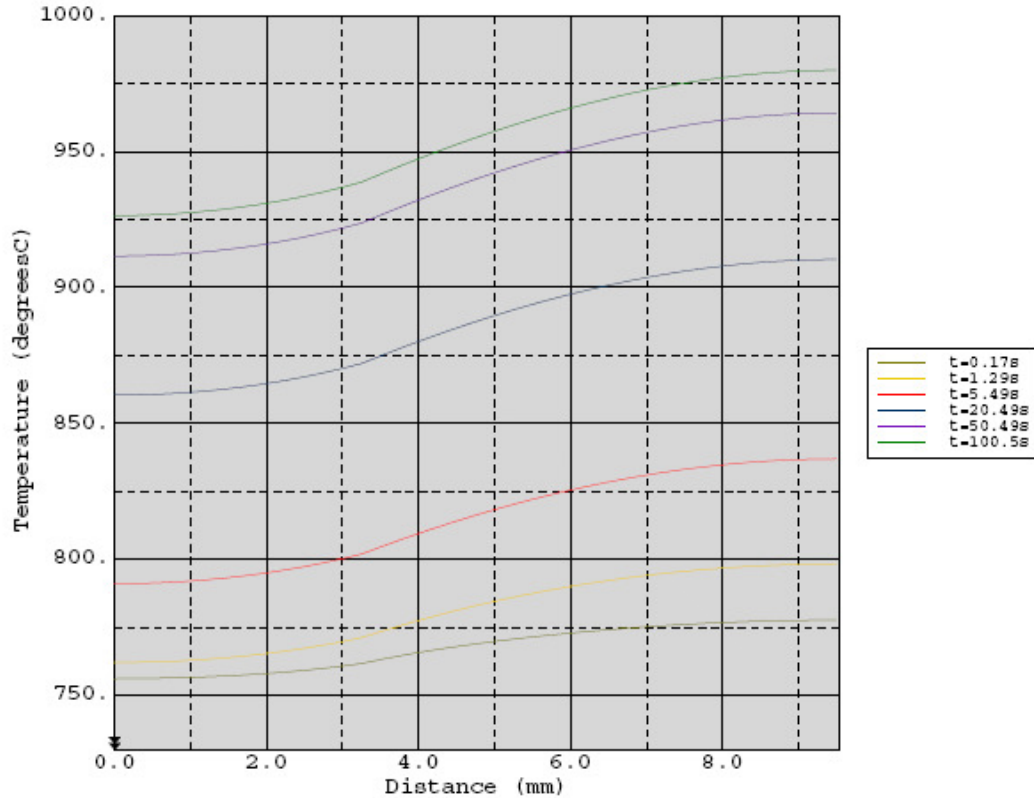


Figure A.1.6: Transient model 2 - temperature profiles at various times along the right edge of the model



A.2 Development of Meso-Scale Sub-Models

A.2.1 Previous Analytical Steady State Approach

The derivation of the analytical steady state model presented in Section 5.3.1 is presented below.

In the simplified geometry of Figure 5.3.2, neglecting heat generation and axial conduction within the graphite, the one-dimensional heat conduction equation is:

$$\frac{1}{r} \frac{d}{dr} \left(r k_G \frac{dT_c}{dr} \right) = 0$$

where k_G is the thermal conductivity of the graphite. Integrating gives:

$$k_G \frac{dT_c}{dr_c} = \frac{A_c}{r_c}$$

where A_c is a constant and a further integration gives:

$$T_c = \frac{A_c}{k_G} \ln r_c + B_c$$

where B_c is a constant also. The boundary condition on the outer surface is the imposed *effective* surface heat flux from the fuel. The effective heat flux is used because the circumference of the domain is greater than the combined circumference of two fuel compacts, therefore the heat flux has to be modified so that the correct total heat input is imposed:

so at $r_c = r_{graph}$:

$$k_G \left. \frac{dT_c}{dr_c} \right|_{r=r_{graph}} = \dot{q}_{f,eff}'' = \frac{2\dot{q}_f}{2\pi r_{graph} L} = \frac{\dot{q}_f'' d_{fuel}^2}{4r_{graph}} = \frac{A_c}{r_{graph}}$$

where d_{fuel} is the diameter of a fuel compact.

Giving:

$$A_c = \frac{\dot{q}_f'' d_{fuel}^2}{4},$$

so, the temperature profile becomes:

$$T_c = \frac{\dot{q}_f'' d_{fuel}^2}{4k_G} \ln r_c + B_c$$

Heat flux to the coolant by convection is given by:

$$\dot{q}_{chn}'' = h(T_{chn} - T_{He}).$$

So the channel wall temperature is:

$$T_{chn} = \frac{\dot{q}_{chn}''}{h} + T_{He}.$$

Equating this and the temperature profile evaluated at the channel wall gives:

$$B_c = \frac{\dot{q}_{chn}''}{h} - \frac{\dot{q}_f'' d_{fuel}^2}{4k_G} \ln r_{chn} + T_{He}.$$

For steady state heat transfer in the absence of heat conduction out of the unit cell:

$$r_{chn} \dot{q}_{chn}'' = r_{graph} \dot{q}_{f,eff}'' = \frac{\dot{q}_f'' d_{fuel}^2}{4}.$$

So the temperature profile in the vicinity of the coolant channel is:

$$T_c(r_c) = T_{He} + \frac{\dot{q}_f''' d_{fuel}^2}{4} \left(\frac{1}{k_G} \ln \left(\frac{r_c}{r_{chn}} \right) + \frac{1}{h r_{chn}} \right).$$

The differential equation representing heat generation and conduction through the domain surrounding a fuel channel, as shown in Figure 5.3.4 is:

$$\frac{1}{r_f} \frac{d}{dr_f} \left(r_f k_F \frac{dT_f}{dr_f} \right) = \dot{q}_f''' \quad \text{for } 0 < r_f < r_{fuel}$$

and

$$\frac{1}{r_f} \frac{d}{dr_f} \left(r_f k_G \frac{dT_f}{dr_f} \right) = 0 \quad \text{for } r_{fuel} < r_f < r_{f,graph}.$$

The general solution within the graphite annulus that surrounds the fuel compact (i.e., $r_{fuel} < r_f < r_{f,graph}$) is:

$$T_f = \frac{A_f}{k_G} \ln r_f + B_f.$$

When $r_f = r_{fuel}$:

$$k_G \frac{dT_f}{dr} = \frac{A_f}{r_{fuel}} = \frac{\dot{q}_f''' d_{fuel}^2}{8 r_{fuel}}$$

giving the first constant as; $A_f = \frac{\dot{q}_f''' d_{fuel}^2}{8}$.

So the graphite temperature in the vicinity of fuel compact is:

$$T_f(r_f) = \frac{\dot{q}_f''' d_{fuel}^2}{8 r_{fuel} k_G} \ln r_f + B_f.$$

The value of the second constant B_f is selected to enforce equality of the mean graphite temperatures obtained from the coolant channel unit cell and fuel compact unit cell models:

$$\frac{1}{(r_{graph}^2 - r_{chn}^2)} \int_{r_{chn}}^{r_{graph}} T_c r_c dr_c = \frac{1}{(r_{f,graph}^2 - r_{fuel}^2)} \int_{r_{fuel}}^{r_{f,graph}} T_f r_f dr_f$$

Within the fuel compact, the solution is that for a solid cylinder with uniform heat generation with its surface temperature dictated by the surrounding graphite;

$$T_f(r_f) = T_f(r_{fuel}) + \frac{\dot{q}_f'''}{4k_F} (r_{fuel}^2 - r_f^2)$$

A.2.2 New Multi-Scale Approach

The derivation of the new multi-scale model as presented Section 5.3.2 is presented below. Figure 5.3.7 showing the original hexagonal cell with the super-meso and meso-scale domains overlaid, and Figures 5.3.8 and 5.3.9, which show the latter two domains separately, present the geometries considered in this derivation.

Neglecting heat conduction in the axial direction, for the moment, reduces the problem to a 2-dimensional transient conduction problem with heat generation. Expressing this in polar co-ordinates with the origin of the co-ordinate system at the center of the coolant channel gives;

$$(\rho c_p)(r, \theta) \frac{\partial T}{\partial t} = \frac{1}{r} \frac{\partial}{\partial r} \left(r k(r, \theta) \frac{\partial T}{\partial r} \right) + \frac{1}{r^2} \frac{\partial}{\partial \theta} \left(k(r, \theta) \frac{\partial T}{\partial \theta} \right) + \dot{q}'''(r, \theta, t)$$

With heat generation in the graphite of the block neglected, and assuming that all of the compacts generate the same power and that heat generation within a compact is uniformly distributed, the heat generation has a distribution that is described by a mean value plus a perturbation within the heated zone and zero outside of it;

$$\dot{q}'''(r, \theta, t) = \bar{q}'''(t) + \hat{q}'''(\hat{r}, t) \quad \text{for } r > r_A$$

and

$$\dot{q}'''(r, \theta, t) = 0 \quad \text{for } r < r_A$$

Where the radial co-ordinate with respect to the center of a compact is not an independent variable in this context, but $\hat{r} = \hat{r}(r, \theta)$.

The power generated by a coolant channel's share of its six neighboring fuel channels (equivalent to the heat generated in two channels) is averaged over the area of the heated zone in the original hexagonal geometry and expressed as the mean power density;

$$\bar{q}'''(t) = \frac{2\dot{q}_f''' r_{fuel}^2}{A_{hex} / \pi - r_A^2} = \frac{\dot{q}_f''' r_{fuel}^2}{r_A^2}$$

where A_{hex} is the area of the original hexagonal unit cell including the sectors of fuel compacts and the coolant channel that lie within, which in this case is 3 times the area of a hexagon that surrounds a fuel compact (or the small hexagon that surrounds the coolant channel, therefore $A_{hex} = 3\pi r_A^2$).

In the circular domain approximation the heated zone has a greater area than the original hexagonal unit cell. Therefore, the average power density is reduced so that the total heat input is preserved:

$$\bar{q}_{eff}'''(t) = \frac{A_{hex} / \pi - r_A^2}{r_B^2 - r_A^2} \bar{q}'''(t) = \frac{2r_A^2}{r_B^2 - r_A^2} \bar{q}'''(t)$$

The perturbation is described, with respect to the distance from the center of a compact, as:

$$\hat{q}'''(\hat{r}, t) = \hat{q}_f'''(t) - \bar{q}'''(t) \quad \text{for } \hat{r} < r_{fuel} \quad (\text{a heat source within the compact})$$

and

$$\hat{q}'''(\hat{r}, t) = -\bar{q}'''(t) \quad \text{for } r_{fuel} < \hat{r} < r_D \quad (\text{a heat sink in the surrounding graphite}).$$

The temperature field is decomposed into super-meso and meso-scale contributions:

$$T(r, \theta, t) = T_{SM}(r, t) + T_M(\hat{r}, t)$$

where again, in this context \hat{r} is not an independent variable, but is a function of r and θ , i.e., $\hat{r} = \hat{r}(r, \theta)$.

The 2-dimensional transient conduction equation with heat generation in cylindrical co-ordinates is decomposed into a pair of 1-dimensional equations representing heat transfer on the super-meso and meso-scales with the effective mean power density and the power density perturbation assigned to these equations respectively. Azimuthal conductivity variations are smeared and the heat capacity is corrected for the non-preservation of domain area (as mentioned above) to give effective values which gives the super-meso-scale differential equation as:

$$\overline{(\rho c_p)}(r) \frac{\partial T_{SM}}{\partial t} = \frac{1}{r} \frac{\partial}{\partial r} \left(r k_{eff}(r) \frac{\partial T_{SM}}{\partial r} \right) + \bar{q}_{eff}'''(t) \quad \text{for } r_A < r < r_B$$

$$\overline{(\rho c_p)}(r) \frac{\partial T_{SM}}{\partial t} = \frac{1}{r} \frac{\partial}{\partial r} \left(r k_{eff}(r) \frac{\partial T_{SM}}{\partial r} \right) \quad \text{for } r_{chn} < r < r_A$$

and

$$\overline{(\rho c_p)}(\hat{r}) \frac{\partial T_M}{\partial t} = \frac{1}{\hat{r}} \frac{\partial}{\partial \hat{r}} \left(\hat{r} k(\hat{r}) \frac{\partial T_M}{\partial \hat{r}} \right) + \hat{q}'''(\hat{r}, t)$$

for the meso-scale.

Using a forward difference for the time derivative gives an explicit finite difference equation for the super-meso-scale temperature distribution;

$$T_{SMi}^{t+\Delta t} = T_{SMi}^t + \frac{\Delta t}{(\rho c_p)_i} \frac{1}{r_i(r_{ei} - r_{wi})} \left(r_{ei} k_{eff,ei} \frac{T_{SMi+1}^t - T_{SMi}^t}{r_{i+1} - r_i} - r_{wi} k_{eff,wi} \frac{T_{SMi}^t - T_{SMi-1}^t}{r_i - r_{i-1}} \right) + \frac{\Delta t}{(\rho c_p)_i} \bar{q}_{eff,i}''(t)$$

for $r_A < r < r_B$, where:

$$r_{ei} = \frac{(r_{i+1} + r_i)}{2}; r_{wi} = \frac{(r_i + r_{i-1})}{2}; k_{eff,ei} = k_{eff}(r_{ei}); k_{eff,wi} = k_{eff}(r_{wi})$$

and similarly for $r_{chn} < r < r_A$:

$$T_{SMi}^{t+\Delta t} = T_{SMi}^t + \frac{\Delta t}{(\rho c_p)_i} \frac{1}{r_i(r_{ei} - r_{wi})} \left(r_{ei} k_{eff,ei} \frac{T_{SMi+1}^t - T_{SMi}^t}{r_{i+1} - r_i} - r_{wi} k_{eff,wi} \frac{T_{SMi}^t - T_{SMi-1}^t}{r_i - r_{i-1}} \right)$$

Similarly for the meso-scale:

$$T_{Mi}^{t+\Delta t} = T_{Mi}^t + \frac{\Delta t}{(\rho c_p)_i} \frac{1}{\hat{r}_i(\hat{r}_{ei} - \hat{r}_{wi})} \left(\hat{r}_{ei} k_{ei} \frac{T_{Mi+1}^t - T_{Mi}^t}{\hat{r}_{i+1} - \hat{r}_i} - \hat{r}_{wi} k_{wi} \frac{T_{Mi}^t - T_{Mi-1}^t}{\hat{r}_i - \hat{r}_{i-1}} \right) + \frac{\Delta t}{(\rho c_p)_i} \hat{q}_i''(t)$$

The boundary conditions applied to the super-meso-scale equation are a convective boundary condition at the coolant channel surface and adiabatic boundary at the outer edge of the domain. However, at the inner edge of the heated zone, the contribution from the meso-scale solution has to be included because the convective boundary condition applies to undecomposed temperature field and the contribution from the meso-scale solution is significant because the length scales of both domains are similar. For simplicity, the contribution from the meso-scale solution is added at the surface of the coolant channel, whilst this is an approximation, it is believed to be not significant as the inner edge of the heated zone is only a small radial distance from the coolant channel wall. Therefore, the channel wall boundary temperature is:

$$T_{chn}^{t+\Delta t} = T_{SM0}^{t+\Delta t} + T_{Mn}^{t+\Delta t}$$

and the surface heat flux crossing the coolant channel wall is:

$$\dot{q}_{chn}'' = h(T_{chn}^{t+\Delta t} - T_{He}) = h(T_{SM0}^{t+\Delta t} - T_{He} + T_{Mn}^{t+\Delta t})$$

In an explicit scheme, this is approximated by using "old" temperatures:

$$\dot{q}_{chn}'' = h(T_{chn}^t - T_{He}) = h(T_{SM0}^t - T_{He} + T_{Mn}^t)$$

Replacing the conductive heat flux term at the channel wall with the above convective form and modifying the geometrical terms to account for the presence of the channel wall gives for the super-meso-scale:

$$T_{SM0}^{t+\Delta t} = T_{SM0}^t + \frac{\Delta t}{(\rho c_p)_0} \frac{1}{(r_{e0}^2 - r_{chn}^2)} \left(2r_{e0} k_{eff,e0} \frac{T_{SM1}^t - T_{SM0}^t}{r_1 - r_0} - 2r_{chn} h (T_{SM0}^t - T_{He} + T_{Mn}^t) \right)$$

The adiabatic boundary at the outer edge of the super-meso domain is applied by setting the temperature gradient at the boundary to zero, which gives:

$$T_{SMN}^{t+\Delta t} = T_{SMN}^t + \frac{\Delta t}{(\rho c_p)_N} \frac{1}{(r_B^2 - r_{wN}^2)} \left(-2r_{wN} k_{eff,wN} \frac{T_{SMN}^t - T_{SMN-1}^t}{r_N - r_{N-1}} \right) + \frac{\Delta t}{(\rho c_p)_N} \bar{q}_N'''(t)$$

The boundary conditions on the meso-scale domain are symmetry at the compact center and adiabatic at the outer edge of the domain. At the center of the compact, the finite difference equation is modified to avoid the division-by-zero introduced by the $1/\hat{r}$ term:

$$T_{M0}^{t+\Delta t} = T_{M0}^t + \frac{\Delta t}{(\rho c_p)_0} \frac{1}{\hat{r}_{e0}^2} \left(2\hat{r}_{e0} k_{e0} \frac{T_{M1}^t - T_{M0}^t}{\hat{r}_1 - \hat{r}_0} \right) + \frac{\Delta t}{(\rho c_p)_0} \hat{q}_0'''(t)$$

Similarly at the outer edge of the meso-scale domain, the temperature gradient at the boundary is forced to be zero:

$$T_{Mn}^{t+\Delta t} = T_{Mn}^t + \frac{\Delta t}{(\rho c_p)_n} \frac{1}{(\hat{r}_n^2 - \hat{r}_{wn}^2)} \left(-2\hat{r}_{wn} k_{wn} \frac{T_{Mn}^t - T_{Mn-1}^t}{\hat{r}_n - \hat{r}_{n-1}} \right) + \frac{\Delta t}{(\rho c_p)_n} \hat{q}_n'''(t)$$

The above finite difference equations represent an explicit scheme that is solved using a simple marching procedure. Conversion to a more stable implicit scheme simply involves replacing the 'old' T^t with the unknown 'new' values, $T^{t+\Delta t}$ values. The solution is obtained by inverting the resulting matrices for both length scales on each time step. However, these matrices have simple tri-diagonal structures allowing the equation systems to be solved directly, and exactly, using a simple recursion formula without requiring full inversions of the matrices.

Appendix B: Fuel Element to Fuel Element Heat Transfer Models – Additional Results and Derivation of Mathematical Models

This appendix contains additional results and details of derivations presented in Section 7, “Whole-Core (Macroscopic) Heat Transfer”.

B.1 Finite Element Solutions for the Macro-Scale Domain

This part of Appendix B presents the additional results of the finite element solutions over the macro-scale domain for the ‘Intra-block’, ‘Inter-block’ and ‘Combined’ cases referred to in Section 7.2. Figures B.1.1 to B.1.6 show sample finite element meshes for each geometry, and Figures B.1.7 to B.1.17 show the heat flux distributions produced for each model variant. The heat fluxes shown are all in units of mW/mm^2 .

Figure B.1.1: Intra-block sample finite element mesh

(Mesh consists of 33134 elements)

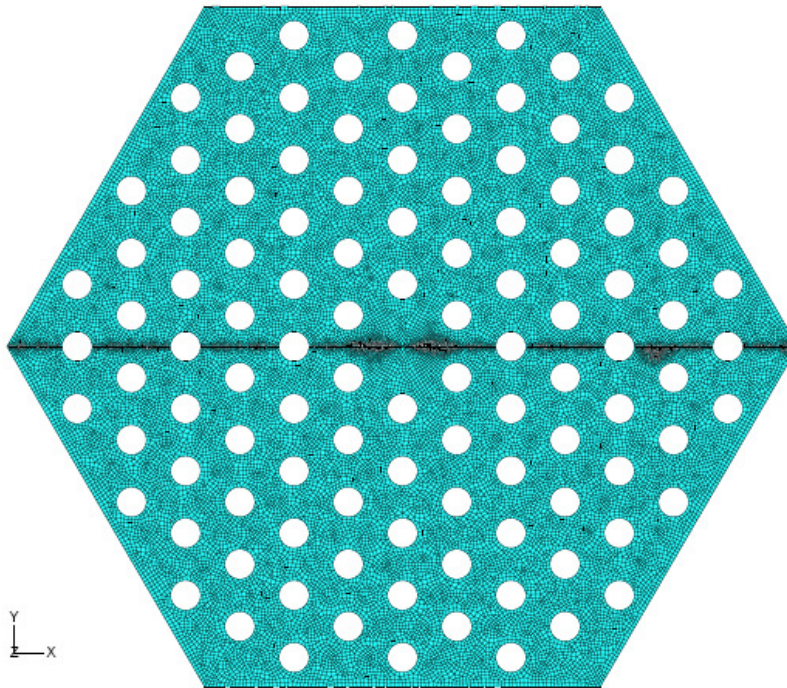


Figure B.1.2: Intra-block close up of sample finite element mesh

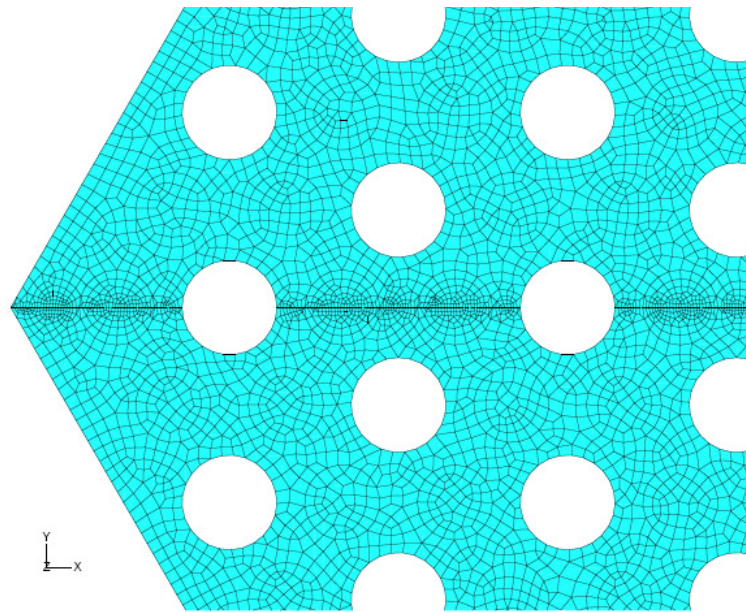


Figure B.1.3: Inter-block finite element mesh

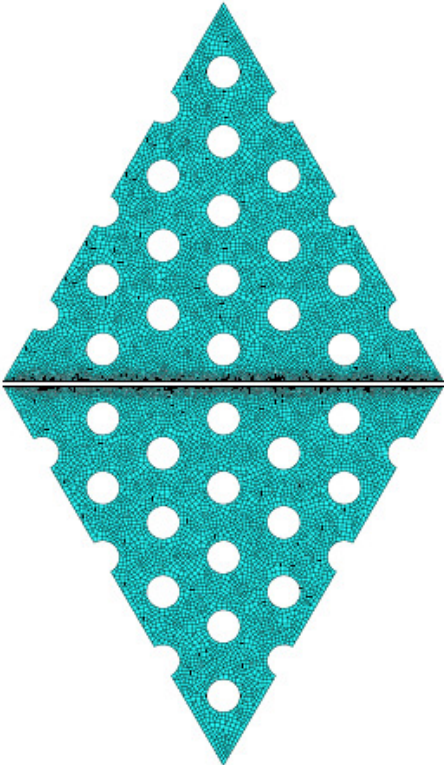


Figure B.1.4: Inter-block close up of finite element mesh

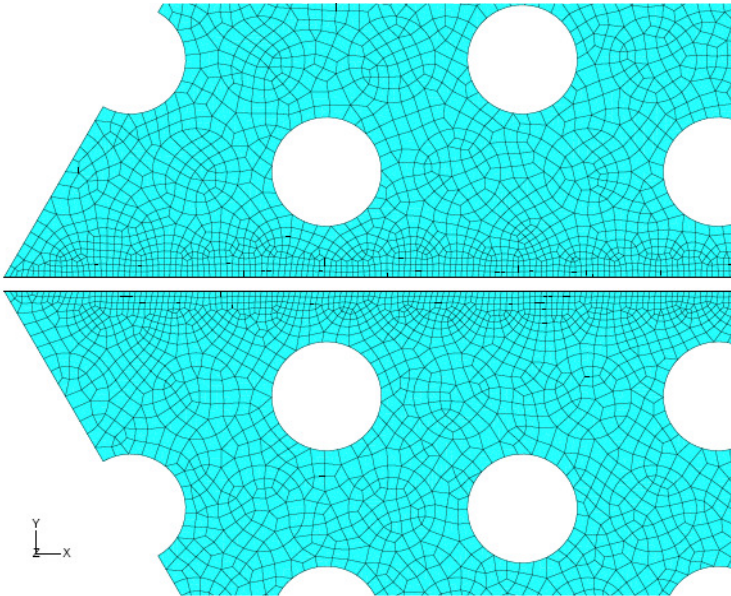


Figure B.1.5: Combined model finite element mesh

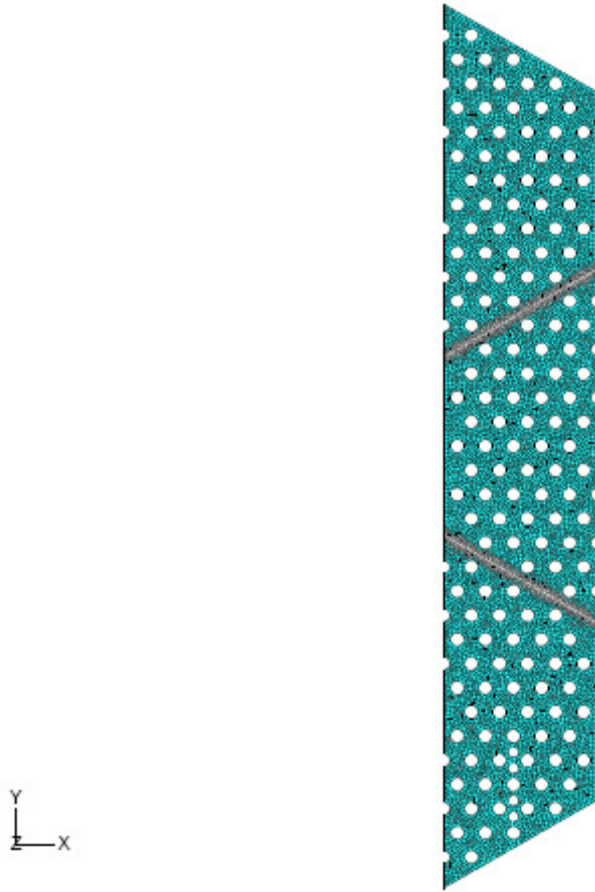


Figure B.1.6: Combined model close up of finite element mesh

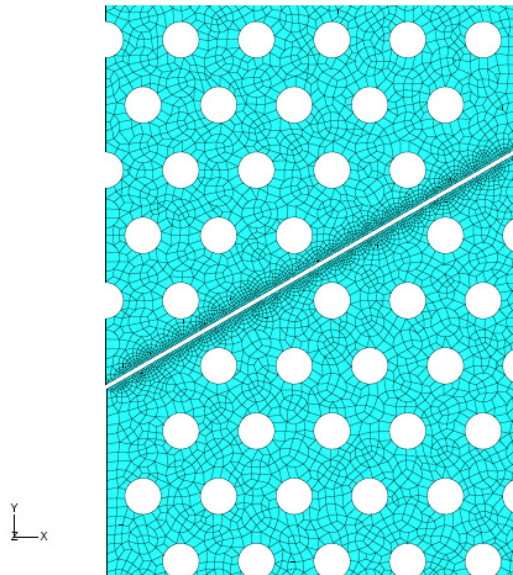


Figure B.1.7: Intra-block variant 1 finite element contour plot of heat flux magnitude

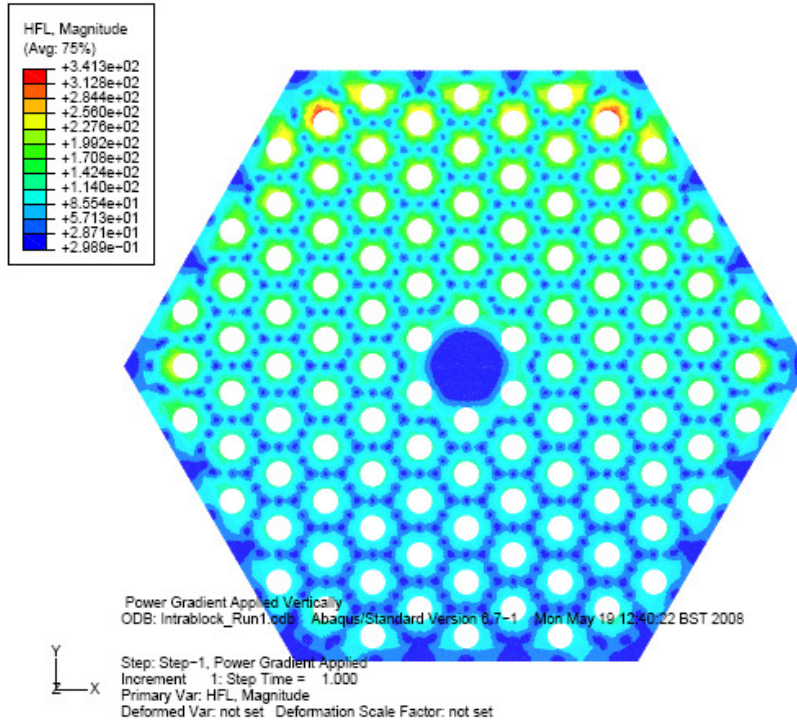


Figure B.1.8: Intra-block variant 1 finite element contour plot of heat flux in vertical direction

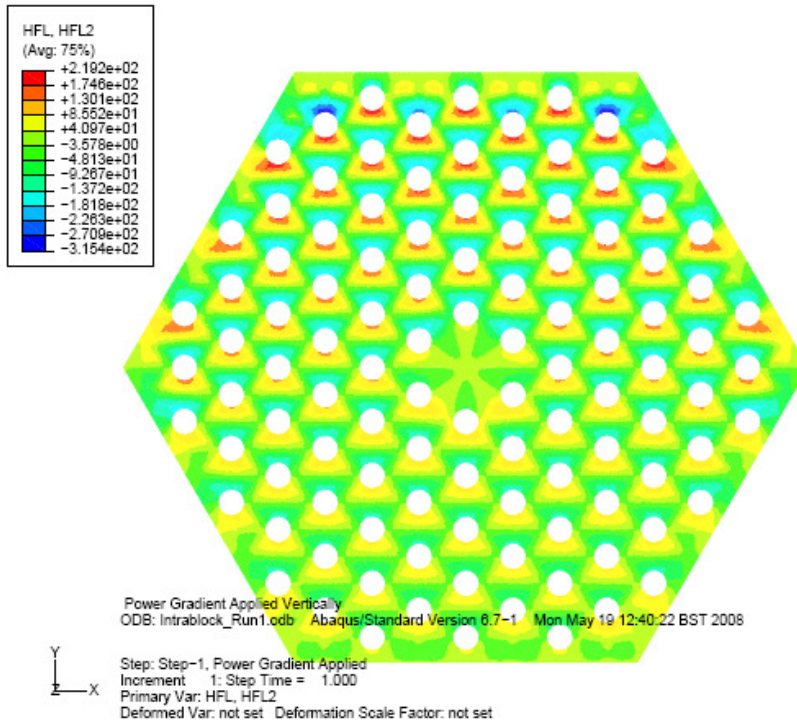


Figure B.1.9: Intra-block variant 2 finite element contour plot of heat flux magnitude

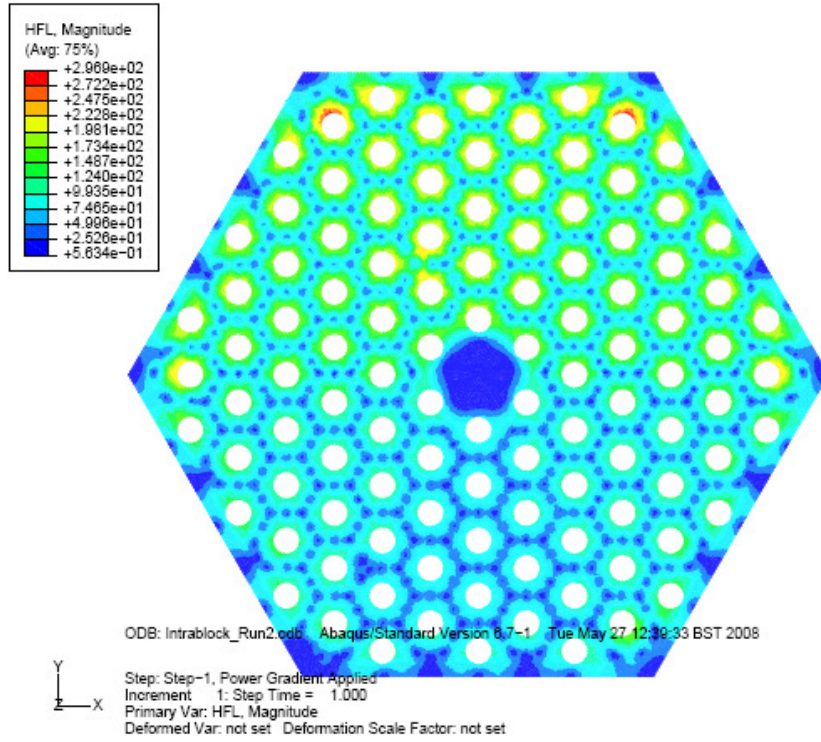


Figure B.1.10: Intra-block variant 2 finite element contour plot of heat flux in vertical direction

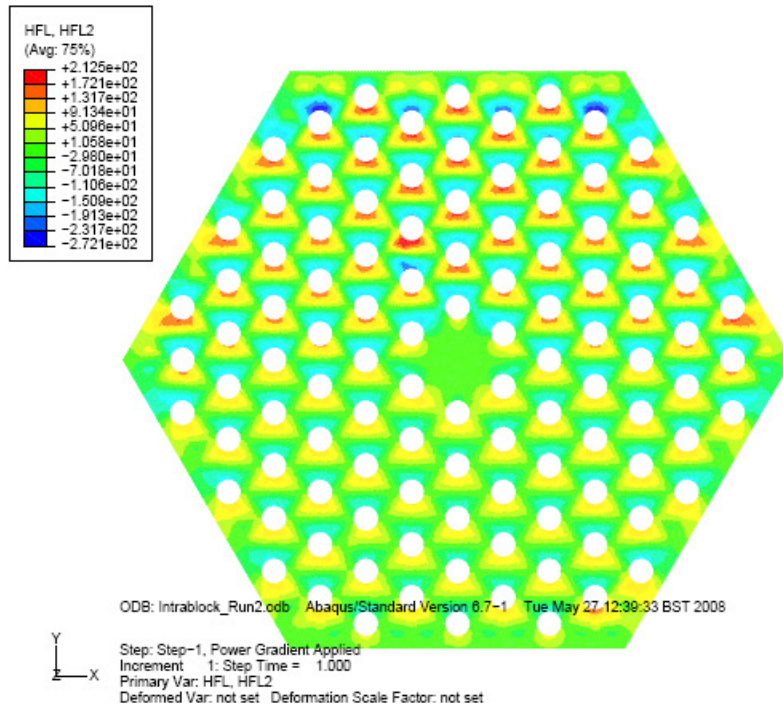


Figure B.1.11: Inter-block variant 1 finite element contour plot of heat flux

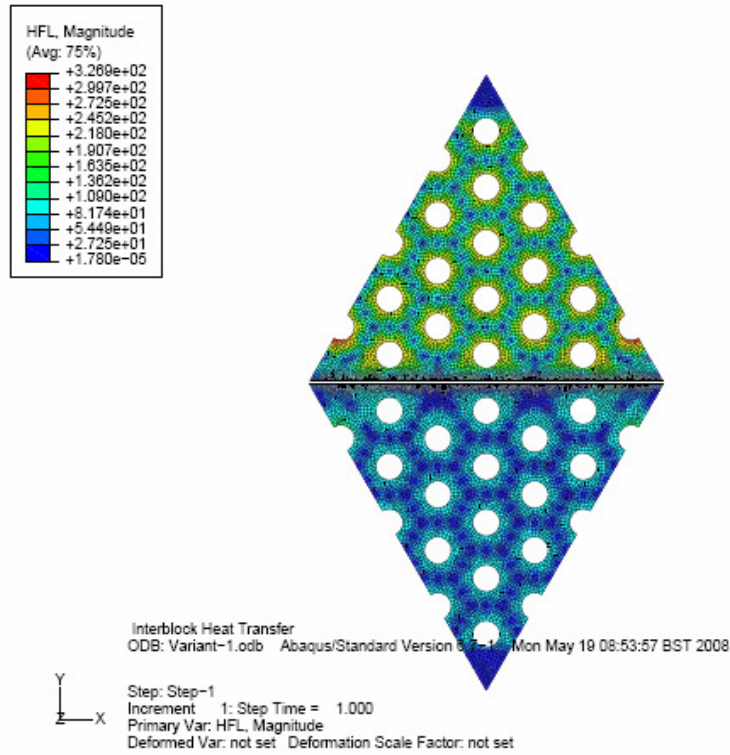


Figure B.1.12: Inter-block variant 1 finite element contour plot of heat flux in vertical direction

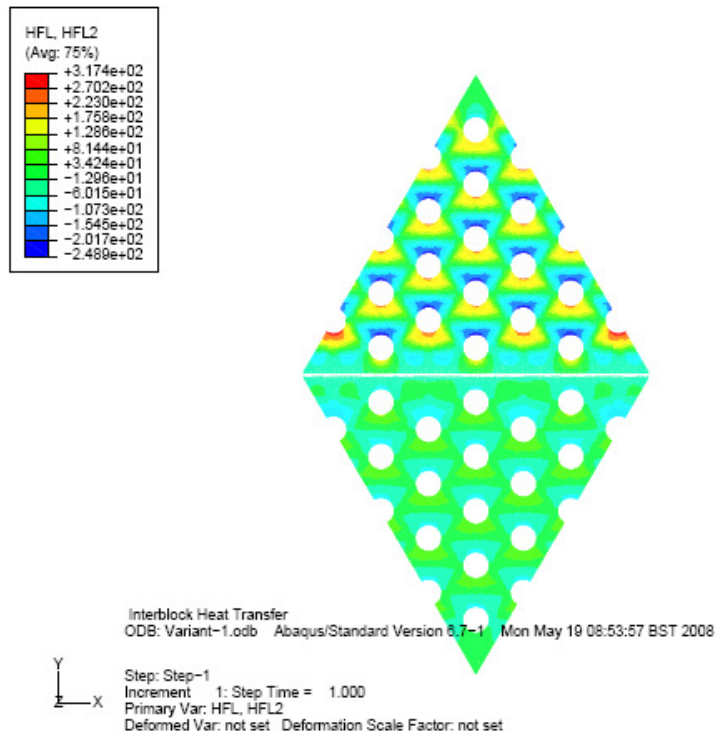


Figure B.1.13: Inter-block variant 2 finite element contour plot of heat flux

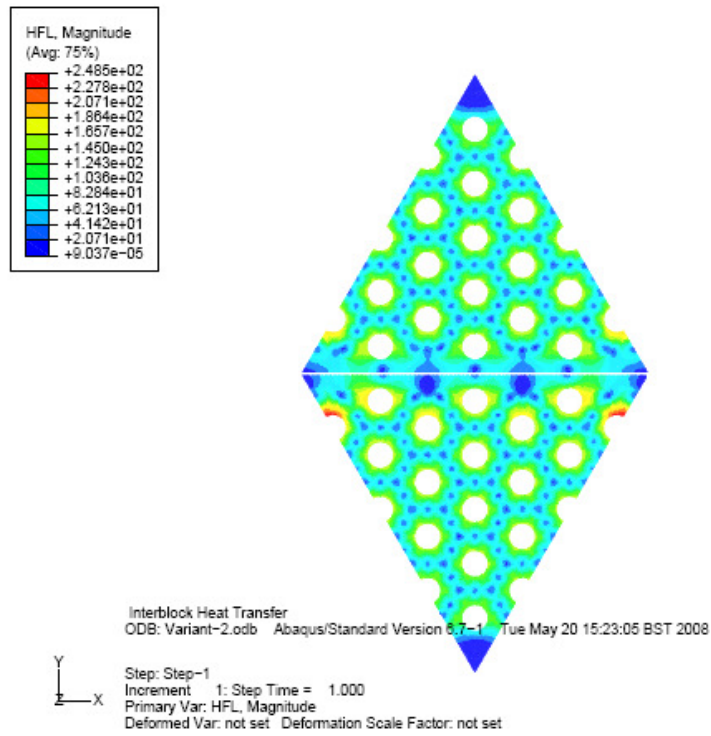


Figure B.1.14: Inter-block variant 2 finite element contour plot of heat flux in a vertical direction

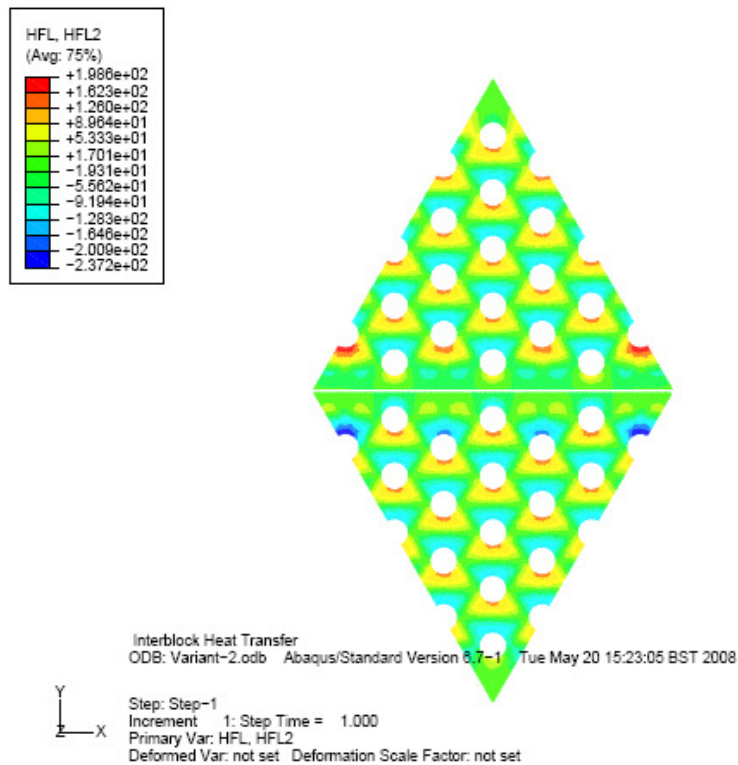


Figure B.1.15: Combined model variant 1 finite element contour plot of heat flux magnitude

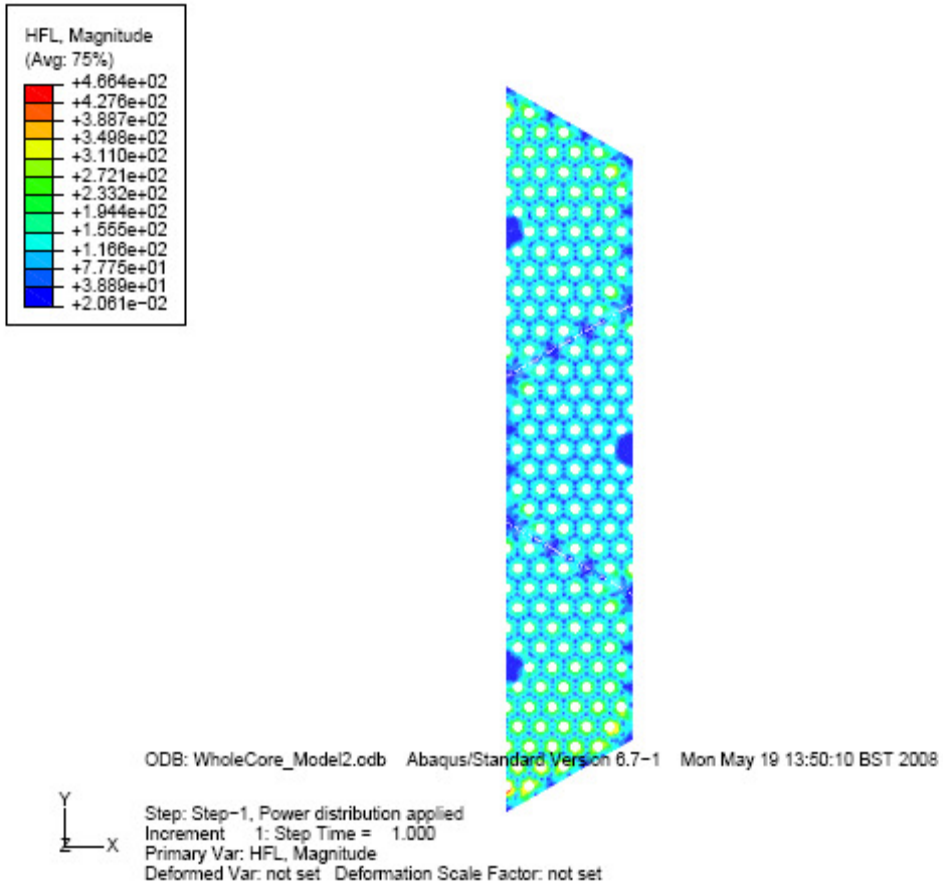


Figure B.1.16: Combined model variant 2 finite element contour plot of heat flux magnitude

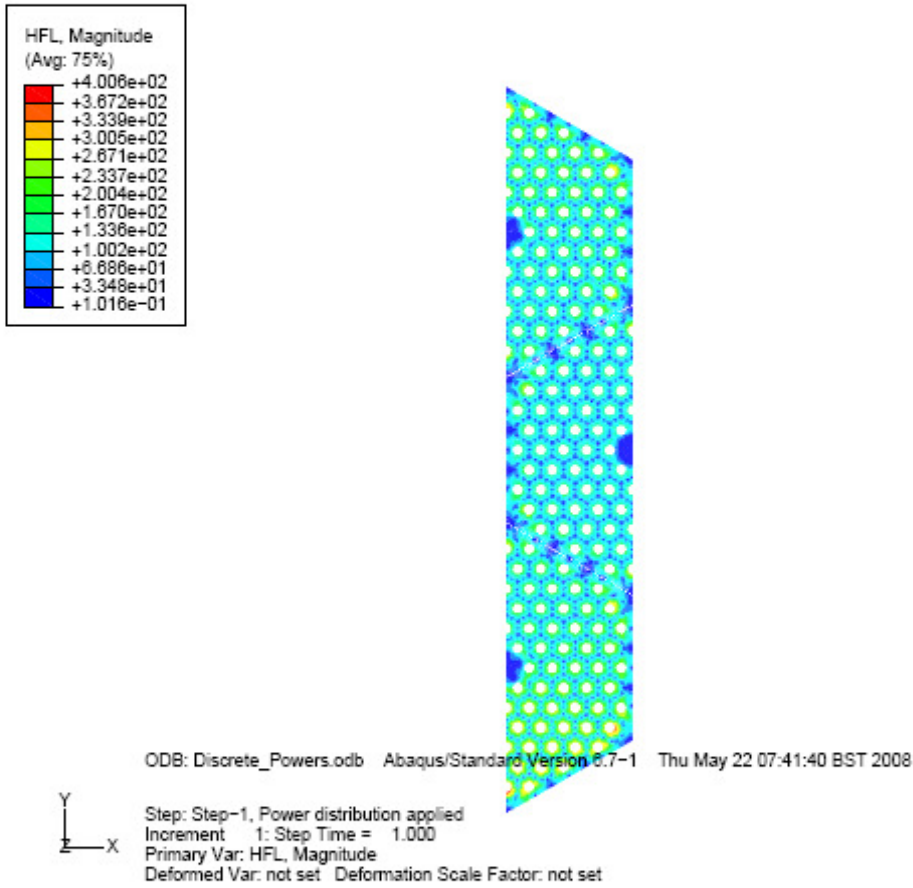
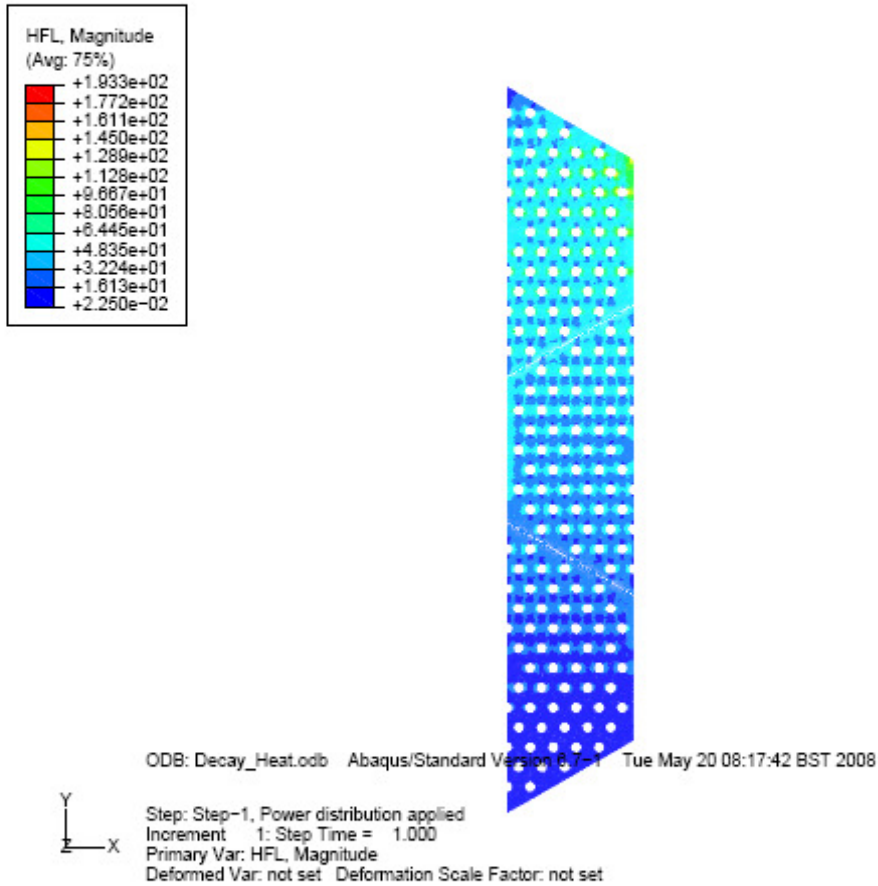


Figure B.1.17: Combined model variant 3 finite element contour plot of heat flux magnitude



In addition, the agreement is shown between the FE results for the gap heat flows for Variant 3 of the Combined Model and the heat generated in each fuel block.

The fuel power density has been applied as a gradient across the FE model, but an approximate calculation can be performed by assuming that the power density of the fuel compacts in each triangle is 0.5% of the power densities given in section 7.2.4.3 (and used in the Variant 2 model). These are 54.93 mW/mm³, 45.23 mW/mm³, 38.80 mW/mm³, 35.22 mW/mm³, 34.05 mW/mm³, 34.86 mW/mm³, 37.20 mW/mm³, 40.66 mW/mm³ and 44.78 mW/mm³.

The heat generated can be calculated using the following equation:

$$\text{Heat Generated} = 0.005 * \text{Power Density} * 36 * \text{Cross-sectional Area of a Fuel Compact}$$

Where 36 is the number of fuel compacts in each triangle and the diameter of a fuel compact is 12.7mm.

The calculated heat generated in each fuel block (from the center of the core outwards) is 3168 W/m, 2374 W/m and 2796 W/m. The heat flow across the gap closest to the center of the core is therefore in agreement with the calculated value of 3.2 kW/m from the FE models. The heat flow across the gap further from the center of the core is equal to $3168+2374=5542$ W/m. This is agreement with that calculated using the FE models of approximately 5.5 kW/m. The heat flow across the outside edge is the total heat generated is calculated to be 8338 W/m ($3168+2374+2796$) and is in agreement with the value calculated from the FE model of approximately 8.3 kW/m.

B.2 Development of Macro-Scale Models

This part of Appendix B presents some details of the derivations of the steady-state analytical models described in Section 7.3.

B.2.1 Super-meso Scale Model

The steady-state solution to the super-meso scale temperature distribution is derived as follows.

The 1-D conduction equation, with heat generation, in an annular domain is:

$$\frac{1}{r} \frac{\partial}{\partial r} \left(rk \frac{\partial T}{\partial r} \right) = -\dot{q}''' ,$$

where r is radius, T is temperature, k is the conductivity and \dot{q}''' is the volumetric heat generation. This has the general solution:

$$k \frac{\partial T}{\partial r} = -\frac{1}{2} r \dot{q}''' + \frac{c_1}{r} \quad (\text{B.2.1})$$

$$T = -\frac{1}{4k} r^2 \dot{q}''' + \frac{c_1}{k} \ln(r) + c_2 \quad (\text{B.2.2})$$

where c_1 and c_2 are constants of integration. The solution within the first annulus, from r_{chn} to r_A is:

$$k_g \frac{\partial T_1}{\partial r} = \frac{1}{2} r \dot{q}_{macro}''' + \frac{A}{r} \quad (\text{B.2.3})$$

$$T_1 = \frac{1}{4k_g} r^2 \dot{q}_{macro}''' + \frac{A}{k_g} \ln(r) + B \quad (\text{B.2.4})$$

where k_g is the conductivity of pure graphite. The solution within the second annulus, from r_A to $r_B - r_{fuel}$ is:

$$k_g \frac{\partial T_2}{\partial r} = \frac{1}{2} r (\dot{q}_{macro}''' - \dot{q}_{eff}''') + \frac{C}{r} \quad (\text{B.2.5})$$

$$T_2 = \frac{1}{4k_g} r^2 (\dot{q}_{macro}''' - \dot{q}_{eff}''') + \frac{C}{k_g} \ln(r) + D \quad (\text{B.2.6})$$

The solution within the third annulus, from $r_B - r_{fuel}$ to r_B is:

$$k_{mix} \frac{\partial T_3}{\partial r} = \frac{1}{2} r (\dot{q}_{macro}''' - \dot{q}_{eff}''') + \frac{E}{r} \quad (B.2.7)$$

$$T_3 = \frac{1}{4k_{mix}} r^2 (\dot{q}_{macro}''' - \dot{q}_{eff}''') + \frac{E}{k_{mix}} \ln(r) + F \quad (B.2.8)$$

where k_{mix} is the effective conductivity of the mixture of plain graphite and fuel compacts.

B.2.1.1 Boundary conditions

The outer boundary of the problem is adiabatic at $r = r_B$:

$$k_{mix} \frac{\partial T_3}{\partial r} \Big|_{r=r_B} = 0.$$

Using Equation B.2.7:

$$\begin{aligned} \Rightarrow \frac{1}{2} r_B (\dot{q}_{macro}''' - \dot{q}_{eff}''') + \frac{E}{r_B} &= 0, \\ \Rightarrow E &= -\frac{1}{2} r_B^2 (\dot{q}_{macro}''' - \dot{q}_{eff}'''). \end{aligned} \quad (B.2.9)$$

Continuity of the heat flow on the boundary between the second and third annuli, at $r = r_B - r_{fuel}$:

$$k_g \frac{\partial T_2}{\partial r} \Big|_{r=r_B - r_{fuel}} = k_{mix} \frac{\partial T_3}{\partial r} \Big|_{r=r_B - r_{fuel}}.$$

Using Equations B.2.5 and B.2.7:

$$\begin{aligned} \Rightarrow \frac{1}{2} (r_B - r_{fuel}) (\dot{q}_{macro}''' - \dot{q}_{eff}''') + \frac{C}{(r_B - r_{fuel})} &= \frac{1}{2} (r_B - r_{fuel}) (\dot{q}_{macro}''' - \dot{q}_{eff}''') + \frac{E}{(r_B - r_{fuel})}, \\ \Rightarrow C &= E. \end{aligned} \quad (B.2.10)$$

Continuity of temperature on the boundary between the second and third annuli, at $r = r_B - r_{fuel}$:

$$T_2(r_B - r_{fuel}) = T_3(r_B - r_{fuel}),$$

Using Equations B.2.6 and B.2.8:

$$\begin{aligned}
& \frac{1}{4k_g} (r_B - r_{fuel})^2 (\dot{q}_{macro}''' - \dot{q}_{eff}''') + \frac{C}{k_g} \ln(r_B - r_{fuel}) + D \\
&= \frac{1}{4k_{mix}} (r_B - r_{fuel})^2 (\dot{q}_{macro}''' - \dot{q}_{eff}''') + \frac{E}{k_{mix}} \ln(r_B - r_{fuel}) + F \\
\Rightarrow F &= D + E \left(\frac{1}{k_g} - \frac{1}{k_{mix}} \right) \ln(r_B - r_{fuel}) + \frac{1}{4} \left(\frac{1}{k_g} - \frac{1}{k_{mix}} \right) (r_B - r_{fuel})^2 (\dot{q}_{macro}''' - \dot{q}_{eff}'''). \quad (\text{B.2.11})
\end{aligned}$$

Continuity of the heat flow on the boundary between the first and second annuli, at $r = r_A$:

$$k_g \left. \frac{\partial T_1}{\partial r} \right|_{r=r_A} = k_g \left. \frac{\partial T_2}{\partial r} \right|_{r=r_A}$$

Using Equations B.2.3 and B.2.4:

$$\begin{aligned}
\Rightarrow \frac{1}{2} r_A \dot{q}_{macro}''' + \frac{A}{r_A} &= \frac{1}{2} r_A (\dot{q}_{macro}''' - \dot{q}_{eff}''') + \frac{C}{r_A}, \\
\Rightarrow A &= C - \frac{1}{2} r_A^2 \dot{q}_{eff}''', \\
\Rightarrow A &= E - \frac{1}{2} r_A^2 \dot{q}_{eff}'''. \quad (\text{B.2.12})
\end{aligned}$$

Since $C = E$ (Equation B.2.10).

Continuity of temperature on the boundary between the first and second annuli, at $r = r_A$:

$$T_1(r_A) = T_2(r_A).$$

Using Equations B.2.4 and B.2.6:

$$\begin{aligned}
\Rightarrow \frac{1}{4k_g} r_A^2 \dot{q}_{macro}''' + \frac{A}{k_g} \ln(r_A) + B &= \frac{1}{4k_g} r_A^2 (\dot{q}_{macro}''' - \dot{q}_{eff}''') + \frac{C}{k_g} \ln(r_A) + D, \\
\Rightarrow \frac{A}{k_g} \ln(r_A) + B &= -\frac{1}{4k_g} r_A^2 \dot{q}_{eff}''' + \frac{C}{k_g} \ln(r_A) + D.
\end{aligned}$$

Using Equation B.2.12 to substitute for A and Equation B.2.10 to replace C with E :

$$\Rightarrow \frac{E}{k_g} \ln(r_A) - \frac{1}{2k_g} r_A^2 \dot{q}_{eff}''' \ln(r_A) + B = -\frac{1}{4k_g} r_A^2 \dot{q}_{eff}''' + \frac{E}{k_g} \ln(r_A) + D,$$

$$\begin{aligned} \Rightarrow -\frac{1}{2k_g} r_A^2 \dot{q}_{eff}''' \ln(r_A) + B &= -\frac{1}{4k_g} r_A^2 \dot{q}_{eff}''' + D, \\ \Rightarrow D &= B - \frac{1}{2k_g} r_A^2 \dot{q}_{eff}''' \ln(r_A) + \frac{1}{4k_g} r_A^2 \dot{q}_{eff}'''. \end{aligned} \quad (B.2.13)$$

Finally, at the coolant channel wall:

$$k_g \left. \frac{\partial T_1}{\partial r} \right|_{r=r_{chn}} = h(T_{SM+M}(r_{chn}) - T_c),$$

where h is the convective heat transfer coefficient to the coolant and T_c is the coolant gas temperature.

There is a subtlety here. The temperature perturbation supplied by the meso-scale model at the coolant channel wall, $\hat{T}_M(\hat{r} = r_D)$, is not zero. The boundary condition described above applies to the total temperature solution at the channel wall, i.e. to

$T_{SM+M}(r_{chn}) = T_{SM}(r = r_{chn}) + \hat{T}_M(\hat{r} = r_D)$. The boundary condition is therefore:

$$k_g \left. \frac{\partial T_1}{\partial r} \right|_{r=r_{chn}} = h(T_1(r_{chn}) + T_{offset} - T_c)$$

where $T_{offset} = \hat{T}_M(\hat{r} = r_D)$ is the value of the meso-scale temperature perturbation at the channel wall:

$$T_{offset} = \hat{T}_M(r_D) = \frac{1}{4k_g} r_D^2 \dot{q}_{sink}''' + \frac{Y}{k_g} \ln(r_D) + Z$$

and T_1 is the super-meso-scale solution in the first annulus.

Using Equations B.2.3 and B.2.4:

$$\begin{aligned} \Rightarrow \frac{1}{2} r_{chn} \dot{q}_{macro}''' + \frac{A}{r_{chn}} &= h \left(T_{offset} - T_c + \frac{1}{4k_g} r_{chn}^2 \dot{q}_{macro}''' + \frac{A}{k_g} \ln(r_{chn}) + B \right) \\ \Rightarrow \frac{1}{2} r_{chn} \dot{q}_{macro}''' &= h \left(T_{offset} - T_c + \frac{1}{4k_g} r_{chn}^2 \dot{q}_{macro}''' + \frac{A}{k_g} \ln(r_{chn}) - \frac{A}{hr_{chn}} + B \right) \\ \Rightarrow B &= T_c - T_{offset} - \frac{1}{4k_g} r_{chn}^2 \dot{q}_{macro}''' + \frac{1}{2h} r_{chn} \dot{q}_{macro}''' + A \left(\frac{1}{hr_{chn}} - \frac{\ln(r_{chn})}{k_g} \right) \end{aligned} \quad (B.2.14)$$

B.2.1.2 The case of macroscopic conduction only

If cooling by convective heat transfer to the coolant gas is removed then the inner boundary becomes adiabatic and the heat removed by long-range conduction must equal the heat input:

$$\dot{q}_{macro}''' (r_B^2 - r_{chn}^2) = \dot{q}_{eff}''' (r_B^2 - r_A^2) \quad (B.2.15)$$

The constants of integration E , C and A can still be calculated using Equations B.2.9, B.2.10 and B.2.12. The relationships between B , D and F still hold, but with zero convection B becomes undefined and the absolute level of the temperature solution becomes arbitrary (at the level of the isolated super-meso-scale model). The temperature solution becomes fixed when the macro-scale conduction between sectors is included.

Equation B.2.15 requires the inner boundary of the solution to be adiabatic, which requires that:

$$A = -\frac{1}{2} r_{chn}^2 \dot{q}_{macro}''' \quad (B.2.16)$$

Using Equation B.2.4 at $r = r_{chn}$ plus T_{offset} to solve for the coolant channel wall temperature:

$$T_{wall} = \frac{1}{4k_g} r_{chn}^2 \dot{q}_{macro}''' + \frac{A}{k_g} \ln(r_{chn}) + B + T_{offset}$$

Substituting for B using Equation B.2.14 leads to:

$$T_{wall} = \frac{1}{4k_g} r_{chn}^2 \dot{q}_{macro}''' + \frac{A}{k_g} \ln(r_{chn}) + T_c - T_{offset} - \frac{1}{4k_g} r_{chn}^2 \dot{q}_{macro}''' + \frac{1}{2h} r_{chn} \dot{q}_{macro}''' + A \left(\frac{1}{hr_{chn}} - \frac{\ln(r_{chn})}{k_g} \right) + T_{offset}$$

Now substituting for A using Equation B.2.16:

$$\begin{aligned} T_{wall} &= \frac{1}{4k_g} r_{chn}^2 \dot{q}_{macro}''' - \frac{1}{2k_g} r_{chn}^2 \dot{q}_{macro}''' \ln(r_{chn}) + T_c \\ &\quad - \frac{1}{4k_g} r_{chn}^2 \dot{q}_{macro}''' + \frac{1}{2h} r_{chn} \dot{q}_{macro}''' - \frac{1}{2h} r_{chn} \dot{q}_{macro}''' + \frac{1}{2k_g} r_{chn}^2 \dot{q}_{macro}''' \ln(r_{chn}) \\ \Rightarrow T_{wall} &= T_c . \end{aligned}$$

I.e. the coolant channel wall temperature is forced to equal the coolant temperature. The convective heat transfer coefficient (h), which goes to zero in the limit of zero convective heat removal, does not feature in this result. This means that the system of solutions and constants A to F can be used to calculate the temperatures as usual, using an arbitrary value of h , providing that the macro-scale heat removal is specified as in Equation B.2.15, i.e. that

$$\dot{q}_{macro}''' = \dot{q}_{eff}''' \frac{(r_B^2 - r_A^2)}{(r_B^2 - r_{chn}^2)}. \quad (B.2.17)$$

B.2.2 Meso scale model

The steady-state solution to the meso scale temperature distribution is derived as follows.

The general solution to the 1-D conduction equation, with uniform heat generation, in the central circular region is:

$$k \frac{\partial T}{\partial \hat{r}} = -\frac{1}{2} \hat{r} \dot{q}'''$$

$$T = -\frac{1}{4k} \hat{r}^2 \dot{q}''' + c$$

where c is a constant of integration. Applying this to the fuel compact region in the meso-scale model gives:

$$k_f \frac{\partial T_4}{\partial \hat{r}} = -\frac{1}{2} \hat{r} \dot{q}_{comp}''' \quad (B.2.18)$$

$$T_4 = -\frac{1}{4k_f} \hat{r}^2 \dot{q}_{comp}''' + X, \quad (B.2.19)$$

where k_f is the conductivity of the fuel compact and X is to be found.

In the annular heat sink region around the fuel compact, the general solution is the same as that in Equations B.2.1 and B.2.2, which give:

$$k_g \frac{\partial T_5}{\partial \hat{r}} = \frac{1}{2} \hat{r} \dot{q}_{sink}''' + \frac{Y}{\hat{r}} \quad (B.2.20)$$

$$T_5 = \frac{1}{4k_g} \hat{r}^2 \dot{q}_{sink}''' + \frac{Y}{k_g} \ln(\hat{r}) + Z, \quad (B.2.21)$$

where k_g is the graphite conductivity and Y and Z are to be found.

B.2.2.1 Boundary conditions

The outer boundary of the problem is adiabatic on $\hat{r} = r_D$:

$$k_g \left. \frac{\partial T_5}{\partial \hat{r}} \right|_{\hat{r}=r_D} = 0$$

Using Equation B.2.19:

$$\Rightarrow \frac{1}{2} r_D \dot{q}_{sink}''' + \frac{Y}{r_D} = 0,$$

$$\Rightarrow Y = -\frac{1}{2} r_D^2 \dot{q}_{sink}''' \quad (\text{B.2.22})$$

Continuity of the heat flux on the boundary between the two regions at $\hat{r} = r_{fuel}$ leads to:

$$k_f \left. \frac{\partial T_4}{\partial \hat{r}} \right|_{\hat{r}=r_{fuel}} = k_g \left. \frac{\partial T_5}{\partial \hat{r}} \right|_{\hat{r}=r_{fuel}}$$

Using Equations B.2.18 and B.2.20:

$$\Rightarrow -\frac{1}{2} r_{fuel} \dot{q}_{comp}''' = \frac{1}{2} r_{fuel} \dot{q}_{sink}''' + \frac{Y}{r_{fuel}}$$

Using Equation B.2.22 to substitute for Y :

$$\Rightarrow -\frac{1}{2} r_{fuel} \dot{q}_{comp}''' = \frac{1}{2} r_{fuel} \dot{q}_{sink}''' - \frac{1}{2} \frac{r_D^2}{r_{fuel}} \dot{q}_{sink}'''$$

$$\Rightarrow r_{fuel}^2 \dot{q}_{comp}''' = -r_{fuel}^2 \dot{q}_{sink}''' + r_D^2 \dot{q}_{sink}'''$$

$$\Rightarrow \dot{q}_{comp}''' = \frac{(r_D^2 - r_{fuel}^2)}{r_{fuel}^2} \dot{q}_{sink}'''$$

which recovers the condition in Equation B.2.17 requiring the whole domain to have zero net heat generation.

Continuity of temperature on the boundary between the two regions at $\hat{r} = r_{fuel}$:

$$T_4(r_{fuel}) = T_5(r_{fuel}) .$$

Using Equations B.2.19 and B.2.21:

$$\Rightarrow -\frac{1}{4k_f} r_{fuel}^2 \dot{q}_{comp}''' + X = \frac{1}{4k_g} r_{fuel}^2 \dot{q}_{sink}''' + \frac{Y}{k_g} \ln(r_{fuel}) + Z . \quad (\text{B.2.23})$$

Using Equation B.2.22 to substitute for Y :

$$\begin{aligned} \Rightarrow -\frac{1}{4k_f} r_{fuel}^2 \dot{q}_{comp}''' + X &= \frac{1}{4k_g} r_{fuel}^2 \dot{q}_{sink}''' - \frac{1}{2k_g} r_D^2 \dot{q}_{sink}''' \ln(r_{fuel}) + Z, \\ \Rightarrow X &= Z + \frac{1}{4k_f} r_{fuel}^2 \dot{q}_{comp}''' + \frac{1}{4k_g} r_{fuel}^2 \dot{q}_{sink}''' - \frac{1}{2k_g} r_D^2 \dot{q}_{sink}''' \ln(r_{fuel}). \end{aligned} \quad (B.2.24)$$

A further constraint comes from the requirement for the total internal energy associated with the meso-scale solution to be zero over its own domain:

$$\iint \rho c_p \hat{T}_M dA = \left[\rho_{fuel} c_{p,fuel} \int_{\hat{r}=0}^{\hat{r}=r_{fuel}} T_4(\hat{r}) 2\pi r dr \right] + \left[\rho_g c_{p,g} \int_{\hat{r}=r_{fuel}}^{\hat{r}=r_D} T_5(\hat{r}) 2\pi r dr \right] = 0,$$

where ρ_{fuel} , ρ_g , $c_{p,fuel}$ and $c_{p,g}$ are the mass density and specific heat capacities of the fuel and graphite.

Using Equations B.2.19 and B.2.21 to substitute for the temperature solutions:

$$\Rightarrow \left[\rho_{fuel} c_{p,fuel} \int_{\hat{r}=0}^{\hat{r}=r_{fuel}} \left(-\frac{1}{4k_f} \hat{r}^3 \dot{q}_{comp}''' + X \hat{r} \right) dr \right] + \left[\rho_g c_{p,g} \int_{\hat{r}=r_{fuel}}^{\hat{r}=r_D} \left(\frac{1}{4k_g} \hat{r}^3 \dot{q}_{sink}''' + \frac{Y}{k_g} \hat{r} \ln(\hat{r}) + Z \hat{r} \right) dr \right] = 0,$$

Which gives,

$$\begin{aligned} \Rightarrow \rho_{fuel} c_{p,fuel} \left[-\frac{1}{16k_f} r_{fuel}^4 \dot{q}_{comp}''' + \frac{1}{2} X r_{fuel}^2 \right] + \\ \rho_g c_{p,g} \left[\frac{1}{16k_g} (r_D^4 - r_{fuel}^4) \dot{q}_{sink}''' + \frac{Y}{k_g} \left(\frac{r_D^2}{2} [\ln(r_D) - \frac{1}{2}] - \frac{r_{fuel}^2}{2} [\ln(r_{fuel}) - \frac{1}{2}] \right) + \frac{1}{2} Z (r_D^2 - r_{fuel}^2) \right] = 0 \end{aligned}$$

Using Equation B.2.23 and rearranging:

$$\begin{aligned} \Rightarrow Z \left[\rho_{fuel} c_{p,fuel} r_{fuel}^2 + \rho_g c_{p,g} (r_D^2 - r_{fuel}^2) \right] + \\ \rho_{fuel} c_{p,fuel} \left[\frac{1}{8k_f} r_{fuel}^4 \dot{q}_{comp}''' + \frac{1}{4k_g} r_{fuel}^4 \dot{q}_{sink}''' + \frac{Y}{k_g} r_{fuel}^2 \ln(r_{fuel}) \right] + \\ \rho_g c_{p,g} \left[\frac{1}{8k_g} (r_D^4 - r_{fuel}^4) \dot{q}_{sink}''' + \frac{Y}{k_g} \left(r_D^2 [\ln(r_D) - \frac{1}{2}] - r_{fuel}^2 [\ln(r_{fuel}) - \frac{1}{2}] \right) \right] = 0 \end{aligned}$$

Which gives,

$$\begin{aligned} & \rho_{fuel} c_{p,fuel} \left[\frac{1}{8k_f} r_{fuel}^4 \dot{q}_{comp}''' + \frac{1}{4k_g} r_{fuel}^4 \dot{q}_{sink}''' + \frac{Y}{k_g} r_{fuel}^2 \ln(r_{fuel}) \right] \\ & + \rho_g c_{p,g} \left[\frac{1}{8k_g} (r_D^4 - r_{fuel}^4) \dot{q}_{sink}''' + \frac{Y}{k_g} (r_D^2 [\ln(r_D) - \frac{1}{2}] - r_{fuel}^2 [\ln(r_{fuel}) - \frac{1}{2}]) \right] \quad (B.2.25) \\ \Rightarrow Z = & \frac{\quad}{-\rho_{fuel} c_{p,fuel} r_{fuel}^2 - \rho_g c_{p,g} (r_D^2 - r_{fuel}^2)} \end{aligned}$$

B.2.3 Calculation of the Mean Solid Temperature

Taking the mean solid temperature to be the mean of the super-meso scale solution, averaged over its own domain:

$$\begin{aligned} T_g &= \frac{\iint \rho c_p T_{SM} \cdot dA}{\iint \rho c_p \cdot dA} = \frac{\int \rho c_p T_{SM}(r) \cdot r \cdot dr}{\int \rho c_p \cdot r \cdot dr} \\ & \frac{\rho_u c_{p,u} \int_{r=r_{chn}}^{r=r_A} \left(\frac{1}{4k_g} r^2 \dot{q}_{macro}''' + \frac{A}{k_g} \ln(r) + B \right) r dr}{\frac{1}{2} \rho_u c_{p,u} (r_A^2 - r_{chn}^2) + \frac{1}{2} \rho_h c_{p,h} (r_B^2 - r_A^2)} \\ & + \rho_h c_{p,h} \int_{r=r_A}^{r=r_B-r_{fuel}} \left(\frac{1}{4k_g} r^2 (\dot{q}_{macro}''' - \dot{q}_{eff}''') + \frac{C}{k_g} \ln(r) + D \right) r dr \\ & + \rho_h c_{p,h} \int_{r=r_B-r_{fuel}}^{r=r_B} \left(\frac{1}{4k_{mix}} r^2 (\dot{q}_{macro}''' - \dot{q}_{eff}''') + \frac{E}{k_{mix}} \ln(r) + F \right) r dr \quad (B.2.26) \end{aligned}$$

where ρ_u , ρ_h , $c_{p,u}$ and $c_{p,h}$ are the effective mass density and specific heat capacities of the unheated and heated annuli.

Consider the integration of the general temperature solution in an annular geometry:

$$\begin{aligned} & \int_{r=r_1}^{r=r_2} (\alpha r^2 + \beta \ln(r) + \gamma) r dr \\ & = \frac{1}{4} \alpha (r_1^4 - r_2^4) + \frac{1}{2} \beta \left[r_2^2 (\ln(r_2) - \frac{1}{2}) - r_1^2 (\ln(r_1) - \frac{1}{2}) \right] + \frac{1}{2} \gamma (r_1^2 - r_2^2). \quad (B.2.27) \end{aligned}$$

Taking Equation B.2.26 and multiplying both the numerator and denominator by 4:

$$T_g = \frac{x_1 + x_2 + x_3}{2\rho_u c_{p,u} (r_A^2 - r_{chn}^2) + 2\rho_h c_{p,h} (r_B^2 - r_A^2)}, \quad (B.2.28)$$

where the terms in the numerator are (using Equation B.2.27):

$$x_1 = \frac{1}{4k_g} \rho_u c_{p,u} \dot{q}_{macro}''' (r_A^4 - r_{chn}^4) + \frac{1}{4k_g} \rho_h c_{p,h} (\dot{q}_{macro}''' - \dot{q}_{eff}''') (r_B - r_{fuel})^4 - r_A^4 \\ + \frac{1}{4k_{mix}} \rho_h c_{p,h} (\dot{q}_{macro}''' - \dot{q}_{eff}''') (r_B^4 - [r_B - r_{fuel}]^4)$$

$$x_2 = \frac{2A}{k_g} \rho_u c_{p,u} \left(r_A^2 \left[\ln(r_A) - \frac{1}{2} \right] - r_{chn}^2 \left[\ln(r_{chn}) - \frac{1}{2} \right] \right) \\ + \frac{2C}{k_g} \rho_h c_{p,h} \left((r_B - r_{fuel})^2 \left[\ln(r_B - r_{fuel}) - \frac{1}{2} \right] - r_A^2 \left[\ln(r_A) - \frac{1}{2} \right] \right) \\ + \frac{2E}{k_{mix}} \rho_h c_{p,h} \left(r_B^2 \left[\ln(r_B) - \frac{1}{2} \right] - (r_B - r_{fuel})^2 \left[\ln(r_B - r_{fuel}) - \frac{1}{2} \right] \right)$$

and

$$x_3 = 2B \rho_u c_{p,u} (r_A^2 - r_{chn}^2) + 2D \rho_h c_{p,h} ([r_B - r_{fuel}]^2 - r_A^2) + 2F \rho_h c_{p,h} (r_B^2 - [r_B - r_{fuel}]^2).$$

B.2.4 Derivations of the Sector Boundary Temperature Relationships

B.2.4.1 Assuming a distributed 1-D heat source

A 1-D model, with a distributed heat source \dot{q}''' and conductivity k_{hex} has a quadratic temperature solution:

$$k_{hex} \frac{\partial^2 T}{\partial x^2} = -\dot{q}''' \\ \Rightarrow T = -\frac{\dot{q}'''}{2k_{hex}} x^2 + c_1 x + c_2.$$

Applying an adiabatic boundary condition at $x = 0$ leads to $c_1 = 0$. If the heat flow leaving the 1-D domain at $x = L$ is known to be \dot{q}'_b , then the final temperature solution is:

$$T = T_g - \frac{\dot{q}'_b}{2k_{hex}LS} x^2,$$

where S is the length of the boundary of the domain and T_g is the temperature at $x = 0$. The temperature, T_b , at $x = L$ is therefore:

$$T_b = T_g - \frac{\dot{q}'_b L}{2k_{hex} S}$$

If this 1-D domain is taken to stretch from the centroid of a triangular sector to the center of a boundary then $L = \frac{d_{hex}}{6}$ and $S = \frac{d_{hex}}{\sqrt{3}}$, then (with some rearranging):

$$\dot{q}'_b = 2 \cdot (2\sqrt{3})k_{hex} \cdot (T_g - T_b).$$

B.2.4.2 Assuming a distributed 1-D heat source and the effect of coolant channels

This model is also 1-D, but incorporates the effect of the coolant channels in addition to a distributed source of heat input:

$$k_{hex} \frac{\partial^2 T}{\partial x^2} = -\dot{q}''' + \alpha(T - T_c), \quad (\text{B.2.29})$$

where T_c is a fixed coolant temperature and α is a coefficient linking the volumetric heat lost to the coolant and the difference between the coolant temperature and the local graphite temperature T . This is not simply related to h , the convective heat transfer coefficient between a coolant channel and the coolant channel wall, since it must also account for the thermal resistance between the local average graphite temperature (T) and the channel wall. Fortunately, the resistance, α , can be calculated from the coolant gas, channel wall and average graphite temperatures which have been derived from the super-meso and meso-scale solutions. These models strictly apply to a typical coolant channel in the sector, and α may vary slightly close to the edge of a sector, but this difference is small and can be neglected.

The solution to Equation B.2.29 is:

$$T = c_1 \exp\left[\left(\frac{\alpha}{k_{hex}}\right)^{\frac{1}{2}} x\right] + c_2 \exp\left[-\left(\frac{\alpha}{k_{hex}}\right)^{\frac{1}{2}} x\right] + \frac{\dot{q}'''}{\alpha} + T_c. \quad (\text{B.2.30})$$

If the solution is adiabatic on $x = 0$ then:

$$k_{hex} \frac{\partial T}{\partial x} \Big|_{x=0} = c_1 (\alpha k_{hex})^{\frac{1}{2}} - c_2 (\alpha k_{hex})^{\frac{1}{2}} = 0,$$

$$\Rightarrow c = c_1 = c_2,$$

$$\Rightarrow T = 2c \cosh\left[\left(\frac{\alpha}{k_{hex}}\right)^{\frac{1}{2}} x\right] + \frac{\dot{q}'''}{\alpha} + T_c,$$

which leads to a heat flow of:

$$\Rightarrow k_{hex} \frac{\partial T}{\partial x} = 2(\alpha k_{hex})^{\frac{1}{2}} c \sinh \left[\left(\frac{\alpha}{k_{hex}} \right)^{\frac{1}{2}} x \right]. \quad (\text{B.2.31})$$

Requiring $T = T_g$ at $x = 0$ in Equation B.2.30:

$$T_g = 2c + \frac{\dot{q}'''}{\alpha} + T_c. \quad (\text{B.2.32})$$

Requiring $T = T_b$ at $x = L$:

$$T_b = 2c \cosh \left[\left(\frac{\alpha}{k_{hex}} \right)^{\frac{1}{2}} L \right] + \frac{\dot{q}'''}{\alpha} + T_c. \quad (\text{B.2.33})$$

Equations B.2.32 and B.2.33 then lead to:

$$T_g - T_b = 2c \left\{ 1 - \cosh \left[\left(\frac{\alpha}{k_{hex}} \right)^{\frac{1}{2}} L \right] \right\}. \quad (\text{B.2.34})$$

If the heat flow leaving the 1-D domain at $x = L$ is known to be \dot{q}'_b , then using Equation B.2.31:

$$k_{hex} \frac{\partial T}{\partial x} \Big|_{x=L} = -\frac{\dot{q}'_b}{S} = 2(\alpha k_{hex})^{\frac{1}{2}} c \sinh \left[\left(\frac{\alpha}{k_{hex}} \right)^{\frac{1}{2}} L \right],$$

where S is the length of the boundary. Rearranging for c :

$$c = \frac{-\dot{q}'_b}{(\alpha k_{hex})^{\frac{1}{2}} S \sinh \left[\left(\frac{\alpha}{k_{hex}} \right)^{\frac{1}{2}} L \right]},$$

and now substituting into Equation B.2.34 and rearranging:

$$\dot{q}'_b = (\alpha k_{hex})^{\frac{1}{2}} S \left(\frac{\sinh \left[\left(\frac{\alpha}{k_{hex}} \right)^{\frac{1}{2}} L \right]}{\cosh \left[\left(\frac{\alpha}{k_{hex}} \right)^{\frac{1}{2}} L \right] - 1} \right) (T_g - T_b).$$

If this 1-D domain is taken to stretch from the centroid of a triangular sector to the center of a boundary then $L = \frac{d_{hex}}{6}$ and $S = \frac{d_{hex}}{\sqrt{3}}$:

$$\dot{q}'_b = f \cdot (2\sqrt{3}) k_{hex} \cdot (T_g - T_b)$$

where the enhancement factor is given by:

$$f = \frac{\theta \sinh \theta}{\cosh \theta - 1} \quad \text{where } \theta = \left(\frac{\alpha}{k_{hex}} \right)^{\frac{1}{2}} \left(\frac{d_{hex}}{6} \right).$$

In the limit of poor cooling or high block conductivity:

$$\theta = \left(\frac{\alpha}{k_{hex}} \right)^{\frac{1}{2}} \left(\frac{d_{hex}}{6} \right) \rightarrow 0$$

and since

$$\lim_{\theta \rightarrow 0} [f] = \lim_{\theta \rightarrow 0} \left[\frac{\theta \sinh \theta}{\cosh \theta - 1} \right] = \lim_{\theta \rightarrow 0} \left[\frac{\theta(e^\theta - e^{-\theta})}{e^\theta + e^{-\theta} - 2} \right] = \lim_{\theta \rightarrow 0} \left[\frac{\theta(1 + \theta + \frac{1}{2}\theta^2 + \dots) - \theta(1 - \theta + \frac{1}{2}\theta^2 + \dots)}{(1 + \theta + \frac{1}{2}\theta^2 + \dots) + (1 - \theta + \frac{1}{2}\theta^2 + \dots) - 2} \right] = \frac{2\theta^2}{\theta^2} = 2$$

the enhancement factor reduces to $f \rightarrow 2$, recovering the expected result for distributed heat but with no cooling. In the limit of very good cooling or low block conductivity:

$$\theta = \left(\frac{\alpha}{k_{hex}} \right)^{\frac{1}{2}} \left(\frac{d_{hex}}{6} \right) \rightarrow \infty$$

and since

$$\lim_{\theta \rightarrow \infty} [f] = \lim_{\theta \rightarrow \infty} \left[\frac{\theta \sinh \theta}{\cosh \theta - 1} \right] = \lim_{\theta \rightarrow \infty} \left[\frac{\theta e^\theta}{e^\theta - 2} \right] = \theta,$$

the enhancement factor reduces to $f \rightarrow \left(\frac{\alpha}{k_{hex}} \right)^{\frac{1}{2}} \left(\frac{d_{hex}}{6} \right)$.

B.2.5 Global Parameters Used in the Analytical Models

Parameter	Symbol	Value	Units
flat-to-flat distance across a fuel assembly hexagon	d_{hex}	0.36	m
length of one side of the fuel assembly hexagon	S	$(d_{hex}/\sqrt{3})$ ~ 0.2078	m
distance from sector centroid to boundary	L	$(d_{hex}/6)=0.06$	m
assumed gap between two fuel assembly hexagons	d_{gap}	2×10^{-3}	m
number of coolant channels in a single sector	N_{sec}	18	-
radius of coolant channel	r_{chn}	8×10^{-3}	m
radius of unheated annulus in super-meso-scale model	r_A	$\left(\frac{r_B^2 \sqrt{3}}{2\pi}\right)^{\frac{1}{2}}$ $\sim 9.9757 \times 10^{-3}$	m
radius of heated annulus in super-meso-scale model (distance from center of coolant channel to center of fuel compact)	r_B	19×10^{-3}	m
radius of fuel compact	r_{fuel}	6.35×10^{-3}	m
radius of domain in meso-scale model	r_D	$\left(\frac{r_B^2 \sqrt{3}}{2\pi}\right)^{\frac{1}{2}}$ $\sim 9.9757 \times 10^{-3}$	m
conductivity of pure graphite	k_g	30	W/m/K
conductivity of fuel compact	k_f	20	W/m/K
effective conductivity of heated annulus in super-meso-scale model	k_{mix}	24.0945	W/m/K
effective conductivity of fuel assembly hexagon	k_{hex}	17.55	W/m/K
parameters in helium conductivity empirical relationship $(k_{gap} = \alpha(1 + \beta p)T_c^{\gamma(1+\delta p)})$	α	2.682×10^{-3}	W/m/K
	β	1.123×10^{-3}	/bar
	γ	0.71	-
	δ	-2.0×10^{-4}	/bar
heat capacity of pure graphite	$\rho_g c_{p,g}$	2.9068×10^6	J/m ³ /K
heat capacity of fuel compact	$\rho_f c_{p,f}$	2.9068×10^6	J/m ³ /K
effective heat capacity of unheated annulus in super-meso-scale model	$\rho_u c_{p,u}$	2.9068×10^6	J/m ³ /K
effective heat capacity of heated annulus in super-meso-scale model	$\rho_h c_{p,h}$	2.2125×10^6	J/m ³ /K
convective heat transfer coefficient (to coolant; section 7.2.3)	h	2615	W/m ² /K
Stefan-Boltzmann constant	σ	5.67051×10^{-8}	W/m ² /K ⁴
emissivity at inter-block gap surface	ϵ	0.8	-

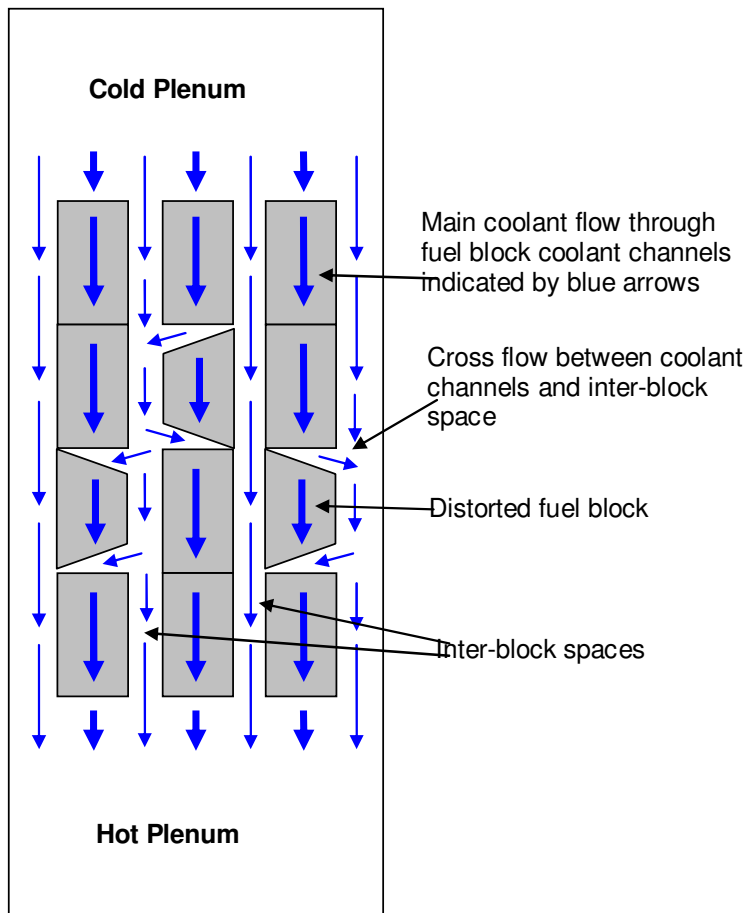
Appendix C: TRACE Model of a Section of the Core including Bypass Flow between the Inter-block and Cooling Channel

This appendix contains details of a TRACE model (version 5.141) developed by Alexander Velázquez,-Lozada, Matthew Bernard and Kimberley Tene at the U.S. NRC. It has been developed in order to independently verify the RELAP5 core bypass model presented in Section 8, and is presented as part of this report for completeness.

C.1 Introduction

The TRACE model was configured to investigate leakage between the coolant channels and inter-block spaces (core bypass flow) as shown in Figure C.1.1.

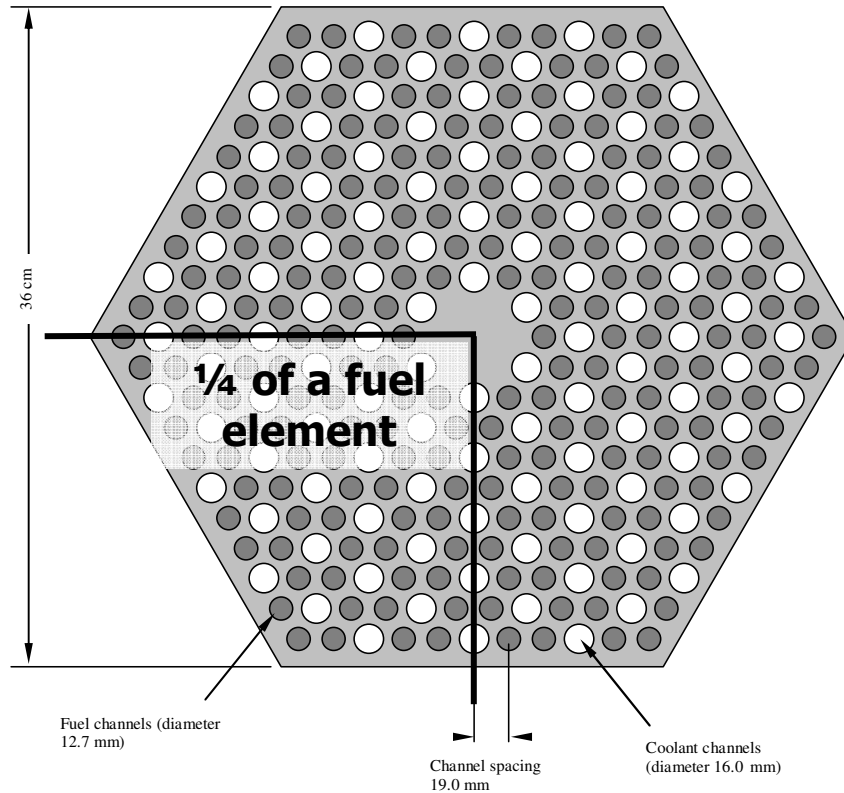
Figure C.1.1: Schematic view of core bypass due to cross-flow through end-face gaps



A portion of the core (Figure 2.3.3) was modeled using a channel equivalent to 1/302 part of the core, which represents $\frac{1}{4}$ of a fuel element (Figure C.1.2). This equivalent channel represents 54 fuel rods and 27 coolant sub-channels.

The total reactor power of 600×10^6 Watts is distributed among 16320 fuel rods. Thus the equivalent channel represents $54/16320$ of the total power; for a total of 1.985×10^6 Watts.

Figure C.1.2: Cross-section of a GT-MHR fuel element showing coolant and fuel compact channels



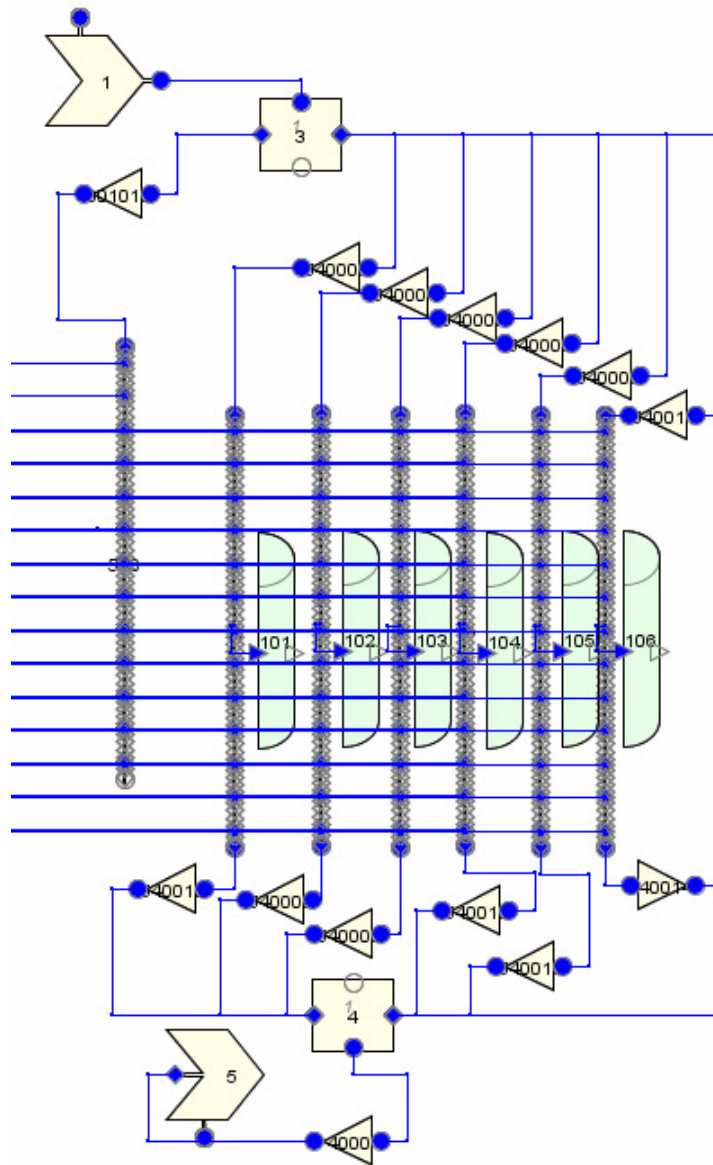
C.2 TRACE Model Description

A transient model with six equivalent channels was developed in TRACE and run using 100% Helium as the working fluid. A representation of the model is shown in Figure C.2.1.

A fill-component was used to inject helium to the upper plenum and a breaker-component was used as a reservoir at the lower plenum. Pipe-components were used to model the cooling and inter-block channels while single-junctions were used to model the leakage between the cooling channel and the inter-block space. A heat structure with 19 radial nodes and three different types of material was used to model the fuel and the graphite.

The fill component injects Helium at 763 K and 7,000 kPa at a rate of 4.763 kg/s to the upper plenum, which is connected to the top of the cooling and inter-block channel. The break is set to the same conditions as the fill and is connected only to the bottom of the cooling channel.

Figure C.2.1: Six channel TRACE model representation



The pipe component, used to model the cooling channel, has 65 cells with a hydraulic diameter of 0.083m and a total height of 10.6m. The inter-block channel, also a pipe component, has the same number of cells and the same height as the cooling channel but has a hydraulic diameter of 0.054m.

The junctions used at the top and bottom connections were set to have a friction factor of 0.5; while the friction factor for the side junctions, simulating the leakage between the cooling channel and the inter-blocks, was set to 3.2.

C.3 Results

Results of the TRACE model are shown in Figures C.3.1 and C.3.2. Figure C.3.1 shows the temperature profile of the steam in the cooling channel and Figure C.3.2 shows the mass flow rate from the inter-block to the cooling channel. Quite similar results were obtained using the RELAP5 model detailed in section 8 (see Figures 8.5.10 and 8.5.12). Further validation of these models could be obtained once experimental results are available.

Figure C.3.1: TRACE results for the gas temperature at the cooling channel and inter-block

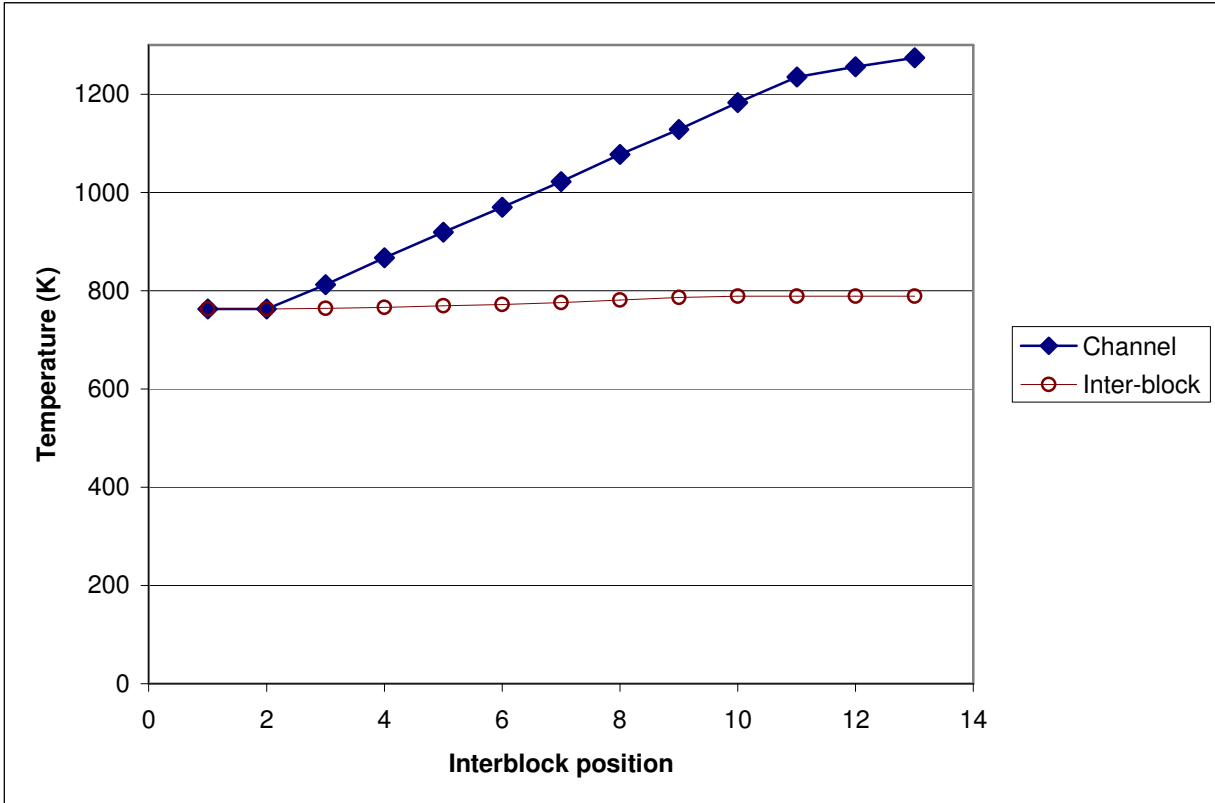


Figure C.3.2: TRACE results for the mass flow rate from the inter-block sub-channel to the coolant channel

